LEABHARLANN CHOLÁISTE NA TRÍONÓIDE, BAILE ÁTHA CLIATH | TRINITY COLLEGE LIBRARY DUBLIN
Ollscoil Átha Cliath | The University of Dublin

Terms and Conditions of Use of Digitised Theses from Trinity College Library Dublin

Copyright statement

All material supplied by Trinity College Library is protected by copyright (under the Copyright and Related Rights Act, 2000 as amended) and other relevant Intellectual Property Rights. By accessing and using a Digitised Thesis from Trinity College Library you acknowledge that all Intellectual Property Rights in any Works supplied are the sole and exclusive property of the copyright and/or other IPR holder. Specific copyright holders may not be explicitly identified. Use of materials from other sources within a thesis should not be construed as a claim over them.

A non-exclusive, non-transferable licence is hereby granted to those using or reproducing, in whole or in part, the material for valid purposes, providing the copyright owners are acknowledged using the normal conventions. Where specific permission to use material is required, this is identified and such permission must be sought from the copyright holder or agency cited.

Liability statement

By using a Digitised Thesis, I accept that Trinity College Dublin bears no legal responsibility for the accuracy, legality or comprehensiveness of materials contained within the thesis, and that Trinity College Dublin accepts no liability for indirect, consequential, or incidental, damages or losses arising from use of the thesis for whatever reason. Information located in a thesis may be subject to specific use constraints, details of which may not be explicitly described. It is the responsibility of potential and actual users to be aware of such constraints and to abide by them. By making use of material from a digitised thesis, you accept these copyright and disclaimer provisions. Where it is brought to the attention of Trinity College Library that there may be a breach of copyright or other restraint, it is the policy to withdraw or take down access to a thesis while the issue is being resolved.

Access Agreement

By using a Digitised Thesis from Trinity College Library you are bound by the following Terms & Conditions. Please read them carefully.

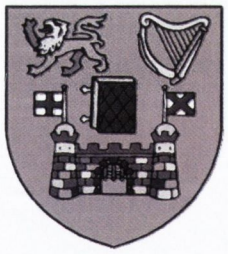
I have read and I understand the following statement: All material supplied via a Digitised Thesis from Trinity College Library is protected by copyright and other intellectual property rights, and duplication or sale of all or part of any of a thesis is not permitted, except that material may be duplicated by you for your research use or for educational purposes in electronic or print form providing the copyright owners are acknowledged using the normal conventions. You must obtain permission for any other use. Electronic or print copies may not be offered, whether for sale or otherwise to anyone. This copy has been supplied on the understanding that it is copyright material and that no quotation from the thesis may be published without proper acknowledgement.

Generation, characterisation and solidification of crystalline microfoams

by
Antje van der Net

A thesis submitted to
The University of Dublin
Trinity College Dublin
for the degree of

Doctor of Philosophy



SCHOOL OF PHYSICS
UNIVERSITY OF DUBLIN
TRINITY COLLEGE

July 2008

TRINITY COLLEGE
0 6 NOV 2008
LIBRARY DUBLIN

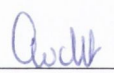
THESIS
8654

Declaration

This thesis is submitted by the undersigned author to the Trinity College Dublin, University of Dublin. It has not been submitted as an exercise for an degree at any other University.

Except where otherwise stated, the work described in this thesis has been carried out by the author alone.

Due to confidentiality obligations to a third party, a five-year stay has been put on this thesis. During that period, this thesis may NOT be consulted, lent or copied without prior written consent of Trinity College Dublin, (through Trinity Research & Innovation, O'Reilly Institute). After 5 years this thesis may be consulted, lent or copied upon request with permission of the Librarian, Trinity College Dublin, University of Dublin.



Antje van der Net

Dublin, July 8^{th} 2008

Summary

This study is centered around the spontaneous ordering of equally sized microbubbles on top of a liquid pool, forming wet crystalline microfoams. This type of ordering was firstly observed by Bragg and Nye in 1947 and only recently taken up for further research.

With the technique 'micro fluidic flow focusing' we created equally sized bubbles ranging between 100 and 800 μm in diameter, using surfactant solution and nitrogen. We found, in agreement with the literature, a dripping and jetting regime, where the bubble diameter D depends on the orifice width O_w times a factor of 1.19 ± 0.20 and ratio of the gas and liquid flow rate Q_g, Q_l to the power of 0.33 ± 0.06. Orifice length, surfactant choice and viscosity in a flow rate controlled device do not influence the bubble size. We observed a 'squeezing regime' at low gas and liquid flow rates hindering the microbubble generation, dependent on the entrance geometry, with bubbles created in the order of mm. This points out that geometry plays a role in the performance of the bubble generator and should be further investigated in the future.

Fractal optical patterns at the surface of the crystalline foams were used for extraction of information on the ordering of the bubbles by the use of computational ray tracing techniques. A self-developed 2D backwards ray-tracing program was used to derive analytic relations between visible patterns and the actual foam geometry. This showed that bubbles are visible by an optical ring slightly smaller than their perimeter. For multiple layers, the bubbles behave as divergent lenses projecting optical patterns of lower layers inside their own patterns. Light source position, dimensions and camera settings are critical. A 3D commercial ray-tracing software was used to compute optical images related to more complicated input geometries and experimental set-ups.

The wet crystalline microfoams were found to consist of grains ordered in familiar crystalline structures fcc(111), fcc(100) and hcp, at least for the first 3-5 layers at the flat gas-foam surface and the foam-liquid interface, where terraces were present. Based on analysis of the interfaces fcc was with 60% prevalence the most frequent occurring crystal. How the system finds the optimal packing with the preference for fcc is unknown. Preliminary simulations suggest templating and deposition rate are not solely resulting in crystalline foams. Other factors that need further investigation are the influence of stress and hydrodynamics. Ordering could be forced in confined systems as wedges and parallel plates up to 4-5 layers. A distinction could be made between triangular (fcc(111) and hcp) and square top layers (fcc(100)). Dry ordered foams were made by draining the ordered wet structures, resulting in dried fcc/hcp structures and Kelvin cells up to 8 layers.

Crystalline microfoams exposed to the atmosphere did not remain ordered for longer than 30 minutes. Due to gas diffusion into the atmosphere bubbles in the top layer started to shrink immediately after deposition. This created space, resulting in the creation of bidisperse top layer. This process could repeat up to 5 times. The diffusion rate was found linearly dependent on the number of layers up to 25 layers. This is possibly due to an increase in area of the top film either by the extra force from the layers below or by the decreased liquid fraction of the films.

The lifetime of the crystalline microfoams was extended by solidification using ingredients for a radical polymerisation reaction creating a super absorber. Foam polymerisation was obstructed by phase separation between the polymerisable ingredients and the foamed solvent. This was overcome by applying a recipe with a fast polymerisation speed of 11 seconds. The standard bubble generator was adapted for dual solution injection, with mixing occurring inside the bubble generator and reaction starting right before the actual bubble generation. This led to the successful generation of multiple layers of polymerised foams and threads. The sample size was limited by the polymerisation time and bubble production. The foamed super absorbers showed quicker liquid absorption than their non-foamed variant. This could become of great use in applications. Phase separation will need better understanding to extend the range of polymer products and increase the sample size.

Foam production is not always preferred. We explored the breaking of crystalline microfoams with the use of static electricity. First shown by Taylor, semi-hemispherical bubbles undergo an instability if the accumulated electrostatic charge reaches a critical limit such that the electrostatic forces overcome the counteracting surface tension. The instability results in the deformation of the bubble into an ellipsoid, where from the tip charged droplets are ejected and child bubbles are created at different stages of the instability. These showed large similarities with modes in electro-spraying. The charged bubbles could be used as a macroscopic comparison and to further explore the exact mechanism behind this technique. When a foam was charged the same instabilities occurred at the surface, where one by one the bubbles were broken. For dry foams the instabilities occurred randomly at the surface while for wet foams, a peak was formed which attracted bubbles that subsequently broke. We believe that these initial findings have the potential to be developed into a new method for foam-breaking.

In summary, this thesis has revealed some of the unique properties of crystalline microfoams, together with their potential for exciting applications, as templates for solidified foamed materials, enabling development of new liquid absorbers and lightweight materials.

Acknowledgements

To this work contributed directly or indirectly many who I would like to thank. First of all my supervisor Stefan Hutzler and very closely involved Wiebke Drenckhan, vielen Dank! I would like to thank also Denis Weaire for all the critical remarks and advice and for solving my housing emergency, Anthony Saugey for modelling advice in Matlab, Peter Whittaker for starting up the 3D Studio Max simulations, William Rossen for pointing out the images of aphrons, James Hilton for the collaboration on the Rayleigh instability.

I am very grateful to Ronan Daly, Joe Barry and Wiebke Drenckhan for proofreading my thesis. I would like to thank the remaining members of foam group who I did not mention yet, who came and went over the years and made the work in the office and lab interesting and enjoyable; Paul McGuinness, Gary Delaney, Eric Janiaud, Vincent Langlois, Vincent Carrier, Mohammad Saadatfar, Ricardo Coelho and Stephen Hardiman. Do not forget the 666 students eating sushi in a space shuttle!

Thanks to the technicians and glassblower John Kelly in the School of Physics, who created some nice equipment. Thanks to Fiona Lyng in the Dublin Institute of Technology for testing foam visualisation with their confocal microscope. I would like to thank Pacelli Zitha and Ilse van Kesteren helping me out of my PhD midlife crisis. Thanks to Margaret Woods and Naoise Gaffney for sorting out my patenting issues. The involvement of the summer students Ludivine Blondel, Niall Cullinane and Aaron Meagher are much appreciated.

I am very grateful for the invitation of Francois Graner to visit his group in the Université Joseph Fourier in Grenoble, France. Thanks as well to Philippe Marmorante, Christhophe Raufaste, Jan-Paul Raven and Jos Käfer. Related to the collaborating project with BASF initiated by Wiebke Drenckhan I like to thank Meik Ranft for the collaboration and hosting my visit in BASF in Ludwigshafen and Alex Gryson as a nice lab partner. Also the help and efforts of Florence Elias and Cosima Stubenrauch are greatly appreciated.

Further more thanks to all the soccer girls, people from the pottery class and housemates, who made my stay in Ireland a great experience. Last but not at all least my family; mam, pap en Hilde, ver weg maar toch ook dichtbij, bedankt voor alles, veel liefs Antje!

This work was financed by the Science Foundation Ireland (RFP05/RFP/PHY0016). Additional financial support was received from BASF for the foam polymerisation project.

Contents

1 Introduction **1**

1.1 Foams everywhere 1

1.2 Important parameters of foam 2

1.3 Structure of the thesis 8

2 Generation of Microbubbles **11**

2.1 Introduction 11

2.2 Overview of methods for the generation of monodisperse bubbles 13

2.3 Our experimental set-up 20

2.4 Visualisation of the bubble regimes 23

2.4.1 Squeezing regime 23

2.4.2 Dripping regime 24

2.4.3 Jetting regime 26

2.5 Calibration of the bubble generator 26

2.5.1 Squeezing regime 28

2.5.2 Dripping-Jetting regime 31

2.6 Discussion 36

2.7 Conclusions and Outlook 37

3 Simulating and interpretating images of bubbles with computational ray-tracing techniques **39**

3.1 Introduction 39

3.2 Experimental set-up 42

3.3 Computational Method 43

3.3.1 General input parameters and assumptions 44

3.3.2 Ray-tracing 46

3.3.3 Simplified 2D ray path visualisation model 47

3.3.4 Practical application of the method 49
3.4 Individual bubble 49
3.5 Two touching bubbles 51
3.6 Bubble layer 52
3.7 Two layers 53
3.8 Wet bubble crystals 55
3.8.1 Hcp(0001) 55
3.8.2 Fcc 56
3.9 Variations on the implemented foam properties 58
3.10 Conclusions and Outlook 59

4 Ordering of microbubbles in the wet foam limit **63**
4.1 Introduction 63
4.2 Experimental set-up and procedure 64
4.3 Crystal Structure 66
4.4 Imperfections 68
4.5 Terraces 70
4.6 Statistics on the occurrence of crystalline structures 72
4.7 Mechanism of crystallisation 74
4.7.1 Experimental observations 74
4.7.2 Numerical simulation of frictionless hard spheres 76
4.8 The tendencies of systems to order 78
4.9 Order by confinement 83
4.10 Formation of dry ordered foams 89
4.11 Conclusions and Outlook 91

5 Rearrangement and elimination of ordered surface layers of crystalline bubble structures due to gas diffusion **95**
5.1 Introduction 95
5.2 Experimental method and analysis 96
5.3 The creation of bidisperse top layers 98
5.4 Diffusion rate 105
5.4.1 Basic model 106
5.4.2 Diffusion rate of single bubbles and monolayers 108
5.4.3 Modeling of 3D bubble crystal diffusion 112
5.4.4 Discussion 114
5.5 Conclusions and Outlook 117

6 Polymerisation of ordered foam structures **119**
6.1 Introduction . . . 119
6.2 Materials . . . 121
6.2.1 Chemical composition . . . 122
6.2.2 Foam stability . . . 123
6.2.3 Role of the polymerisation time . . . 123
6.3 Mixing of ingredients within the bubble generator . . . 126
6.4 Generation of ordered polymerised foam structures . . . 129
6.5 Hydrogel foams as super-absorbers . . . 133
6.6 Discussion . . . 134
6.7 Conclusions . . . 136
6.8 Outlook . . . 137

7 Foam rupture by static electricity **141**
7.1 Introduction . . . 141
7.2 Principles of the Rayleigh instability . . . 142
7.3 Experimental method . . . 144
7.4 A charged hemispherical bubble . . . 146
7.4.1 Experimental observations . . . 146
7.4.2 Experimental estimation of the critical voltage . . . 148
7.4.3 Simulations . . . 150
7.4.4 Discussion . . . 151
7.5 Break-up of foams . . . 153
7.5.1 Macrofoam . . . 154
7.5.2 Microfoam . . . 155
7.5.3 Discussion . . . 159
7.6 Conclusions and Outlook . . . 160

8 General conclusion and outlook **163**

A Simulating and interpretating images of surface Plateau borders with computational ray-tracing techniques **169**
A.1 Surface Plateau borders . . . 169
A.2 Experimental set-up . . . 170
A.3 General description of the geometry and patterns . . . 171
A.4 Regime I . . . 174
A.4.1 Infinite light source . . . 174

A.4.2 Special case: Finite light source 177
A.5 Regime II 181
A.5.1 Pair 1 181
A.5.2 Pair 2 181
A.5.3 Pair 3 183
A.6 Influence of the glass-plates 185
A.6.1 Refraction 185
A.6.2 Total reflection 185

B Coherent grain boundaries **191**

C Derivation of equations for the diffusion model **195**
C.1 Derivation of Equation 5.1 195
C.2 Derivation of Equation 5.2 196
C.3 Derivation of Equation 5.4 197
C.4 Taylor expansion of Equation 5.4 200

D Foam solidification **203**
D.1 Preliminary results on generation of gelatine foam and frozen foam 203
D.1.1 Gelatine foams 203
D.1.2 Frozen foam 204
D.1.3 Discussion 205
D.2 Role of polymerisation time 205
D.3 Investigation of parameters controlling the phase separation in the radical polymerisation 209

List of Publications

The following articles resulted from the research presented in this thesis.

1. A. van der Net, L. Blondel, A. Saugey, W. Drenckhan, "Simulating and interpretating images of foams with computational ray-tracing techniques", Journal of Colloids and Surfaces A: Physicochemical and Engineering Aspects 2007, 309, 1-3, 159-176.

2a. A. van der Net, W. Drenckhan, D. Weaire and S. Hutzler, "The crystal structure of bubbles in the wet foam limit", Soft Matter, February 2006, 2, 129-134.

2b. A. van der Net, W. Drenckhan, D. Weaire, S. Hutzler, "The crystal structure of bubbles in the wet foam limit (vol 2, pg 129, 2006), correction", Soft Matter, June 2006, 2, 523-523.

3. A. van der Net, G. W. Delaney, W. Drenckhan, D. Weaire, S. Hutzler, "Crystalline structures of wet microbubbles" Journal of Colloids and Surfaces A: Physicochemical and Engineering Aspects, 2007, 309, 1-3, 117-124.

4. A. van der Net, D. Weaire, S. Hutzler, "Rearrangement and elimination of ordered surface layers of crystalline bubble structures due to gas diffusion", submitted.

W. Drenckhan, M. Ranft, A. van der Net, A. Gryson, "Ordered fluid foams as templates for new cellular fibers", Feasibility study for BASF, Ludwigshafen, Germany.

5. A. van der Net, A. Gryson, M. Ranft, F. Elias, C. Stubenrauch, W. Drenckhan, "Fancy jumpers from ordered, polymerised soap foams?", submitted.
Patent application submitted.

6. J. Hilton, A. van der Net, "Rayleigh Plateau instabilities in charged hemispherical soap bubbles", submitted.
Foam rupture by static electricity; Orienting on the possibilities of patenting.

Further publications

7. S. Hutzler, D. Weaire, S. J. Cox, A. van der Net and E. Janiaud, "Pre-empting Plateau:

The nature of topological transitions in foam", Europhysics Letters, 77, 28002, 2007.

8. W. Drenckhan, H. Ritacco, A. Saint-Jalmes, A. Saugey, P. McGuinness, A. van der Net, D. Langevin, D. Weaire, "Fluid dynamics of surfactant rivulets between vertical plates", Physics of Fluids, 19, 102101, 2007.

9. S. Hutzler, M. Saadatfar, A. van der Net, D. Weaire, S. J. Cox, "The dynamics of a topological change in a system of soap films", Journal of Colloids and Surfaces A: Physicochemical and Engineering Aspects, 323, 123-131, 2008

Chapter 1

Introduction

1.1 Foams everywhere

People know how to enjoy foams; sitting in a bubble bath, drinking a beer, eating chocolate mousse or even singing about it like the West Ham United fans do with their anthem 'I'm forever blowing bubbles' (written by Jaan Kenbrovin in 1918). Foams or soap froths are dispersed gas bubbles surrounded by a continuous liquid phase. In Figure 1.1 further examples show the use of foams in daily life.

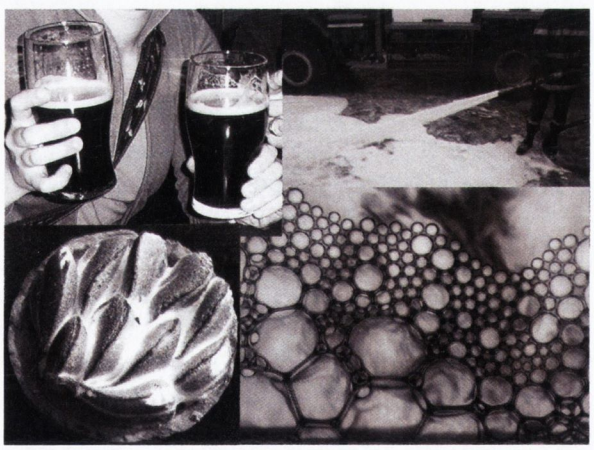


Figure 1.1: Examples of foams in daily life. Beer, fire fighting foams, mousse and foams as a form of art.

Lesser known are the applications of foams in industrial processes. For example in the petroleum industry foams are used to stimulate oil recovery by foam injection into an oil reservoir to push the oil out. Foams are also used to break rocks to make fresh fractures in oil wells. In the mining industry foams are used to separate minerals. By bubbling gas

through a liquid containing ore particles, hydrophobic ore particles are taken with the bubbles, forming a foam which can be easily separated from the remains of the liquid containing the hydrophilic particles. This process is named froth flotation.

So far we mentioned examples where foams are be used for a specific purpose and where foam occurrence is stimulated. However, the creation of foams or their excessive presence is not always desirable. For example antifoaming agents are included in laundry powders to restrict the amount of foam created. In industrial applications foams can reduce flow efficiency through pipes [1].

Foam research is therefore focused both on creation of foams and avoidance of foams. Aside from the practical applications, foams are of value to obtain more insight into the fundamental behaviour of other physical systems, e.g. solids and fluids, for example in the area of crystallisation as we discuss later.

1.2 Important parameters of foam

Gas, liquid, a stabilising agent and some kinetic energy are the key elements required to form a foam: a dispersed gas phase surrounded by a continuous liquid phase in the form of films, stabilised by surfactant molecules. The surfactant molecules generally consist of a hydrophilic polar head and a hydrophobic non-polar tail. Therefore it is energetically favourable for them to settle at the gas-water interface. This decreases the surface energy of the entire system as strong water bonds will not be present at the surface anymore. The lower the surface tension of the liquid is, the more stable is the system. Fairy Liquid®[1] is the predominant stabiliser used for the creation of the foams described in this thesis, as it forms very stable foams compared with pure surfactants.

The surface tension of a liquid depends on the concentration of the surfactant, its temperature and its salt concentration [2]. In Figure 1.2 the variation of the surface tension as a function of the concentration of the commercial detergent Fairy is shown. The measurements were performed using the Du Nouy ring method [3], where surface tension is the maximum force needed to detach a ring from the liquid surface. At the initial stage of adding surfactant, the surfactant molecules fill the surface and therefore decrease the surface tension. Once the surface is covered, the excess surfactant molecules start to form micelles in the bulk liquid (spherical aggregate of the surfactant molecules with the hydrophylic heads pointing outwards, see inset in Figure 1.2), this will not decrease the surface tension any further. The

[1] produced by Procter and Gamble, UK

minimum concentration needed to obtain the lowest surface tension is the *critical micelle concentration* (CMC). For Fairy this was determined to be at a volume fraction [surfactant volume/solvent volume] of 1×10^{-3}. The minimum surface tension is then 27.0±0.2 mN/m. In all the samples created we used a concentration of ten times the CMC of Fairy.

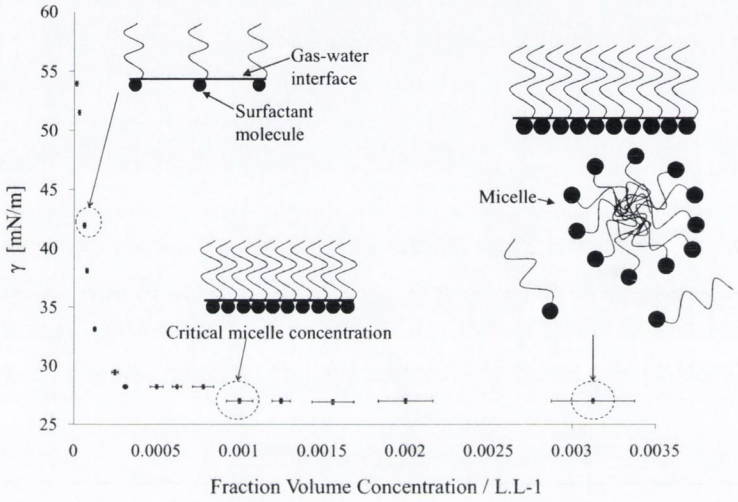


Figure 1.2: The variation of the surface tension γ of water as a function of increasing concentrations of the commercial detergent Fairy Liquid. The insets show the change in occupation of surfactant molecules at the surface with increasing surfactant concentration.

An important parameter of foam is its *liquid fraction* ϕ, defined as the ratio between the volume of liquid and the total volume of the foam. When a foam contains only a small amount of liquid (less than 18%) the bubbles form polyhedral shapes and the foam is defined as *dry*, see Figure 1.3. The faces are thin films and a *Plateau border* is formed where the films meet.

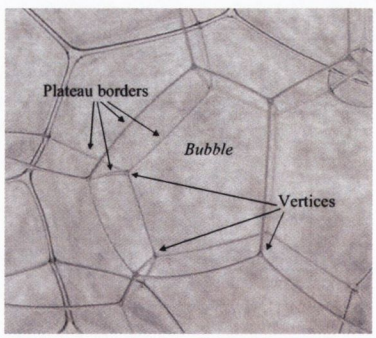


Figure 1.3: Dry foams consist of *Plateau borders* (lines), where 3 films meet and *vertices* (points), where four Plateau borders meet.

According to Plateau's rules [4] in dry foams only three films can meet in a Plateau border with angles of 120^o between them. Four Plateau borders meet in a *vertex* with an angle of acos(-1/3)$\approx$ 109.43^o relative to each other. With increasing liquid fraction the Plateau borders, vertices and films fill with more and more liquid, resulting in bubbles which get increasingly spherical. In a wet foam the bubbles are almost spherical. If the liquid fraction is increased even further, bubbles lose contact and form a *bubbly liquid.*

A foam is considered wet with a liquid fraction above 18% [5]. The balance between capillary suction from the Plateau borders between the bubbles and gravity determines the liquid fraction in a foam at equilibrium. Once a thick layer of small bubbles has been created, the foam does not expel liquid under gravity to the same extent as one containing larger bubbles. It remains wet (close to the wet limit where the bubbles are spherical) up to a height h above an underlying liquid surface, given by the capillary length l_o , defined by

$$l_o^2 = \frac{\gamma}{\rho g}, \tag{1.1}$$

where γ is the surface tension [N/m], ρ is the density of the liquid $[kg/m^3]$ and g is the gravitational acceleration $[m/s^2]$ [5]. For Fairy Liquid based foams this length is about 1.6mm, similar to the pure surfactant Sodium Dodecyl Sulfate (SDS). Foams consisting of such small bubbles remain wet for a considerable number of layers of bubbles N, which can be estimated as $N \simeq \left(\frac{l_0}{d}\right)^2$ [5], where d is the bubble diameter.

Wet foams

Until recently, most research interest in foams has focused on the study of relatively dry samples ($\phi < 10\%$). However, advances in the area of microbubble generation (particularly flow focusing techniques, see Chapter 2) has allowed for the generation of extremely small (<100 μm) monodisperse bubbles [6–8], and thus for the generation of 3D wet foams of which an example is shown in Figure 1.4. Formation of microbubbles has applications in inkjet printing, drug delivery, microfluidics based lab-on-chip technologies, optical devices and new insulation materials [7, 9–14]. We will characterise in Chapter 2 our microfluidic flow focusing device.

Crystalline structures

In crystallography ordered structures are described, named crystals, for example atomic crystalline structures. Similarly ordered structures are observed made of the equally sized bubbles in the wet microfoams, the main focus of this thesis, which will be discussed in Chapter 4. The *unit cell* characterises the crystalline structures by its smallest repetitive structure. The

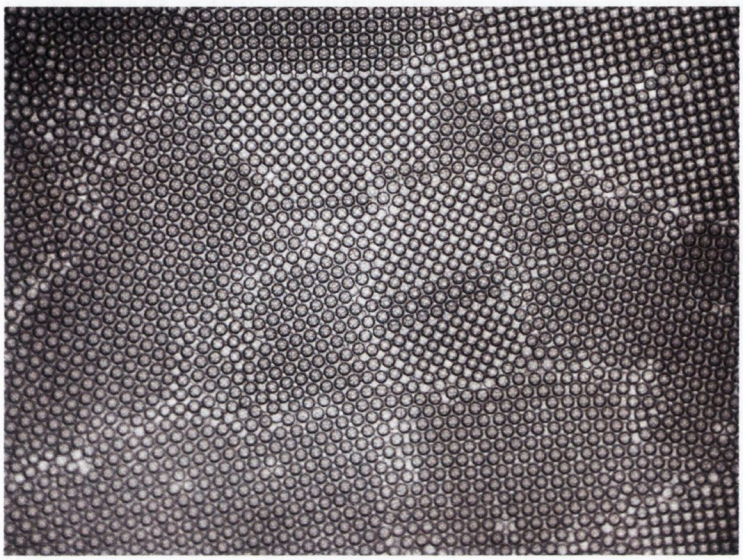


Figure 1.4: An example of an wet crystalline microfoam, the focus of this thesis.

three different structures of relevance to the work in this thesis are body centered cubic (bcc), face centered cubic (fcc) and hexagonal closed packed (hcp), the latter two are found in microfoams. In Figure 1.5 their unit cells are shown. The different planes in the structures are

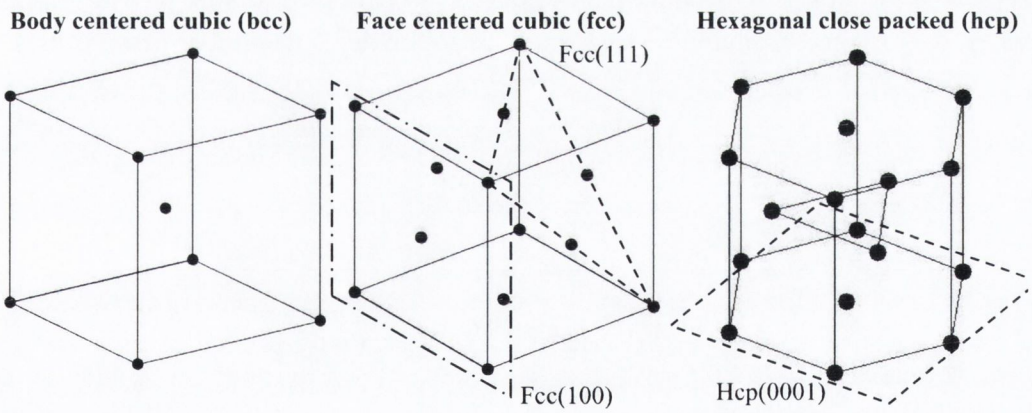


Figure 1.5: The unit cells of the crystalline structures body-centered cubic (bcc), face centered cubic (fcc) and hexagonal closed packed, (hcp).

named according to the Miller index, where the numbers represent the reciprocal values of the coordinates of intersection with the axes, see e.g. Figure1.5(b) where the planes fcc(100) and fcc(111) are marked, which are the two common occurring planes we see at the surface of microbubble crystals. Note that the notation with [ ] brackets presents the vector normal

to the plane. Fcc(111) and hcp(0001) planes form triangular packed layers, which can be positioned in 3 different ways, which are labeled A,B and C. For fcc(111) the triangular layers are stacked ABCABC.. and for hcp(0001) they are stacked ABABABA... Fcc(100) planes show a square structure toplayers. When we talk about crystalline microfoams we refer to a collection of different crystals, which are ordered in a particular crystalline structure. The different crystals can also be called grains, which are separated by grain boundaries.

Dry ordered foams

In contrast to wet ordered foams, dry ordered foams are more difficult to obtain. As explained in [5] and following from Equation 1.1, foam becomes dry when its height grows above its capillary length. Water drains out of the films causing the bubbles to deform into polyhedral shapes. For a long time it was thought the most optimal structure (based on surface minimisation) for packing dry three dimensional monodisperse bubbles was the Kelvin cell, a tetrakaidecahedron, with six four sided faces and eight hexagonal sided faces, see Figure 1.6. In 1994 a new structure was found to have a slightly lower surface energy; the Weaire-Phelan structure, a combination of two cell types with five and six sided cells. Unfortunately this structure has only been partly viewed once experimentally [5]. The Kelvin cells are less rare as they can be easily created when being confined, where the boundaries stimulate high order. Generally bubbles do not order, when they are flowing into a large vessel, even though they are equally sized. When controlling the placing of the bubbles [15] bulk Kelvin cells can be made. We will show in Chapter 4 an easy way to create dry ordered foam strucutures.

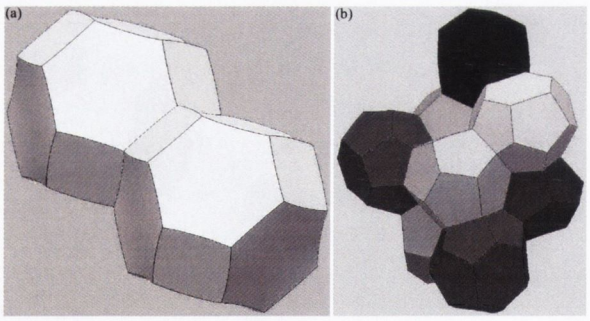


Figure 1.6: (a) The Kelvin cell and (b) the Weaire-Phelan structure, 14 cells of two cell types with five and six sided cells. Images are generated with the surface minimisation program Surface Evolver [16].

Tendency to order

Why some systems in nature find order and others do not has for many centuries been a very intriguing question. It is surprising that monodisperse bubbles in wet foams order almost

perfectly in three dimensions, especially when we compare them to similar systems. Examples of such comparable systems are shown in Figure 1.7; monodisperse dry foams, monodisperse emulsions, spherical monodisperse granular materials and hard sphere colloidal suspensions. Bubbles in dry foams and spherical grains in granular matter become jammed as soon as they are deposited. They do not find the optimal ordering, unless deposited in a special way they order. Colloids order, but it takes days to weeks while for bubbles the rearrangements and ordering occur instantly. Compared with colloids bubbles are macroscopic and do not undergo Brownian motion to rearrange. In Chapter 4 we go into more detail on this comparison, showing the uniqueness of crystalline microfoams.

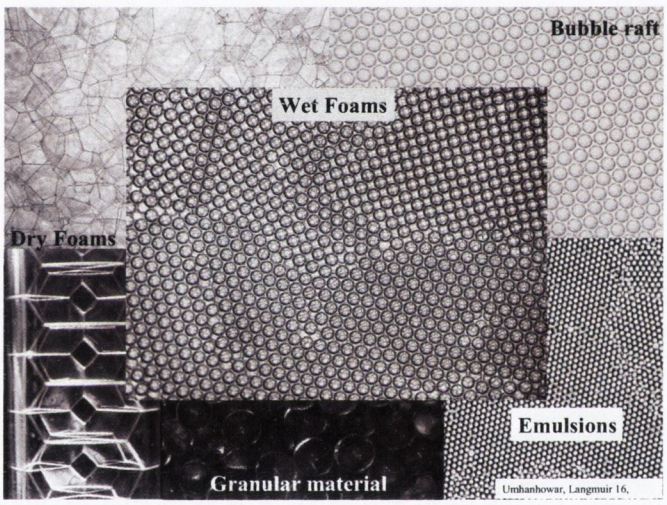


Figure 1.7: Wet foams and similar systems. What causes wet foams (center of image) to order so easily? Examples of ordered packings: ordered 2D bubble raft, confined dry foams and emulsions and examples of disordered packings: dry foams and granular materials.

Coarsening and Drainage

Foam is a metastable system, which evolves in time. This is visible for example when a beer stands for too long and the foam disappears. Two processes play a large role in the evolution or aging of foams.

Firstly, small bubbles disappear due to *diffusion* of gas from small bubbles to larger bubbles. The larger bubbles expand and small bubbles disappear. This process is named *coarsening*. Bubbles with a smaller radius have a higher gas pressure according to the Young-Laplace equation:

$$P_g - P_w = \frac{2\gamma}{R}, \tag{1.2}$$

with P_g the gas pressure inside the bubble, P_w the pressure of the surrounding water, γ the

surface tension and R the radius of the bubble. Gas permeates from bubbles with high gas pressures (smaller bubbles), through the liquid film into bubbles with lower pressure (larger bubbles), leading to the eventual disappearance of the smaller bubbles. The diffusion rate depends highly on the solubility of the gas in the liquid and the gas concentrations in the case of gas mixtures. For example by the use of perfluorhexane with nitrogen, the diffusion can be slowed down.

Secondly, the breaking of the films due to *drainage*, plays a role [6, 17]. Water can drain out of the foam due to gravity, thus thinning the films of the bubbles to the minimum thickness of $\sim 5\ \mu m$, the Newton black film [5]. Thinner films are more sensitive to mechanical disturbance and break sooner.

The aspects of coarsening, drainage and diffusion have been extensively studied in foam research. In this thesis we will generally consider foams before the onset of coarsening. A special kind of diffusion, occurring between the top layer of our bubble crystals and the atmosphere, is discussed in Chapter 5.

1.3 Structure of the thesis

The central subject of this thesis is the exploration of the unique crystalline microfoams, first observed by Bragg and Nye in 1947 [18]. Their work was mainly centered around dynamics of a crystalline single bubble layer floating in a water surface (a bubble raft, see Figure 1.7), used as a model for crystalline structures of metals. However, they mentioned observations of 3D ordered crystalline microfoam. Bragg and Nye did not subsequently pursue this area of research into ordered crystalline microfoams and nor did anyone else at that time [19]. Using new bubble generation techniques together with various methods of image analysis, including our newly developed method described in Chapter 3 based on computational ray tracing techniques, it has now become easier to investigate the properties of very wet foams. This allowed us [20] and others [21] to follow up the work of Bragg and Nye. We have extended the work on the surprising observations of ordering in Chapter 4 and consider new aspects, as will be discussed throughout this thesis.

In the Chapter 2, we explain microfluidic flow focusing, the now common method of equally sized microbubble generation. This will contribute to a better understanding of the physics behind the method, which is currently not fully understood. Chapter 3 is the novel method of the use of computational raytracing techniques to extract information on foam structures from their optical images.

1.3. STRUCTURE OF THE THESIS

In the main part of the thesis, Chapters 4 and 5, we discuss the characterisation of crystalline microfoams. We report details of the different crystalline structures and structural defects which are formed by the equally sized microbubbles. We show that we can use confinement to force the microbubbles into crystalline structures in specific orientations. We will see also how diffusion causes the disappearance of the top layers of the crystalline microfoams in a highly ordered sequence.

After generation and characterisation of the foam it is considered how we might use the knowledge gained. In Chapter 6, we discuss the use of microfoams for the first successful creation of ordered polymerised foam structures. This will conserve the structure beyond effects of coarsening and drainage. In Chapter 7 we finish with the discussion of a newly found method for the destruction of the microfoams by the use of static electricity. This method will decrease the foam life time severely, for the cases where foams are unwanted.

Chapter 2

Generation of Microbubbles

2.1 Introduction

Traditional methods of foam generation, such as beating, whipping or release of dissolved gas in an over-saturated liquid, result in polydisperse foam. To achieve monodispersity, a nozzle (such as that of a syringe) may be used to issue bubbles one at a time below a liquid surface [5] at a required constant gas pressure. It is generally necessary to maintain a low rate of bubble generation, as the process of bubble detachment can become chaotic at higher rates [22].

Already in 1947 Bragg and Nye [18] realised that the size of monodisperse bubbles can be drastically reduced by having a co-flow of gas and liquid. They used a rotating box filled with surfactant solution and with a needle dipped into it, as shown in Figure 2.1. The rotating liquid created a drag along the outlet of the needle, which enabled them to make bubbles between 100 and 700 μm in diameter.

Smith in 1949 [23] developed this concept further by designing a system where a gas jet is focused by a nozzle into a surfactant solution flowing through another nozzle (Figure 2.2) under a constant hydrostatic head, creating bubbles as small as 120 μm in diameter.

Perrin in 2000 [24] used shearing of polydisperse foams to generate monodisperse foams with bubble diameters of 30 μm. Ganan-Calvo *et al.* [7, 9, 10, 25] re-invented Smith's technique and named it *microfluidic flow-focusing*. They presented the first detailed experiments and theory on flow-focusing for microbubbles, which was taken up afterwards by many others [6, 8, 12, 14, 26–30] due to its relevance in academic research and industrial applications.

Typical applications for such microbubbles and similarly created microdroplets are in inkjet printing, drug delivery, microfluidics based lab-on-chip technologies, optical devices

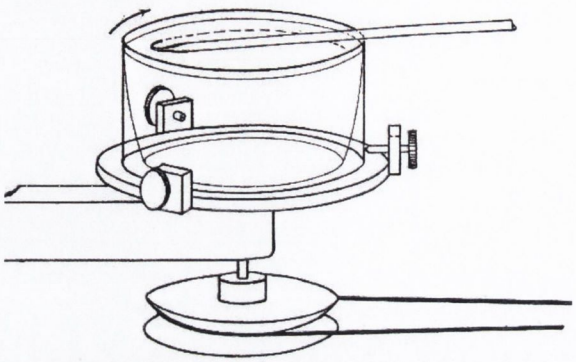


FIGURE 3. Apparatus for producing bubbles of small size.

Figure 2.1: The sketch made by Bragg and Nye [18] of the set-up they used to create monodisperse bubbles. A needle was placed in a rotating beaker, blowing bubbles into the rotating liquid, with speeds of up to 180 cm/sec of liquid flow along the needle.

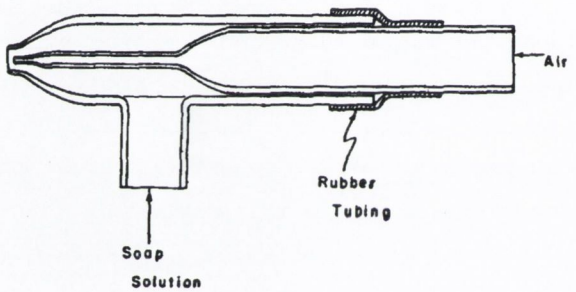


FIG. 1. Nozzle for blowing small soap bubbles.

Figure 2.2: Image from the article of Smith in 1949 [23] showing his device proposed to create monodisperse bubbles; the first 'flow-focusing device'.

and new insulation materials [7, 9–14].

Following the lead of Ganan-Calvo and others, we applied the technique of microbubble generation to create samples of foams, consisting of equal sized bubbles. These equally sized microbubbles order in familiar crystalline structures, which we discuss extensively in the following chapters. In this chapter we discuss the generation of the equally sized microbubbles. Firstly, we will give an overview of the different methods described in the literature, including the different regimes under which microbubbles can be created. Secondly, in Section 2.4 we visualise the different regimes possible in our bubble generation device. This is followed by a calibration of the device in Section 2.5, where we explore the dependence of bubble size on different parameters.

2.2 Overview of methods for the generation of monodisperse bubbles

Here we provide an overview of currently used methods for generation of highly monodisperse bubbles.

We classified the methods of monodisperse bubble generation based on whether the continuous phase flows, and if so, in what direction compared to the dispersed phase. For the generation of bubbles the continuous phase is liquid and the dispersed phase is gas. This results in the following categories summarised in Figure 2.3, independent of whether bubbles are formed in either quasi-two or three dimensional bubble generators.

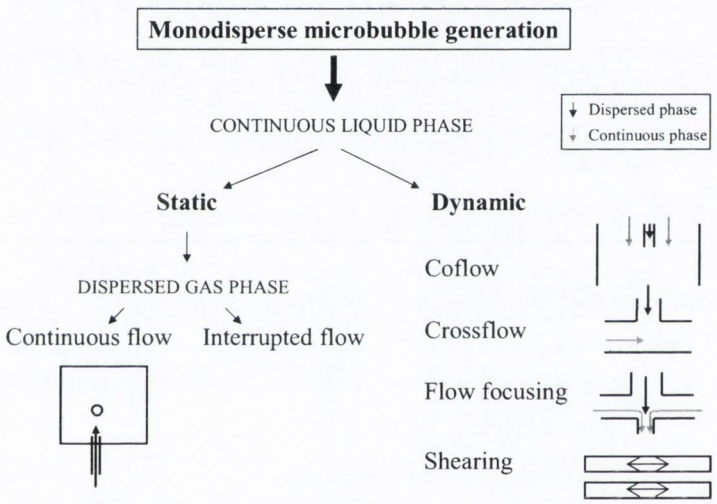


Figure 2.3: An overview of our classification of the general methods of generation of monodisperse micro-bubbles (or droplets). The first separation is based on whether the continuous phase flows. If it does not the flow characteristics of the dispersed phase determine the sub-categories. If the continuous phase flows, the geometry determines the sub-categories.

Note that the methods used for bubble generation are used as well for droplet production, so the above categories apply to both.

Static liquid phase

In this category the liquid does not flow, only the gas phase flows. We can further distinguish between methods where the flow of the liquid phase is continuous or interrupted:

Continuous flow of the gas phase

In this scenario the gas flows into a static liquid phase e.g. blowing gas bubbles with a needle

placed in a liquid pool. (bubbles [31–34], for droplets [35]). The bubble size depends on the needle size, gas flow rate and viscosity. The smallest bubbles to our knowledge made with this method are approximately 130 μm [31]. Two different bubble regimes are possible dependent on the flow rate of the gas,

1. *Dripping*

   Once the gas flows out of the needle the gas is pinched off close to the needle outlet, due to a balance of surface tension and buoyancy forces [31]. Two stages within the bubble generation at the dripping stage can be distinguished, as seen in Figure 2.4; an expansion phase (a), where the gas-liquid interface grows outside the needle and expands in all directions, forming a spherical interface if gravity has no influence. This is followed by a detachment/collapse phase (b). No expansion occurs in this stage, only the neck grows slightly along the flow direction, where the expanded gas-liquid interface is attached to the needle and then breaks just below the expanded section.

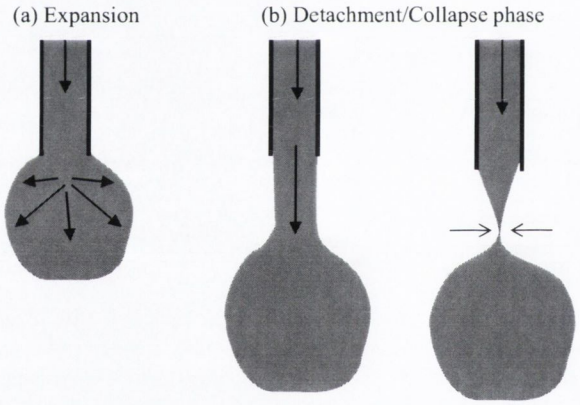


Figure 2.4: The two stages in the dripping regime of bubble generation within a static liquid phase: (a) the expansion phase and (b) the detachment and collapse phase.

2. *Bubbling jet*

   A gas jet is formed outside the needle, which breaks up into bubbles according to the Rayleigh-Plateau instability [36], see Figure 2.5. The gas rates are subsonic (below the speed of sound $\sim$344 m/s).

Discontinuous flow of the gas phase

In this second sub-category of the static liquid category, the gas flows into a static liquid phase in constant and discrete volumes. This is how bubbles are generated with the Microdisperser© device [37] (originally designed and calibrated for droplet generation). The

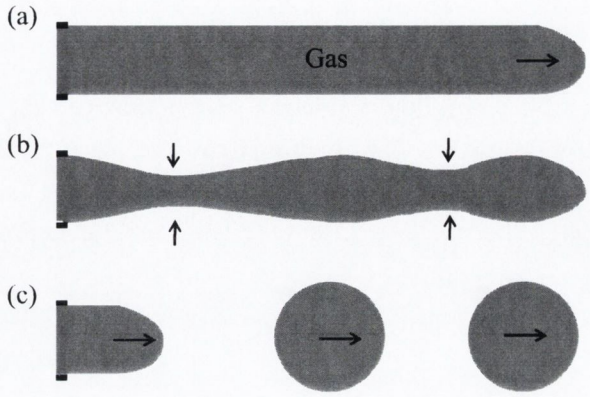


Figure 2.5: A sketch of the formation of bubbles according the Rayleigh-Plateau instability in the 'bubbling jet' category. (a) A jet is formed which becomes unstable when its length exceeds the jet circumference (b) and breaks up in monodisperse bubbles (c).

device consists of a needle connected to a gas reservoir. Inside the reservoir, the influx of gas into the needle is regulated by a movable magnet. The magnet is controlled by a coil surrounding the reservoir, as shown in Figure 2.6. The opening time regulated by the magnet and the applied pressure in the gas reservoir determines the bubble size and frequency. The minimum bubble diameter that could be generated by the microdispenser device was 600 μm.

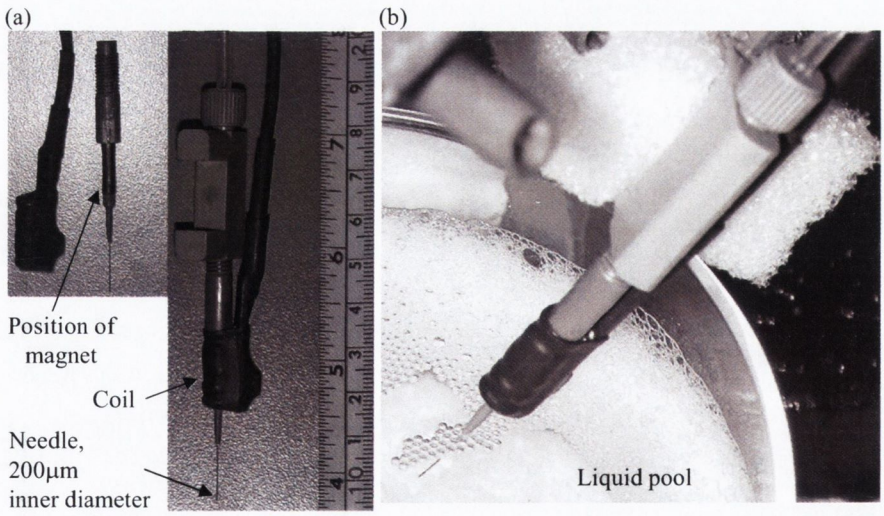


Figure 2.6: The microdisperser with all the parts indicated (a) and as being used in an experiment (b).

Dynamic liquid phase

In this second category both the liquid and gas phases flow during the bubble generation. In general the bubbles become smaller as the extra drag force from the liquid flow forces the bubbles to pinch off quicker. A subdivision can be made here based on the geometrical differences between the bubble generator designs. Four sub-categories can be distinguished:

1. **Co-flow** (bubbles [18, 32, 38, 39], droplets [11])

The gas phase flows out of a needle into a flowing liquid phase, as seen in Figure 2.7. Generally

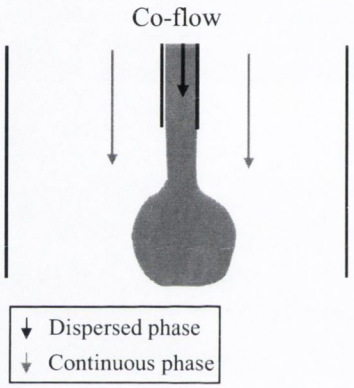


Figure 2.7: The co-flow method for the generation of monodisperse micro-bubbles or -droplets

the ratio between the needle diameter and the outer channel/box diameter is < 0.27, meaning the continuous flow is barely influenced by the boundaries. One example is the blowing of bubbles with a needle into a rotating beaker as demonstrated by Bragg and Nye in 1947 [18], see Figure 2.1. The minimum bubble size made with this method created to our knowledge is 40 μm [32]. As in the static situation we can also distinguish two stages within the co-flow bubble generation [32, 38, 39] at low flow rates. These are: (a) an expansion phase where the jet outside the needle grows out in all directions and (b) a detachment/collapse phase where expansion of the whole jet ceases and a neck grows slightly along the flow direction, as is depicted in Figure 2.4, and breaks just below the expanded section.

2. **Cross-flow**, [13, 40–43]

In this method the gas phase flows in a T-junction into the flow of the liquid phase as shown in Figure 2.8. The minimum bubble size obtained with this method so far is 170 μm [42].

Two regimes are recognised by Garstecki *et al.* [43] depending on the acting surface and

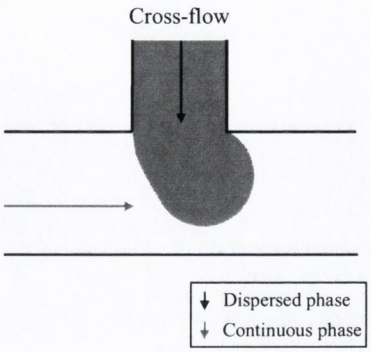


Figure 2.8: The cross flow method for the generation of monodisperse micro-bubbles or -droplets

viscous forces, which ratio is expressed as the *capillary number*, Ca [44]:

$$Ca = \frac{v\mu}{\gamma}, \tag{2.1}$$

with v as velocity, μ the viscosity and γ as the surface tension of the liquid.

The first regime is *squeezing* ($Ca < 10^{-2}$), where the gas flow blocks the complete outlet channel. This increases the upward liquid pressure, until the liquid pressure is high enough to squeeze the neck of the gas thread, which results in the formation of a bubble. This regime is dominated by pressure [43]. The second regime is *dripping* where shear dominates [43]. Shear stresses of the liquid along the gas thread break the gas thread into droplets.

3. Shearing [24, 45–47]
In this method we start with a polydisperse foam or emulsion. It is sheared between two moving plates creating monodisperse bubbles and droplets. Shear forces compete with surface tension forces [48]. Under the shear the polydisperse bubbles are deformed. If the shear forces are large enough the bubbles can be stretched such that they become unstable and break up into multiple bubbles, generally two. Dependent on the shear forces the bubbles can be split up to a limiting size, to our knowledge with minimum bubble diameter of 40 μm [24]. The reason why the bubbles end up monodisperse is not yet clear.

4. Flow focusing (for bubbles [7, 10, 12, 23, 27, 29, 49, 50], for droplets [9, 14, 28, 51–53])
Here the dispersed and continuous phases are focused through a small orifice, see Figure 2.9, which breaks up in small monodisperse bubbles.

The jet size of the dispersed phase depends on the ratio of the dispersed and continuous

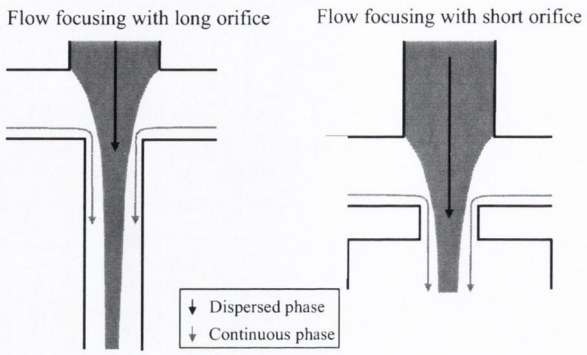


Figure 2.9: The flow focusing method for the generation of monodisperse micro-bubbles or -droplets. The orifice length can differ, but does not have an influence on the bubble sizes generated as we will discuss later.

phase flow rates and the orifice width. The minimum bubble size obtained with this method so far is 5 μm [7, 29, 49]. In the literature, three regimes of bubble generation are found, depending on the ratio between viscous forces and surface tension which is expressed as the capillary number (Equation 2.1) and the *Weber number* defined as the balance between surface tension and inertia forces [10, 14, 54]:

$$We = \frac{\rho v^2 L}{\gamma}, \tag{2.2}$$

with ρ as the density, v the velocity, L as the characteristic length of the channel and γ the surface tension. In general, at the scale of less than a millimeter, gravity does not play a role. The three regimes occurring with increasing ratios of gas and liquid flow rates are:

- *Plugging regime.* At very small gas and liquid flow rates, gas pressure is just sufficient for the gas to enter the orifice, but there it stops flowing and blocks liquid from entering the orifice. As there is a low liquid flow, in time the liquid squeezes the gas thread and a bubble pinches off [54].

- *Dripping regime.* In this regime the gas thread is formed, which remains at the entrance of the orifice. It expands and pinches off repeatedly, while liquid continues to flow. According to Garstecki *et al.* [44] dripping occurs at low capillary numbers where break-up is controlled by the pressure balance in the liquid and gas. A lateral liquid pressure difference enables expansion of the gas thread [10], followed by pinch off of the bubble.

- *Jetting regime.* At large liquid flow rates compared with the gas flow rate a long gas jet

is formed surrounded by liquid inside the orifice. This occurs at high Weber numbers ($We \gg 1$) where the inertial forces overrule the surface tension forces, which enables a gas jet to develop before an instability breaks up the jet due to surface tension forces. This jet can break up in different manners, considering a fixed gas rate and increasing liquid rate [27]:

- Monodisperse regime: The gas jet grows along the flow direction, a bubble pinches off and the gas jet retracts out of the orifice before it starts growing again.
- Bifurcation/satellite bubbles [27, 51]: The jet grows along the flow direction, breaks up and partially retracts out of the orifice. It then grows slightly, breaks up, creating a smaller bubble and then retracts completely before the process is repeated.
- Polydisperse regime: The gas jet irregularly breaks up, creating different sizes of bubbles. According to Garstecki *et al.* [44] bifurcations and polydispersity can occur at the transition region where both inertial and interfacial forces are of similar magnitude ($We \sim 1$).

Note that the *jetting* regime for the bubble generation in literature is not always clearly presented and it is more pronounced in droplet formation [14, 51].

Our devices belong to the flow focusing category. Generally in the literature only dripping and jetting are discussed. To our knowledge plugging was only mentioned by Weber *et al.* [54] in a computational study. We found a regime similar to a pronounced plugging regime (Section 2.5.1), although showing some key differences from the plugging regime observed by Weber *et al.*. They observed in the plugging regime that the gas flow stopped once it entered the orifice, as there was not sufficient gas pressure for the gas to continue flowing. They also state that the bubbles in the plugging regime are significantly *smaller* then in the flowing regime. We will show in Sections 2.4.1 and 2.5.1 that this does not hold in our observations. Therefore, to distinguish our regime from that of Weber *et al.* we name our regime *squeezing regime*. We show in Section 2.5 that there is an overlap between the squeezing and dripping regime, and that the squeezing regime is highly dependent on the geometry of the bubble generator.

2.3 Our experimental set-up

Figure 2.10 shows the devices we designed to create the microfoams described in this thesis, either made by the internal workshop or glass blower [1]. Our bubble generators fall into the category of 'flow focusing' devices.

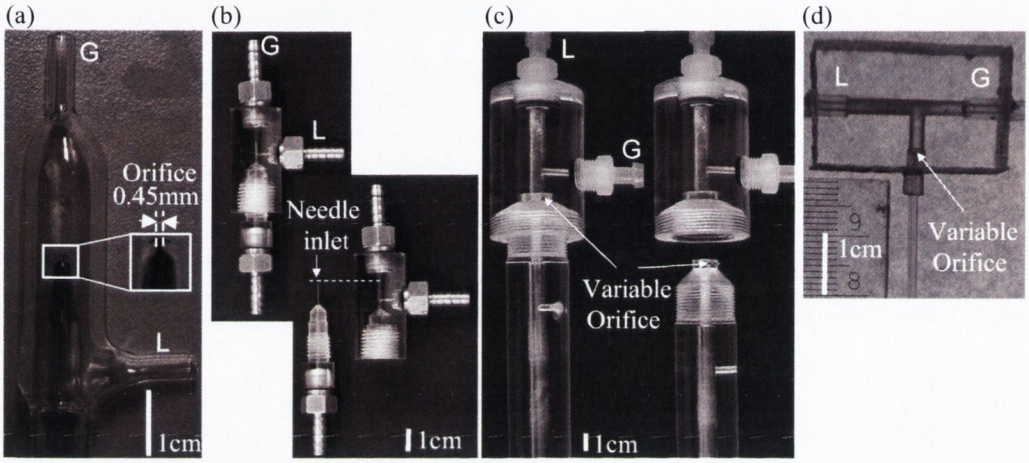


Figure 2.10: The different micro bubble generators used for the study in this thesis (a) glass version made by our glassblower John Kelly, (b) perspex design I with interchangeable iron needle placed in between gas and liquid inlet, (c) perspex design II with glass needles placed below the gas and liquid inlet (see Figure 2.11 for technical details) (d) perspex design IV with the same geometry as device(c). The latter 3 designs are made by the workshop. L labels the liquid inlet, G the gas inlet.

The glass version (Fig 2.10 (a)) has a short orifice length of smaller than a millimeter. Perspex design I (Fig 2.10 (b)) has a long metal orifice (1.5 cm) (see Figure 2.11 for technical details). In perspex design II (Fig 2.10 (c)) the orifice length is variable, by employment of pre-fabricated glass micro-capillaries. The latter worked the best, mainly because the size of the channel before the orifice is smaller than the capillary length, such that gravitational forces place a limited role.

Our set-up is shown in Figure 2.12. The bubble generator was connected to two dual piston pumps (Pharmacia Biotech Pump P-500 or KD Scientific two syringe infusion pump, KDS200-CE), which provided gas and liquid at controlled flow rates. To ensure a stabilised flow rate 5 minutes are allowed to pass after each flow rate change before samples are created. Figure 2.13 shows a typical sequence of bubble sizes that can be created by controlling the gas and liquid flow rate. The bubble generator was held such that the outflow of the bubbles was directed downwards. In Section 2.4 we illustrate the regimes as we observed them with a

[1] in the School of Physics, Trinity College Dublin

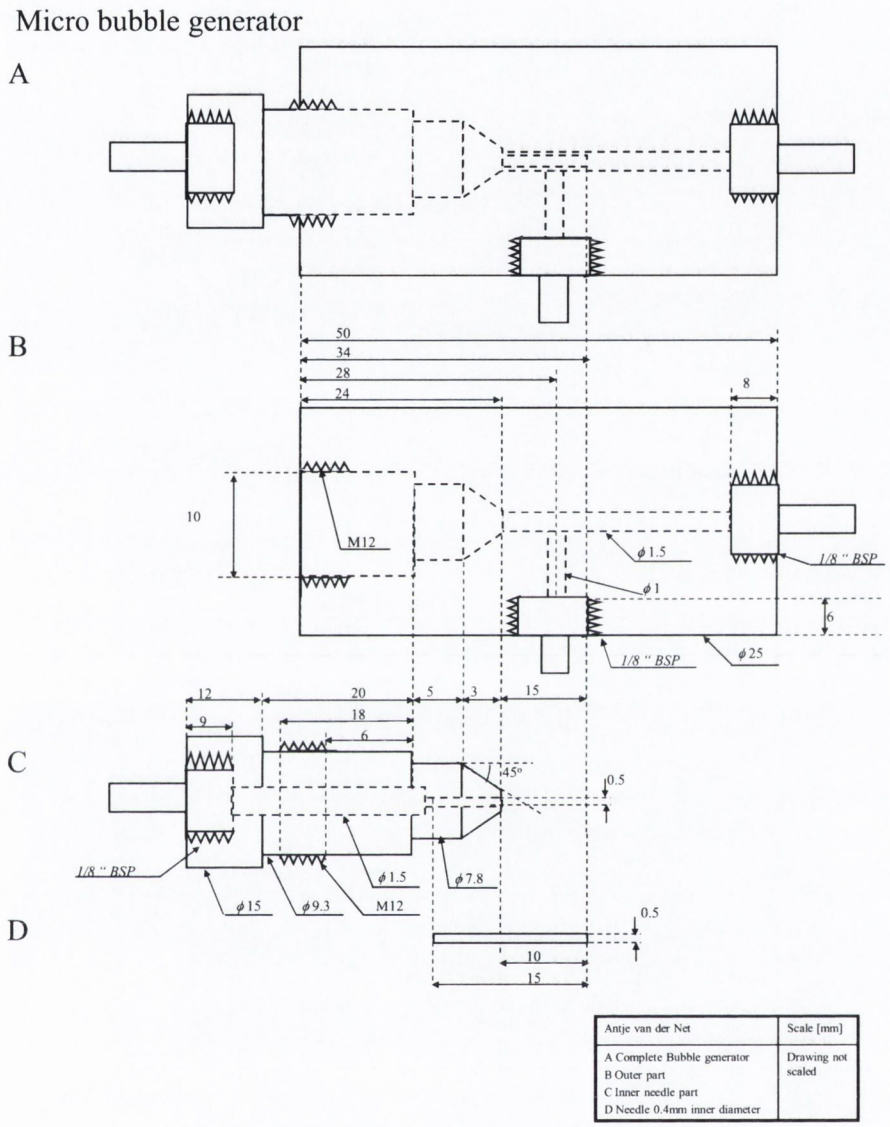


Figure 2.11: The technical drawing of perspex design I (see Figure 2.10 (b)) made by the workshop, with a metal needle with its entrance placed between the gas and liquid inlet.

high speed camera (Photron ultima FASTCAM APX-RS)[2] at 25000 frames per second with a glass fiber light source.

The bubbles were deposited in one layer on top of a thin liquid layer, see Figure 2.12(b). With transmitted lighting we imaged the bubbles, creating the patterns described in Chapter 3.6. The bubble sizes of small bubbles (less than one millimeter diameter) were determined

[2]performed at BASF, Ludwigshafen, Germany

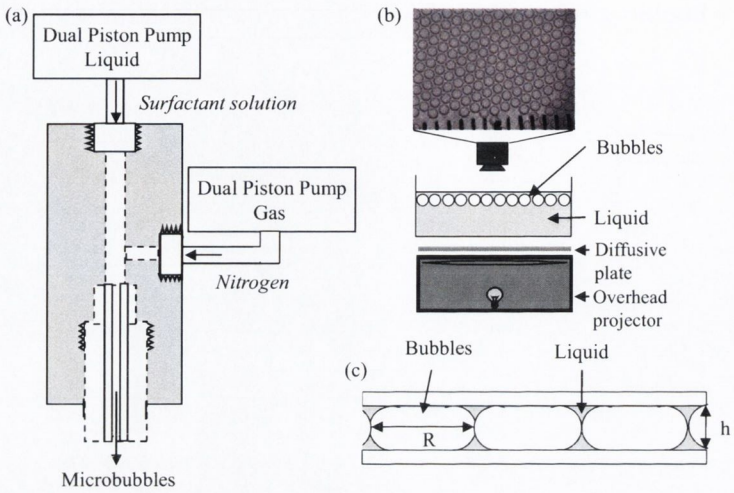


Figure 2.12: The set-up to create monodisperse micro bubbles with the micro bubble generator (a). The bubbles smaller than 1 mm were deposited onto a bubble pool as a single layer to measure the bubble sizes (b). The larger bubbles were confined between two plates to measure their bubble diameters (c).

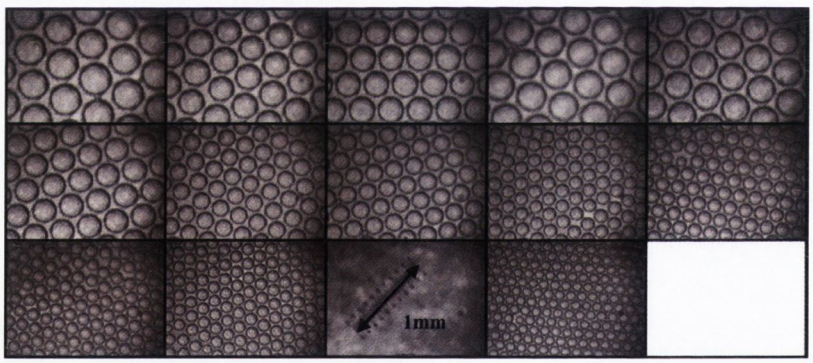


Figure 2.13: Decrease of bubble size in our device achieved by increasing the liquid flow rate Q_l from 2-8 ml/min, with steps of 0.5 ml/min whilst leaving the gas flow rate unchanged at 8.3 ml/min.

from photos of single bubble layers on top of a liquid surface, by measuring the distance between the bubble centers in the image analysis program ImageJ [55]. Since larger bubbles deform under gravity we confined them in a monolayer between two narrowly spaced plates, with sufficient amount of liquid to ensure that the bubble edges are semi-spherical , see Figure 2.12 (c). The apparent bubble radius R was corrected for the squeezing to the correct radius r:

$$r = \sqrt[3]{\frac{\frac{\pi}{4}h(R-h)^2 + 1/8\pi^2 h^2 R + 1/8h^3\pi[4/3-\pi]}{4/3 * \pi}}, \tag{2.3}$$

with h as the plate spacing. For the derivation of this equation it is assumed that the sides of the squeezed bubble have a radius of half the plate separation h and the center of mass for a semi-circle is taken at $\frac{4}{3\pi}R$. The standard deviation in monodispersity of the bubble size was measured by using the image analysis program ImageJ [55], by tracking the optical patterns of the bubbles. Bubbles are considered monodisperse when the standard deviation in bubble size is smaller than 2% [29, 49].

2.4 Visualisation of the bubble regimes

In the category of 'flow focusing', three bubble regimes are encountered with increasing liquid (or decreasing gas) flow rate: squeezing, dripping and jetting. Here we discuss these regimes observed with a high speed camera (Photron ultima FASTCAM APX-RS). To avoid lensing effects of cylindrical tubing present in device (c) (Figure 2.10) we used the square perspex device (d) seen in Figure 2.10.

2.4.1 Squeezing regime

Figure 2.14 shows an image sequence of the squeezing regime (Q_l = 0.4 ml/min; Q_g=0.67 ml/min). When sufficient gas pressure is built up, the gas thread (dark coloured) enters the orifice and blocks it completely. The water flow through the orifice is stopped and therefore squeezes the gas thread at the top of the orifice, which pinches off a bubble. The gas thread retracts far back from the orifice before it starts to build up pressure again to re-start the sequence as Figure 2.15 illustrates. This oscillation of the interface is easily identifiable and will be used for the bubble generator calibration in Section 2.5 to identify the squeezing regime.

Bubbles in the squeezing regime are monodisperse, significantly larger than the orifice width and significantly larger than in any other regime, as shown later in Section 2.5.1. Note that in Figure 2.14 the pinch off is not symmetrical as the orifice is slightly off-centered. The inlet channel is larger than the capillary length, which expresses the balance between capillary suction and gravitational forces, indicating gravity plays a role. At the limit of high gas flow rates and low liquid flow rates the gas thread runs all along the capillary without breaking up until it reaches the end of the capillary.

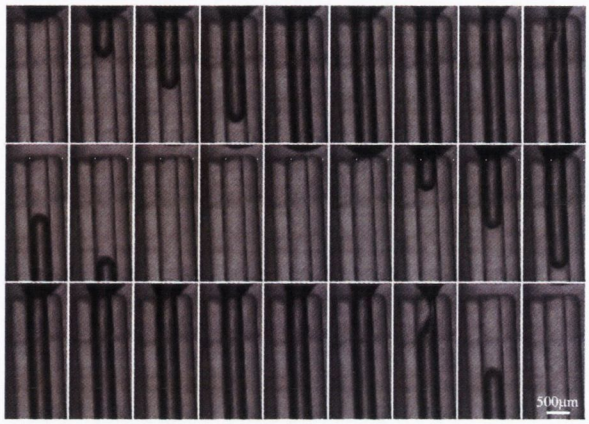


Figure 2.14: Bubble generation in the *squeezing* regime (Q_l=0.4 ml/min, Q_g=0.67 ml/min, 20 milliseconds interval between each picture). The dark gas thread fills the total orifice, blocking the liquid flow, which therefore pinches off the gas thread if the water pressure is large enough. The gas thread completely retracts out of the orifice, before it comes back and bubble generation continues.

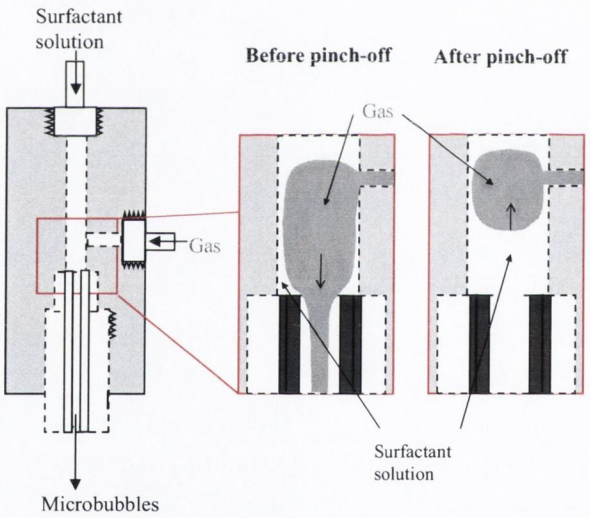


Figure 2.15: The oscillation of the interface in the squeezing regime. Before pinch off the gas thread is elongated into the narrow orifice. After pinch off the gas thread retracts out of the orifice up to its inlet, where after it will slowly move towards to the orifice again. These large interface oscillations are clearly visible during the bubble generation.

2.4.2 Dripping regime

Figure 2.16 shows an example of bubble generation in the dripping regime (Q_l=3 ml/min; Q_g=0.67 ml/min). Here, both liquid and gas are flowing simultaneously through the orifice. Like being the inverse of a dripping tap, the gas thread becomes unstable right at the orifice

entrance, where it pinches off. Unlike in the squeezing regime, the gas thread remains in

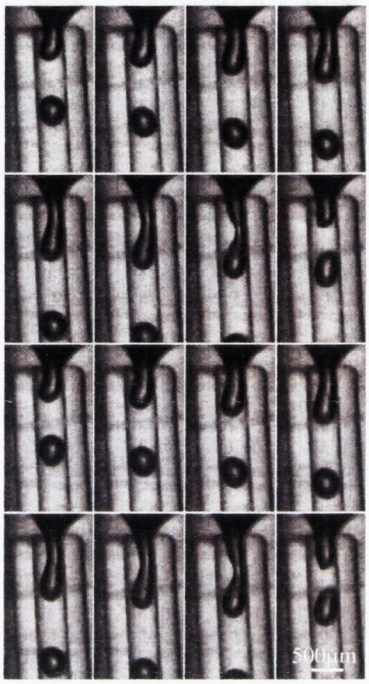


Figure 2.16: Bubble generation in the *dripping regime* ($Q_l = 3\ ml/min$, $Q_g = 0.67\ ml/min$, 1 msec interval between images). Bubbles are generated by pinch off of a gas thread directly at the entrance of the orifice.

the orifice due to the drag force of the liquid and sufficient gas pressure and grows from there before becoming unstable again. The gas thread is thinner and destabilizes quicker with increasing liquid flow rate (Q_l) and fixed gas rate, which results in generation of smaller bubbles at higher liquid flow rates. Once the instability occurs and the gas thread locally starts to narrow, the system can not re-stabilise and moves further away from equilibrium. This can be explained considering the Young-Laplace equation:

$$P_c = P_g - P_w = \sigma(\frac{1}{R_1} - \frac{1}{R_2}), \tag{2.4}$$

with P_c as the capillary pressure, P_g and P_w as the gas and water pressure and R_1, R_2 the interface radii. With a decreasing radius of curvature the capillary pressure increases. With an assumed constant gas pressure in the thread [10] this corresponds to lower water pressure compared to the water pressures at the locations where the thread has not narrowed. In order to compensate, water will flow from high to low pressures towards the narrowing neck, inducing a further narrowing of the neck. This will finally result in the pinch off of the droplet.

The repetition of the pinch off in the dripping regime is very regular, creating highly monodisperse bubbles with diameters of the order of the capillary width.

2.4.3 Jetting regime

At liquid flow rates higher than gas flow rates, the gas thread extends far into the capillary due to the drag force of the liquid flow around it. Due to the Rayleigh-Plateau instability the jet breaks up into bubbles. We did not observe long gas jets breaking up into monodisperse bubbles. Figure 2.17 shows our observation where the gas thread becomes unstable and breaks into several drops of (generally) differently sized bubbles. As in the squeezing regime, after the pinch off, the gas thread has entirely left the capillary. Surface tension is at that moment stronger than the drag forces, which can not keep the thread inside the orifice. Then the whole process needs to start again from the beginning, leaving regular gaps in the bubble generation process. The bubble sizes generated in the jetting regime are generally more polydisperse and smaller than the capillary diameter.

2.5 Calibration of the bubble generator

For each experiment we measured the bubble size for a combination of gas and liquid flow rates. There was no high speed camera available during these measurements to identify the dependence of different regimes on the flow rates. However, the squeezing regime can be easily distinguished by the widely oscillating interface and generation of significantly larger bubbles. The difference between dripping and jetting can not be easily detected without visualisation of the actual bubble generation. Therefore we only distinguish here between the 'squeezing' and 'dripping-jetting' regimes.

The aim of the calibration is to find the relation between bubble diameter and various parameters, such as: gas and liquid flow rates, surfactant choice, liquid viscosity and different geometric parameters such as orifice width and length. We can use these relationships later to obtain a specific bubble size by setting the right combination of bubble generator parameters. The main interest is in the dripping regime as in this regime microbubbles are created. In the literature [10, 29] it is found that for the dripping regime there exists an exponential dependence of the bubble diameter on the ratio of gas to liquid flow rate. There is also a linear dependence on orifice width or orifice volume. Therefore we fitted our dripping data

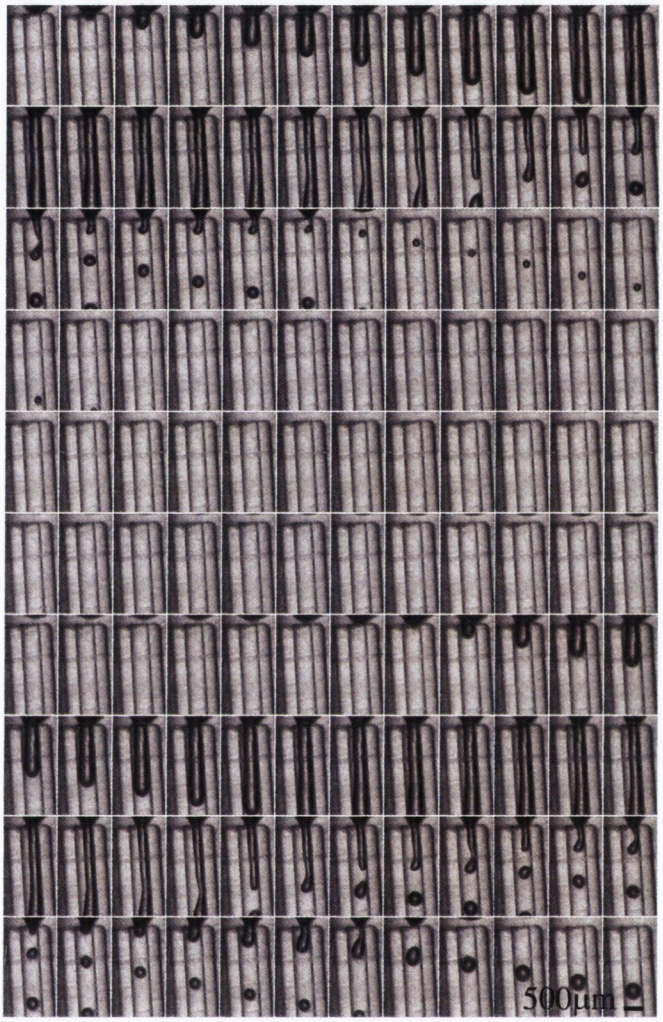


Figure 2.17: Bubble generation in the *jetting* regime (Q_l=3.33 ml/min, Q_g=0.67 ml/min; 1 millisecond interval between the images). A gas jet is created which breaks up at different positions in the orifice, creating polydisperse bubbles. After generation of 3 bubbles the gas thread retracts completely from the orifice and if gas pressure has built up enough a gas thread will be entering the orifice again.

with a function of the shape $D = aO_w \left[\frac{Q_g}{Q_l}\right]^b$.

The exploration of the squeezing regime is more focused on the geometrical influence. It is of importance to avoid this regime with the large bubble creation, as it interferes with microbubble generation and large bubbles can be made more easy with other methods. Geometry of the bubble generator is expected to play a role in the appearance of this regime.

Figure 2.18 shows all the geometrical parameters. Our base set-up is an orifice width

of 550 μm, a length of 17.2 cm and an inlet width of 3 mm, using a surfactant solution of Trimethyl Tetradecyl Ammonium Bromide, $TTAB$ at ten times the Critical Micelle Concentration (CMC of 3.5 mM, equal to 12 $g/liter$), with the viscosity of water, 1mPas at room temperature.

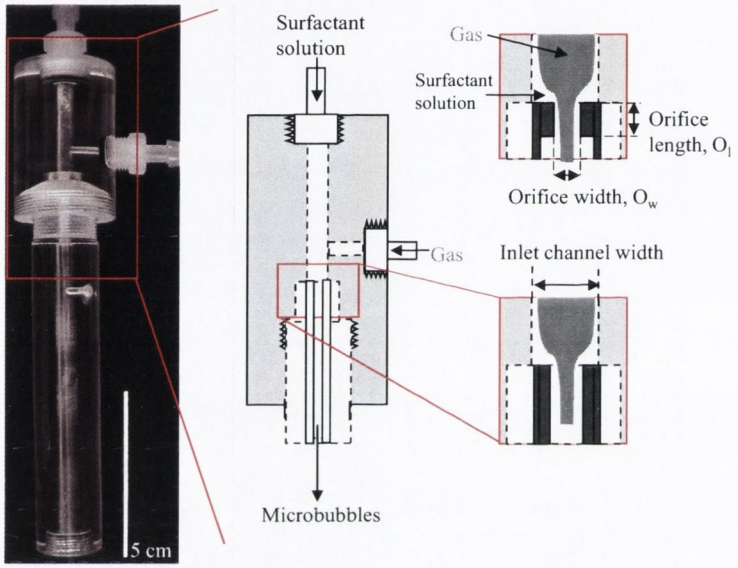


Figure 2.18: The bubble generator employed in this project. Gas (air or nitrogen) and surfactant solution are forced simultaneously through a narrow orifice. This creates a gas jet which becomes unstable and breaks into highly monodisperse bubbles.

2.5.1 Squeezing regime

The squeezing regime overlaps with the dripping regime at low gas-liquid flow rate ratios between 0-2 and low flow rates overall (around 1 ml/min). This regime (earlier visualised in Section 2.4.1) has not been observed before. The reason for the overlap is so far unknown. As sketched in Figure 2.19, when starting with a low Q_g (0.3 ml/min) and fixed but low Q_l (1 ml/min) and the Q_g is gradually increased, the squeezing regime occurs initially. At an unpredictable value of Q_g the squeezing regime passes into the dripping regime, with a drastic decrease in bubble diameter. However, when starting with a high Q_g (8 ml/min) dripping is and remains the dominant regime. It appears that the occurrence of squeezing or dripping regime is history dependent. With an increasing liquid rate (larger than 3 ml/min) the dripping regime occurs over the total range of gas rates and passes over in the jetting regime at large liquid rates. Squeezing does not occur anymore.

We carried out preliminary tests on whether the geometry of the bubble generator played

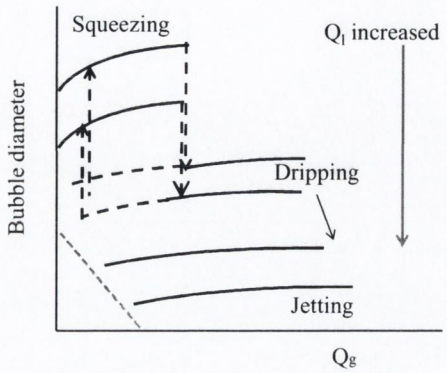


Figure 2.19: Sketch of the variation of the bubble diameter with variable gas rates Q_g for different fixed Q_l. The dripping and squeezing regime overlap and show hysteresis. At higher liquid flow rates only dripping occurs, which transfers into the jetting regime.

a role in the squeezing regime, generating two data-sets for each of the following factors:

- Orifice width, O_w
- Orifice length, O_l
- Channel width of the inlet, I_w.

This enables us to define where to focus future studies. The set-up is the same as the one described in Section 2.3. Figure 2.20 gives an overview of the generated data. In this graph the bubble sizes are plotted versus the ratio of gas to liquid flow rate Q_g/Q_l, which is the standard method for presenting data of this kind.

We performed an experiment with different orifice widths. In Figure 2.20 datasets (a) and (b) show the bubble diameters versus the ratio of gas to liquid flow rate for different orifice widths, respectively 500 and 1000 μm. Initially with Q_g/Q_l smaller than approximately 0.4 the data overlaps, but after approximately 0.4 the data shows a clear difference in bubble size beyond the experimental error. The larger orifice width results in larger bubble diameters. This shows the orifice width has an influence on the bubble size, at least for Q_g/Q_l larger than approximately 0.4. The data range is not large enough to say whether the relation between bubble size and ratio of gas to liquid flow rates behaves as a power law, as is found in the dripping regime described in the next section. The reason for the jump in bubble size in the data set (a) at Q_g/Q_l approximately 0.4 is so far unknown. Also in dataset (c) two jumps in bubble sizes appear at low Q_g/Q_l. The change in bubble size could be due to a temporary obstruction in the orifice, but this occurred twice at the same gas-liquid ratios and may be

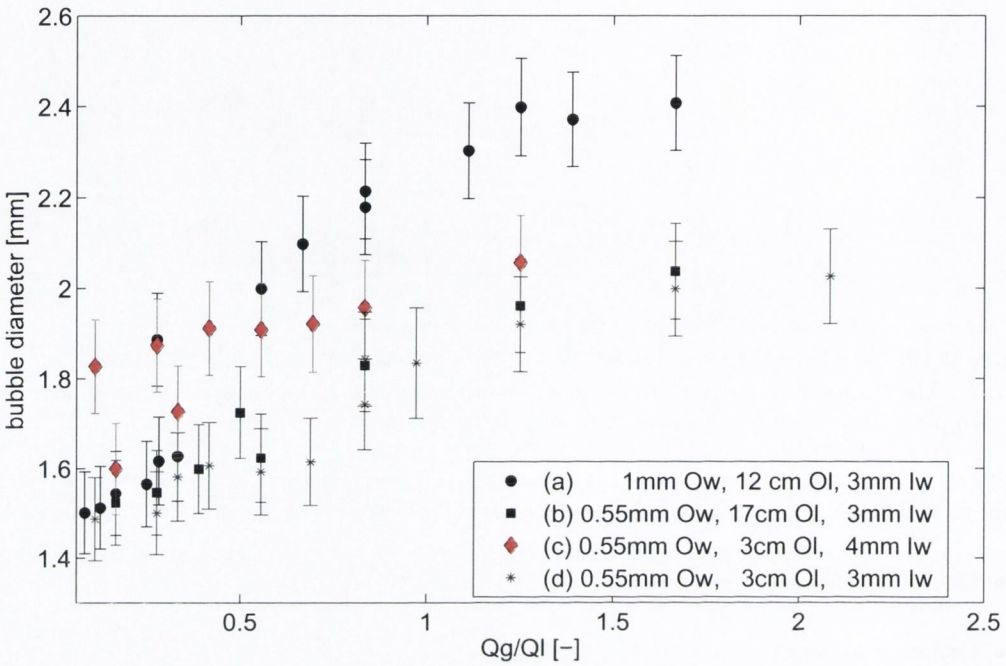


Figure 2.20: The bubble diameter as a function of Q_g/Q_l for different parameters in the squeezing regime. Datasets (a) and (b) show the dependence on the orifice width of $550\mu m$ and $1000\mu m$. Datasets (b) and (d) show the independence of the bubble size on the orifice length between 3 and 17 *cm*. Datasets (c) and (d) show the effect of the channel width of the inlet of 3 and 4 *mm* on the bubble size.

more than just a coincidence. It could be the presence of other stages within the squeezing regime.

Datasets (b) and (d) in Figure 2.20 show the independence of bubble sizes on the orifice length for 3 and 17 *cm* within the experimental error. This corresponds to our finding for the dripping regime, as discussed in the next section.

Finally we carried out preliminary tests on the influence of the channel width of the inlet on the bubble size as shown in datasets (c) and (d) in Figure 2.20. The change in the width of the channel from 3 *mm* to 4 *mm* has an effect on the bubble sizes during the squeezing regime, especially at low Q_g/Q_l ratios. At equal Q_g/Q_l ratios the bubbles are larger with a wider inlet channel width.

This dependence is present only in the squeezing regime. This could be explained by the characteristics of the way the bubbles are generated during this regime. At the pinch-off the interface completely retracts from the orifice, as illustrated in Figure 2.15. Afterwards the

gas thread almost completely fills the inlet channel (marked in Figure 2.18) and enters the orifice when the gas pressure in the thread has reached the pressure required to allow entry of the orifice $P_g = 4\sigma/O_w + P_w$, with σ the surface tension, O_w the orifice width and P_w the water pressure. The water first fills the corners of the inlet channel, before it pinches off the gas jet. In a wider channel this volume is larger. It will therefore take longer before the water is able to squeeze the gas thread and during this time the thread can continue to grow longer. At the time of pinch off, the bubble will therefore be larger compared to one made with a smaller inlet channel. The effect appears to become less significant at higher gas-liquid ratios but more data points are needed to confirm this.

2.5.2 Dripping-Jetting regime

In this regime we calibrated the foam generation of our device (Figure 2.18) as a function of the following parameters:

- Orifice width, O_w
- Orifice length, O_l
- Different surfactants
- Viscosity of the liquid solution, μ.

The data is plotted in a log-log plot of bubble diameter versus ratio of gas to liquid flow rate and the data is fitted with the function $a\left[\frac{Q_g}{Q_l}\right]^b$ with a=$1.19 * O_w$ and b=0.34 as we will discuss at the end of this section (Equation 2.6).

Influence of the orifice width

We studied the effect of the orifice width by using five different capillaries with internal radii of 250, 500, 550, 1000 and 1250 μm. The results of their influence on the bubble size are shown in Figure 2.21. The measured standard deviation in the bubble sizes is less than 20 μm, smaller than the general scattering of the data. For the orifice size of 1250 μm no bubbles were generated inside the orifice. This size is of the order of the capillary length, such that gravity affects the bubble generation and the gas thread could reach the end of the capillary.

It can be seen that the smaller the orifice width, the smaller the sizes of bubbles which can be generated. The bubbles generated with the 250 μm show the same trend as the other 3 orifice widths, but the data is more scattered. This is due to the fact that we work with

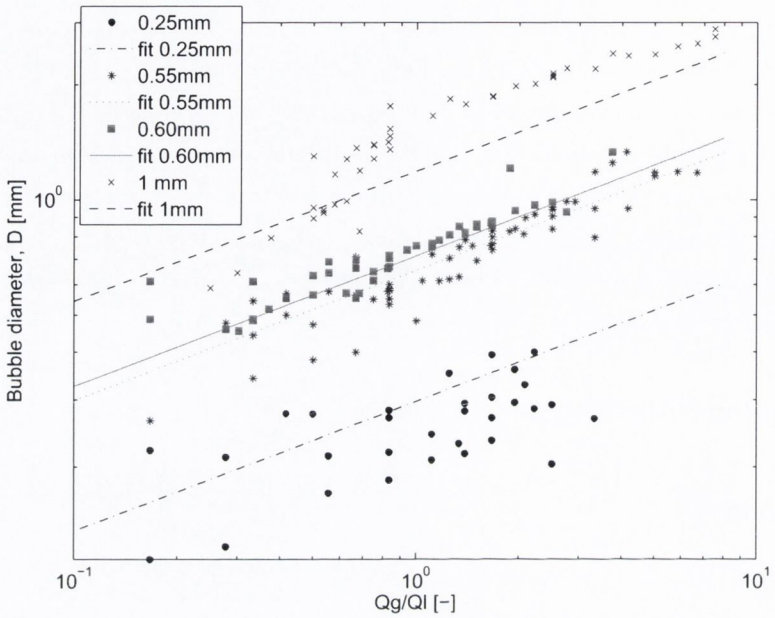


Figure 2.21: A log-log plot of the bubble diameter as a function of Q_g/Q_l for different orifice widths, showing their exponential relation. The bubble sizes are linearly dependent on the orifice width, they become smaller with smaller orifices. Data is fit with Equation 2.6, with a prefactor of $1.19 * O_w$.

flow rate regulated pumps. Generally scattering occurs due to temporary variations of flow rates for example due to vibrations. For small orifice sizes pressure adjustment in the flow rate regulated pumps takes a long time due to the high pressure build-up. This time is generally longer than the interval between the piston change in the dual piston pumps, i.e. equilibrium is difficult to reach in our measurements, increasing the scattering of the data for small orifices.

The data is fitted with a function of the form $a\frac{Q_g}{Q_l}^b$, which we will further discuss at the end of this section, with a=$1.19O_w$ [mm] (Equation 2.6).

Influence of the orifice length

We determined the effect of the orifice length by changing it from 1 *mm* to 1 *cm*, 3 *cm* and 17.2 *cm*. Figure 2.22 shows the orifice length barely influences the bubble size in our set-up and bubble diameters can be considered independent of the orifice length.

Long orifices however require large pressures due to the high dissipation on small length scales. These results are different from the results shown by Lorenceau et al. [29] but consistent with Raven *et al.* [56]. Raven *et al.* [56] found that if the pinch-off of the bubble

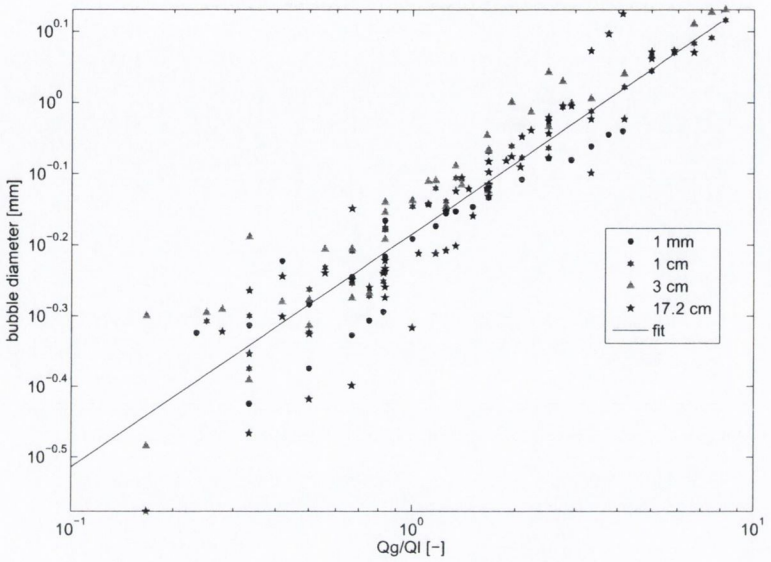


Figure 2.22: The variation of bubble size as a function of Q_g/Q_l is independent of the orifice length. Data is fit with Equation 2.6.

occurs in the orifice this always occurs at the same position for equal gas and liquid flow rates. When the pinch-off occurs in the orifice the bubble size is independent of the orifice length. Raven found that if the bubble size is scaled by the pinch-off volume (length of pinch off neck times cross-sectional area), then all their data, including the seemingly contradicting data of Lorenceau, collapsed onto one graph being independent of the orifice length. The precise explanation for their observed collapse is still lacking [57].

Influence of the viscosity of the liquid

We tested the effect of the viscosity of the liquid solution. The viscosity was changed by adding glycerol to the water, according to Table 2.1.

Volume % Glycerol	Viscosity[mPas]
0	1.0
10	1.36
20	1.85
40	3.79
80	55

Table 2.1: The effect of glycerol on the viscosity when added to water at 20° C [58].

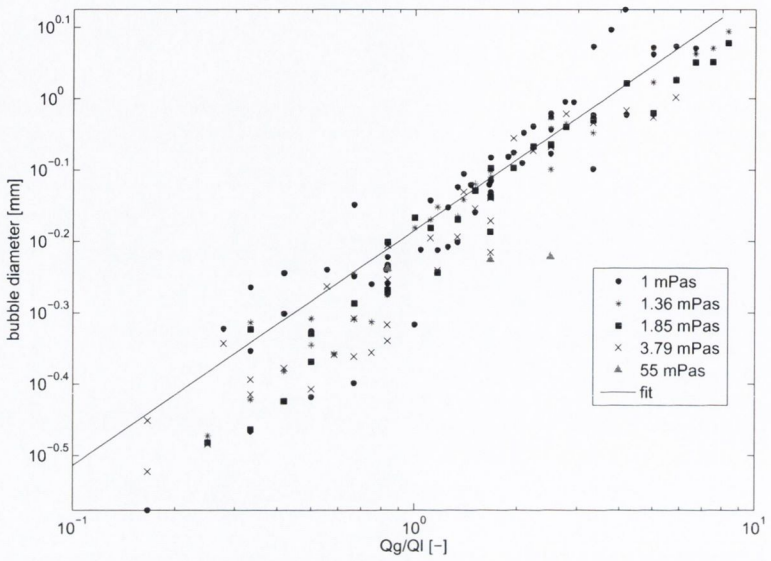


Figure 2.23: The bubble size as a function of Q_g/Q_l generated with liquids of different viscosities by the addition of glycerol. The viscosity does not influence the bubble size, until at the highest viscosity bubbles could no longer be generated. Data is fitted with Equation 2.6.

Figure 2.23 shows that the bubble size is not influenced significantly by the viscosity. This is due to the fact that in a flow rate controlled system the pressure adjusts to compensate for a change in viscosity, as described by Poiseuille's law. The Poiseuille law relates the flow rate Q in a pipe of radius R to the pressure difference according to:

$$Q = \frac{\pi R^4 \Delta P}{8 \mu L}, \tag{2.5}$$

with μ as the viscosity and L as a characteristic length. In the case of a pressure regulated system the bubble diameter is inversely proportional to the viscosity [49]. Only at the highest concentration of glycerol with 80% volume fraction can viscosity prevent bubble generation, as seen in Figure 2.23. At this stage the viscous forces have become much larger than the surface tension forces. The latter drives the pinch off of the gas thread and it is therefore thought that bubble generation completely ceases.

Influence of surfactants

Finally we considered the effect of using different surfactants, Tetradecyl Trimethyl Ammonium Bromide (TTAB), the commercial surfactant Fairy, Sodium Dodecyl Sulfate (SDS) and combinations of TTAB with dodecanol and SDS with dodecanol shown in Table 2.2.

Surfactant	Chem. formula	CMC	Used conc.	γ [mN/m]	μ_s[kg/s]
TTAB(cationic)	$C_{17}H_{38}NBr$	3.5 mM	12 g/lit	38[60]	2×10^{-8}[60]
Fairy	Mixture	1 ml/lit	10 ml/lit	27	$1.9 \pm 0.5 * 10^{-7}$[61]
SDS(anionic)	$C_{12}H_{25}OSO_3Na$	8.2 mM	24 g/lit	36 [61], 37[60]	$6 \pm 4 \times 10^{-8}$[61], 2×10^{-8}[60]
Dodecanol	$C_{12}H_{26}O$	-	0.3 g/lit	-	-

Table 2.2: The information on the used surfactants, with their chemical formula, the used concentration during the experiments, the surface tension γ and surface shear viscosity which influences the surface mobility.

The dodecanol decreases the surface mobility of the gas/liquid interface, thus making it more rigid [59] and so could effect the dynamics of the pinch-off.

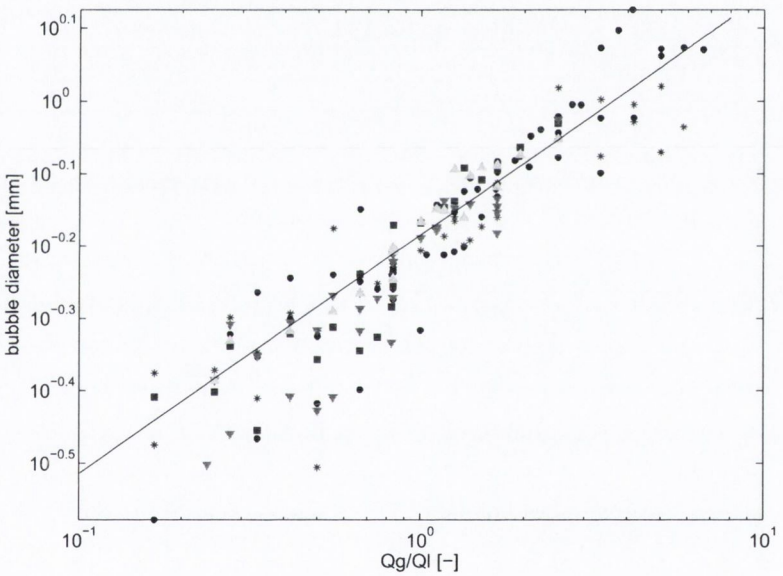


Figure 2.24: The bubble size as a function of Q_g/Q_l for 5 different surfactant solutions. It shows that the choice of surfactant does not influence the bubble size. Data is fit with Equation 2.6.

The results show that the difference between the bubble generation for different solutions is negligible for our purposes. Small differences in surface tension and surface mobility do not appear to matter. We have not observed a noticeable influence of the dodecanol. However, care needs to be taken regarding further conclusions of this observation, as dodecanol tends to be trapped in micelles at our high surfactant concentration (approximately ten times CMC) [60]. It is unknown whether the dodecanol concentration is high enough to saturate the micelles. Shear viscosity measurements on the used solutions should be performed to clarify this. Our results imply that surfactants can be chosen freely with the aim of optimising foam

stability.

With orifice widths of between 250 and 1000 μm the device generates highly monodisperse bubbles with diameters between 100 and 2500 μm. Smaller bubbles can be generated using smaller orifices and better pumps [29, 62], but this was not our goal here.

Based on the laws established in the literature [10, 29] we fitted all our data found in the dripping regime with a function of the shape $D = a\left[\frac{Q_g}{Q_l}\right]^b$. For our device, we established a relationship between the bubble diameter D, the gas flow rate Q_g, the liquid flow rate Q_l and the orifice width O_w:

$$D = (1.19 \pm 0.20)O_w \left[\frac{Q_g}{Q_l}\right]^{0.33\pm0.06} \tag{2.6}$$

We have to be careful with assigning a power law to the data sets as they only cover one order of magnitude. However our power law corresponds very well with those found in literature. Ganan-Calvo *et al.* [10, 27] obtained an exponent b of 0.4 and a prefactor a of 1.1. Lorenceau *et al.* [29] found an exponent of 0.38. The prefactor dependence was obtained from the data set varying the orifice width. The 1 mm orifice dataset deviates quite significantly from this value, with the least square fit of a is 1.44. Possibly at this size the effects of gravity can already start to play a role, increasing the bubble size by an extra drag on the liquid flow.

2.6 Discussion

As we studied the characteristics of the bubble generator we found a new regime named *squeezing* regime, at low gas to liquid flow rates. As mentioned, the orifice is blocked by the inflowing gas until the liquid is able to squeeze the gas thread such that it can also flow through the orifice. The presence of the large interface in our device perhaps explains why the squeezing regime to our knowledge is not described in literature. In literature either quasi-2D devices are used or the gas inlet is located very close to the orifice [12, 49, 51], in contrast to our design. Weber *et al.* [54] simulated what they named a plugging regime, where gas also blocks the orifice. However, this is not similar to our observations. They observed blocking of the orifice in the case of no gas flow and the resulting bubbles were smaller than the ones observed during the dripping regime. We observed plugging of the orifice with a continuous

gas flow which produced much larger bubble than those generated in the dripping regime and is therefore considered as a different regime.

The pinch-off shows similarities with *snap-off*, described as the creation of bubbles in porous media [63–69]. A porous media consists of pores connected by narrower pore necks. When both liquid and gas are present, the liquid collects in the pore necks due to capillary pressure differences according to Equation 2.4. A bubble is created when the pore neck is completely filled. This is of interest to the study of foam flow in porous media [70]. The pore neck can be considered as being an orifice. For the better understanding of the bubble generation using a microbubble generator it would be of interest to compare the bubble generation in our system with the bubble generation in porous media.

We can use Equation 2.6 to predict or set the bubble diameter by varying the orifice width and ratio of gas to liquid flow rate. A particular ratio of gas to liquid flow rate can be obtained with different combinations. This choice influences other parameters such as production rate and liquid fraction of the foam. By the choice of gas flow Q_g and bubble size D the production rate N of produced bubbles per second is determined according to

$$N = \frac{1/6\pi D^3}{Q_g}. \tag{2.7}$$

By fixing the gas and liquid flow rates the liquid fraction ϕ of the foam flowing out of the bubble generator is set, when no drainage has yet occurred, as:

$$\phi = \frac{Q_l}{Q_l + Q_g}. \tag{2.8}$$

Figure 2.25 summarises the experimental results in various representations. The bubble radius is plotted against Q_g/Q_l for four different capillary sizes and versus Q_g for four different production rates. The overall liquid fraction is also plotted against Q_g/Q_l. This representation emphasises that it is possible to accurately control bubble size, liquid fraction and production rate with this device.

2.7 Conclusions and Outlook

Preliminary experiments on the *squeezing* regime show a dependence on the inlet geometry. This regime shows the same behaviour as the *dripping* regime, being dependent on the orifice width but independent of the orifice length. The importance of understanding the squeezing

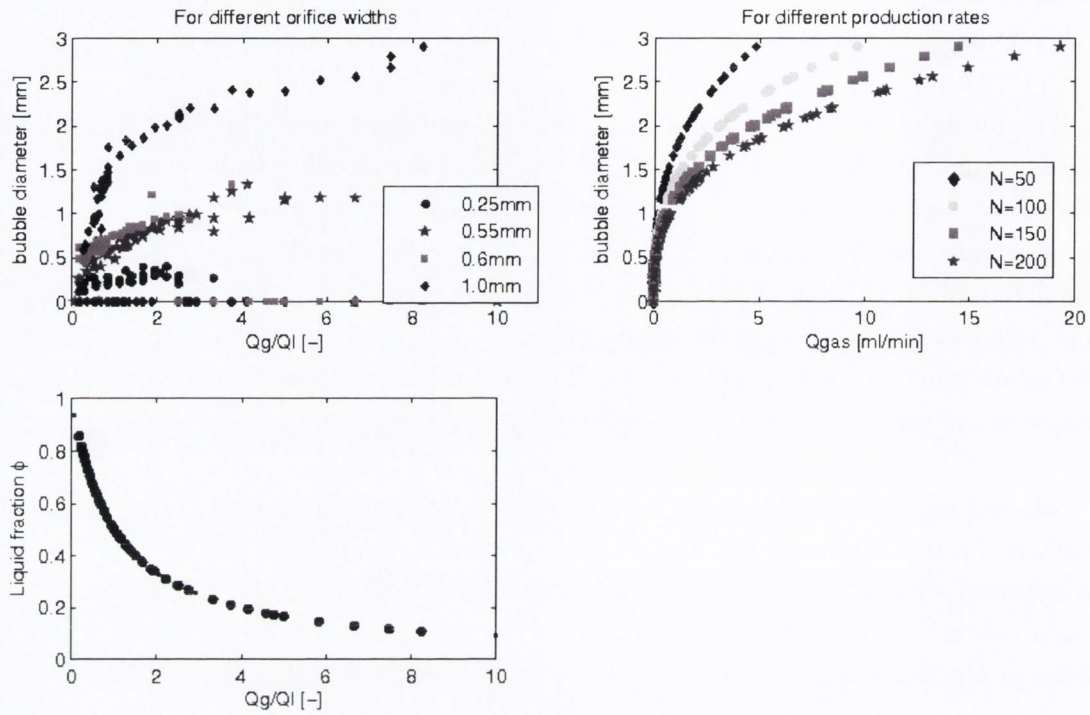


Figure 2.25: An overview of the relations between parameters, gas and liquid flow rates Q_g and Q_l and orifice widths, to control bubble size, liquid fraction and production rate. Bubble sizes and liquid fraction are plotted versus gas and liquid flow rates Q_g and Q_l, respectively, for different orifice widths. For different production rates bubble sizes are plotted dependent on gas flow rate.

regime is not directly for its use in bubble generation, as the bubbles are significantly larger than in the dripping regime. As the squeezing regime interferes with the dripping regime it is important to find the origin of this regime and reduce its occurrence. Based on our experiments, the dependence on the geometry will be especially important. Simulations of the system would be useful to single out different parameters. One of our former group members James Hilton is developing a simulation program which can help in determining the effect of the geometry of the bubble generator on the bubble generation. The program is based on the Level Set method [71], such that it can deal with creation of interfaces and new objects, in our case the pinch-off of new bubbles. Our findings on the dripping regime show good correspondence with those found in the literature.

The flow focusing technique is a very useful to create monodisperse bubbles. We will use the formation of equally sized microbubbles to generate crystalline microfoams, which are discussed in the following chapters.

Chapter 3

Simulating and interpretating images of bubbles with computational ray-tracing techniques

As outlined in the introduction, images of foams may feature some optical illusions and their presence makes analysis of the geometry a difficult task. For the interpretation of the complex images of the observed crystalline structures of microbubbles in wet foams we developed a simple computational ray-tracing method. The method is generally applicable to a range of foam geometries and experimental set-ups. In this chapter we focus on the images of different arrangements of spherical bubbles.

3.1 Introduction

Liquid foams consist of a discrete gas phase dispersed in a continuous liquid phase, which creates a system with unique optical and mechanical properties. Many of these properties depend significantly on the foam structure, which in turn is closely related to its *liquid fraction* ϕ, defined as the ratio between the liquid volume and the total volume of the foam. As shown at the top of Figure 3.1, dry foams ($\phi \to 0$) consist of polyhedral gas-cells separated by thin liquid films. At higher liquid fraction bubbles become increasingly spherical (bottom of Figure 3.1), and finally come apart to form a *bubbly liquid*.

In order to experimentally study the relationship between the structure of a foam, its liquid fraction and its (fluid) mechanical properties, it is important to find ways of accurately

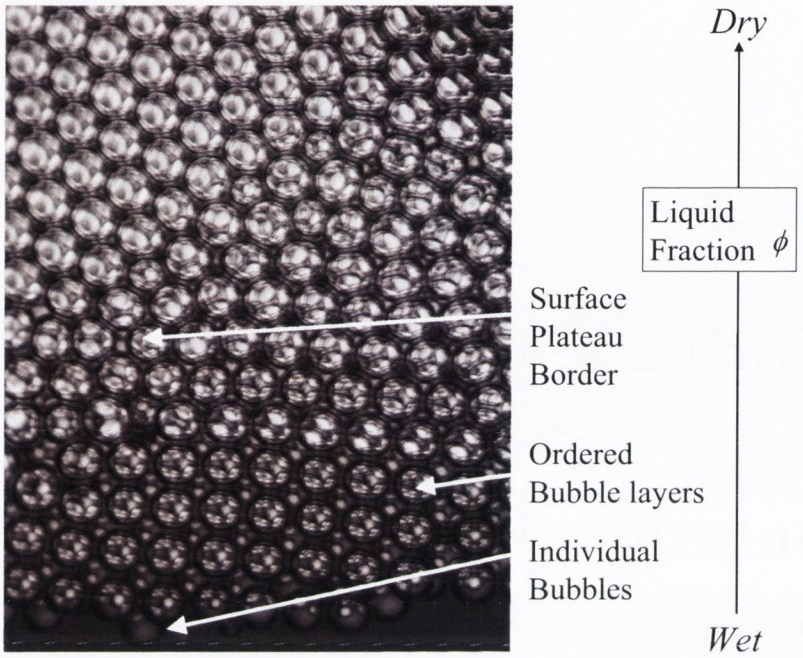


Figure 3.1: A column of monodisperse foam confined between two glass-plates (bubble diameter approximately 400 μm). Gravity-driven drainage leads to a variation of liquid fraction ϕ with significant influence on the local foam geometry. In the dry foam at the top, bubbles are polyhedral and disordered, whilst in the wetter foam towards the bottom they become increasingly spherical and ordered.

measuring its relevant geometrical/structural parameters. For instance: What is the size of a bubble? How are bubbles arranged with respect to each other? How thick are the liquid-carrying channels? What is the topology of their network?

To answer some of these questions, various measurement techniques have been suggested and attempted, including optical, acoustical, mechanical and electrical conductivity methods [5]. Of all these, only the first one seems appropriate to accurately determine *local* geometrical and topological properties of the foam (i.e. non-statistical opposite to what is done in the diffusive light spectroscopy [72, 73]). However, for a light ray a foam is a complex system of different shaped lenses, at which light is reflected and refracted multiple times. Another degree of complication is added by the fact that foams and bubbles are commonly imaged between glass plates, which create additional boundary conditions that influence the optics. In the attempt to measure structural parameters of foams or foam-like systems, the experimentalist therefore faces images like those shown in Figure 3.2, which are generated by an often complex interplay of the imaged objects and the imaging conditions. As a result, foam research provides multiple examples of optical illusions, which can lead to incorrect

physical interpretations. Examples include Sebba's gas-water aphron theory [74], which is partly based on images, which are discussed in Section 3.5, and the misinterpretation of the (100) direction of an fcc bubble crystal as bcc structure (Section 3.8). It is therefore necessary to develop tools which allow to accurately relate the structure of a foam and the image it creates under specific imaging conditions.

The propagation of light in foams has received attention for many years. In 3D polydisperse foams, diffusing-wave spectroscopy uses light-scattering to extract information on topological rearrangements [72, 75, 76], whilst diffusive transmission spectroscopy can be used to obtain bubble size distributions and liquid fractions [77]. Some work has been done on scattering of light in single bubbles [78] in order to determine the bubble size. Biogiovanni et al. [79] published on the imaging of single bubbles in back-lit diffusive light with a camera close by, whilst others developed bubble size measurements using Mie scattering [80].

We introduce here a computational ray-tracing method which can be used straightforwardly by experimentalists in the preparation and analysis of experiments. Since it is impossible to cover the full range of geometrical and physical parameters which influence the final image, we have chosen to present the general computational method (Section 3.3) and a number of simplified cases which demonstrate the underlying principles. In this chapter we investigate the local relationship between the geometry and optical patterns of *bubbles* in different configurations, when imaged with transmitted light. In Appendix A we give an other example of the application of method of two Plateau borders between two glass-plates (also named a rivulet or liquid bridge) (similar to Figure 3.2 (a)).

A bubble immersed in a liquid carrier acts as a diverging lens. If viewed in front of an infinitely large, diffusive light source, it would therefore only be detectable as a result of intensity changes due to Fresnel effects, which describe the amount of reflectance depending on the angle of interval. For example when light hits a water liquid interface at an angle of 90°, 4% of the light is reflected back, so the light intensity that passes the interface is decreased by 4%. Only this kind of intensity decrease can allow the bubble to be seen. However, the interaction with additional interfaces (like those of neighbouring bubbles or container walls) leads to well defined optical patterns, which can be used for imaging and analysis purposes, see Figure 3.2 (c).

In the following we shall analyse this pattern formation by going from an individual bubble (Figure 3.2 (b)) to fully three-dimensional crystals of equal-sized bubbles (Figure 3.2), whose

occurrence we will extensively describe in Chapter 4 based on this optical analysis. For detection of the bulk-order of such crystals is essential to understand the origin of their patterns. Optical analysis of this order is a challenge as a result of the multiple reflections/refractions occurring at the gas/liquid interfaces. However, as we shall show, if experiments are accompanied by appropriate ray-tracing simulations, the details of bulk ordering of the first layers can be inferred from simple photographs of the bubble crystal.

Our results are generally obtained from a 3D animation program 3D Studio Max [81] and a 2D ray-tracing model (Section 3.3). Where feasible, we compare our predictions with analytic models and experimental images.

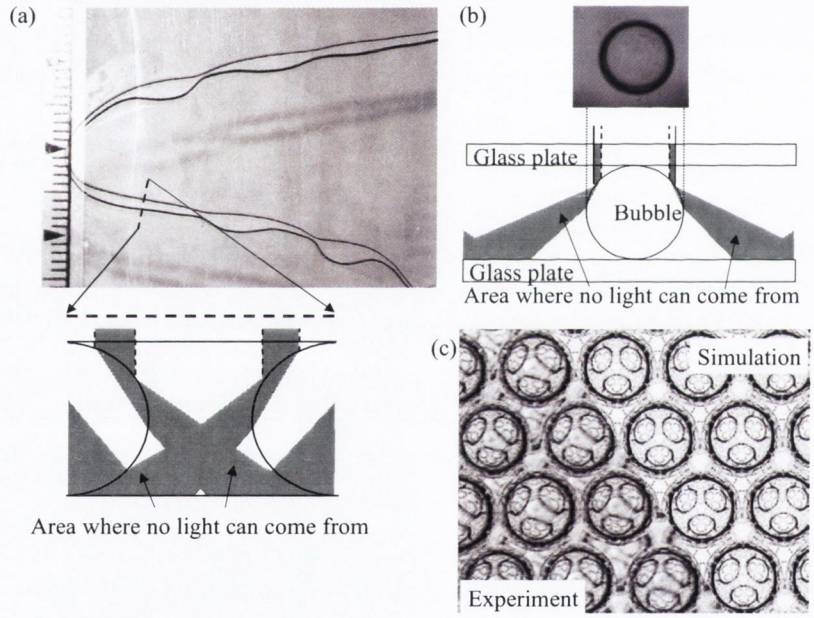


Figure 3.2: Puzzling examples of image formation in foam and foam-like systems: (a) An undulating liquid bridge between two glass plates seen in the plane of the plate and (b) a bubble between two glass-plates appear as black stripes. (c) A crystal arrangement of equal-sized bubbles generates a fractal-like pattern of black rings. Note that none of the black boundaries correspond to the actual boundaries of the object, which can be misleading in the analysis of experiments.

3.2 Experimental set-up

Our experimental set-up used for the comparison of computational images with experimental ones is sketched in Figure 3.3. The set-up consists of an overhead projector with a diffusive screen transmitting diffusive white light through the foam structure, which was imaged

through a microscope (magnification 1-3x, $\approx$ 20 cm away from the foam) using a digital camera (Coolpix Nikon 4500). The small bubbles with diameters in the order of 200 μm were created using a microfluidic flow focusing device [7, 23] described in Chapter 2.

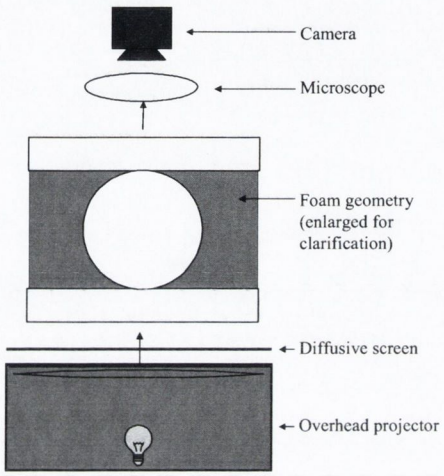


Figure 3.3: A sketch of the experimental set-up for the imaging of bubbles and foams.

3.3 Computational Method

In order to simulate the images formed in the experimental set-up light rays need to be traced as they travelled from the light source through the foam geometry to the camera. To realise this we need to:

1. computationally represent the foam geometry and the set-up.

2. follow light rays as they pass through this system, applying physically accurate laws of refraction and reflection (*ray-tracing*).

For both ingredients we resorted to commercially available software which, thanks to recent developments of sophisticated 3D-animation techniques, provided powerful and sufficiently accurate algorithms for our purposes.

The creation of the foam geometry and set-up was done using 3D Studio Max®[81], into which we implemented Final Render®[82] to control the physical properties of each item of the set-up and to perform the ray-tracing (Section 3.3.2). Since Final Render has been developed with more emphasis on efficiency than scientific accuracy, we checked the results

against simulations that implement Maxwell Renderer®[83]. This renderer was developed with the aim of providing physically accurate modeling.

Since commercial tools only provide the final ray-tracing image, we wrote a simplified two-dimensional model in MATLAB®[84] (Section 3.3.3) to visualise the individual ray paths through the foam structures. This helps greatly in the development and illustration of analytical relationships, which link the geometry of the object and the final image.

3.3.1 General input parameters and assumptions

The key input parameters of our computational imaging procedure can be divided into two main categories: the geometry of the foam and the overall imaging set-up, including lighting conditions, camera position and additional conditions such as glass plates or a container walls. Figure 3.4 sketches an example of a computational set-up with a liquid bridge between two glass-plates, consisting of two surface Plateau borders connected by a thin film. Unlike many experiments, simulations provide easy access to a broad range of parameters. The following subsections elaborate on these parameters and the various assumptions and simplifications used in this chapter.

Foam geometry and imaging set-up

In general, any geometry can be implemented by addition and subtraction of standard geometrical shapes, such as spheres, cubes and cylinders. The bodies of the set-up are represented by polyhedral areas, called meshes which can be arbitrarily refined (at the cost of computational time) to ensure accuracy of the result. The material properties of each item (including the camera) are managed by 3D Studio Max, but controlled by the renderer. In this study we concentrate on gas/water systems with refractive indices of $n_g = 1$ and $n_l = 1.333$ respectively. The demonstrated principles are equally applicable to systems with the same ratio of refractive indices. Examples for different ratios are shown in Section 3.9. Systems are (sometimes) bounded by glass plates with $n_{gl} = 1.5$. In our descriptions, *'top'* and *'bottom'*, (eg. the 'top Plateau border' or 'bottom glass-plate') refer to the object closest to or furthest away from the camera, respectively. All images are shown accordingly.

In this chapter we will focus on examples of the appearance of spherical bubbles in different configurations; a single bubble, two touching bubbles and bubble crystals of various numbers of layers (Figure 3.2).

Lighting

Foams are generally imaged in experiments in front of a diffusive light source. In our simu-

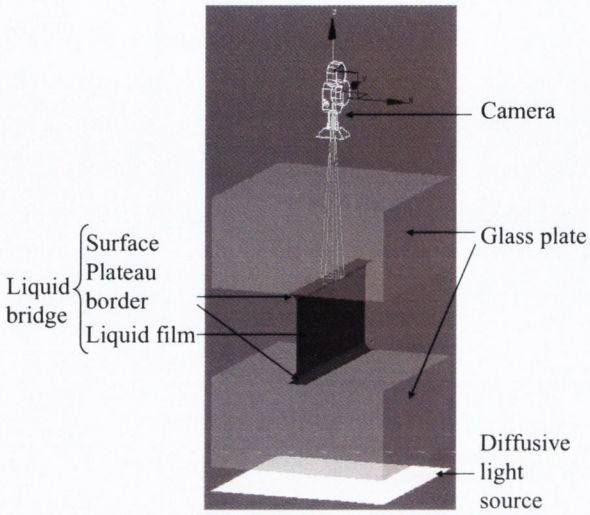


Figure 3.4: Illustrative example of a typical computational set-up in 3D studio Max, which includes a diffusive light source, a camera, glass-plates and the foam geometry (here consisting of two surface Plateau borders connected by a thin film). In our simulations the camera is placed far away from the object and the light source and glass plates are much larger.

lations this was done by placing the imaged object between the camera and *light source*. A light source was created by assigning self-illuminating properties to the plane sheet, which was large enough such that it could be assumed to be effectively infinitely large. This could be tested by checking changes in the optical pattern when enlarging the light source. When no changes occur the light source can be assumed infinitely large. Generally in our computational examples we used a infinite light source. Only in the Appendix A.4.2 we show the effect of a finite light source on the optical pattern of a Plateau border.

Imaging

The patterns were observed and recorded using a *virtual camera*, which closely represents a real camera. Parameters like the target depth, aperture and depth of field, could be set by the user to resemble the camera used in experiments. In order to avoid complications related to camera aperture and to simplify mathematical derivations, we placed the camera sufficiently far away such that it can be assumed to be 'infinitely' far away from the object. This allowed us to only take into account light rays, which left the object perpendicular to the imaging plane. This is justified in many experiments, in which the length scale of the foam is negligibly small in comparison to its distance from the camera. The assumption can be checked by enlarging the distance between the camera and the object and observe if the optical images changes. If the optical pattern changes, the light can not be assumed parallel.

To ensure agreement with the assumption of observation of parallel light, the separation between the camera and object in the simulations was approximately 1000 times the typical length scale of the foam. The maximum aperture was 36 *mm*. The field of view (FOV) of the camera was set as small as the objects in the set-up allowed.

Experimentalists need to check carefully if such assumptions apply to their set-up. Especially when working with a microscope or microlenses, the finite aperture might have to be taken into account.

Additional boundary conditions

Foams are commonly contained between two glass plates (Hele-Shaw cell) or in glass containers, which influences the optical patterns depending on the material, shape and size of the cell. The examples we discuss here, the individual bubble and the pair of bubbles are presented between glass plates. The crystal structures formed out of bubbles are presented without them, only liquid gas boundaries are present.

3.3.2 Ray-tracing

Within the computational raytracing software the behaviour of light rays needs to be accurately simulated. When light hits an interface between media of different optical densities it is partially refracted (transmitted) and partially reflected. The geometrical relationship between the incident and outgoing ray is given by *Snell's law*

$$n_i \sin \Theta_i = n_t \sin \Theta_t, \tag{3.1}$$

where n_i, n_t are the refractive indices of the two media, Θ_i is the angle of incidence and Θ_t is angle of refraction (transmission) [85]. The reflected part (subscript $_r$) of the light travels according to the rule

$$\Theta_i = \Theta_r. \tag{3.2}$$

If $n_i > n_t$ there exists a critical *angle of total reflection* Θ_c, beyond which only reflection occurs. For a liquid/gas interface

$$\Theta_c = \text{asin}(\frac{n_g}{n_l}). \tag{3.3}$$

This critical angle is 48.7 degrees for a gas-water interface and plays an important role in describing and understanding the optical patterns of bubbles.

The relative intensities of the reflected and refracted rays are given by the Fresnel equations [85]. In complex geometries, Snell's law and the Fresnel's equations have to be applied multiple times as light bounces between interfaces. Render machines supply efficient algo-

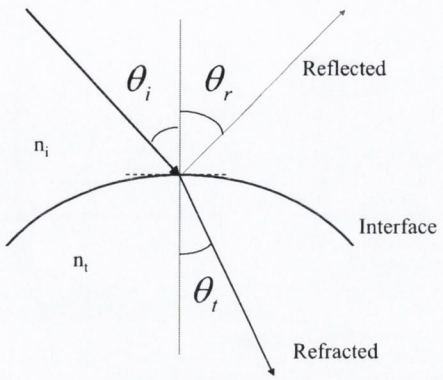


Figure 3.5: Refraction and reflection at an interface, with $n_t > n_i$.

rithms to manage this complexity. One of their key ingredient is *backward ray-tracing*, in which 'imaginary' light rays are sent out from the camera and traced back through foam geometry in its set-up. Only those which hit a light source, within a set maximum number of bounces, are considered for the final image generation. The intensity changes are then calculated along the established paths. We neglected the influence of polarisation, interference or diffraction, as we expected these to not to have an effect in our examples. Multiple scattering results in loss of polarisation. As we see later, experimental images correspond very well with the simulations, so these assumptions appear to be reasonable.

For efficiency reasons we mostly used Final Render®for our calculations, which worked by scanning rectangular areas, so called *bucket rendering* [82]. Within this, computation time was saved by *Lazy Data Handling* [82], which ensured that simulation time was efficiently distributed between more and less significant parts of the image.

The simulation results are scale independent, within the limits of the assumptions.

3.3.3 Simplified 2D ray path visualisation model

We wrote a simplified two-dimensional MATLAB®program to visualise some of the most important ray paths through the objects and to quantitatively test some key features of the 3D simulations and mathematical derivations.

We only applied Snell's law (Equation 3.1), hence ignoring the ray splitting and the accompanying intensity changes. Therefore reflection was only encountered in the regime of total reflection. As we used the results of this model to derive mathematical relations, this simplification was checked each time by comparing the location of the boundaries with 3D Studio Max simulations, where the Fresnel effect was included.

We used *backward ray-tracing* [86], as described in Section 3.3.2. Rays which did not

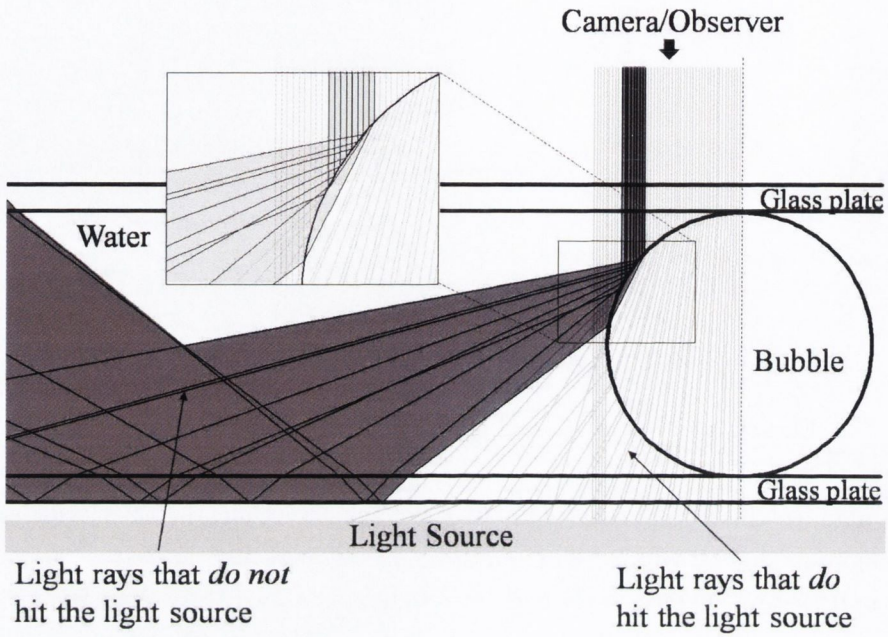


Figure 3.6: An illustrative example of our 2D model. Light rays are traced backwards from the camera (*backward-raytracing*), applying only Snell's law (Equation 3.1). They are colored black if they do not hit the light source after a set finite number of reflections.

hit the light source within 200 reflections were treated as being physically not real and we therefore coloured them black. For an illustrative example (which is discussed in more detail in Section 3.4) see Figure 3.6. Note that in the remaining chapter neither the camera nor the light source will be shown in the images generated by the 2D model. The set-up is always as shown in Figure 3.6.

Since we only considered light rays which leave the object perpendicular to the imaging plane (here parallel to the glass plates), the ray-paths in cross-sections of systems with translational symmetry were correctly modelled by this approach (neglecting Fresnel effects). In 3D bubble crystals this is true, if the cross-sectional planes are considered which are perpendicular to the image plane and which contain the centres of the relevant bubbles. This is because a light ray which is reflected or refracted on a spherical bubble interface always remains in the plane which contains the bubble centre and the incoming ray. As well for the light rays which hit the liquid-gas interface perpendicular, so that no reflection or refraction occurs and they go straight through.

3.3.4 Practical application of the method

With the existing experimental set-up, our approach is to implement the complete set-up, including the expected foam geometry, in the 3D animation program, 3D Studio Max. The resulting computational images should be compared with the experimental ones to check whether they correspond in a qualitative manner. The implemented foam geometry can now be compared with the obtained optical pattern and it can be determined how the measurements on the optical pattern deviate from the required foam geometry. If the set-up is 2D symmetric the set-up can also be implemented in the 2D raytracing program and analytical relations can be derived relating measurable features in the optical patterns to the geometrical dimensions wanted. The assumptions of using parallel light needs to be met in this case. This can be checked by enlarging the position of the camera to the foam geometry. If the new optical image differs from the initial image, and light falling into the camera is not parallel. In the same way the light source can be checked on infinite size. In Appendix A.4.2 we give an example of the effect of a finite light source on the optical pattern of a liquid bridge. The set-up can also be adapted such that it meets the assumptions made here so that the relations can be used that we found and will discuss in the following sections for bubbles.

In the following sections we will give examples obtained from the simulations for different configurations of bubbles and compare them qualitatively to experimental images.

3.4 Individual bubble

When imaging an individual bubble in a Hele-Shaw cell or a shallow bubble pool, which is back-lit with diffusive light from an effectively infinite light source, a black ring is observed (Figure 3.7). The diameter of this ring is often incorrectly assumed to be the bubble diameter. This ring is actually just an image of the surroundings: as a result of the interplay of the curved gas/liquid interfaces of the object, the bubble projects parts of the surrounding area into the camera, which does not emit any light. This becomes particularly clear within the framework of backward-ray tracing. This stripe is generated by the trapping of rays between the top and bottom liquid/gas (or glass/gas) interfaces, due to total reflection at the interfaces. The parameters used here are shown in Figure 3.8.

The *inner boundary* B_i (Figure 3.8) corresponds to the first ray which is totally reflected at the bottom interface after having been refracted twice at the curved liquid/gas interface (Figure A.10). Solving the appropriate set of equations in the style of Appendix A.4, we

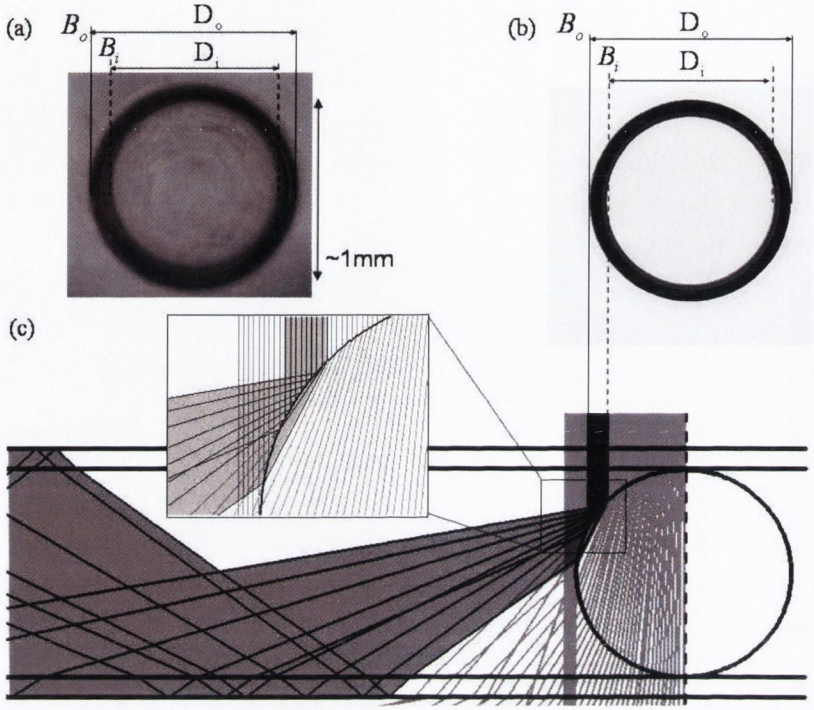


Figure 3.7: A single bubble between two glass-plates. (a) the experimental image, (b) the 3D-simulation, (c) the 2D-simulation.

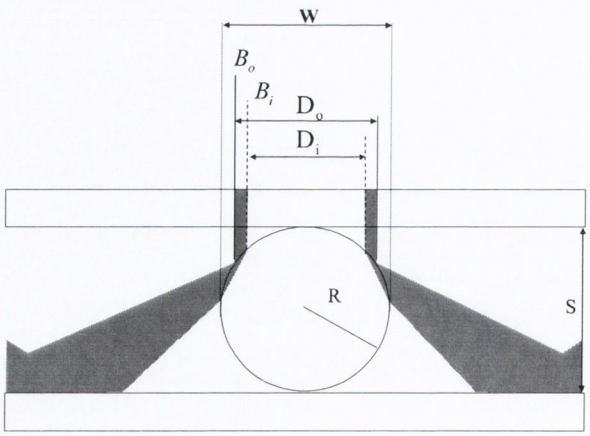


Figure 3.8: The labeling scheme for the analysis of the image of a single bubble between two glass plates.

obtain

$$W = S = \frac{1}{0.698} D_i = 1.43 D_i. \tag{3.4}$$

Due to Fresnel effects, the inner part of the ring is gray, instead of black. This is caused by the part of the ray refracting towards the light source enabling some light to come in making the ring less dark. B_i corresponds to the inner boundary of this ring.

The *outer boundary* B_o is given by two equations of total reflection at the curved and bottom interface. We therefore obtain analytically

$$W = \frac{D_o}{\cos[\frac{\Theta_c}{2}]}. \tag{3.5}$$

Which gives

$$W = 1.097 D_o \tag{3.6}$$

for an air/water or air/water/glass system.

While these equations corresponded well with the results obtained in 3D Studio Max, they were not yet tested in experiments. One method could be to compare the size estimated by the above described method with bubbles size estimations by putting a known number of bubbles in a tube with a known volume so the bubble volume can be estimated, or the method of the rising bubble can be used. Also making a bubble with a known volume could be applied. Note that in order to use these equations, the experimental set-up needs to be tested for the assumptions of having an infinite light source and observation of parallel light.

3.5 Two touching bubbles

As shown in Figure 3.9, adding a second bubble to the previous system (Section 3.4) interferes with the ray paths in such a way that the image looks as if the bubbles 'kiss'.

This was interpreted mistakenly as a physical (rather than purely optical) effect by Sebba [74], who concluded that films are deformed as a result of attractive forces. More recently an equal misinterpretation was done by Bremond *et al.* [87] explaining coalescence of droplets by the formation of two facing 'nipples' at either side of the droplets. The same patterns can be obtained with perfectly spherical bubbles or droplets as we show here.

Figure 3.9 (c) shows the ray paths through the mirror-plane of the two-bubble system through the bubble centres.

The pattern changes around the point of contact as here light rays will interfere with the additional curved gas/liquid interfaces of the second bubble. Concerning the cross-section through the centres of the bubbles the second interface bends light rays towards the light source, such that the black ring becomes narrower close to where the bubbles touch. The inner boundary B_i moves towards the bubble boundary.

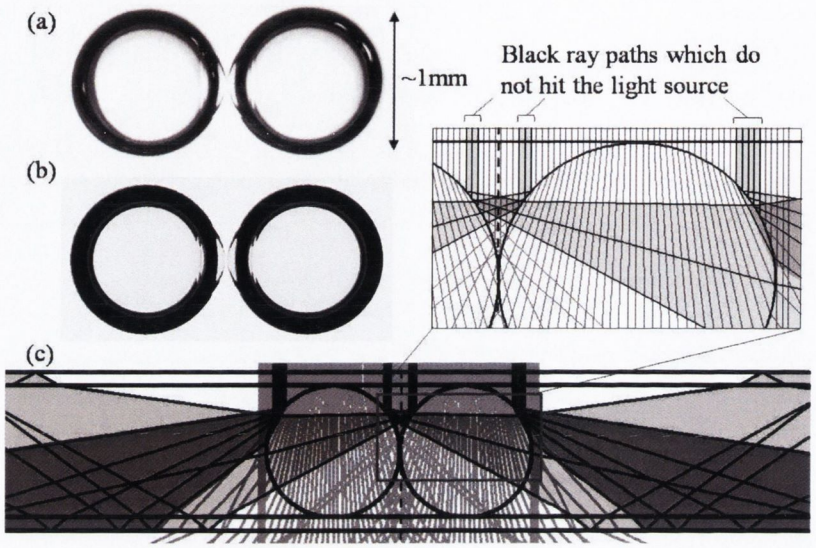


Figure 3.9: Two touching bubbles in a Hele-Shaw cell. (a) Experimental image. (b) 3D-simulation (b) (c) Corresponding ray paths in the 2D-model (Section 3.3.3) of the plane through the centres of the two bubbles. The simulation shows that the set-up in which the picture was taken was finite.

Note, that the diameter of each bubble can still be determined separately by application of the analysis of the individual bubble (Section 3.4) using the appropriate cross-section through the centre of the bubbles, if the assumptions are correct.

3.6 Bubble layer

The effect of two touching bubbles (Section 3.5) is amplified by having a closely packed layer of bubbles between two glass plates or in a shallow liquid pool, as shown in Figure 3.10.

The pattern consists of rings, which are slightly hexagonal. Sometimes a hexagonal pattern is seen within the ring, see Figure 3.10 (c). Note again, that even though the bubbles are touching, the black rings are not. The optical black rings in a layer of bubbles are smaller than for a single bubble. We do not provide here mathematical correlations between bubble size and pattern, as the bubble diameter can be determined by measuring the distance between the bubble centres. Note that then we assume that the bubbles are not squeezed.

We shall add a note regarding mono-layers of bubbles floating on deep pools, i.e. in which the optical interaction with the bottom plate can be neglected. In such a constellation, individual bubbles would not generate a well defined image. However, as shown in Figure 3.11, adding neighbouring bubbles influences the optical properties such that a significant fraction of light rays is bent upwards in such a way that they never hit the light source and

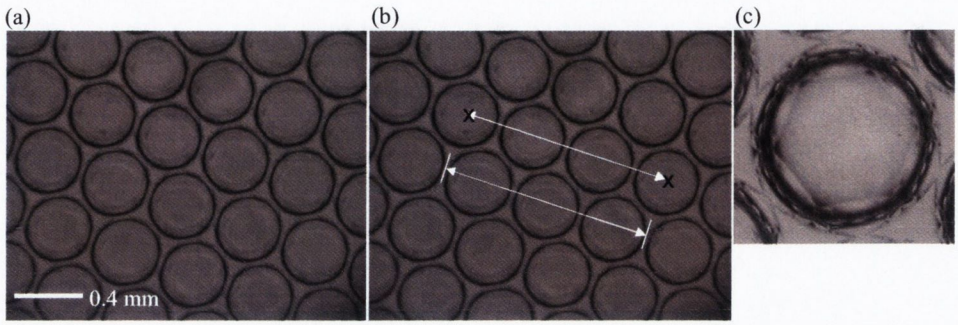


Figure 3.10: (a) Photograph of one layer of monodisperse bubbles packed between two glass plates. (b) shows the method of the bubble size determination, either using the bubble centres or sizes. The bubble diameter is length measured/ number of bubbles. (c) The rarely observed hexagonal pattern inside the ring pattern.

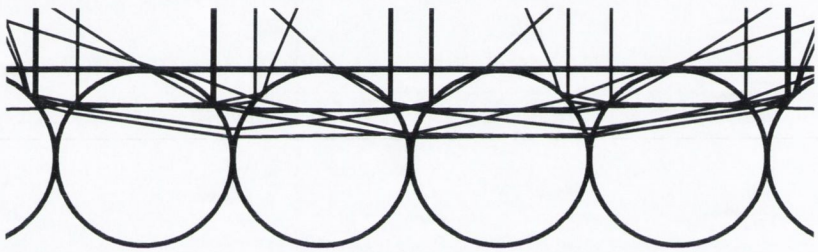


Figure 3.11: A layer of bubbles at a gas-water interface in an infinitely large pool and light source. For clarity only those rays are drawn which do not hit the light source.

therefore generate well defined black rings. This can be summed up in a simple rule: bubbles can generally be imaged if there are several of them.

Note that there is a slight difference in having a top glass plate or just a water-surface. As the water surface is slightly deformed by the top layer bubbles [88, 89], bubbles create more reflections, see Figure 3.10 (c).

3.7 Two layers

We will work with multiple layers of bubbles, therefore we explored computationally the effect of multiple bubbles packed below each other. Figure 3.12 shows an example in which only one bubble is positioned underneath a single bubble layer. Its image can be seen within the three touching bubbles on top. Note that these are *not* the boundaries of flat films formed as a result of bubbles touching, as can be seen in Figure 3.12 (b) showing the ray-paths through representative cross-sections.

In Figure 3.13 all positions of the second layer are completely filled for the triangular

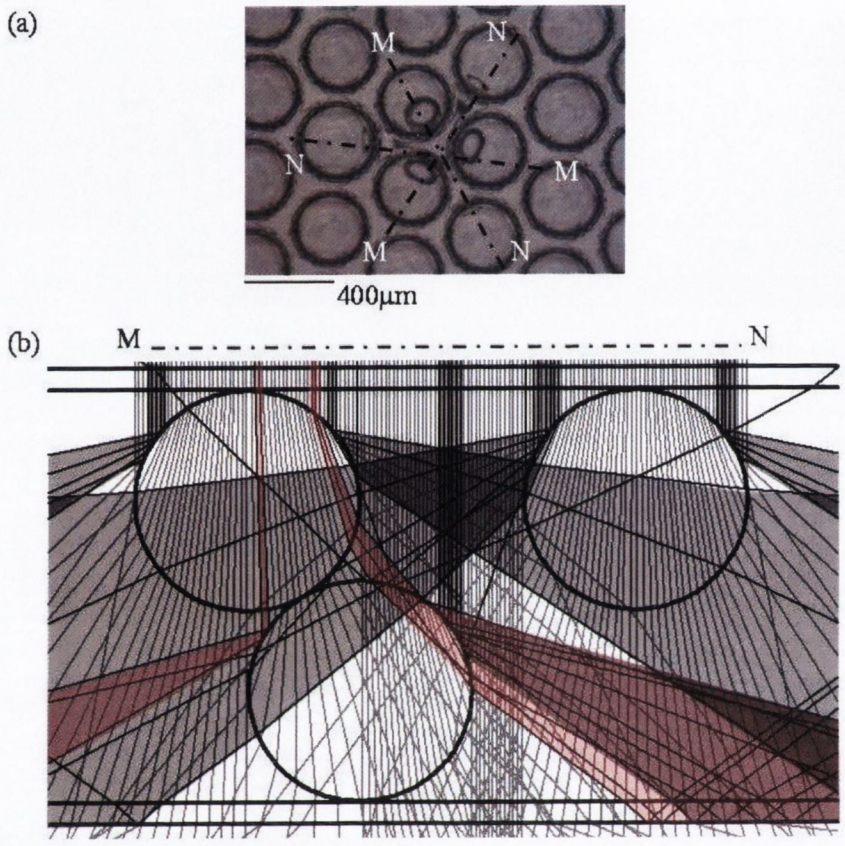


Figure 3.12: The effect of lensing of one bubble underneath a layer of bubbles. (a) Experimental image viewed from the top. (b) Ray paths though the cross-section marked M-N.

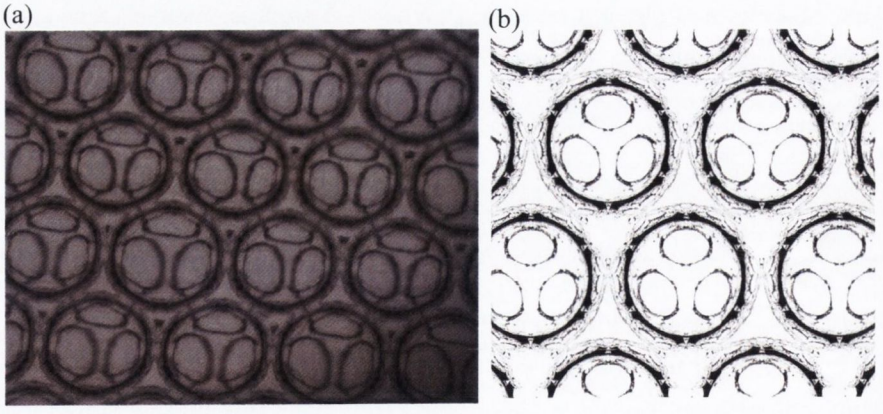


Figure 3.13: Two images of triangular ordered layers of bubbles between two glass plates, experiment (a) and simulation (b).

packing. The optical patterns of the 3 contacting bubbles of the second layer are projected inside the optical pattern of the surface bubble.

In all cases the determination of the bubble sizes can be done using the pattern of the top layer, as discussed in Section 3.6.

3.8 Wet bubble crystals

As we saw in the last section, each bubble acts as a diverging lens and the bubble layers therefore 'recursively' image the optical patterns generated by the bubbles underneath. This leads to the generation of beautiful fractal-like patterns in bubble crystals consisting of multiple layers, which makes it possible to extract information on the crystal ordering for 3-5 layers into the bulk. With the help of the compiled images with a known crystalline structure as an input geometry, comparisons can be made with the images of crystalline microfoams to obtain information of the present crystalline structure in the foam.

There are different 3D close packed crystalline structures in which equally sized spherical objects such as monodisperse bubbles can order. Considering a triangular layer, as seen in Figure 3.11, there are three ways (A, B and C) of stacking these layers with respect to each other. This generates different sequences of ordering to make up various types of structures: hexagonal close-packed (hcp, ABABA..), face-centered-cubic (fcc, ABCABCA..), and random hexagonal close-packed (rhcp). As we will see later, the fcc-crystal is observed in two different orientations: in the (111) orientation, with the triangular top layer and the (100) orientation, with square-packed top layers.

3.8.1 Hcp(0001)

As illustrated in Figure 3.14 (a) and (b), in hcp crystals the close-packed layers occur in ABAB... sequence, which means that every second layer is in the same position. Figure 3.14 (c) shows the experimental and computational images which allow us to clearly distinguish between the first three layers. The contribution of each of the three layers is illustrated more clearly in Figure 3.15 (b), which shows a close-up of one of the bubbles in Figures 3.14 (c).

Both the experimental images and the simulation show a pattern of the third layer where one ring is positioned close to the centre of the top layer bubble and 2 rings further outwards. The experiment and simulation correspond well and it can therefore be concluded the bubble in this experimental image are stacked in the hcp crystalline structure at least for the first 3 layers. The patterns of the fourth layers experimentally not visible anymore.

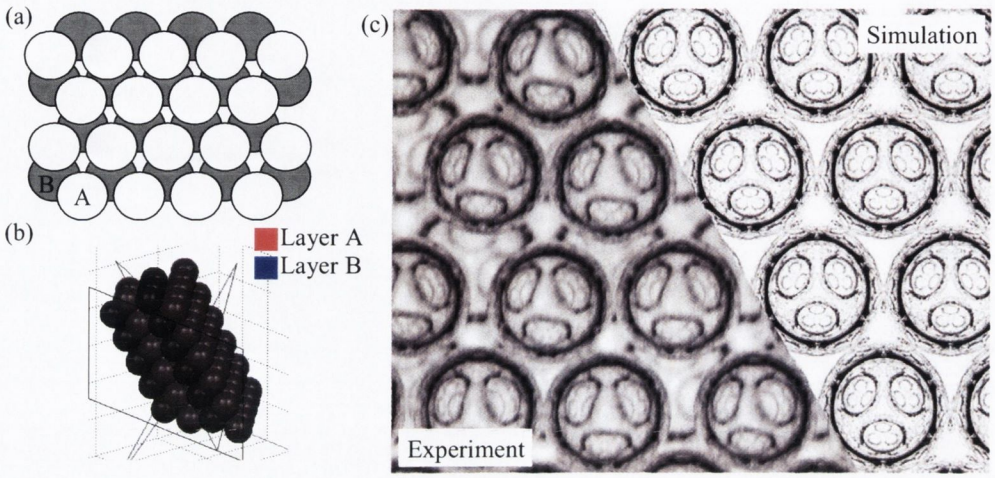


Figure 3.14: The hcp crystalline structure. Sphere packing in layering of ABAB (a) seen in the (001)direction and (b) under a slight angle, created with Matlab®[84]. (c) Experimental and computational image of bubbles packed in the hcp crystalline structure.

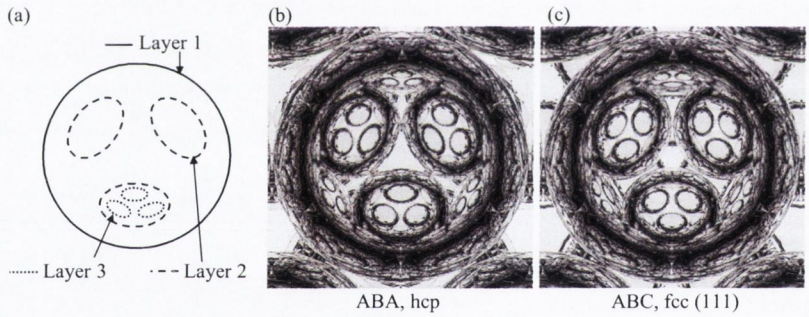


Figure 3.15: Computational images generated by crystals with layering ABA (hcp)(b) and ABC (fcc(111))(c). The contribution of each layer to the image is given in sketch (a). The pattern of the third layer can be used to distinguish between the fcc(111) 'ABC' or hcp 'ABA' crystalline ordering.

3.8.2 Fcc

(111)-orientation

As shown in Figure 3.16 (a) and (b), fcc-crystals consist of layers stacked in a ABCABC... sequence, in which every third layer is in the same position. Figure 3.16 (c) show the experimental and computational image generated by an fcc-crystal which is viewed at the (111) orientation. Again the patterns match very well and therefore the conclusion can be drawn that the bubbles in an experimental image showing these optical patterns are stacked as a fcc (111) oriented crystal. Comparing Figure 3.15 (b) and (c), illustrating the layer contributions to the optical pattern, one can clearly see that the patterns of the hcp and fcc structure differ

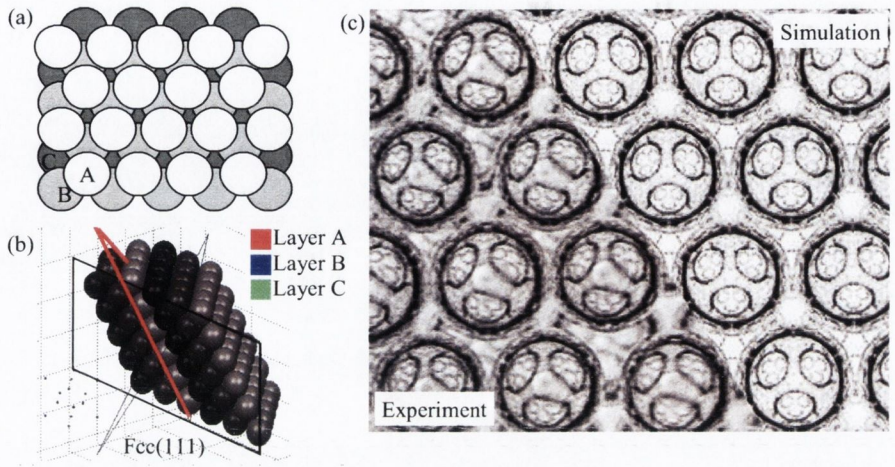


Figure 3.16: The fcc(111) crystal structure. Layering 'ABC...' with solid beads, in (a) seen in the (111) direction and (b) under a slight angle, created with Matlab®[84]. (c) Experimental and computational image of bubbles stacked in the fcc(111) crystal structure.

in the arrangement of the small rings generated by the third bubble layer.

(100)-orientation

In this orientation, the viewer looks at close-packed square layers, which is illustrated in Figure 3.17 (a). In this particular example it is easy to be misled to think that the bubbles

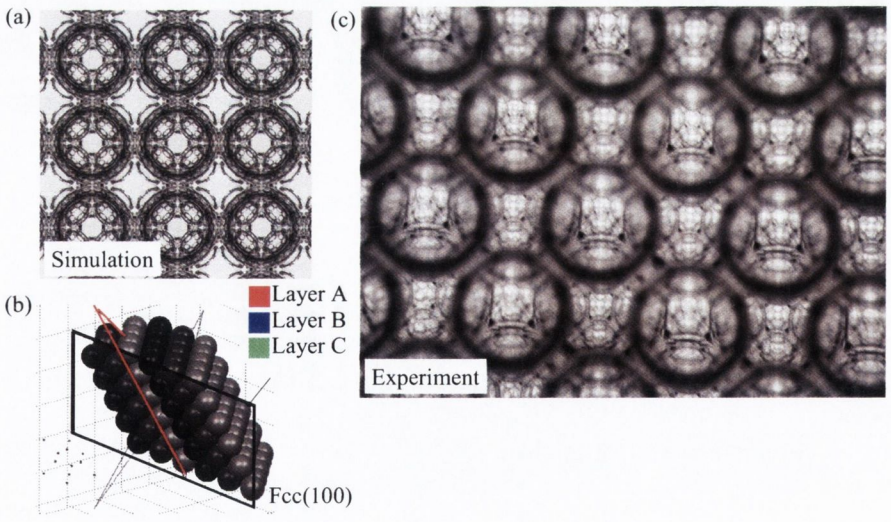


Figure 3.17: The square fcc(100) crystalline structure, simulated in 3D Studio Max (a) and in the experiment (c). (b) shows the orientation of the fcc(111) (red triangle) with the colored layers labeled ABCABC, the black rectangle shows the orientation fcc(100) made in Matlab®[84].

are arranged in a bcc (body-centered packing), which looks very similar, as shown in Figure 3.18. However, a bcc bubble-structure is not close-packed and is therefore energetically unstable [20]. As we can show with the simulations, the confusion is a result of the optical illusion that bubbles are not touching in the fcc-structure. Note that a complication arises due to the effect described in Chapter 5, where diffusion can cause the bubbles of the first layer to shrink, such that the bubbles actually lose contact. But this is then only occurring for the first layer.

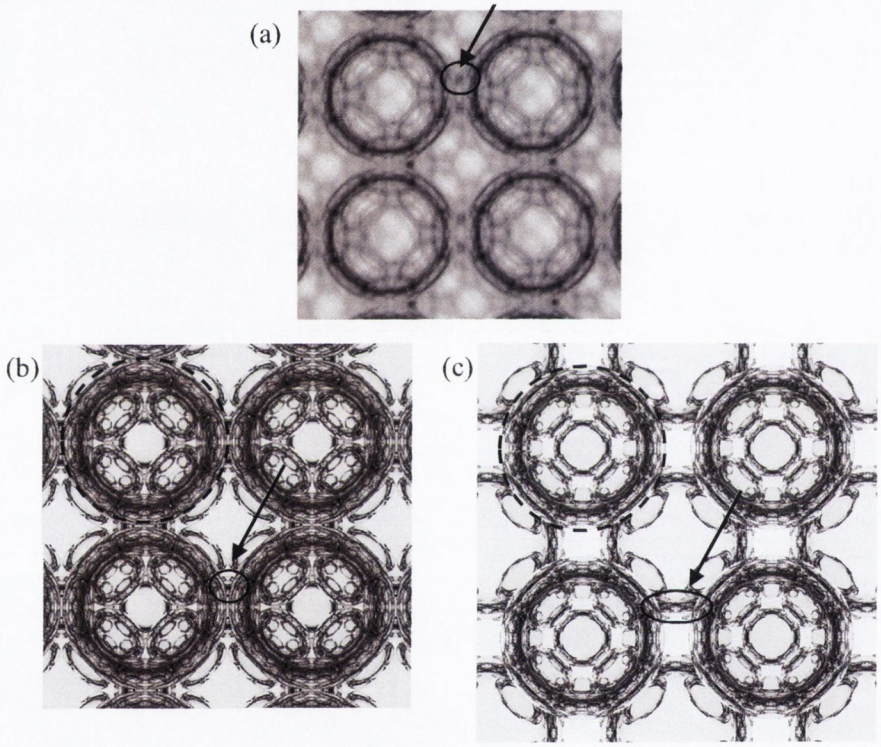


Figure 3.18: The simulation of the fcc(100) oriented structure (b) compared with simulation of the bcc structure (c). This shows that the experimental image (a) is fcc(100).

3.9 Variations on the implemented foam properties

Variation of refractive index ratio

To illustrate the effect of the ratio n_d/n_c of the refractive indices of the disperse and the continuous phase, we show some examples of widely used systems in Figure 3.19, like emulsions, generated by 3D Studio Max. With increasing ratio n_d/n_c, the overall image becomes brighter and the optical features less pronounced.

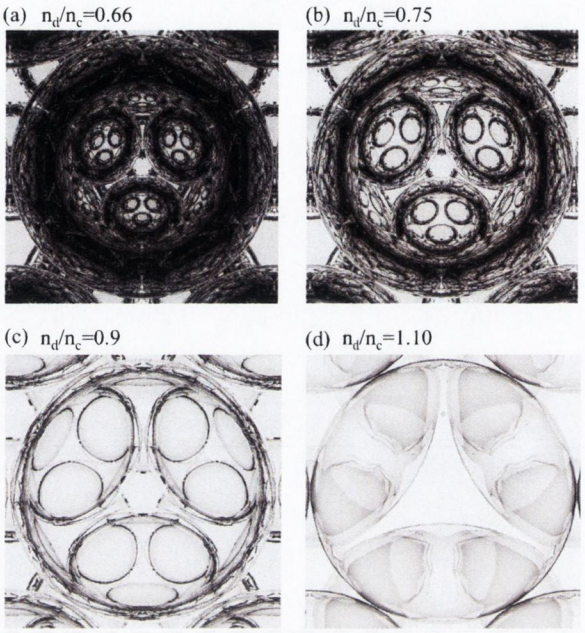


Figure 3.19: Simulation examples for four different refractive index ratios n_d/n_c of commonly used systems, generated in 3D Studio Max. n_d is the refractive index of the dispersed phase, whilst n_c that of the continuous phase. (a) Gas bubble in glass, (b) Gas bubble in water, (c) Water droplet in oil, (d) Oil droplet in water.

Squeezed bubbles

In our simulations we used perfectly spherical bubbles. In experiments bubbles may be squeezed due to effects of gravity. Figure 3.20 illustrates the change in the optical pattern, when bubble crystals (a) hcp, (b) fcc(111) and (c) fcc(100) are squeezed by (an exaggerated) 50 % perpendicular to the image plane. As a result, the central part of the pattern is enlarged with respect to that on the boundary of the bubble. This makes it possible to infer the sphericality of the bubbles from a single image. This knowledge is critical when requiring measurements of bubble sizes from the image.

3.10 Conclusions and Outlook

We have introduced a simple computational method to relate images of foam structures to their geometry. We have employed this method in some representational examples of different bubble configurations and quasi-2D foams (Appendix A). We have established a number of mathematical relationships between images and geometries of these structures, which may guide the analysis of related experiments. From bubble patterns in microfoams, information

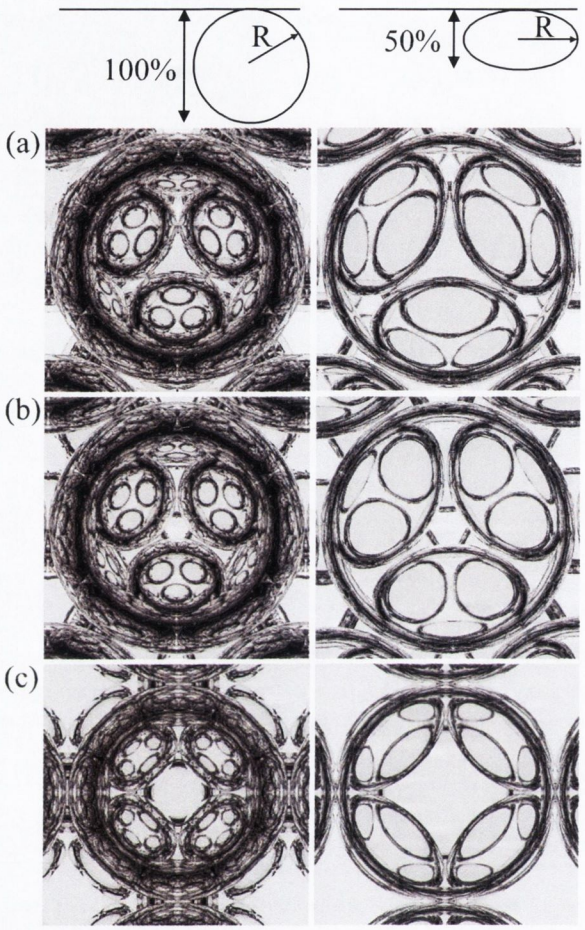


Figure 3.20: Change of the optical pattern when bubbles are squeezed perpendicular to the imaging direction for (a) hcp (b) fcc(111) and (c) fcc(100) bubble crystals. The left column shows the patterns with spherical bubbles. In the right column bubbles are squeezed by 50% in the direction perpendicular to the image plane.

on crystalline structures can be extracted. Many of our examples emphasize that care needs to be taken in drawing conclusions from foam images, as many of the apparent boundaries do not correspond to the actual ones.

We have introduced some key-elements of ray-tracing techniques for foams. However, a vast number of applications remains to be explored. For instance, similar tools can be used to investigate images created by the use of reflected light, which lighting technique is also often used in experiments, beside transmitted lighting.

Furthermore, our simple geometries should be replaced by the output of simulations, which can model less regular geometries, as they occur in polydisperse foams and/or those

deformed by additional stresses. Simulations performed with software packages like Surface Evolver [16] could then be coupled with raytracing software, to not only predict the physically correct shape of an object, but also to see what features will be experimentally visible.

In the next chapters we will use the optical analysis on crystalline bubble structures to further analyse the crystalline microfoams.

Chapter 4

Ordering of microbubbles in the wet foam limit

4.1 Introduction

Bragg and Nye in 1947 [18] described for the first time observations of ordering of equally sized microbubbles in multiple layers in wet foams, as shown in Figure 4.1, but to our knowledge no research followed this up thereafter for over 50 years. The paper in question is a familiar reference, often cited for the introduction of the two-dimensional single bubble layer or a so called bubble raft (or 2D foam) as an analogue to metallic crystals. Two dimensional bubbles rafts have since been subject of much research [90–94], unlike the multiple layered system. Three-dimensional crystalline microfoams were briefly mentioned by Ganan-Calvo [7], who named them mesocrystals. Recently, the study of these crystalline microfoams has been taken up again by us and other groups [21] and has greatly gained from (computational) imaging techniques.

As foams are systems with multiple interfaces they diffuse light such that the internal structure cannot be observed by shining light onto the foam sample. By use of appropriate lighting and raytracing software as described in Chapter 3, we are able to reliably infer the structure of as many as three to five layers below the top surface depending on the specific crystalline arrangement. Based on these observations we discuss in Sections 4.3 and 4.5 the occurrence of different crystalline structures and imperfections. Our own findings are highly consistent with those of Bragg and Nye, but are more detailed and wide-ranging. In Section 4.4 we discuss the imperfections that can occur. The frequency of occurrence of the different crystalline structures is determined in Section 4.6. We discuss also observations of

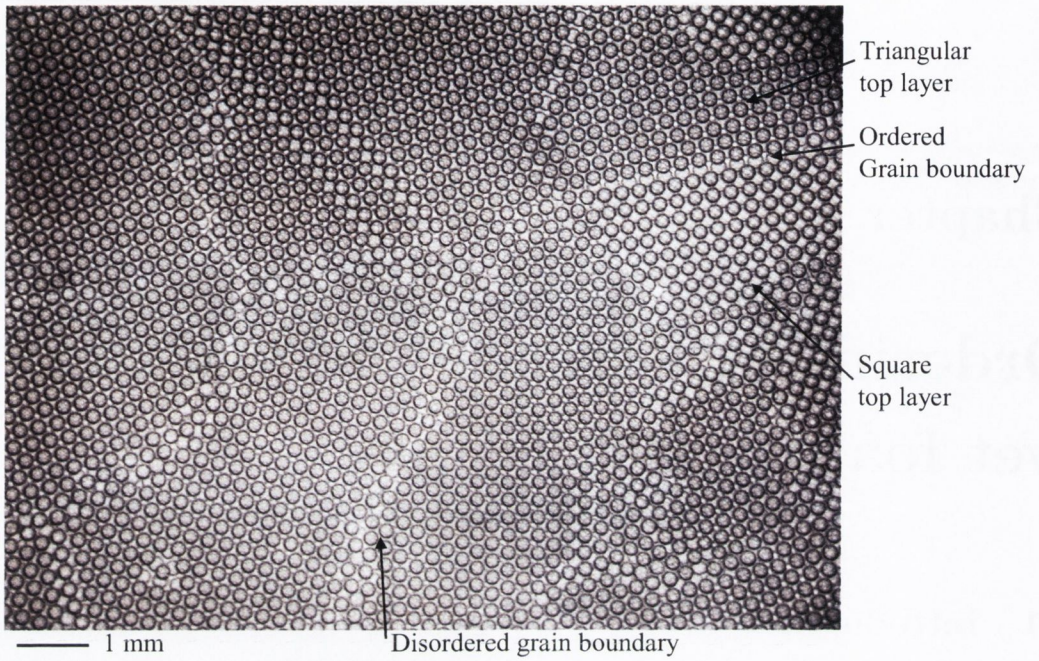


Figure 4.1: A view of the top of a monodisperse foam (height $\sim$ 1 cm, bubble diameter $\sim$ 250μm) reveals grains with a crystalline arrangement.

the crystallisation process and factors discussed in the literature that influence the tendency of the microbubbles to order. In Section 4.9 we show how confinement can be used for obtaining specific crystalline orientations. In Section 4.10 we explain how the wet crystalline microfoams can be used for the creation of dry ordered foams. Finally, we compare the tendency of ordering of the microbubble system with the behaviour of similar systems in Section 4.8.

4.2 Experimental set-up and procedure

Sample creation

We created highly monodisperse bubbles with Fairy Liquid surfactant solution of ten times the critical micelle concentration (CMC) and nitrogen, applying the microfluidic flow focusing technique [12, 14, 26]. This produces a rapid stream of small bubbles with diameters between 100 and 800 μm (Chapter 2). The bubbles were continuously expelled from a 10 cm long tube attached to the outlet of the bubble generator. They were allowed to flow into a box with a diameter of 15 cm in a liquid consisting of the same surfactant solution, see Figure

4.2. The bubbles gathered at the liquid surface, where they ordered in crystalline microfoams.

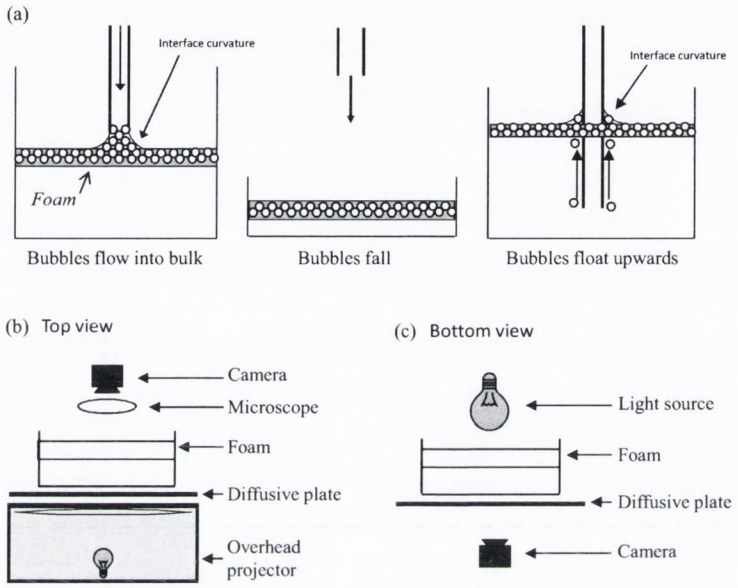


Figure 4.2: (a)The different set-ups used to deposit microbubbles on/into a liquid pool, plus the set-ups to analyse the foam samples from the top (b) and bottom (c).

The occurrence of the crystalline microfoam appears independent of which deposition method is selected from those shown in Figure 4.2 (a). The tube could be positioned slightly above a liquid pool such that the bubbles flowed out into the foam, it could be submerged in the liquid such that the bubbles floated up individually and it could also be located high above the liquid such that drops filled with bubbles fell down onto the liquid. Whichever method was used 3D crystalline microfoams were generated.

Due to surface tension the top surface of the crystalline microfoams can be considered flat. This is different from the bottom of sample where we observed terraces. In the Section 4.3 and 4.5 we will discuss different features present at the top and bottom surface of the crystalline microfoams.

Sample analysis

We took photographs of the top layers of the foam through a microscope (low magnification 2-3x) using a diffusive light source (overhead projector) placed underneath the foam sample, as shown in Figure 4.2 (b). As foam scatters light you can not look inside the foam. To gain more information on the characteristics of the foam the set-up was also reversed for

observations of the bottom of the sample, see Figure 4.2 (c). The sample was placed on an elevated transparent plate. A diffusive light was placed above the sample. We either used a mirror or camera to make observations.

4.3 Crystal Structure

As described by Bragg and Nye [18] two different surface patterns can be observed in the top bubble layer. These are triangular and square surface arrangements, as seen in Figure 4.1. The different ordered arrangements are called the grains of the crystalline microfoams.

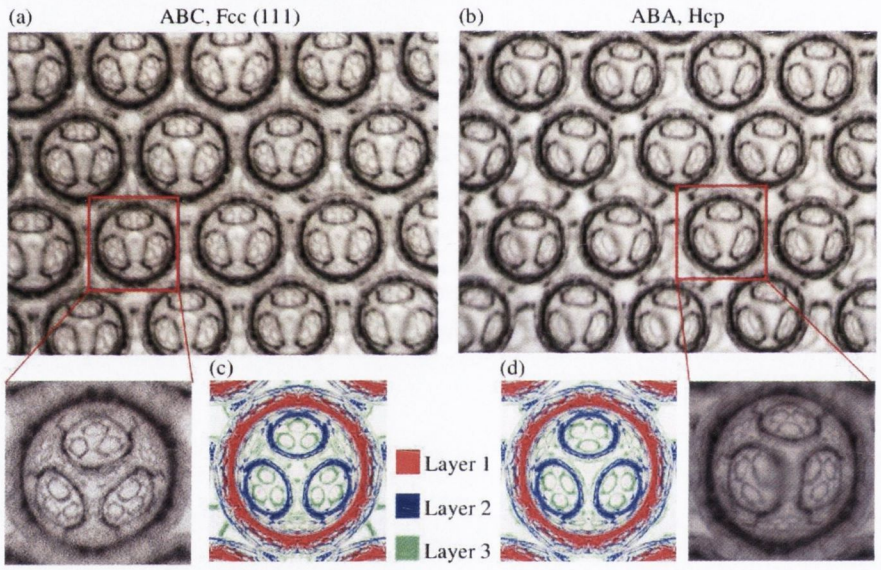


Figure 4.3: A close-up on the two different hexagonal surface patterns seen in Figure 4.1; (a) fcc(111) and (b) hcp, including the simulation, (c) for fcc(111) and (d) for hcp, showing the contribution of the different layers to the optical patterns seem from above (bubble diameter $\simeq 0.5\ mm$) (see Chapter 3).

The most commonly observed triangular pattern is as shown in Figure 4.3(a), which is produced by the *fcc*(111) (ABC..) packing (explained in Chapter 1). This was also noted by Bragg and Nye (who were able to see up to three layers). Figure 4.3(b) presents a second observed triangular sequence, which is generated by *hcp (0001)* (ABA..) structure. The patterns correspond very well with the computational simulations of these structures, described in Chapter 3. Note that beyond three layers the continuation of the fcc or hcp structure is undetermined. There are, of course, many possibilities, including *(rhcp)* (random sequence of layers). However, we believe that other evidence given in later Sections 4.5 and 4.7.1 points to substantial bulk ordering in simple crystal structures of fcc and hcp.

The square arrangement is that of the (100)-oriented *fcc* structure, as shown in Figure 4.4. With the ordered optical patterns within the fcc(100) bubble surface, we were able to observe up to five layers into the bulk structure depending on the bubble size. With the ordered optical patterns within the fcc(100) bubble surface, we were able to observe up to five layers into the bulk structure, depending on the bubbles sizes.

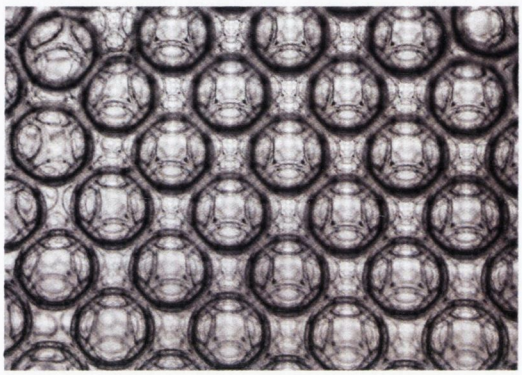


Figure 4.4: Photograph showing at least five layers of bubbles arranged in an *fcc* packing in the direction [100]. One might mistake this for *bcc* packing on account of optical effects (bubble diameter $\simeq 0.5\ mm$).

The grains are separated by grain boundaries. These can be coherent (ordered) or disordered. In Figure 4.5 different arrangements are shown. Figure 4.5 (d) shows an example

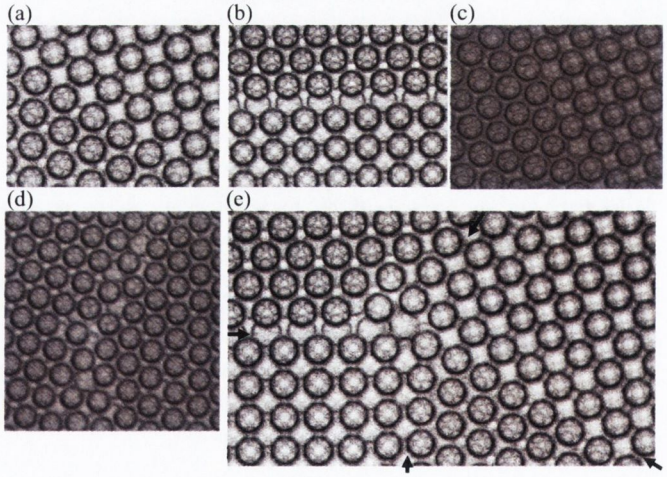


Figure 4.5: Different grain boundaries present in bubble crystals. (a,b,c) are ordered grain boundaries between fcc(100) and fcc(111) grains, (e) shows a rare junction of ordered grain boundaries. (d) shows a disordered grain boundary between two fcc(111) grains.

of a disordered grain boundary, which are the most common grain boundaries found. Three different kinds of coherent grain boundary between fcc(100) and fcc(111) oriented grains are shown Figure 4.5 (a), (b) and (c). In Appendix B a theoretical description is given for the expected arrangement of a coherent grain boundary between fcc(100) and fcc(111) oriented grains shown in Figure 4.5 (a) and (b). It can be seen that in (a) the second layer of the fcc(111) grain proceeds partly under the fcc(100) top layer, where (b) shows the opposite movement. It is expected both crystals fit together only when positioned under an angle, as Bragg and Nye already mention in their paper [18], which is expected to be 195.8° considering the surface planes of the crystals. A rare junction of ordered grain boundaries can be seen in Figure 4.5 (e).

4.4 Imperfections

Beyond the order of the grains, the crystalline microfoams show a variety of interesting defects of the type that can be found for example, in metal structures [95].

Surface defects

We observed simple vacancies at the surface, such as the point defect in Figure 4.6, where one bubble is missing in the structure.

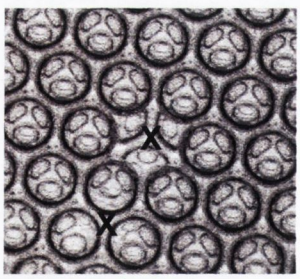


Figure 4.6: Photograph of two vacancies seen in the surface layer of a *hcp* packing marked with an X (bubble diameter $\simeq 200\mu m$). One vacancy is in the top layer, clearly visible, and the other is in the second layer (bottom left).

Divacancies, i.e. vacancies of two bubbles, often take the form shown in Figure 4.7. If the surface layer is of type B and the underlying one is of type A, then the central bubble resides in a C site, which we have dubbed the 'shamrock defect'.

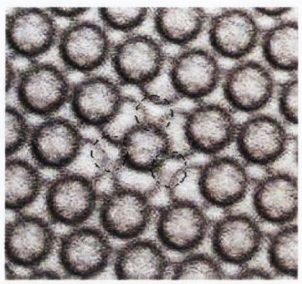


Figure 4.7: Photograph of a surface divacancy in a (111) *fcc* packing (bubble diameter $\simeq 250\mu m$). There are two missing bubbles in the A layer, which sits on top of a complete B layer. The dotted lines indicate the unoccupied sites of the top A layer. One bubble resides in the central (C) position.

Stacking faults

Typically, the grains are not perfect and stacking faults occur. A *stacking fault* is a location within the grain where layers of bubbles are completely displaced with respect to the unit cell stacking. There are two kinds of stacking faults: (i) an *extrinsic stacking fault* when according to the packing order of the layers an extra layer is included e.g. $ABAB|C|ABAB$, (ii) an *intrinsic stacking fault* when a layer is missing e.g. $ABC|BCAB$.

Figure 4.8 shows an experimental image (c) which is example of an intrinsic stacking fault

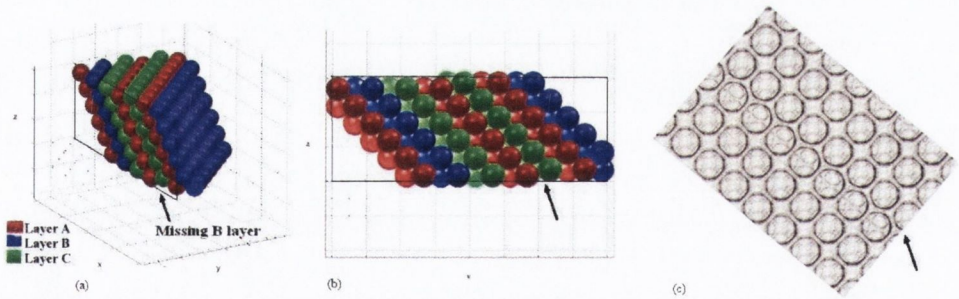


Figure 4.8: Intrinsic stacking fault of ABCA|CAB in an *fcc* packing. The computer generated structure (a) shows the layers ABCA|CAB, which are viewed in the [100] direction in (b). In the experimental observation (c) the foam (bubble diameter $\simeq 350\mu m$) was contained in a Hele-Shaw cell with a spacing of 3 mm.

with layers packed according to ABCA|CAB in the fcc[111] orientation (a), but they are viewed from the fcc[100] orientation (b). The images (a) and (b) are generated in Matlab. The program enables stacking of planes defined in different orientation, and visualisation of

cross-sections through the created structure in any possible orientation.

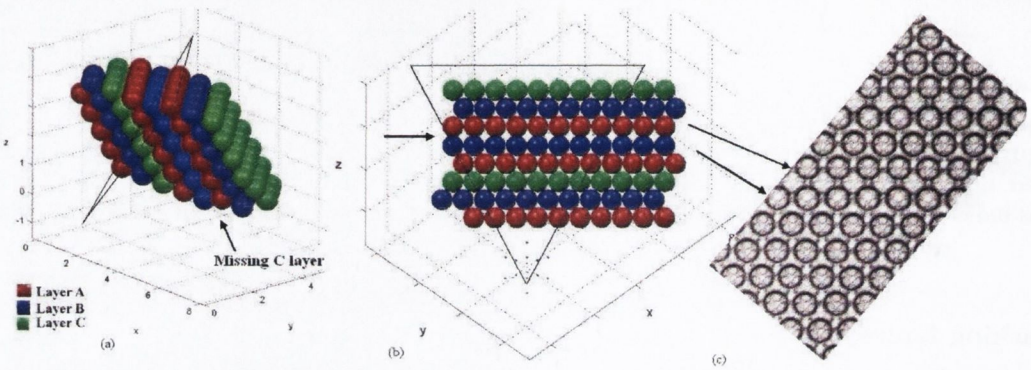


Figure 4.9: Intrinsic stacking fault of ABCAB|ABC in an *fcc* packing. The computer generated structure (a) shows the layers ABCAB|ABC, which are viewed in the [11-1] direction in (b). The corresponding experimental realisation is shown in (c) (bubble diameter $\simeq 350\mu m$).

Figure 4.9 shows a second example of an intrinsic stacking fault(c) with layers packed ABCAB|ABC in the fcc(111) orientation (a) but now viewed in the fcc[11-1] direction (b). The fcc(11-1) plane also results in triangular ordered top layer when perfectly packed. Finally, Figure 4.10 show an example of an extrinsic stacking fault CA|C|BC in the planes packed according to the fcc(111) plane (a) but viewed in the fcc[100] direction (b,c).

Similar patterns are seen in opal crystals [96]. If planes are not completely, but only partly, displaced the fault is called a *dislocation*. This is for example the case when only a line defect occurs in the first layer and the layers below are complete. Note that as we can only see up to 3-5 layers into the bulk, we assume that if for this number of layers a line defect is visible the defect will progress further and we name it a stacking fault, else it is a dislocation.

4.5 Terraces

The foam-air interface in our samples is generally quite smooth and flat, apart from slight height differences between grains of different orientation. In contrast to this the foam/liquid interface at the bottom of the sample generally consists of dense arrangements of terraces, associated with close-packed planes, angled with respect to the interface, see Figure 4.11. We could identify sequences of up to seven *fcc* planes with the terraces. The presence of terraces

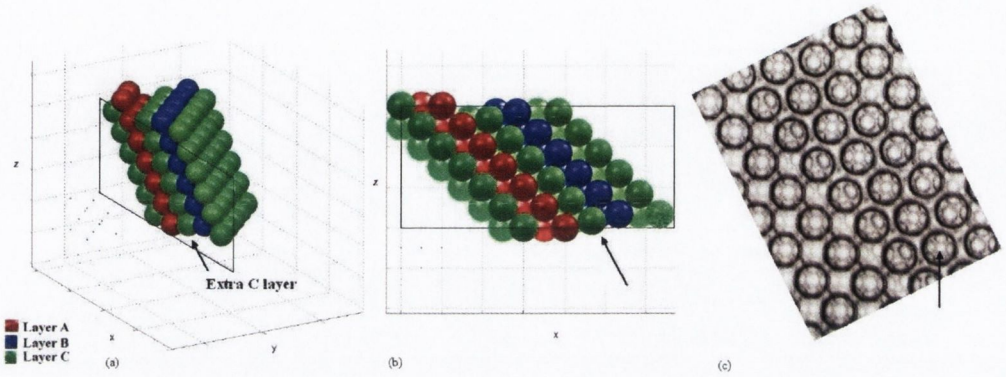


Figure 4.10: Extrinsic stacking fault in an *fcc* packing. The computer generated structure (a) shows the layers CA|C|BC, which are viewed in the [100] direction in (b). The bubbles in the photograph (c) have a diameter $\simeq 350\mu m$.

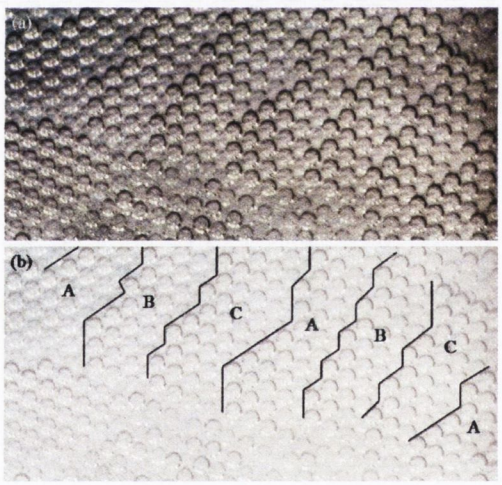


Figure 4.11: (a) Photograph of a set of terraces formed at the foam-liquid interface, viewed from below. (b) Indication of the terrace boundaries, showing seven (111) *fcc* planes.

strongly indicates bulk ordering.

Just as at the top of the foam sample we observed grain boundaries, stacking faults and dislocations in the terraces were observed at the bottom of the sample. Occasionally we were able to follow them clearly over a sequence of terraces into the bulk structure of the foam, as

shown in Figure 4.12.

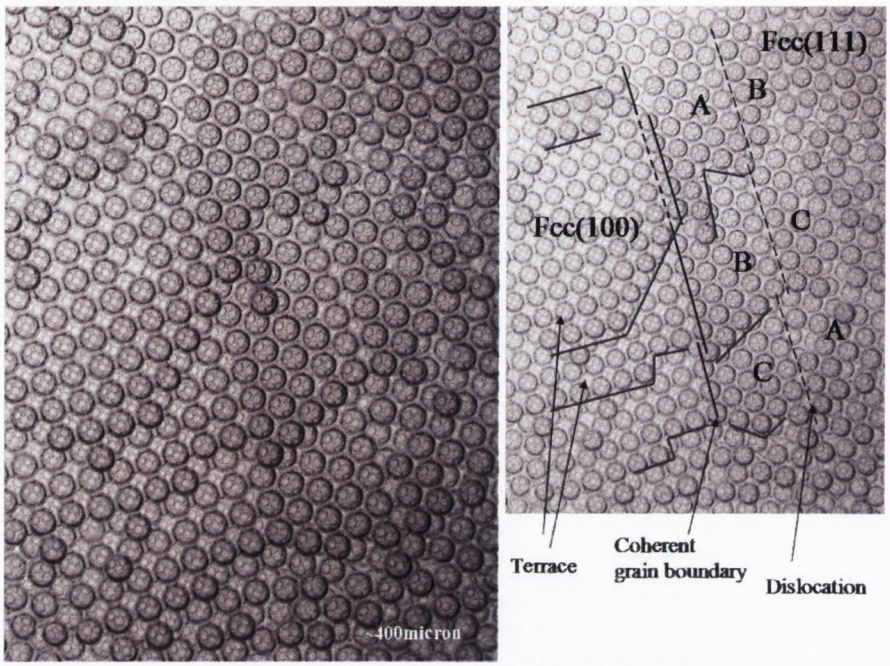


Figure 4.12: Terraces, including a coherent grain boundary between fcc(100) and fcc(111) and a dislocation at the foam-water interface.

4.6 Statistics on the occurrence of crystalline structures

The ability to identify the ordering of the top three layers of bubbles with the simulated images of the crystalline structures in Chapter 3 enabled us to investigate the occurrence of fcc(111), fcc(100), hcp and other structures. We identified the type of ordering of the bubbles in 202 regions contained within 28 separate samples of foam. Seven to eight random sampling points were chosen in each sample using a plastic sheet with random dots, which assigned the sampling position when placed over the surface. This method was applied to avoid any sampling prejudice. The results of this analysis are given in Table 4.1. The error estimation is obtained by sample standard deviation devided by the square root of the total number of samples. A preference for fcc was found, with 59% of the regions examined showing an fcc structure.

The terraces at the foam-water interface were also used to extract information about the order. For the analysis of the terraces we have analysed the stacking sequence of the triangular

Type of Ordering	Number of observations	Fraction
fcc(111)(ABC)	107	0.53±0.11
fcc(100)(ABC)	12	0.059±0.060
hcp(ABA)	63	0.31±0.088
undefined	20	0.099±0.065
Total number of observations	202	1.0

Table 4.1: 202 observations of different types of ordering in the top layer of 28 foam samples.

layers. We used the optical patterns as described previously and also compared the positions of the bubble centres of successive layers. This gave us the advantage of analysing more than 3 successive layers.

Type of Ordering	Number of observations	Fraction
fcc(111)	15	0.58±0.32
hcp	4	0.15±0.11
other	7	0.27±0.15
Total number of observations	26	1.0

Table 4.2: Observations of different types of ordering inferred from analysis of terraces (of 4 layers or more) at the foam-water interface.

It was generally quite difficult to find large terraces perfect enough (see Figure 4.12) for analysis. The optical patterns were in general less clear due to a lower light intensity used in the set-up. Therefore random sampling was not applied here. This could result in finding only undefined structures. To avoid this the whole sample was checked for terraces where four or more layers could be identified. We did not make an estimate for the difference in occurrence of square or triangular ordered terraces. In nine foam samples, we analysed 43 terraces, of which 26 enabled the analysis of four layers or more. The results are shown in Table 4.2. Here we made the distinction between stackings consistent with fcc (ABCABC), hcp (ABAB) and other possible sequences, ABAC etc. We found that 58% of the terraces examined corresponded to an fcc arrangement. This shows exclusion of the fcc(100) structure in this terrace analysis is not a problem. The end conclusion would remain the same, as its inclusion would make the preference for fcc even stronger.

Considering all of the data from the top and bottom of our crystalline microfoam samples there is a preference for the fcc crystalline structure with 58% over (r)hcp with 42%. If structures were created randomly with 228 samples the percentages would be $50-50\%$. Note that we assumed here that the measurements were independent of each other. We sampled

different grains based on the top or bottom view but there is the possibility that the 'grains' share layers. Therefore it is not entirely clear how independent the measurements are. As we do not know exactly how the order is achieved this is the only option we have available to estimate the occurrence of the different crystals. 3D imaging would be a solution to determine the complete structure of the crystal.

4.7 Mechanism of crystallisation

In this chapter until now we have discussed the observations after deposition. In this section we go into more detail on the dynamics of the crystallisation process.

4.7.1 Experimental observations

Standard experiment

Described in the experimental set-up, Section 4.2, the microfoams were made in a fifteen centimeter wide circular box. Initially as the bubbles were released into the liquid the bubble crystal built up, starting with a single layer. The first bubbles released reached the surface of the liquid and ordered in triangular ordered layers due to the surface tension [97].

Before the complete surface of the box was filled by one single layer the second layer started to build up. At the same time the structure built outwards at the surface; the already formed layers split partly open and new bubbles move towards the surface. This can create new grain boundaries or stacking faults. From bottom observations the bubbles were seen to move outwards in bubble 'trains', rows of four to five bubbles at once. Quickly after the start of deposition a pile structure was created as shown in Figure 4.13 for different set-ups. The most commonly used deposition method is with the outlet completely submerged. As the bubbles are deposited from one injection point this could stimulate the formation of terraces.

With the new bubbles continuously floating up, surface rearrangements were observed along grain boundaries. Sometimes these rearrangements resulted in the square fcc(100) ordered grains. They either disappeared as new rearrangements took place or they remained stable when no new rearrangements occurred, while a deposition from below continued to build up the structures. This suggests stresses in the structure can initiate formation of the fcc(100) structures.

Experiments to test tendency to order

An ordered top surface induced by surface tension forces could act as a template to form a

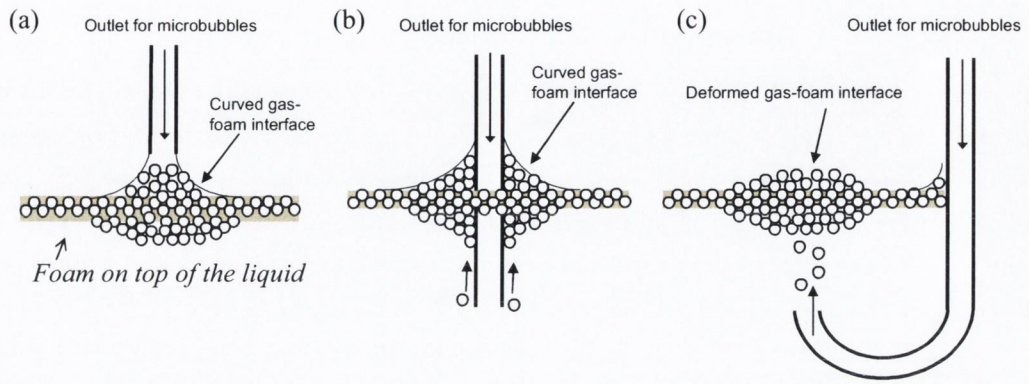


Figure 4.13: The different methods of depositing the bubbles into the liquid pool, (a) with the outlet slightly above the liquid surface, under the liquid surface either with the bubble floating up along the outlet (b) or not (c).

3D crystalline structure. To test the effect of templating we carried out an experiment where initially the top surface was filled with a dry foam consisting of large bubbles ($\sim 5mm$). No order could therefore be obtained by the first layer and it was observed whether they would reorder as they initially hit this uneven surface. The microbubbles were released randomly from the bottom in a two centimeter wide tube filled with large dry foam bubbles. Surprisingly, after a while we saw ordered grains forming at the bottom. The bubbles located at the tube wall followed the boundary but in the centre, grains were formed, which did not follow the boundary. Note that the tube was wide enough to have at least 50 bubbles across, where only the first six to seven layers close to the wall were seen to be influenced by the boundary.

In experiments where we attempted to make the ordered structures out of gelatin (see Appendix D.1) we observed that with a high viscosity the bubbles did not order anymore, at least not in the time span of an hour. The freedom to move was resisted too much by the viscous drag that they did not find a close packed order.

Surfactant choice or solution does not seem to influence the tendency of the bubbles to order. In Chapter 6 we will show that even with polymerisable ingredients, ordered structures can be formed. However, with pure surfactants like TTAB (Tetradecyl Trimethyl Ammonium Bromide) or SDS (sodium dodecyl sulfate) stability of the foams can be problem, as the bubbles rupture before enough bubbles are deposited to form a multi-layered crystalline structure.

4.7.2 Numerical simulation of frictionless hard spheres

To determine the factors which play a role in ordering we investigated the degree to which *templating* effects of an ordered top layer can assist complete ordering in frictionless sphere systems. Order can be induced by use of a special kind of boundary, a template [98]. Numerical simulations were developed and performed by one of our former group members Gary Delaney [99] of the deposition of spheres onto both triangularly packed and square packed surface layers.

The simulations consisted of a simple 'toy model' in which a time integration was performed of Newton's equations of motion with appropriate inter-sphere and sphere-liquid interactions. Spheres were introduced at the bottom of the simulation cell. The presence of a liquid was simulated by including a buoyancy force and viscous dissipation. Colliding spheres interacted via the Hertzian law for spheres, where the force between the interacting spheres is defined as $F = k(2r - d)^{3/2}$, with k the spring constant, r the bubble radius and d the distance between the bubble centres. Dissipative effects were incorporated into the simulations via the inclusion of a velocity dependent Stokes force acting on the bubble while moving through the liquid ($F = -\mu v$, with μ the liquid viscosity and v the velocity of the sphere) and the consideration of viscoelastic dissipation in sphere collisions ($F = -\gamma \frac{d\eta^{\beta}}{dt}$, with γ as the visco-elastic dissipation parameter, η is the overlap between spheres and $\beta = \frac{3}{2}$ [100]).

A low dissipation system represents a nearly frictionless system with a low viscosity liquid and elastic collisions between the bubbles. A high dissipation system has a highly viscous liquid and large energy losses whenever bubbles collide. The simulations were performed using a template, filling the top surface with 192 spheres either forming a triangular or square top layer. Without the template, ordered top layers could be made but always with defects. The presence of defects could induce disorder, which can be important but is not a factor we wanted to consider in these initial simulations. Therefore manually perfect templates were implemented.

Triangular template

When a large amount of spheres was released simultaneously into a system with *large* dissipation, the final packing was random. The spheres very quickly lost their energy and did not rearrange easily. The same experiment in a *low* dissipation system formed an rhcp structure. Here the spheres had more energy to keep moving to find their optimal position. This can be compared with the annealing process of granular materials [101].

With a triangular template and releasing spheres one at the time in a low dissipation

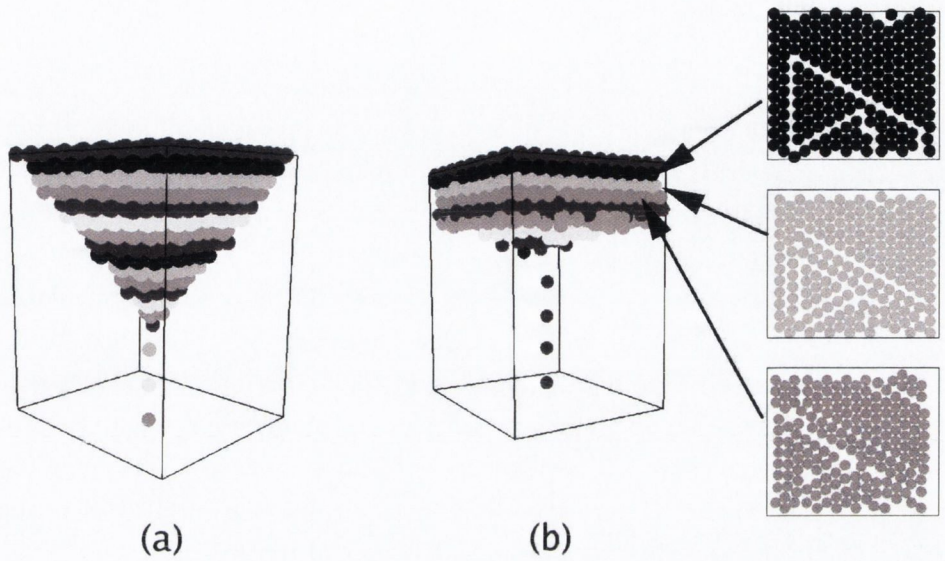


Figure 4.14: Simulation of the deposition (from below) of spheres onto a triangularly packed surface layer. The ordering of the spheres is controlled by the amount of dissipation in the system. While for low dissipation a large number of defects are generally observed (b), a perfect fcc ordering can be achieved if dissipation is increased (a). (Courtesy of Gary Delaney).

system a rhcp structure was formed, see Figure 4.14 (a). However, in a system with high dissipation the spheres formed a fcc structure, see Figure 4.14 (b). The latter shows an inverted pile was formed where the slope induced the fcc structure with smooth walls while for the observed hcp packing this was not the case. The results are summarised in Table 4.3.

	△ 2000	△ 1-1	□ 2000	□ 1-1
High dissipation	random closed packed	fcc	fcc	fcc
Low dissipation	rhcp	rhcp	-	-

Table 4.3: The resulting packing ordering with either a triangular △ or square □ template in a system of either high or low dissipative forces. 2000 stands for the method of random releasing at once 2000 spheres, 1-1 stand for the method of releasing bubbles one by one. ('-' indicates no simulations have been performed.)

Square template

The use of square templates shows, independent of the method of deposition used, the formation of a perfect ordering in fcc crystals in the high dissipative system. The tendency for spheres to pack perfectly with a square top layer is logical, considering there is only one way to pack the next layer, while for a triangular top layer there are two ways of packing the next layer, B or C. This can introduce defects if rearrangements after initial deposition are not

possible anymore.

The simulations show the method of deposition (one by one or all at once) matters in the case of a high dissipative system, while for low dissipative system no difference is seen and only rhcp is formed. In experiments, deposition methods do not appear to affect the tendency of ordering of the system. We expect to have experimentally a low viscosity system. However, experimentally we saw occurrence of fcc crystals and not rhcp as simulations suggest. Note for this experimental analysis we could not observe the entire bulk structure. Simulations show fcc occurrence in high dissipation systems, but only for the deposition method of releasing bubbles one by one, which again experimentally seems not to be a requirement. The simulations clearly show how templating stimulates ordering, especially in the case when the surface layer is square. However as experimentally only between 5-15% of the grains are fcc(100), this can not explain directly the high degree of fcc present.

Overall the simulations suggest that the effect of dissipation, deposition method and templating are not sufficient to fully explain the experimental observation of crystallisation with a preference for the fcc structure. It shows us that more factors play a role in the crystallisation. In the next section we will discuss crystallisation tendencies of comparable systems to address other factors that can be of influence.

4.8 The tendencies of systems to order

Why some systems in nature find order and others do not has for many centuries been a very intriguing question. It is surprising that monodisperse bubbles in wet foams order almost perfectly in three dimensions. It raises the question whether other systems, consisting of particles of spherical shapes, also readily order. Examples of such similar systems which we consider are shown in Figure 1.7; dry foams, emulsions, granular materials and colloidal suspensions. Systems in nature always tend to minimise their energy which in the most ideal case is an ordered close packed structure with the lowest entropy. According to Woodcock [102] the fcc structure is the structure with the lowest entropy.

We briefly discuss in this section the comparable systems to highlight our interest in wet bubble systems and address possible factors worthy of further study to explain the tendency of monodisperse bubble systems to order.

Dry foams

The conjectured optimal arrangement of monodisperse dry bubbles is the Weaire-Phelan structure [103]. Experimentally it is difficult to obtain this optimal ordered dry foam structure. The Weaire-Phelan structure has only been observed experimentally once and only partly. The less rare ordered dry foam structure observed is the Kelvin cell, but this is only obtained under confinement where the boundaries impose order or by placing the bubbles one by one in the right position [15]. As opposed to wet foams, when large bubbles are flowing up into a vessel, bubbles jam as soon as they reach the foam-water interface. Water drains out due to gravity and its surface energy is minimized by forming polyhedral cells. The bubble is no longer able to change position to find its minimum. The energy it costs to change position is too high. A higher liquid fraction would make rearrangement easier as the bubble remains more spherical. Smaller bubbles also have less buoyancy force, which also makes it easier to move.

Summarising the comparison between dry and wet foams, the highly spherical shape, the wetness and the small buoyancy forces for microbubbles are likely to have a positive influence on the spontaneous ordering of small bubbles.

Emulsions

Emulsions, where both the continuous and discontinuous phase are liquids, show a very similar behaviour to foams [104]. To our knowledge there have been no reports published on the spontaneous ordering of droplets for more than two layers in a non-confined system [11].

Only shear induced ordering in emulsions is known to occur under certain circumstances [45–47]. Perrin [46] sheared initially polydisperse droplets between two horizontal plates moving in opposite directions to each other. This resulted in a final steady state of a maximum of 10 hexagonal closed packed ordered layers of monodisperse droplets (3 μm in diameter). The occurrence of crystalline structures has shown to depend on the shear rate [47]. Less order was observed when shear was removed, possibly due to the presence of polydispersity. Note that in Perrin's case shearing is used both to form monodisperse droplets as well as the formation of ordered arrangements. Only the latter is of interest to us.

Granular material

Granular materials range from powders, sand and M&M© chocolate sweets, to rock boulders. Granular materials consist of solid objects suspended in gas or liquid which are large enough not to undergo Brownian motion (random movement under the influence of molecular

interactions [105]). Many studies over the centuries have been devoted to the search for their optimal packing structures and have been looking at the efficiency of packing of different objects. This in general means finding the packing that occupies the least amount of space [106, 107]. This is defined as the packing fraction, the ratio between the volume of the objects divided by the total volume of the sample. For the comparison with our bubbles we will only consider studies with monodisperse hard spheres.

Kepler, in the seventeenth century, stated that the optimal packing fraction of monodisperse spheres is 0.74 according to the fcc/hcp packing [108] and variations. The mathematical proof was not obtained until recently by Thomas C. Hales [109]. Generally granular systems will *not* find their optimal packing. When beads are thrown in a box, the maximum packing fraction is 0.64, named *random close packing*. The least dense structure which can support an external load is the *random loose packing* with a packing fraction of 0.56 [110].

In either case the beads are jammed and unable to pack closer. Due to the Coulomb friction [111] and undeformibility of the spheres, the system can resist stress with less than the maximum of 12 contact points. Arches are formed to distribute the pressures, such that the structure remains intact and does not find its ordered structure [111].

Order can be initiated in two ways. Firstly, the method of deposition can be changed. For example crystals of macroscopic scale can be grown by epitaxial growth, using a low rate of deposition. Secondly, energy can be added to the system to overcome the jamming e.g. shaking can enable spheres to find the optimal packing. A combination of both is the most commonly used option.

Pouliquen *et al.* [98] created crystalline structures by horizontal shaking while slowly filling the box by releasing beads at random locations. Depending on the filling rate, they obtained packing fractions of up to 0.67. As this fraction is above the random close-packing fraction of 0.64, this suggests some order in random hexagonal close packed structure. Defects can decrease the crystalline packing fraction below the optimum value of 0.74. They found that using a template at the bottom surface can induce a packing order. A square mesh obtained fcc(100) oriented crystals.

Nahmad-Molinari *et al.* [112] grew granular single crystals in a container using vertical shaking with a low feeding rate of spheres. They forced a hcp stacking by using a triangular shaped container and an appropriate bead radius. They stated the crystal growth process is a minimisation of both potential energy and energy dissipation, because they found that disordered structures dissipated more energy while vibrating than ordered structures.

Besides providing extra energy during deposition, additional energy can also be added to

an already jammed system. The system's ability to rearrange depends on the level of energy provided. As Carvente *et al.* [101] demonstrated, if enough energy is added to a random close packed structure by vibration, crystallisation can occur due to *vibrational annealing.* At their initial stage of vibration, the energy input was so high that the beads lost every contact with their neighbours and the packing gasified [101]. Vibrations were decreased in time to 'cool' the system and finally, ordered fcc or surprisingly body centered-tetragonal, bct structures[1] were found.

Comparing the bubble system, which orders easily in crystalline structures, to granular materials, it is clear that these systems are different even though they are both macroscopic systems. Friction and non-deformability of the particles prevents spherical granular materials from finding the optimal order. Slow deposition rates and a high energy input can induce order.

Colloidal suspensions

Colloidal suspensions consist of solid particles dispersed in a liquid. The particles in colloidal suspensions are generally between 10-1000 nm [113, 114] in size. They are small enough for Brownian motion to play a role but large enough to be distinguished from molecular solutions. Colloidal suspensions are an order of magnitude smaller than the microbubbles, but they also find order.

Whether the colloidal particles stay in suspension, which is named a *stable* colloidal suspension, depends on a balance between different forces. The system will tend to find its state with the lowest energy configuration. The Van der Waals, Born, steric and electrostatic forces are the four main forces involved and the description of interaction between them is the Derjaguin-Landau-Vervey-Overbeek (DLVO) theory [115, 116]. There is interparticle attraction due to molecular *Van der Waals* forces, and repulsion if they are too close due to short ranged *Born repulsion.* Larger repulsive forces are needed to balance the force of attraction. Two classes of colloids are distinguished; *charge stabilised* and *steric stabilised* colloids [115, 117, 118]. In the former the particles are stabilised due to a repulsive electrostatic surface force, when these charged surfaces are too close to each other. The stability of steric stabilised colloids is controlled by the presence of adsorbed polymers at the surface. The polymers avoid particles from flocculating either through a too large increase in concentration of polymers (osmotic pressure effect) or through a non-preferred drop in en-

[1] A crystalline structure with a bcc unit cell elongated along the y-axis

tropy for the polymer chains [115, 117, 118] when the two layers of polymers start to interact.

There are additional forces which can play a role, e.g. the depletion force, which is an additional attractive force that can occur due to the presence of polymers/surfactants in the solution. Different external fields can be used to influence colloidal stability such as placing colloidal suspensions in a laser optical field, magnetic field or electric field. Finally, application of stress or shear can also influence the stability of the colloidal suspensions [119].

If the attractive forces dominate, the suspension is unstable and the particles start to flocculate and in particular cases they crystallise. Crystals are formed by nucleation in the solution [120, 121] or by sedimentation [122, 123]. By manipulation of the surface and solution properties, this crystallisation can be easily controlled [124]. This makes colloidal suspensions attractive for use as a model for crystalline atomic structures to gain more insight into the mechanism of crystalline ordering and growth.

For the comparison with the microbubbles we are interested in the spontaneous crystallisation of colloids [120, 124–130] or in colloidal epitaxy [131–134] if we consider that our initial layer is always ordered due to surface tension forces [97].

From the literature study it is clear that there are many factors playing a role in the crystallisation process, besides the four main forces discussed above. There are so many variable factors such as the particle properties and solution properties that the different experiments are not straight forward to compare.

The speed of the crystallisation process of colloidal suspensions (their kinetics) depends on many factors such as the temperature of the system and the stability of the colloidal suspension. Generally the crystallisation process takes hours to weeks [122, 123, 130], which is quite slow compared with microbubbles which order instantly, especially considering that the microbubbles are $\sim$100 times larger.

Colloidal suspensions experience Brownian motion, although it is not a necessary ingredient for ordering. Van Megen *et al.* [135] reported that this effect in colloids can be quickly overruled by other forces, such as shear. They observed that with increasing shear rates the crystallisation growth rates increase. Oscillatory shearing is observed to result in an rhcp crystallisation with the layers oriented parallel to the shearing plates [136, 137].

To our knowledge there are few reports regarding the effect of hydrodynamic interactions. One study [138] describes 2D crystallisation under the influence of flow and confinement. Crystalline structures were formed with flow in the direction of sedimentation, which even after occurrence of different kinds of perturbations showed restoring of order.

Summarising, compared with colloidal suspensions microbubbles order very quickly and it is the question whether the forces acting in colloidal suspensions can be of influence at bubbles several orders of magnitudes larger.

4.9 Order by confinement

Hitherto we have shown that bubbles can spontaneously order in fcc or hcp crystalline structures deposited into a bubble pool. The occurrence of the different crystalline structures is not entirely random, however it is not clear what influences their occurrence. We know for larger dry bubbles ($> 1mm$ diameter) and hard sphere colloids that boundaries induce order [139–141]. Bubbles confined in tubes very easily form ordered structures. Structures of foams confined by plates have been studied before as well. Drenckhan *et al.* [142] compressed a single layer of bubbles in a wedge as an example of conformal maps. Weaire *et al.* [143] described for two layers of bubbles the influence of the liquid fraction on the structure. Very little research can be found regarding the transition from 2D (single) bubble layers to multiple layers 3D bubble structures. We show here that we can force order by confinement and create fcc(100) and either fcc(111) or hcp(0001) crystals for different numbers of layers.

We used wedges and parallel plates as confinements. The wedges were created using two glass plates, 3 cm wide and 30 cm long. At the short sides of the plates two spacers were placed with different thicknesses. Generally the angle of the wedges was kept below 1 degree, such that locally the plates can be considered parallel with the use of small bubbles sizes. The spacing of the parallel plates could be varied by using rubber strips or by using two plates which could move independently from each other. The latter enabled us to observe transitions between different structures.

The wet foam structures were created by depositing the bubbles from the bubble generator (Chapter 2) immediately into the confinements. In the case of using a wedge or fixed parallel plates, the structures were observed from the top using transmitted light from below and close-ups were achieved using a microscope (see Figure 4.15 (a)). In the case of using the parallel plates with variable spacing, sequences (Figure 4.15 (b)) were created by increasing or decreasing the spacing in steps. Measurements of the spacing were unsuccessful due to difficulties to perfectly aligning the glass plates and the location of the light source such that accurate measuring tools were difficult to use. An improvement to the set-up would be to place small glass plates in a frame where one of the plates is connected to spacing

controllers, e.g. in the form of screws. This is expected to enable more accurate settings and measurements.

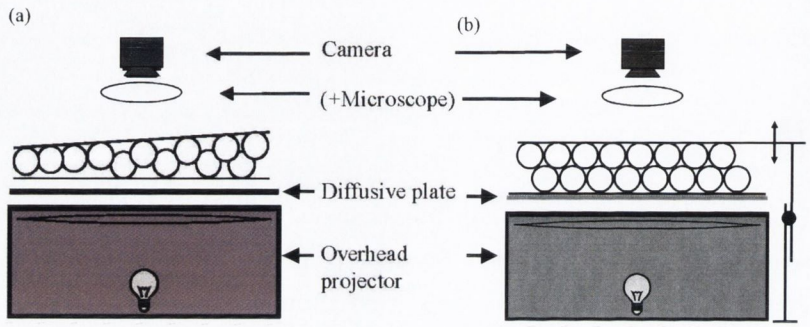


Figure 4.15: The set-up for crystalline microfoams confined in (a) a wedge and (b) between plates, with variable plate separation.

It is known from hard sphere colloids and expected for microbubbles that in confinement they attempt to find the orientation of a closed packed crystal such that the packing density is optimised. The so far observed structures with triangular (fcc(111) or hcp) or square (fcc(100)) ordered layers have different heights in the direction to the normal of the planes. The height between the centres of two layers stacked in fcc(111) is $2\sqrt{\frac{2}{3}}R$, where R is the bubble radius, whereas for fcc(100) this height is $\sqrt{2}R$, see Figure 4.16.

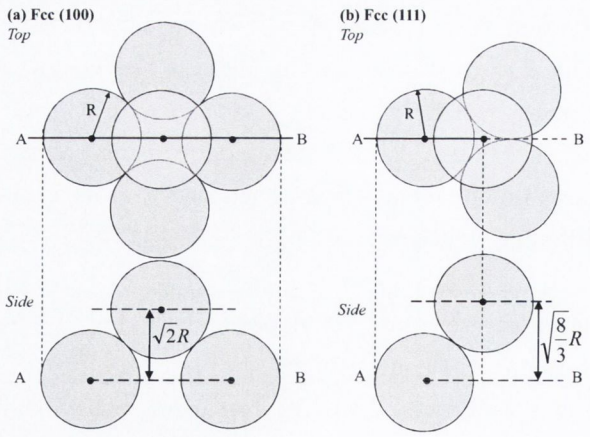


Figure 4.16: A sketch of the determined layer thickness dependent on the bubble radius R, which is $\sqrt{2}$R for layers stacked in the fcc(100) orientation (a) and $\sqrt{\frac{8}{3}}$R for layers stacked in the fcc(111) orientation.

Depending on the height of the wedge, either more bubbles can be packed in fcc(100) or fcc(111)/hcp oriented layers. Here we will show that by varying the plate separation we

indeed obtain different crystalline structures.

We will use the notation used in hard sphere colloidal systems research performed on order under confinement [140, 141, 144–146]. □ is used for square, crystalline fcc(100) oriented layers and △ corresponds to the triangular oriented layers which can be either fcc(111) or hcp(0001) crystals. The number in front of the symbol corresponds to the number of layers present.

Here we show the occurring structures for bubbles in wedges with different angles and spacings. Starting with wedges with small angles we found a transition sequence of 1△ → 2□ → 2△ with a transition for bubbles not observed before, between one layer triangular oriented (1△) to two layers of square (2□), see Figure 4.17. This transition is familiar from hard sphere colloidal systems as *buckle* and noted as 1B [140]. Figure 4.18 shows a close-up view of the structure. Instead of a leveled plane, rows are formed, slightly offset from each other thus increasing the packing fraction.

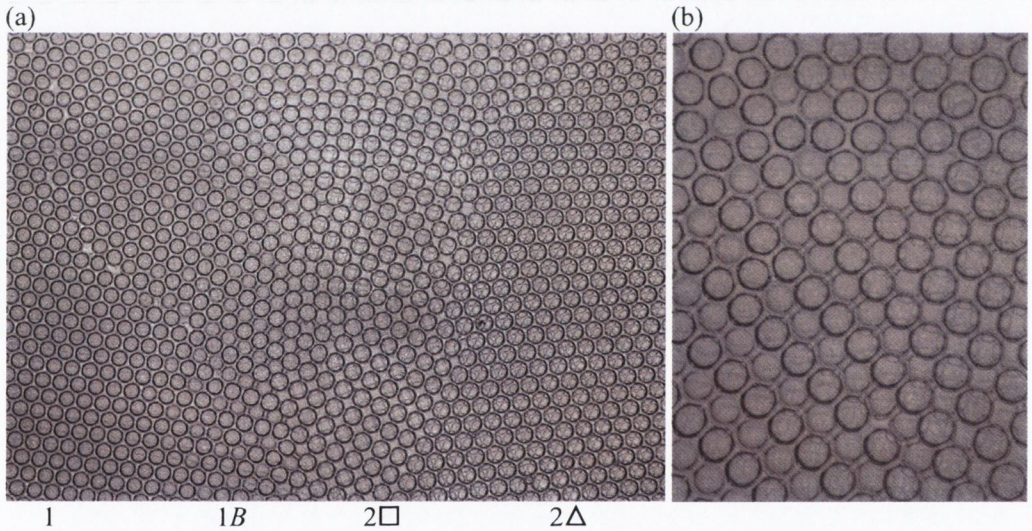


Figure 4.17: Microbubbles confined in a wedge with an opening angle of 1.1 degrees. (a) shows the transition from one single layer fcc(100) (1△) into two layers in a buckle orientation 1B, this is followed by two layers packed in fcc(100) 2□ and afterwards 2△. (b) a close-up of 1B.

At larger spacings but small angles we observed transitions from 3△ → 4□, see Figure 4.19. Here we do not observe the buckle phase, even though the wedge angle of 0.44 degrees is sufficiently small compared with the wedge angle of 1.1 degrees where the buckle phase was found.

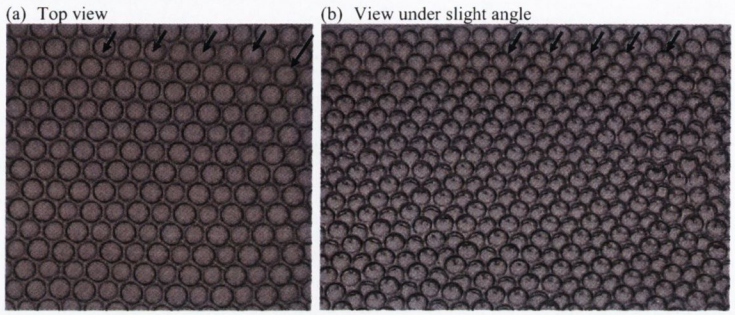


Figure 4.18: A zoom on the buckle state, 1B. Rows of bubbles are in two different planes, which increases the packing fraction compared with one single layer. The arrows mark the higher rows of bubbles, touching the top glass plate.

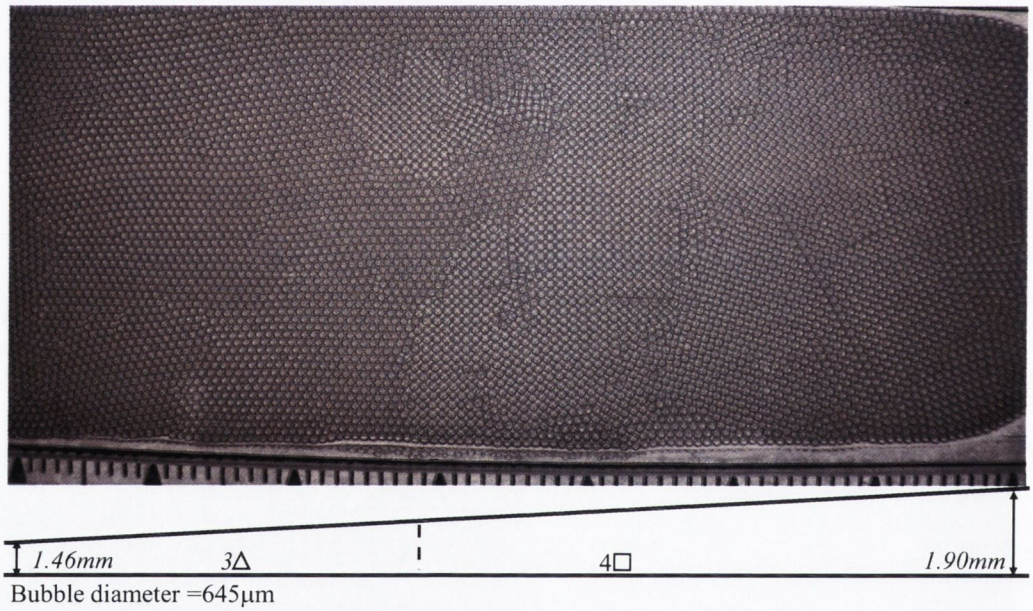


Figure 4.19: The transition from 3 △ to 4 bubble layers □ in a wedge with an angle of 0.44^o

With an increasing wedge angle we observed multiple transitions over a short length as can be seen in Figure 4.20. Here we can see the transitions from: $1\triangle \rightarrow 2\square \rightarrow 2\triangle \rightarrow 3\square \rightarrow 3\triangle \rightarrow 4\square \rightarrow 4\triangle$. As the spacing changes quickly, the grains of fcc(100) are very small. The buckle phase does not appear at all.

At larger spacings, where 5-6 layers could fit, we only observed triangular ordered structures. Square layers did not appear anymore. This could be due to excessive water, caused by the high initial liquid fractions directly deposited from the bubble generator, which led to the bubbles being unaffected by the bottom plate. Also the differences in packing fraction

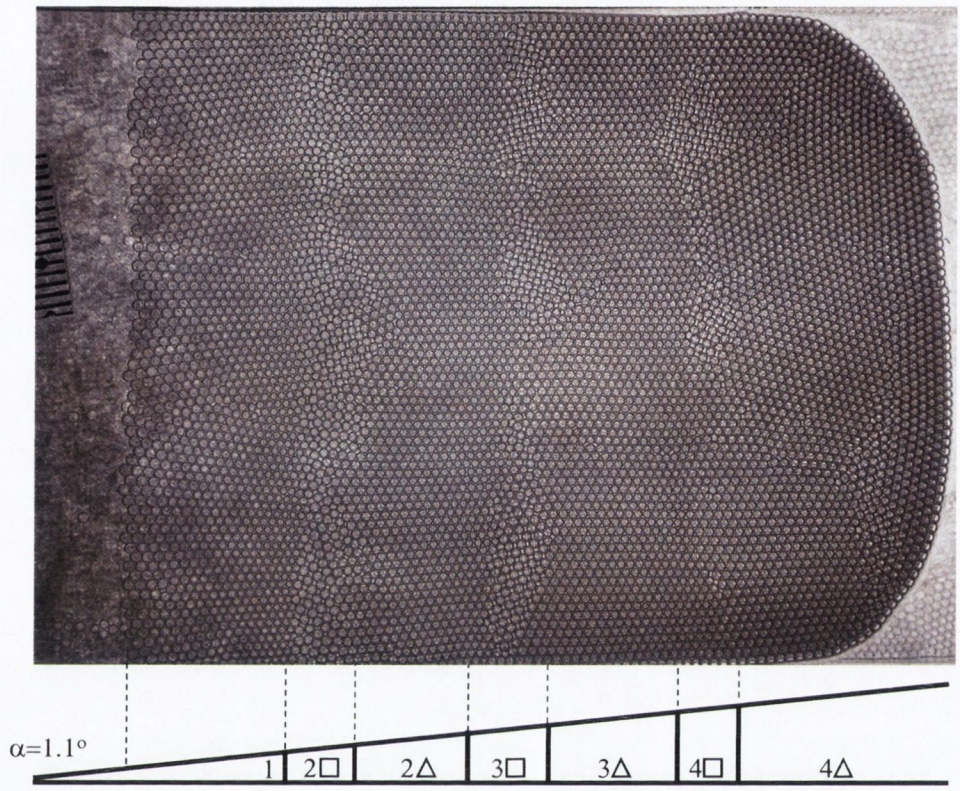


Figure 4.20: Bubbles(400 μm in diameter) under confinement in a wedge with an angle of 1.1degree starting with no spacing at the left side. From left to right the following transitions take place: $1\triangle \rightarrow 2\square \rightarrow 2\triangle \rightarrow 3\square \rightarrow 3\triangle \rightarrow 4\square \rightarrow 4\triangle$.

between the two structures becomes less obvious with more layers.

We expect the transitions to occur for fcc(100) at $W_{expected} = 2R + (n-1)\sqrt{2}R$, with n the amount of layers, for fcc(111) or hcp $W_{expected} = 2R + (n-1)\sqrt{8/3}R$. When we compare the location of transitions in the experiments ($W_{experiment}$) with estimations ($W_{expected}$) made based on the assumption that the bubbles are perfectly spherical, the location of the transition occurs at significantly smaller spacings than expected. For our experiments $W_{experiment}/W_{expected} \approx 0.7 - 0.8$. The assumption of sphericity is not valid for a liquid fraction of 0.36, which is most likely the case in our experiment. Also the bubbles are easily deformable, which can also contribute to the difference in observations between the two systems.

With the parallel plates it was possible to observe transitions between different structures by changing the plate separation. In Figure 4.21 we show an observation of a transition

$1\triangle \rightarrow 2\square$ with increasing plate separation. There is a clear intermediate stage where the two layers have not completely found their optimal structure. It was noted that hysteresis effects occurred. With increasing plate separation the bubbles failed to form closed packed structures. The retracting liquid surface surrounding the bubble structure generally forces the bubbles into multilayers, but due to large liquid fractions this did not occur. This resulted in incomplete layers. The initial liquid content played a large role in this effect. With a larger liquid fraction the bottom plate lost its influence. This became also more severe with larger plate separations. With decreasing plate separation this effect was reduced and resulted in samples with less defects. We created large crystals of two or three layers oriented in fcc(100). In Figure 4.22 an example is shown of three layers of fcc(100). The grains are small with multiple grain boundaries present. Without confinement these large crystals of fcc(100) do not occur.

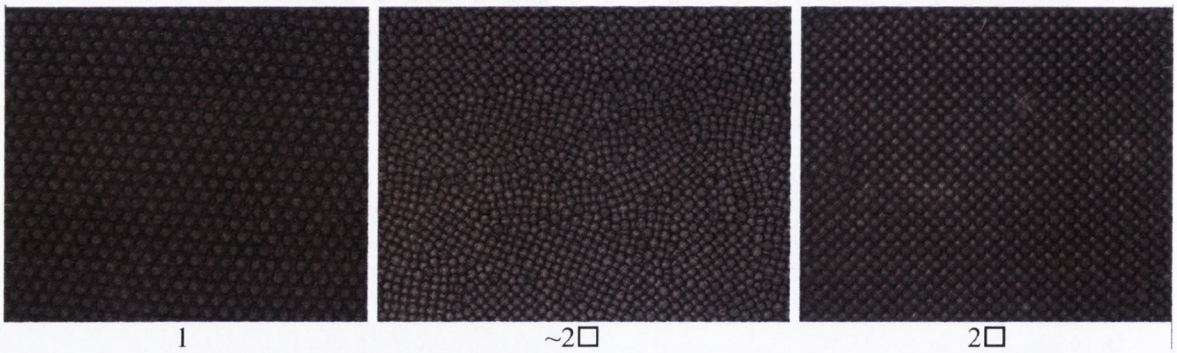


Figure 4.21: The transition from one to two layers $1\triangle \rightarrow 2\square$ with the use of parallel plates with increasing plate separation.

Overall the experiments show qualitatively that confinement can be used to induce different crystalline structures for up to 5-6 layers. Besides the familiar structures with triangular and square top layers formed also in spontaneous crystallisation, newly found structure 'buckle' was observed under confinement. Liquid fraction plays a large role in the effectiveness of the confinement. In future experiments this should be better controlled, which could enable possible discovery of other structures. Future experiments should also focus on forcing bubbles into crystalline structures by depositing them in confinements where instead of top and bottom boundaries side boundaries are present.



Figure 4.22: Three layers of square fcc(100) oriented grains between two parallel plates.

4.10 Formation of dry ordered foams

We pointed out that dry ordered foams are difficult to generate. Due to jamming, the bubbles do not find their optimal positions to form an ordered structure. In the wet structures the bubbles already have found the optimal positions. Order should remain when we drain the water out of these structures by lifting them above the critical height, where gravity prevails over capillary suction (see Equation 1.1).

For this purpose we made columns of crystalline microfoam with a height greater than the capillary length. The foam is confined in a cell consisting of two parallel plates (1x5 cm) separated by 3 mm thick rubber strips placed at the sides. The cell is partly open at the bottom so that excess water can drain. Generally we could make up to 8-10 layers of Kelvin cells in either a wedge or parallel plates.

The image shown in Figure 4.23 was taken of a foam column at a height of 2.5 cm with bubbles of a diameter of $\sim$400 μm. At the top we can see Kelvin cells while at the bottom the foam has an fcc(111) structure. In Figure 4.24 the difference between a dry fcc and hcp

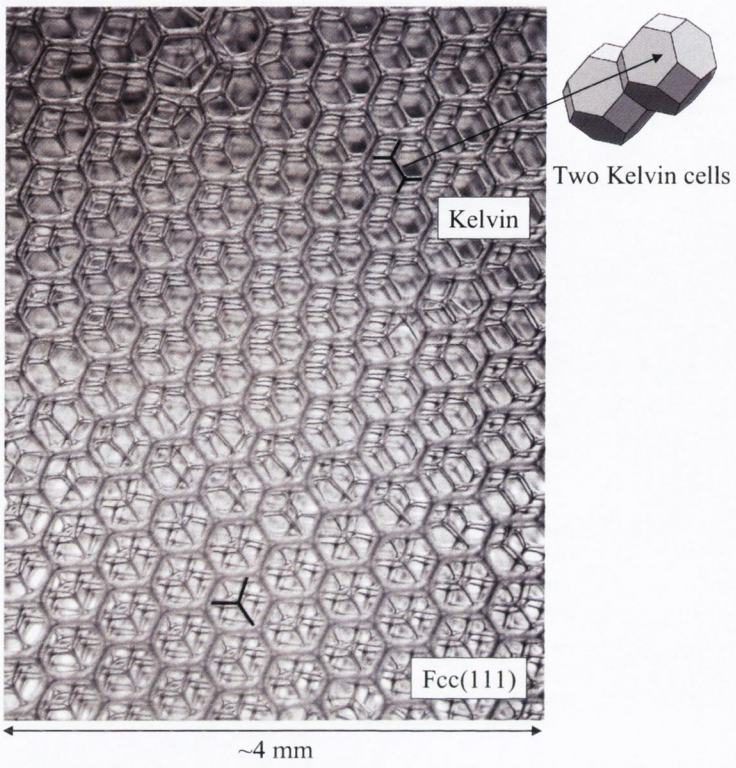


Figure 4.23: Drained bubbles in a Hele-Shaw cell, which initially ordered in the wet foam limit. On top Kelvin cells are present, which order according to a bcc structure, on bottom and at the left side dry cells are packed according fcc(111). The interface of the transition between the two packing structures [5] poses an interesting problem.

structure is shown.

Initially the location of the different crystals was believed to be due to a gradient in liquid fraction. However in some experiments grains of fcc were found above Kelvin cells. This is remarkable, considering the liquid fraction can not be larger higher up in the column.

Recently an explanation was given by Höhler *et al.* [21], who investigated the dependence of the crystalline structures of foams on the liquid fraction. It is known at the limit of low liquid fractions, close to zero, dry foams order as Kelvin cells, and wet foams (liquid fraction of 0.36) in closed packed fcc/hcp structures. Höhler *et al.* explored the transition from wet to dry foam structures at liquid fractions between 0.04-0.08. They found a smooth transition rather than a sharp transition between the crystalline structures, such that gradually more grains of Kelvin cells appeared with decreasing liquid fractions and equally more fcc/hcp grains occurred with increasing liquid fractions. This means that samples can occur with

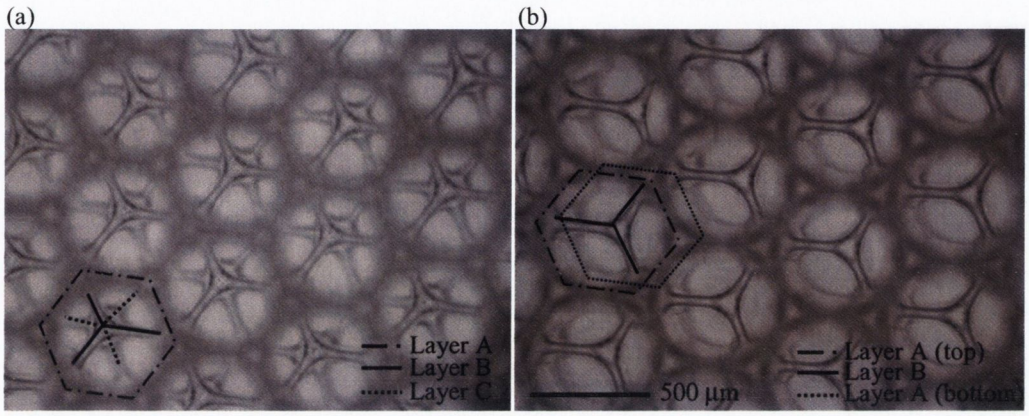


Figure 4.24: The dry versions of three ordered layers in (a) fcc(111) or and (b) hcp.

both Kelvin and fcc structures for intermediate values of liquid fractions, which may explain the occurrence of Kelvin cells located below fcc ordered bubbles in our experiments.

Höhler *et al.* also described a more systematic way of draining crystalline micro foams, by varying liquid pressures via a porous membrane in the bottom of the foam cell. Higher (or lower) liquid pressures make the foam wetter (or dryer).

4.11 Conclusions and Outlook

Wet crystalline microfoams are beautiful and show many features at a macroscopic scale that can be found at atomic scales that otherwise would be much more difficult to observe. Two different crystalline structures are present in the crystalline microfoams, which are formed at the top of a liquid pool; fcc (111), fcc (100) and hcp (0001). We have shown that with the use of wedges and parallel plates, we are able, by confinement, to control the creation of the crystalline microfoams with a thickness of several layers in either fcc(100) or fcc(111)/hcp. The control over the occurrence of the crystalline structure will be of crucial importance in applications of foam, where the structural properties can play a large role. The spontaneous ordering of wet microbubbles enabled us to create dry ordered structures. It also gives us a prospect of finding the Weaire-Phelan structure.

The critical factors needed to explain how the bubble system manages to achieve a state of ordering are still not fully determined. Neither is it explained why the system prefers fcc over hcp, even though they have the same packing fraction, and fcc shows only a slight energetical benefit.

The dynamics of ordering

Templating can stimulate order in the layers of bubbles, similar to colloidal and granular systems [98, 131]. It is, however, not a requirement, as we saw a recurrence of order in experiments where dry foams formed an irregular surface layer. Simulations show that templating and deposition methods in either a high or low dissipative system can not solely explain the highly ordered crystalline structures occurring with a preference to the fcc structure. The type of surfactant or concentration does not seem to play a role as we were able to make structures using different surfactants and even in a polymer solution, see Chapter 6.

From the relevant literature, several other possible factors have been identified by comparing the crystalline microfoams to similar systems in Section 4.8. A main ingredient is the *ability to rearrange after deposition*, which is influenced by the small buoyancy force, sufficient wetness, its associated spherical bubble shape and very low friction between bubbles. Possibly a correct balance between repulsive and attractive forces between bubble-bubble interfaces under influence of the presence of surfactants could play a role as well, if bubble-bubble interactions are strong enough in relation to the used range of bubble sizes.

Another candidate would appear to be the influence of *shearing*, since shear induced ordering is well known to occur under certain circumstances in emulsions [45, 46]. The shear could be caused by the continuous new stream of bubbles deposited and sliding over each other. Shear could also play a role in the occurrence of fcc(100) at the gas-foam surface.

The deposition method does not appear to make a difference in the ordering mechanism. However the *rate of deposition* could play a critical role in the process. The impact of the newly arriving bubbles could add new energy into the system, thereby causing rearrangements. Note that for the impact a sufficient buoyancy force is needed, but which should be sufficiently small to enable rearrangements of the bubble and no immediate jamming.

Hydrodynamics could be another factor playing an important role in the system. Hydrodynamic effects of drainage could create symmetric flow patterns forcing the bubbles to arrange in the fcc structure.

In future experiments one might study these effects by applying shear on a 3D sample, visualising flow patterns in the ordered foam and completing statistical analysis on the occurring crystalline structures based on the different methods. To our knowledge, no experiments have been performed on the ordering abilities of floating beads. This would enable us to

study the effect of surfactants and by changing the bead surface properties the effect of friction could be explored. This is all in an attempt to isolate the key factors required to generate the observed highly ordered crystal structures and the predominant occurrence of fcc over hcp.

Initial steps for simulating the crystallisation of microbubbles have been taken by introducing a model of floating hard spheres. The simulations can be improved by adaption of the sphere interaction [147]. For modeling the hydrodynamical influences the Lattice-Boltzmann model [148] or the Level-set model [71] would be good methods to consider.

Fcc preference

The preference for the fcc structure corresponds quite well to results found in the literature on metals, colloids or hard spheres. In nature there is a preference for fcc above hcp. 25% of the elements in the periodic table are crystallised as fcc and 20% as hcp, while the other 55% of the elements have completely different crystalline structures [102]. Woodstock [102] proved for atomic hard spheres that the fcc structure has a lower entropy than the hcp structure. A lower entropy is indicative of more order [149]. Therefore there is a slight preference for fcc over hcp. It is too early to say whether entropy minimisation is the reason for the crystalline microfoams to show the slight preference for the fcc structure.

For colloidal suspensions Pusey *et al.* [126] showed that by varying the particle concentration different crystalline phases could be found. The only crystalline phase that occurred was fcc. Pusey *et al.* [125] found a relation between the structure and rate of crystalline growth. Quick growth rates show a rhcp structure while if more time is available fcc crystals are formed. With a slower growth rate the particles have more time to find the optimal structure. Hydrodynamic interactions and shear deformations are mentioned as factors which can change the most favoured structure. Zhu *et al.* [120] performed a remarkable experiment on the effect of gravity on crystallisation of colloids. They found that in microgravity only rhcp was present. Under gravity, as found by Pusey [125], rhcp or fcc were present dependent on the growth rate. This suggests that fcc is formed under gravity-induced stresses.

Other factors that can play a role in the fcc preference are boundary effects or the method of deposition. We showed that bubbles in a close confinement of several bubble diameters wide can be forced into a certain structure, which was discussed in Section 4.9. For the spontaneously ordered crystals the size of the box used is several orders of magnitude larger than the bubble size and therefore the effect of the box boundaries are expected not to play a role. Deposition at one location can form a pile of bubbles at the bottom of the foam sample.

This could induce formation of fcc as the walls of the pile can correspond to close packed planes (-1,1,1), (1,-1,1) and (1,1,-1).

3D imaging

Finally we should find an appropriate method to analyse the complete 3D sample, e.g by the use of 3D imaging. Although our optical images reveal more details than the original ones of Bragg and Nye [18], and can be accurately interpreted, it remains the case that we can directly infer crystalline order only within a few bubble diameters of the surface. Intuitively the indirect evidence for bulk order seems compelling, especially considering order at the top, terraces and following the crystallisation, but an observation of the expected internal order is desirable and deserves further pursuit. Attempts were made using a confocal microscope, but due to severe scattering and a small depth in the field of view we were not able to visualise more than 2 layers. The use of a 2-photon microscope or X-ray tomography [150] may be better alternatives.

Given these interesting issues, it would seem the intriguing three-dimensional close packed structures are unlikely to be neglected for so long this time around. In broader terms, it is hoped that our crystalline microfoams will help to shed light on the general problem of crystallisation in mesoscopic systems. In Chapter 6 we will go more into detail on the bright future of solidification of the crystalline microfoams. Firstly, in the next chapter we discuss unique characteristics of the crystalline microfoams, when they are exposed to the atmosphere.

Chapter 5

Rearrangement and elimination of ordered surface layers of crystalline bubble structures due to gas diffusion

5.1 Introduction

Foams have a finite lifetime. They coarsen as bubbles disappear due to the effects of coalescence and diffusion. Diffusion occurs as gas migrates through the films from one bubble to another, from high to low gas pressures, resulting in shrinkage of smaller bubbles, while larger bubbles grow. Also foam films can break if they become too thin due to drainage [6, 17].

Previous coarsening studies focused on dry foams, especially in two dimensions [5]. Current investigations study dry and wet foams in three dimensions using imaging techniques such as diffusive light spectroscopy [72, 73], magnetic resonance imaging [151], X-ray tomography [150, 152] or optical tomography [153]. The main focus of interest in all of this research has been the behaviour of bubbles in the bulk foam. Boundary effects occurring at the foam-atmosphere interface are generally not considered.

The work presented here deviates from this approach by concentrating solely on the behaviour of bubbles at this interface. In particular we study the top layer of crystalline microfoams of equal-sized bubbles with values of liquid fractions larger than twenty percent [18, 20]. While initially diffusion leads to a loss of order in the top layer, eventually order is re-established but in the form of a bidisperse top layer, which happens just within 5 minutes. This effect repeats itself, the smaller bubbles disappear and the new top layer will undergo

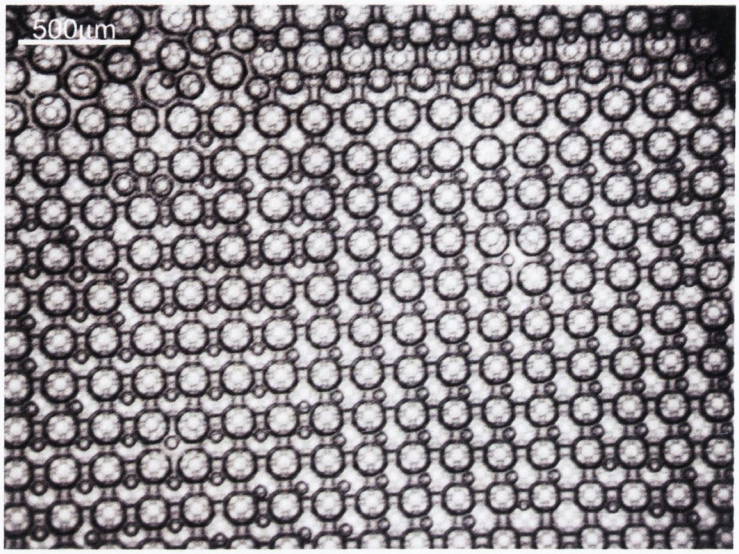


Figure 5.1: The occurrence of a bi-disperse top layer of an fcc(100) oriented bubble crystal.

the same diffusion process, as is described in detail in Section 5.3. The process is examined for the different crystalline structures previously discussed in Chapter 4. Comparison with diffusion experiments on single bubbles and monolayers of bubbles with the diffusion of the crystals shows a significant difference in the timescale of the shrinkage due to diffusion, while single bubbles last for hours, bubbles in a top layer of a crystal disappear generally within 10 minutes. In Section 5.4 we go into more detail on this difference and we show, using a simple model, that the diffusion rate is linearly dependent on the number of layers in the crystals.

5.2 Experimental method and analysis

We performed diffusion experiments for single bubbles, monodisperse layers and different crystalline structures of bubbles, floating on a liquid.

Single bubbles were generated either using the Microdispenser [37], a special device which releases a controlled amount of *air* through a needle (200 μm in diameter) into a liquid, or by the use of our microfluidic flow focusing device to create bubbles filled with *nitrogen*. See Chapter 2.2 for more details on the bubble generation. The latter device was also used to create our monodisperse monolayers or foams consisting of up to 25 layers on a liquid surface. For both the bubble generation and the liquid containing the bubbles we used an aqueous solution with 1% volume fraction of the commercial detergent Fairy Liquid.

Depending on the quantity deposited, the bubbles either form a single monolayer, which

orders in a close-packed triangular pattern [97], or multiple layered crystalline microfoams are created as described in Chapter 4. In the analysis of the multiple layered crystalline microfoams we distinguish between square and triangular ordered surface layers, respectively corresponding to fcc(100) and fcc(111) or hcp crystalline structures.

A liquid pool containing the bubble(s) was placed on an overhead projector in order to visualise the bubble(s) with transmitted light. Using a digital camera (Coolpix Nikon 4500) attached to a microscope, images were taken at regular intervals (5 minutes for bubbles and monolayers and 1 minute for bubble crystals). The data was analysed with the image processing software ImageJ [55] to obtain bubble size distributions as a function of time. A correction factor was applied to account for the 10% underestimation of the bubble radii due to the details of the light propagation in a bubble obtained from the analysis described in Chapter 3. Note that the thresholding of the images can introduce some error in the size determination of the bubbles, the size can vary dependent on the range of grayscales included. This was actually used to determine the variation in bubble sizes for the single bubbles.

The heat generated by the overhead projector led to a gradual increase of the water temperature. Increasing temperatures could lead to an increase in gas permeability of soap films [88, 154], thus to a faster shrinkage of the bubbles. The small temperature difference of 2-3 degrees Celsius between the beginning and end of our experiments might thus contribute to the uncertainty of our permeability measurements.

We will see that the diffusion rate of the top layer depends on the number n of bubble layers in the foam, whose precise value is however not easy to determine, as we can not look inside the foam. Here we proceeded by measuring the local height between the foam-air and foam-water interface, using observations from the side of the box to locate the foam-water interface and a needle tip was used to estimate the position of the foam air interface at the location of measurement. This height difference is labeled as h, and dividing it by the layer thickness for the observed local structure, i.e. $h = (n-1)\sqrt{2}R + 2R$ for fcc(111) or hcp (both have a triangular top layer), or $h = 2(n-1)\sqrt{2/3}R + 2R$ for fcc(100) with its square-ordered top layer. Here R is the bubble radius. For multi-layered foams it is not obvious that a particular type of bubble rearrangement is maintained throughout the section of the sample and the measurement of the thickness includes inaccuracies. Based on this we attach an error of $\pm$ two layers to local thicknesses exceeding 5 layers.

5.3 The creation of bidisperse top layers

In this section we describe observations of the occurrence of bidisperse top layers in crystalline structures oriented in fcc(100) and fcc(111). We discuss further how the continuous diffusion results in elimination of successive layers of the crystal.

Figure 5.2 shows a sequence of images of an fcc(100) oriented surface. Initially, the bubbles in the triangular top layer are approximately monodisperse. As they shrink and lose contact with their neighbours, bubbles from the layers below begin to interpose themselves into the top layer, driven by buoyancy.

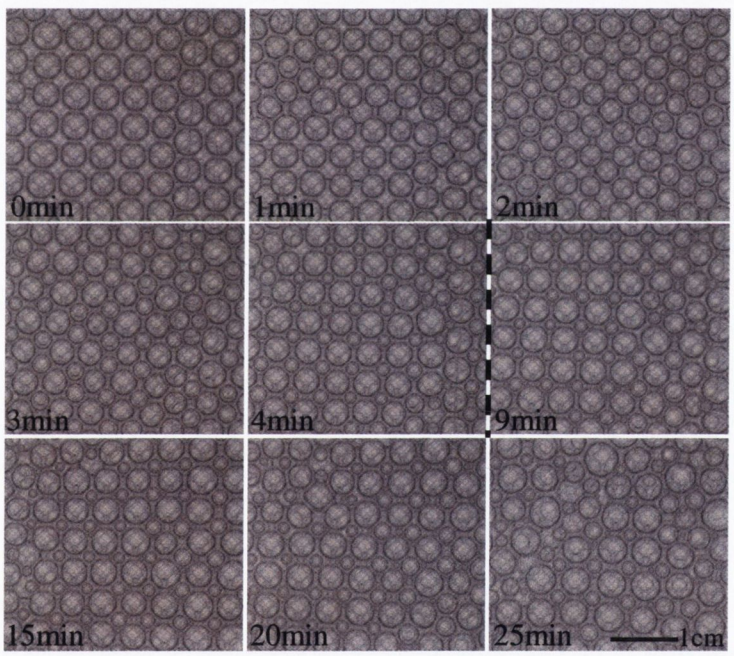


Figure 5.2: Sequence showing the effect of diffusion of an fcc(100) oriented crystalline bubble structure. Here t=0 marks the completion of deposition of the bubbles onto the liquid surface. After 4 minutes a bidisperse top layer is formed, by the initial first and second layer of the crystal. This repeats itself every five minutes, where the bidisperse layers are formed from two successive layers. After 25 minutes defects start to play a large role and diffusion leads to disorder.

Initially this happens somewhat randomly, leading to the creation of a new disordered top layer, consisting of both the bubbles from the second layer and also the smaller bubbles from the initial top layer. Possibly it is the slight polydispersity of 2% in bubble size (Chapter 2) that plays a role in the randomness of where new bubbles appear at the surface. Nevertheless, eventually the bubbles of the original top layer fit into the gaps of the second layer,

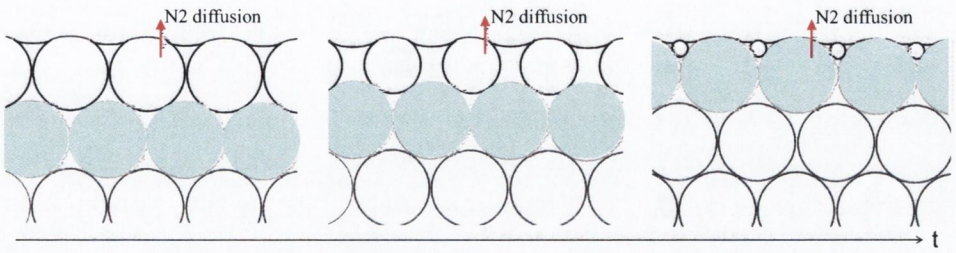


Figure 5.3: A cross-section through a bubble crystal, showing a sketch of the diffusion process. Note that the waterlevel is kept at an constant level throughout the sketch sequence, which in reality is dropping.

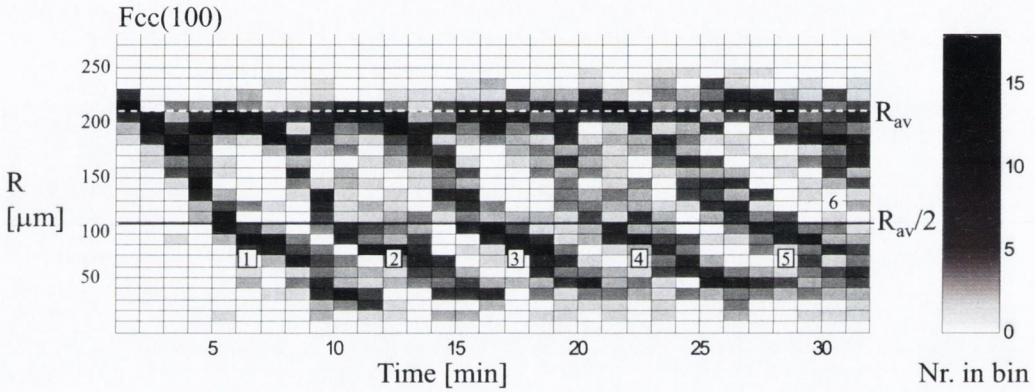


Figure 5.4: Sequence of diffusion data for the square fcc(100) oriented crystalline bubble structure of figure 5.2. The graph shows for each minute the radial size distribution R of the bubbles. The gray scale represents the number of bubbles within a range of bubble sizes. The numbers in the square boxes label the different layers that rise to the top during the diffusion. R_{av} is the average initial bubble radius before diffusion sets in. Bidispersity approximately occurs at $R = R_{av}/2$.

completely moved upwards, and together they form a perfectly *ordered* bidisperse top layer.

Following the diffusion further in time we found that this effect repeats itself. The new top layer proceeds to shrink, disorder and re-order in the same way. We were able to follow the bidisperse surface formation up to the elimination of the fifth layer. At this stage defects, disorder induced at boundaries between grains of different crystalline structures and coarsening start to play a large role and diffusion no longer results in ordered bidisperse surface layers.

Figure 5.4 shows the temporal evolution of histograms of bubble radii, obtained from a comprehensive image analysis of the top layer. A periodic pattern can be seen, where each branch represents the elimination of a layer, numbered $1-6$. It can be seen that initially there is already a difference in bubble sizes, caused by diffusion occurring before the imaging

started. The diffusion speeds up in the next $3-4$ minutes. After 4 minutes a separation is clearly visible in the size distribution and layer 2 appears at the top-surface. At this stage, with bubble radius R smaller than 100-150 μm, the diffusion of layer 1 slows down. The small bubbles remain even after the third layer (3) appears at the surface and forms a bidisperse top layer with the second layer (2). Three generations of bubbles are then present. The bubbles of the initial top layer (1) are randomly distributed and do not influence the ordering of the next layers. After 10 minutes they have disappeared. This process repeats itself for up to 6 layers. Generally a new layer appears every $5-6$ minutes and it remains present for about 10 minutes. Note that the initial bubble radius of the appearing layer increases. This may be caused either due to diffusion between the bubbles of two top layers or internal coarsening.

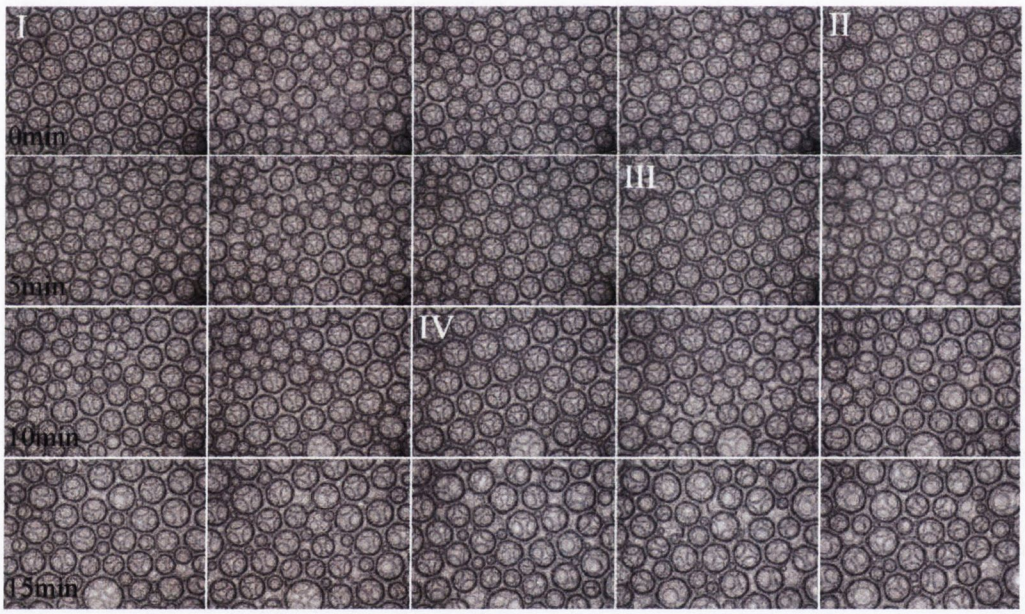


Figure 5.5: The process of diffusion of a triangular oriented crystalline bubble structure. One image is captured per minute, where t=0 marks the end of the deposition of the bubbles onto the water surface. The sequence shows the appearance of new layers labelled II to IV, indicated in Figure 5.6.

In Figure 5.5 and 5.6 the effect of gas diffusion is shown for a triangular fcc(111) surface. Again space is created for the bubbles of the second layer (2) to squeeze towards the gas-water interface.

Eventually the transfer of the second layer to the surface is completed, again forming a bidisperse layer. This time, however, the bubbles of the initial surface layer are much smaller than in the bidisperse top layers of fcc(100), as can be seen in Figure 5.7. For these triangular

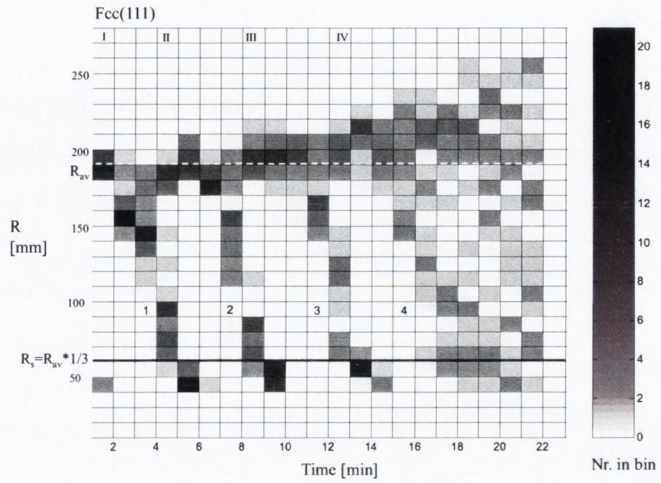


Figure 5.6: The process of diffusion of a triangular oriented crystalline bubble structure fcc(111). The labels I-IV indicate the appearance of the new layers numbered 1-4 as seen in Figure 5.5. R_{av} is the average initial bubble radius before diffusion sets in. Bidispersity approximately occurs at $R = R_{av}/3$.

oriented surfaces there are twice as many holes to fill than there are bubbles present in one layer, hence these can never form a perfectly filled, ordered bidisperse top layer.

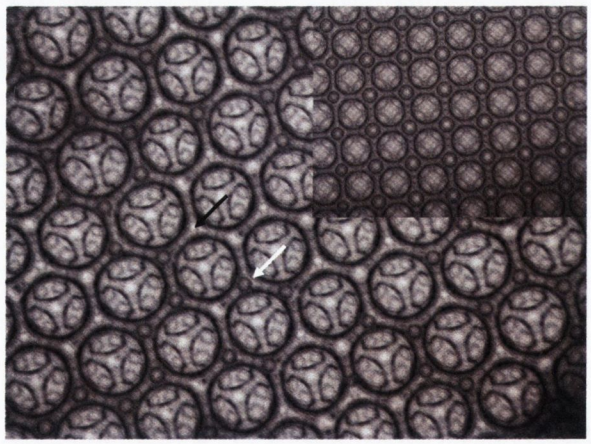


Figure 5.7: The incomplete bidisperse top layer of fcc(111) compared with the complete fcc(100) (inset). The black arrow points to an empty cavity, the white arrow shows a small bubble, which is a remnant of the initial top layer.

In due course the third layer (3) starts to appear at the surface. At this stage the initial top layer has completely disappeared. This process of layer replacement could be followed

for up to 4 layers.

Figure 5.8 shows the normalised average bubble radius $R(t)/R_0$, with R_0 as the bubble radius at the start of the experiment, of the initial surface layer for both triangular and square oriented crystals.

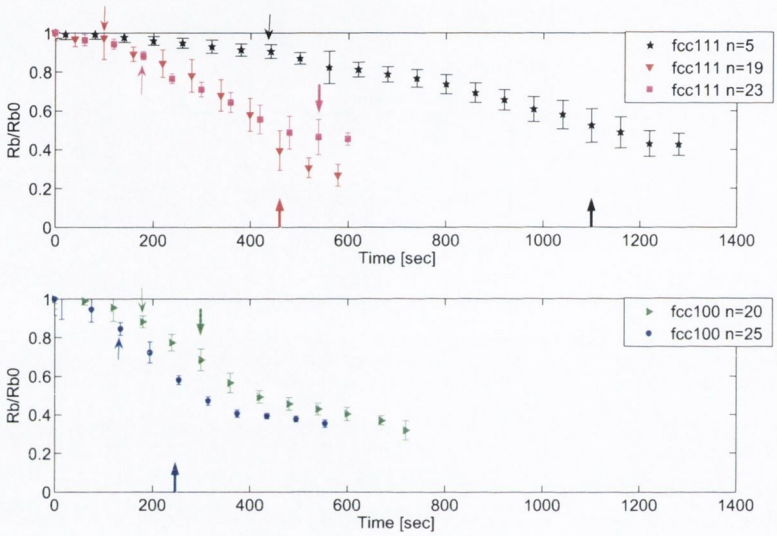


Figure 5.8: Evolution of bubbles over time, in crystals with either triangular top layers(top) or square top layers(bottom). The first arrow marks the appearance of the first bubble of the second layer (stage II), the second arrow in time marks the first occurrence of the visible bidisperse top layer (stage III). n = the number of layers.

Based on the data shown in Figure 5.8 and our observations we can define three stages in the evolution of the bubble size in the top surface layer of a bubble crystal. In *Stage I* the bubbles of the surface layer shrink uniformly. *Stage II* starts at the moment the first bubble of the second layer appears at the top surface. Afterwards in an unpredictable manner more bubbles of the second layer appear. In this stage the diffusion rate increases. *Stage III* is characterised by reordering into a bidisperse surface layer, when all the bubbles of the second layer have appeared. With some delay, a drop in the diffusion rate occurs (further discussed in Section 5.4.4). In Figure 5.8 we have marked the appearance of the first bubbles of the second layer (start of stage II) and the completion of the bidisperse top layer (start of stage III). In Section 5.4.3 we will look in more detail at the initial stage of diffusion, where all surface bubbles shrink at the same rate.

Theoretically, when the smaller bubble fits perfectly into the cavity of the upper layer,

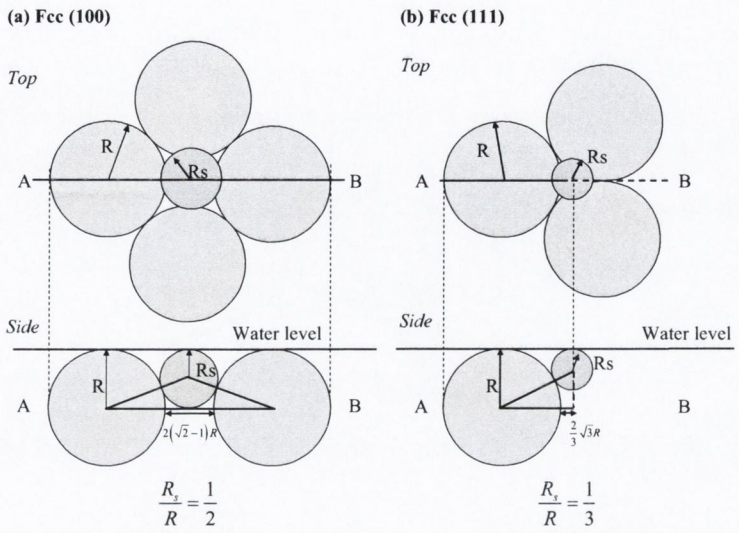


Figure 5.9: Rough estimate of the relative size of interstitial bubbles (a) For fcc(100) the ratio between the top bubble radius R_s and the bubble underneath R is 1/2, (b) for fcc(111) or hcp $R_s/R = 1/3$.

with bubbles with a radius R, as sketched in Figure 5.9 assuming a flat water level, it has radius R_s such that $\frac{R_s}{R} = \frac{1}{2}$ for the fcc(100) surface, while for the fcc(111)/hcp surface layer the ratio is $\frac{R_s}{R} = \frac{1}{3}$. The data in Figure 5.8 shows that in reality the occurrence of bidispersity happens before the estimated bubble size is reached. This indicates the bubbles have already found their position before they are small enough to fit perfectly into the cavity. The bubbles must then be slightly elevated out of the surface. The levels are marked in the Figure 5.4 and 5.6 with a bold dark line and this corresponds quite well with the levels where the rates start to decrease. The ratios can be used as a rough guideline for prediction of the onset of bidispersity.

Whether a bidisperse layer is created is observed to depend on the size of the crystal, specifically its surface area and the number of layers underneath. The crystal is generally confined by disordered grain boundaries. With each appearance of a new layer at the surface, the disorder of the grain boundary leads to a cave-in of the boundaries, decreasing the ordered surface area of the crystal.

The thickness of the crystal below the surface layer determines whether the rearrangements on the surface result in re-ordering into bidisperse top layers. With less than five layers the appearance of bidisperse layers was rare. Once space was created at the surface by the diffusion of the initial top layer, the whole crystal lost its structure, diffusion was

not limited to one surface layer anymore and interbubble diffusion occurred. Defects within the crystal further decreased the evolution of an ordered bidisperse top layer, but could also create symmetrical arrangements, an example of which is shown in Figure 5.10.

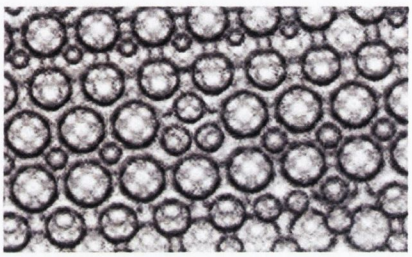


Figure 5.10: Bubbles of multiple sizes form an ordered structure, three small bubbles are filling up the gap of one large bubble; a filled point defect.

In time, also coarsening of the internal structure of the crystal will occur, as described in [155] and [6], making it impossible to create new ordered surface layers.

Occasionally we have observed the emergence of the second layer in rows, as can be seen in Figure 5.11. The surface layer splits open along a row of bubbles and the row from the

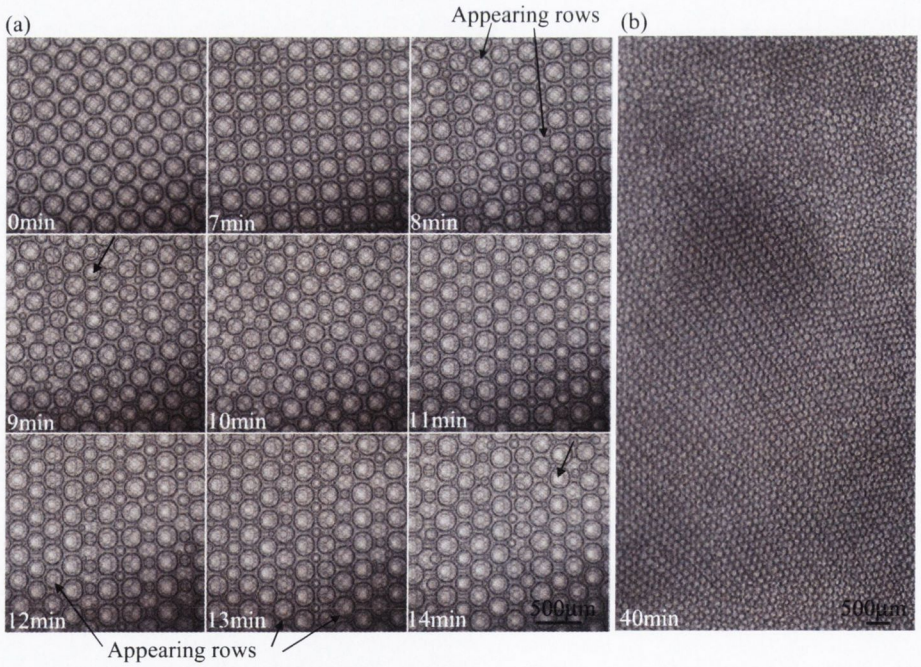


Figure 5.11: (a) An alternative mode of diffusion for fcc(100). The top surface splits open along a row, allowing new rows from the second layer to intrude. In time new rows appear, rather than new layers so no bidisperse foam layers are created. This tended to occur along grain boundaries. This process of crystalline diffusion is visible for a long time at the surface, as seen in (b) after 45 min.

second layer forms a new row at the top surface (marked by arrows). This is more often seen near ordered grain boundaries or stacking faults.

5.4 Diffusion rate

From Figure 5.8 it is obvious that the shrinkage rate of bubbles in the top layer of bubbles increases with the number of layers in the crystal. To further investigate this effect we have conducted experiments with both individual bubbles and monolayers of equal-sized bubbles sitting on a pool of liquid. The data shown in Figure 5.12 indicates that the decrease in bubble size of the top layers of crystals is much quicker compared with that of a single bubble or monolayer at the surface of a liquid pool.

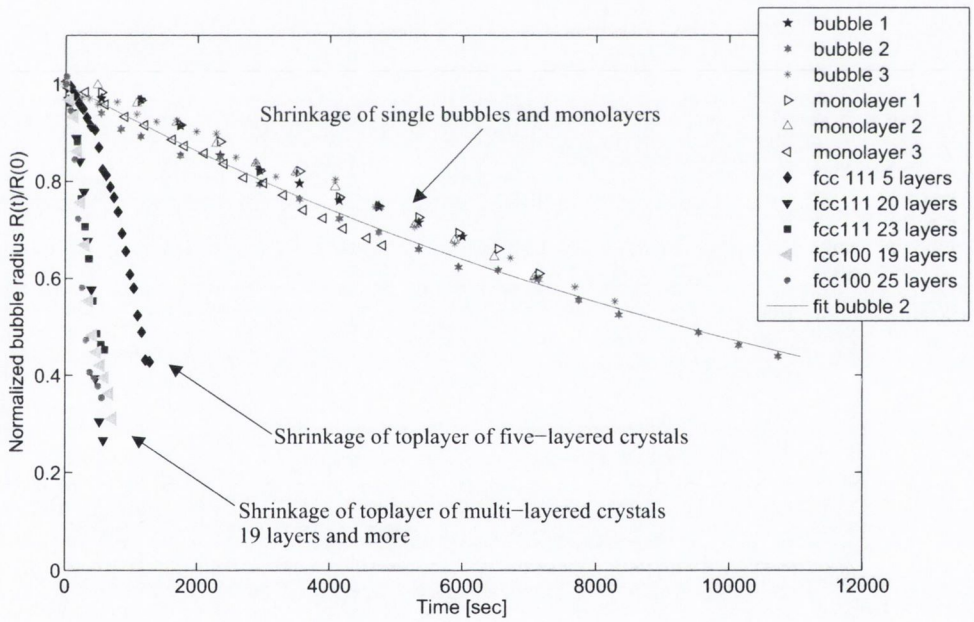


Figure 5.12: The bubble size reduction in time for different configurations of bubbles at a liquid surface. The shrinkage of the top layers of bubbles in crystals is much quicker than for bubbles in a monolayer or for a single bubble.

To gain some insight into the dependence of the diffusion rate on the number of layers, we used a model proposed by Ghosh *et al.* [88] to determine the speed of diffusion of gas $[m/s]$ named the *the permeability* through the top film of the single bubble and of bubbles in monolayers (Section 5.4.2). We determine in Section 5.4.3 the effect of the number of layers

by adapting the Ghosh model.

5.4.1 Basic model

For film permeability measurements Brown [156] and Princen [157, 158] performed measurements on bubbles at the water-gas interface, only considering diffusion through the thin film at the top of the bubble. The diffusion rate was related to the bubble size, type of gas and liquid used, temperature and time of drainage of the film [158, 159]. Ghosh *et al.* [88] measured and modelled the effect of temperature on the permeability of films of bubbles at the liquid/gas interface. We used the proposed model of Ghosh *et al.* [88] to estimate the film permeability k in our experiments.

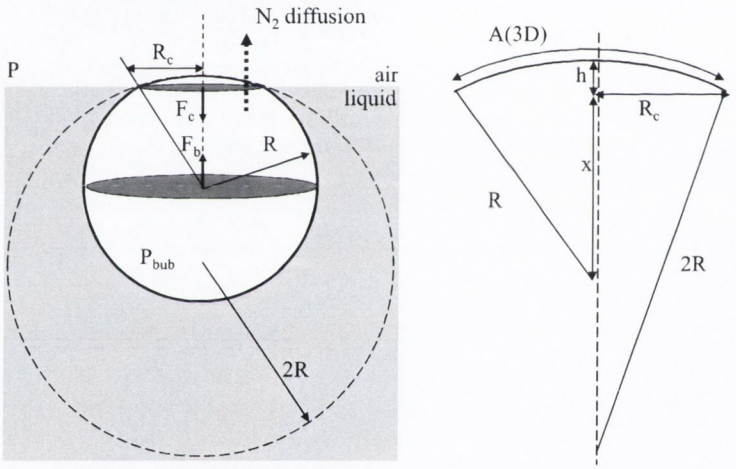


Figure 5.13: The shape of a bubble at the gas/water interface. The bubble shape and position is a balance between capillary forces F_c, depending on the gas pressure, and buoyancy F_b, depending on the bubble volume. This introduces a change in radius of curvature at the surface, which is 2 times the radius of the bubble R. Due to the gas pressure difference between the bubble P_{bub} and air pressure P gas diffusion takes place towards the air with bubble shrinkage.

The volume change of a bubble $\frac{dV}{dt}$ is dependent on the atmospheric pressure P, the gas pressure difference across the film ΔP (in our case the pressure difference between inside and outside the bubble), the bubble cap area A and the film permeability k according to:

$$-P\frac{dV}{dt} = \Delta PAk. \tag{5.1}$$

From experiments $\frac{dV}{dt}$ can be determined. The area of the bubble cap is given by [160]. This results in:

$$A = 8\pi R^2 \left[1 - \sqrt{1 - \left[\frac{R_c}{2R}\right]^2}\right] \tag{5.2}$$

with

$$R_c = 2R^2 \sqrt{\frac{\Delta\rho g}{3\gamma}}, \tag{5.3}$$

see Figure 5.13 and Appendix C.2. Here R_c is the radius of the bubble cap and R the bubble radius, γ is the surface tension, $\Delta\rho$ the density difference between the liquid and gas and g the gravitational acceleration.

Using Equation 5.2 and 5.3 in the integration of Equation 5.1 results in an equation relating time t to the decrease in bubble radius R:

$$t = t_0 + \frac{U}{k} * \left[\sqrt{1-B} - \sqrt{1-CR^2} + ln\frac{1-\sqrt{1-B}}{1-\sqrt{1-CR^2}}\right] \tag{5.4}$$

with

$$U = \frac{3P}{4\Delta\rho g}$$

$$B = \frac{R_0^2 \Delta\rho g}{3\gamma}$$

$$C = \frac{\Delta\rho g}{3\gamma}.$$

R_0 is the initial bubble radius and t_0 is the time of start of the fit (Ghosh *et al.* [88]). See Appendix C.3 for the derivation. The permeability k is the free fitting parameter.

Certain assumptions and approximations are made to arrive at Equation 5.4.

(a) Gas diffusion: The gas composition inside and outside the bubble is assumed to be equal. This corresponds to either only one type of gas or a mixture of gases with equal volume fractions present at both sides of the film. For the value of the permeability one then either uses the single gas permeability or a sum of the individual permeabilities of the gases present in the mixture [158]. According to Muruganathan *et al.* [161] film permeability does not change while the bubble (100 μm in diameter) shrinks. We also assume this in our experiment. Furthermore we assume that gas does not dissolve into the liquid. Also we assume no drainage effects occur after the start of the experiment which could influence the permeability.

(b) Bubble and film shape: The buoyancy force is assumed to act over the whole bubble, instead of only its volume in the water. With a small bubble the surface tension of the gas-water interface can hold the almost spherical bubble sufficiently down to justify this assumption. Only for small bubbles is it valid to assume that the cap radius R_c is equal to two times the bubble radius R. The bubble is assumed to have a cap shaped film, excluding the 'dimple' in the middle of the film which is present according to Princen [160].

5.4.2 Diffusion rate of single bubbles and monolayers

As described in Section 5.2 we performed experiments monitoring shrinkage of a single bubble on top of a bubble pool, see Figure 5.14.

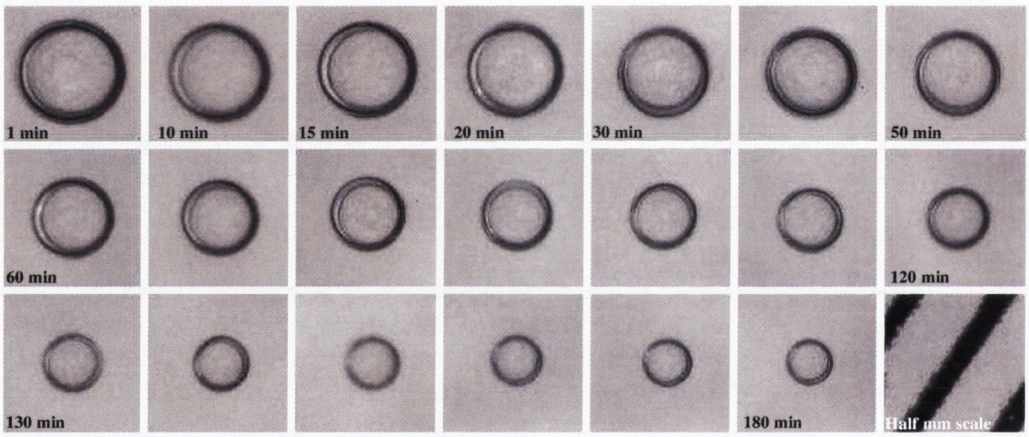


Figure 5.14: Diffusion of one single bubble on top of a liquid pool. The decrease of the bubble radius with time was monitored and plotted in Figure 5.15 as experiment '1 bubble II air'.

This data will be used in Section 5.4.3 to establish a relation between the number of layers and the diffusion rate. The Ghosh model assumes that at both sides of the film the same gases are present. However, in the experiments carried out with our bubble crystals the bubble contained nitrogen, but diffused into the air containing only 78% nitrogen [162]. It is therefore likely that other atmospheric gases present actually diffused into the bubble, decreasing the effective gas flow out of the bubble. We performed experiments with both nitrogen and air filled bubbles to detect a difference in the estimated permeabilities, see Figure 5.15 shows a typical recorded sequence. We estimated the film permeabilities by fitting Equation 5.4 to the data using least square fit in Gnuplot (a data plotting program). The results are shown in Table 5.1.

We found the average permeability for the air filled bubbles was $1.05 \pm 0.2 \times 10^{-3}$ m/s, while for nitrogen we found $1.20 \pm 0.04 \times 10^{-3}$ m/s. This shows a slight deviation in per-

Exp.	k $[m/s]$	T$[^0C]$	Surfactant
1 bubble I	$0.98 \pm 0.02 \times 10^{-3}$(air)	21-22	Fairy
1 bubble II	$1.19 \pm 0.01 \times 10^{-3}$(air)	22	Fairy
1 bubble III	$1.05 \pm 0.02 \times 10^{-3}$(air)	18-21	Fairy
1 bubble IV	$0.97 \pm 0.02 \times 10^{-3}$(air)	20	Fairy
1 bubble V	$1.21 \pm 0.04 \times 10^{-3}$(N2)	20	Fairy
1 bubble VI	$1.19 \pm 0.04 \times 10^{-3}$(N2)	20	Fairy
1 layer I	$1.02 \pm 0.03 \times 10^{-3}$(N2)	18-21	Fairy
1 layer II	$0.98 \pm 0.02 \times 10^{-3}$(N2)	20-21	Fairy
1 layer III	$1.26 \pm 0.02 \times 10^{-3}$(N2)	18-19	Fairy
Princen[157]	1.23×10^{-3}	21	hexadecyltrimethylammonium
Krustev [159]	$0.3 - 1 \times 10^{-3}$ f(conc.NaCl,SDS,Temp)	21-30	SDS/NaCl(air)
Krustev [154]	$0.85 - 1.65 \times 10^{-3}$ f(conc.LiCl,SDS,Temp)	25	SDS/LiCl(air)
Muruganathan[161]	$1.25 \pm 0.02 \times 10^{-3}$	25	Dodecyl Maltoside/Nacl(air)

Table 5.1: The permeabilities obtained from fitting the model to the data as plotted in Figure 5.15 and 5.18, compared with values found in literature also using floating bubbles at a liquid surface.

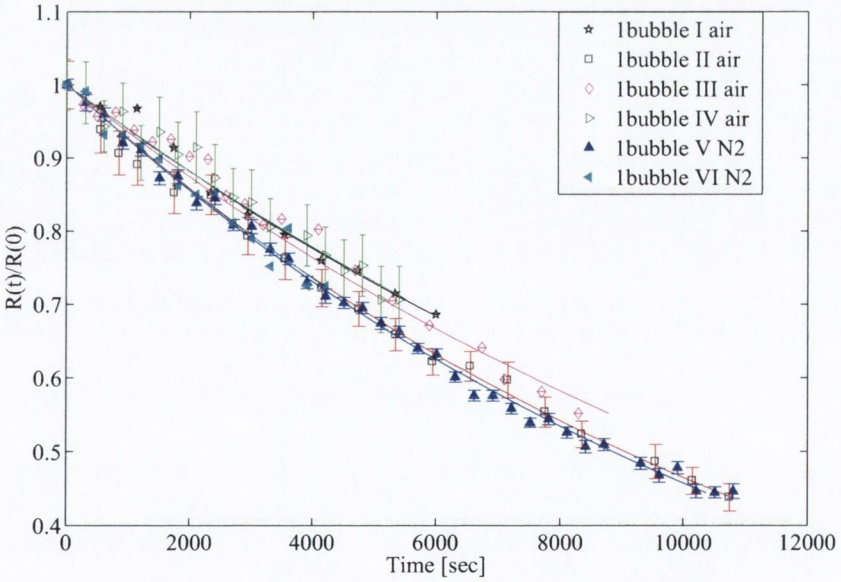


Figure 5.15: Data for the shrinkage of single bubbles in time, plotted as normalised bubble radius versus time. The scatter in the experimental data does not allow to distinguish different values for the permeabilities of air or nitrogen filled bubbles. The data is fit with Equation 5.4.

meability, opposite to our expectations of a damped permeability in the case of the nitrogen filled bubble due to an influx of atmospheric gases. No clear distinction can be made between

diffusion of nitrogen or air filled bubbles when diffusing towards the atmosphere. So we can use Ghosh model also in the case we have nitrogen filled bubbles diffusing towards the atmosphere.

The experiments were repeated with a single layer of monodisperse bubbles to see if the diffusion rate differed. The experiment was stopped when the monolayer became disordered due to increasing polydispersity over time, as can be seen in Figure 5.16.

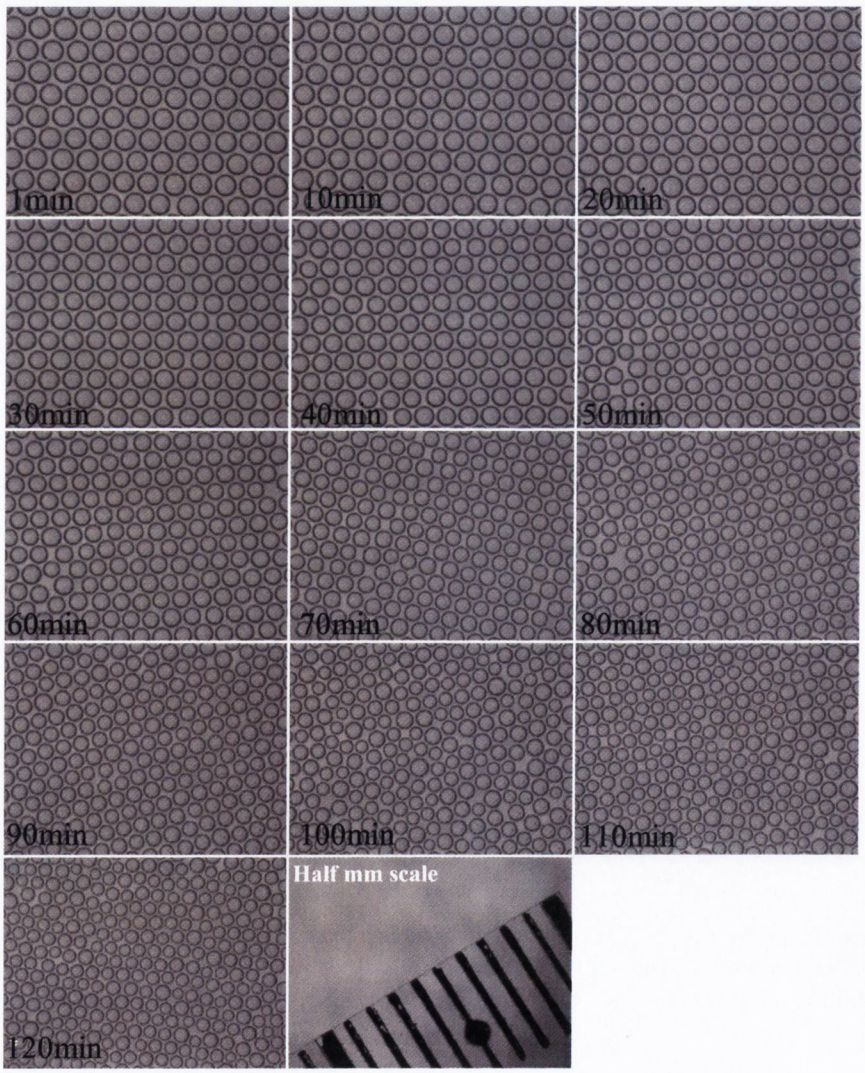


Figure 5.16: Diffusion of a monolayer of bubbles on top of a liquid pool. The decrease of the bubble radius with time was monitored and plotted in Figure 5.18 as monolayer I.

This was caused by the slight polydispersity of the bubbles at the very start of the experiment. This increased variation in bubble sizes can induce diffusion between bubbles, which we do not want to included in the analysis. Note that we monitored the bubble shrinkage in the centre rather than at the edge of the monolayer, as the bubbles at the edges have different diffusion rates, see Figure 5.17. The bubbles elevate the liquid-gas interface as buoyancy forces lift them out of the surface. At the edges of the monolayer the water level curves back to the original level. This exposes the bubbles at the edge more to the atmosphere, the area of diffusion is increased and therefore their rate of shrinkage. Once the outer bubbles are of significant smaller size also diffusion between the bubbles with different sizes starts to play a role.

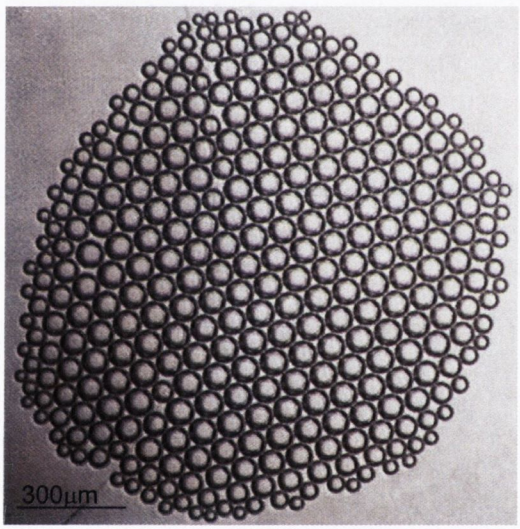


Figure 5.17: A monolayer after 40 minutes. The bubbles at the edge are visibly smaller than the ones in the centre, resulting from a difference in the area of diffusion between bubbles at the monolayer edge and within the monolayer.

The diffusion rates of single bubbles and monolayers match well as shown in Figure 5.18. The data collapses onto one graph if the normalised bubble radius is plotted versus time. The estimated permeability for a monolayer of nitrogen filled bubbles is $1.08 \pm 0.18 \times 10^{-3}$ m/s.

There is no significant difference between the estimated film permeabilities of a single bubble and monodisperse bubble layers. The value seems reasonable when compared with previously published film permeabilities, as seen in Table 5.1. Note that in the literature large variations in permeabilities are found due to the dependence on the film thickness, dependent on many factors as temperature and surfactant concentration, salt addition and gas solubility. As we do not have all information on these parameters direct comparison is

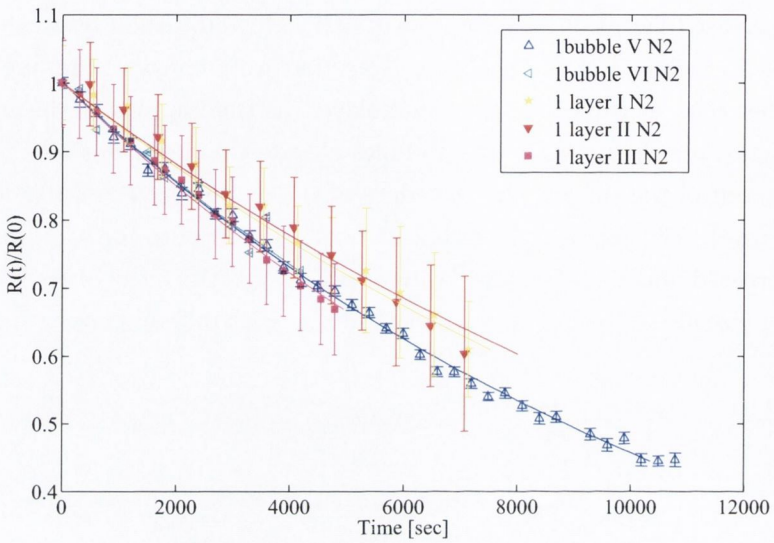


Figure 5.18: Normalised bubble radii as a function of time for nitrogen filled single bubbles and monolayers. The data is fit with Equation 5.4.

difficult.

We conclude therefore that initially the diffusion between the bubbles within the layer is negligible, resulting in an average estimated nitrogen permeability of $1.11 \pm 0.15 \times 10^{-3}$m/s for a film stabilised by a Fairy liquid surfactant concentration of 1% at $18-21°$ C. No distinction can be made between diffusion of nitrogen or air filled bubbles.

The scatter in our data is possibly due to variable environmental factors, e.g. temperature of air and liquid during the experiment [88, 154]. Other factors may be slight polydispersity of the initial bubbles, errors in the image analysis due to the picture quality (due to bubble movement) and optical effects (Chapter 3).

5.4.3 Modeling of 3D bubble crystal diffusion

We adapted the model, discussed in Section 5.4.1, to the case of diffusion of the top layer of 3D bubble crystals. Therefore we assumed that the permeability remained constant, as we are still in the wet limit of the foam. We used the average value found in our experiment of the single bubble and monolayer of $k = 1.11 \times 10^{-3}\ m/s$. Note that we only considered the initial stage of diffusion (stage I) where the surface bubbles shrink uniformly.

At stage I of the experiment (see Figure 5.19) the normalised bubble radii vary roughly linearly. We linearised Equation 5.4 by the Taylor expansion to:

$$\frac{R(t)}{R_0} = (t_0 - t)\frac{2k\Delta\rho g}{3P} - 1 \tag{5.5}$$

This equation shows that there is no dependence on surface tension. As we saw for the experiments the diffusion rate increases with the number of layers. To explore the dependence of diffusion on the number of layers we included an extra correction factor β to Equation 5.5, directly proportional to the permeability:

$$\frac{R(t)}{R_0} = (t_0 - t)\frac{2k\Delta\rho g\beta}{3P} - 1 \tag{5.6}$$

We fit this equation to the data, but only for the first few minutes of the experiment before the bubbles of the second layer start to appear, with t_0=0. The result is shown in Figure 5.19.

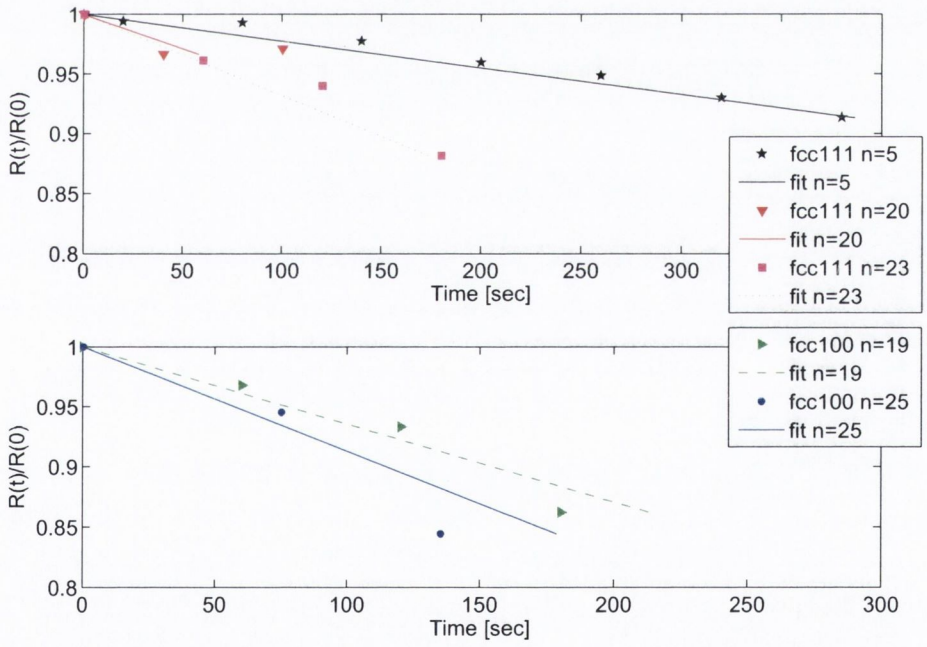


Figure 5.19: Stage I of the variation of the normalised bubbles sizes over time for various multi-layered bubble crystals. Only the radii of the initial top layer are considered. The data is fit to Equation 5.6.

The development of β with the number of layers is shown in Figure 5.20. β increases

almost linearly with the increasing number of layers n according to $\beta = 0.41n + 0.68$. Note that we do not distinguish between the square and triangular top layer. In the next section we will discuss more extensively the different factors possibly included in β.

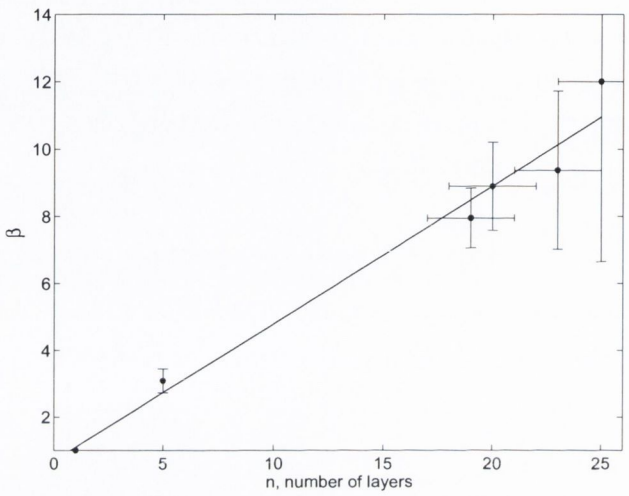


Figure 5.20: The linear dependence of the correction factor β on the number of layers in the crystal.

5.4.4 Discussion

We have presented a model to provide more insight into the increased diffusion rate of the surface layer with increasing numbers of underlaying layers. Here we discuss the factors, that can contribute to β, which increases linearly with the number of layers.

Extra buoyancy force

With extra layers underneath, the force acting on the surface layer bubbles is increased depending on the amount of layers. This extra force is counteracted by the surface tension forces, which does not change with the presence of more layers. This is expected to result in a larger bubble cap area for diffusion to take place and would create a quicker diffusion rate. If extra buoyancy would be the main factor, it would mean when the data would be normalised for the cap area, the data should collapse onto one graph.

In order to theoretically describe the extra buoyancy force acting from the other layers on to the top layer the actual definition of buoyancy in a wet foam needs to be discussed. The definition of the buoyancy force is taken as the gravity force on the replaced liquid volume.

It is based on the density of the liquid, but it is questionable whether this is the appropriate definition in a foam. In the literature much discussion can be found on the correct definition for buoyancy forces in liquid fluidised beds. Here the surrounding particle sizes compared with the considered object is important [163, 164]. Considering monodisperse particles, if the object size (one bubble) is equal to the surrounding particles (bubbles in our system) the fluid density should be used for the determination of the buoyancy force. In our case an extra complication arises as the bubbles do touch each other.

Liquid fraction

With an increased number of bubble layers there will occur a change in liquid fraction of the top layer. The bubbles are drier as they are higher above the water surface and have drained more, even though the foam height is still below the wet limit. Changing liquid fraction can effect the bubble diffusion rate in two ways:

1. Permeability

In our base model we assume to have a *common black film* (CBF), due to the high liquid fractions. In the case of a CBF the permeability rates are determined by the mobility of the gas through the bulk liquid in the film. Krustev et al. [154, 159, 165] performed measurements on the permeability variation with change in film thickness. Generally the permeabilities increase with a thinning film, except for approaching the *Newton black film* (NBF) where the permeability drops and remains constant. The permeability is then only influenced by the two monolayers of surfactant forming the film. We do not know the change in film thickness with a liquid fraction that can vary between $18 - 36\%$ (see the Introduction, page 4). According to the data provided by Krustev [165] the permeability of a CBF can increase severely with a decrease in film thickness. This can be one of the factors which was not perfectly included in the model. Therefore experimental data is needed on the progression of permeability with a forced pressure balance for Fairy as a surfactant to verify our expectance that this effect of a thinner top changing the permeability of the film is neglegible within the large experimental error.

2. Bubble shape

A change in liquid fraction does not only affect the permeability but also the bubble shape. As the foam becomes drier, the bubbles become less spherical and transform towards polyhedral shapes. This increases the top film area and could increase the diffusion rate.

Other factors we need to take into consideration with this model are:

Model assumptions

Note that we assumed in the initial model that the size of the cap is negligible. This could be violated when the force from below is so large that the bubble is lifted far out of the surface. This and the possible changing shape of the bubble in general should be tested in simulations relating the correct force balance to the bubble shape.

The force balance in the film initially reaches an equilibrium state. According to Muruganathan [161], film permeability does not change over time with the bubble shrinkage for a bubble of 100 μm. This is remarkable as during the shrinking the buoyancy force changes. This influences the capillary pressure in the film, changing the force balance and therefore the film thickness. Krustev *et al.* [165] measured the film permeability as a function of pressure difference between gas and liquid. When a bubble with an initial radius of 500 μm shrinks to half its size the pressure difference change is 54 Pa. This is too small for any noticeable effect and stays within the experimental error. So the assumption is justified that permeability remains constant during an experiment and also when comparing the different experiments which did not all start with the same bubble size (200-400μm).

Presence of other atmospheric gases outside nitrogen

Our bubbles contain 100% nitrogen. But only 78% of the air consists of nitrogen [162]. The errors in our measurements showed that no distinction could be made between air and nitrogen bubbles. In more accurate experiments the shrinkage of nitrogen bubbles is expected to be slower as remaining atmospheric gases would diffuse into the bubble. This would reduce the bubble shrinkage.

This effect of diffusion *into* the bubble can be seen if perfluorhexane (C_6F_{14}) is added to the nitrogen, which is generally added to reduce the diffusion between the bubbles [166]. The bubbles expand presumable due to nitrogen and oxygen diffusing into the bubble to balance the concentration difference. The oxygen concentration could even become higher than in the atmosphere as perfluorhexane is known to adsorb oxygen (and carbon dioxide) [167].

Other experimental observations that will need to be explored further in the future:

Stage II-III

So far we studied the first stage in the diffusion of a top layer of a bubble crystal. The model can be further extended by including the diffusion towards the neighbouring bubbles, expected to be present in the second stage (II) in the diffusion of the top layers of bubble crystals (see Figure 5.8). The bubbles are then of different sizes and this is expected to be the cause of the increased diffusion rate of the bubbles compared with the initial diffusion

rate at stage I. This can not completely explain the effect, as in stage III the diffusion slows down again, while the difference in bubble size only increases. In stage III, initially there is still direct contact between the bubbles, as shown in Section 5.3 where we describe the point where theoretically the bubbles of the top layer fit in the cavities of the second layer. With the bubbles of the top layer shrinking further, finally there will be no longer direct contact between the bubbles as the tiny bubbles float freely in-between the new surface layer and then the diffusion should slow down to the initial diffusion rate of stage I. This could explain also the 'delay' between occurrence of bidispersity and drop in diffusion rate. The stage III slope seen in Figure 5.8 appears to approach the initial slope but we do not have enough data to verify that. Also, squeezing can temporarily increases the area for diffusion. This could also be an explanation for the ability of self-reorganisation of the system. 3D sphere simulations are currently being performed by Gary Delaney to gain more insight into this effect.

5.5 Conclusions and Outlook

This chapter described the diffusion of top layers of ordered bubble crystals. Surprisingly, after a disordered stage the diffusion self-organises the top layer into bidisperse layers. This process repeats and can be followed for several sequences. The reason for the re-occurrence of order is not understood. Different magnitudes of squeezing between the bubbles could increase or decrease diffusion rates of individual bubbles dependent on the area, but this will need simulation results to be confirmed.

The average diffusion of bubbles in the top layer of a bubble crystal is such that it takes several minutes for one layer to disappear and hours for a single bubble or monolayer at a liquid surface. The diffusion rate of the top layers is linearly related to the amount of layers in the crystals. An extra buoyancy force from the extra layers below increases the area of diffusion and could be a factor involved in the explanation of this difference. Another factor which can play a role is the change in liquid fraction with the presence of extra layers underneath, which causes the area of the cap to be larger in the case of a dryer top layer of the thicker bubble crystal. Creating a new model to include correct bubble areas that depend on force or liquid fraction, combined with more experimental data, would enable a more elaborate explanation for this problem. We could then answer other questions, such as how β would behave with even more layers, proceeding towards dry ordered surface layers.

In the future, experimental data needs to be generated on the progression of permeability

for Fairy as a surfactant, using a film pressure balance technique to control the film thickness. More knowledge needs to be gained on buoyancy effect in foams in order to completely understand the observed effect of extra layers. It would be interesting to study the effects of different gases and surfactants on the diffusion process.

The coarsening of the surface layer can be considered as peeling off the structure. Following the ordered coarsening of up to 6 layers is another indication, besides the mentioned optical patterns and terraces in Chapter 4, that the bulk structure is ordered.

This effect may be used in the future to study propagation of dislocations or other layer defects, although dislocations can initiate different coarsening rates changing the way of 'peeling off'. In general this unique diffusion effect is something we would like to avoid as it obstructs working with crystals exposed to the air. Sample solidification is one solution, which we discuss in the next chapter.

Chapter 6

Polymerisation of ordered foam structures

6.1 Introduction

Polymer foams have become one of the most commonly used materials in everyday life. Composed of gas bubbles immersed in a continuous polymer phase, they form porous materials with properties much more complex and versatile than those of their pure constituents. They are the key components in products that help us sleep and sit comfortably, they insulate against noise and heat and are of use in cleaning products.

The complex physical properties of foams are governed in particular by their structural parameters, such as the average pore (or bubble) size, the pore (bubble) size distribution, the overall gas-to-volume ratio, and also whether the foam has open (i.e. interconnected) or closed pores. Relationships between these parameters and the overall foam properties are by now quite well understood. Still lacking, however, is the ability to control these parameters to a high degree of accuracy, in particular on an industrial scale. This is because in most standard techniques (such as extrusion [168]), which have been optimised over decades to produce the billions of tonnes of polymer foams required every year, foam generation and polymerisation are coupled in highly complex ways which defy accurate modeling and control due to their statistical nature of bubble nucleation and growth [169].

In this chapter, we propose and test here a solution to the problem of structural control of polymerised foam by clearly separating both processes, i.e. we first produce a liquid foam with accurately defined structural properties from an aqueous monomer (or polymer) solution and then polymerise and solidify it. This allows us to build on the vast expertise

developed in the physics of liquid foams [5, 116] up till now. As a result, aqueous foam structures can now be generated and modelled to such a degree of accuracy [5] that it appears a logical consequence to transfer this understanding into the realm of solid foams by using liquid foams as templates for polymerisation. If suitable polymers can be found, this could also replace the formation of ordered porous structures using colloidal crystals [130, 170]. For this method colloidal crystals, ordered porous arrangements of colloidal particles, are filled with solidifying material. Hereafter the colloidal particles are removed and porous structures remain.

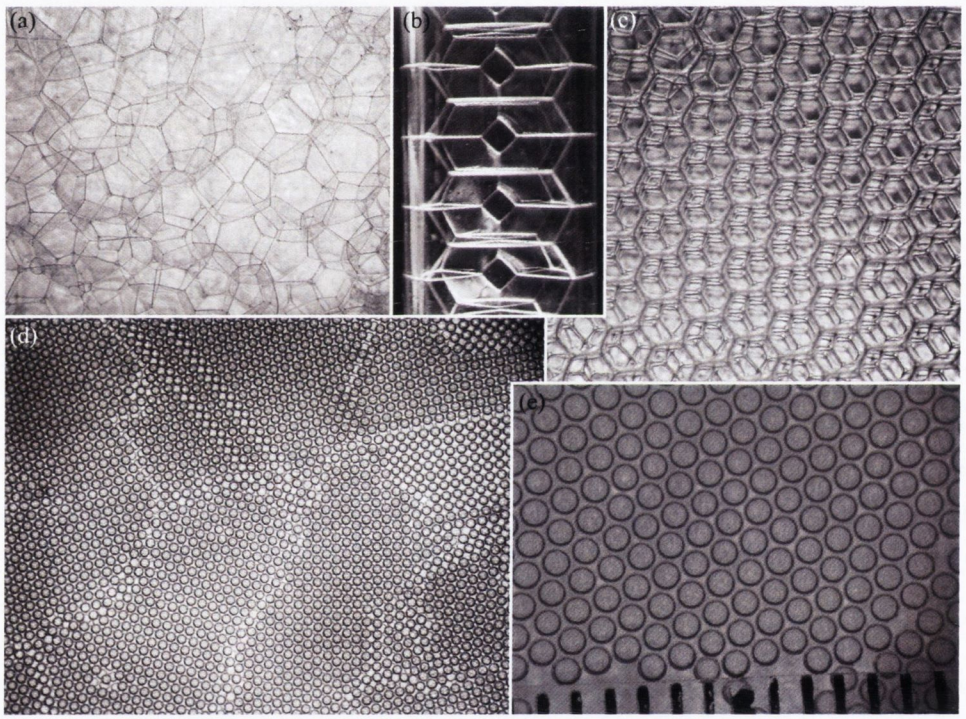


Figure 6.1: Examples of aqueous foam templates for polymerisation: (a) disordered dry foam,(b) ordered microbubbles in a tube, (c) ordered dry foam, (d) crystalline wet foam consisting of microbubbles and (e) one layer of ordered microbubbles (Bubble sizes are between 300 and 500 μm.)

To our knowledge, only two successful studies have been published on the creation of polymer foams [171, 172] from aqueous foams. However in these there was no control over the foam structure due to coarsening during the polymerisation reaction, which took more than 50 hours.

Our feasibility study shows for the first time that by sufficient separation of foam gener-

ation and polymerisation highly ordered, polymerised and cross-linked micro-foams can be formed from initially ordered liquid monomer foams such as those described in Chapter 4. This work was carried out at the Matière et Systèmes Complexes, Université de Paris 7 and was funded by BASF, Germany.

Firstly in Section 6.2 we discuss the required properties of the polymerisable ingredients. This includes the foamability of the ingredients and stability of the created foams during the polymerisation time. Then in Section 6.3 we focus on the physical aspects such as flow and ordering ability involved in the foam generation with polymerisable ingredients.

Finally in Section 6.4 and further we discuss the end product, its properties and prospectives for the future.

6.2 Materials

Polymers are large molecules with a high molecular weight formed by chains of linked monomers [118]. During the polymerisation reaction *monomers* react with each other, either due to a catalyser which will not be included in the end product (step growth polymerisation) or with the assistance of an *initiator* which will become a part of the end product (chain growth polymerisation) [168]. Chain growth polymerisation reactions can be further sub-categorised by the means of their initiation. This can occur either by ions, molecules with extra or lost electrons (ionic polymerisation) or free radical, molecules with a free bonding space by unpaired electrons (free radical addition polymerisation).

Our ingredients react according to the free radical chain growth polymerisation reaction. The initiator forms easily reacting *radicals*, either spontaneously or under the influence of an external energy source such as UV light or heat [118]. Our initiator forms spontaneously radicals, which reacts with the monomers such that polymer radicals are formed. In Figure 6.2 examples are given of reactions taking place during our polymerisation reaction. The reactions are either an initiation, propagation or termination reaction [118]. We added to the monomer and initiator an *accelerator* which forms extra radicals and stimulates the reaction. The reaction speed depends on the initiator and accelerator concentrations. At higher concentrations the reaction takes place more rapidly, as there are more sides where the reaction nucleates but this also leads to shorter final polymer chains. This can affect the mechanical properties of the polymer. To form a network a *crosslinker* was added, which contains two reactive groups which can react with two different polymers and therefore connecting them, see Figure 6.2 (c) for an example. The final ingredient needed was a *solvent*. Some ingredient are powders and we needed the ingredients to form a liquid foam before

polymerisation. Another function of the solvent is to absorb part of the heat generated during the exothermal reaction.

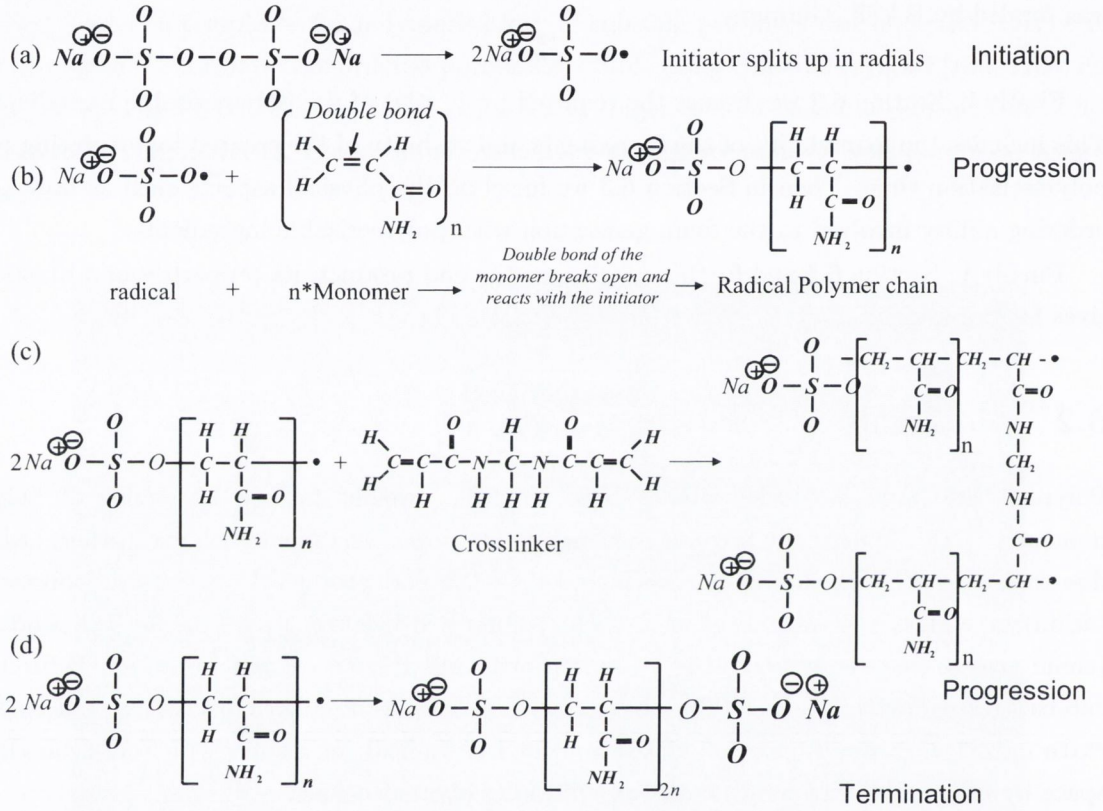


Figure 6.2: Examples of reactions occurring during polymerisation [168]. (a) is an example of initiation, where the initiator forms radicals. (b) and (c) are examples of progression reactions, forming polymer radicals and (d) is an example of a termination reaction, which ends the formation of the polymer chain.

6.2.1 Chemical composition

The chemical components we used in our polymerisation process are listed in Table 6.1 (provided by BASF). As indicated in the table, we divided them into two separate solutions, Liquid I and Liquid II, such that polymerisation occurred only when they were mixed together. This means in practice that the initiator needs to be separated from the rest of the ingredients. Water, the solvent in this recipe, was divided between the two solutions such that they could be brought together in equal volumes, which allowed the use of only one pump, a dual-syringe pump. The final product of this process was a hydrogel, which is a network of linked polymer

chains which can reversibly absorb quantities of water multiple times its own weight.

Component	Function	Liq I	Liq II
Acrylamide(p)	monomer	x	-
N.N'-Methylenbis(acrylamide)(p)	crosslinker	x	-
N,N,N',N'-Tetremethylethylendiamine(l)	accelerator	x	-
Surfactant(l,p)	foam stabiliser	x	-
Distilled water(l)	solvent	x	-
Sodiumperoxodisulfate(p)	initiator	-	x
Surfactant(l,p)	foam stabiliser	-	x
Distilled water(l)	solvent	-	x

Table 6.1: Chemical components of the radical polymerisation, which are divided over the two liquids Liquid I and Liquid II such that polymerisation starts only once both solutions are brought together.

6.2.2 Foam stability

Due to a large quantity of water contained in the monomer solution, foam stability with standard surfactants sufficient here over the short time scales required for polymerisation (up to 17 seconds as we will discuss later). Foam stability was optimised by enclosing the foam in containers to avoid evaporation.

We chose to work in most cases with the technical grade, non-ionic surfactant Lutensol AT18 (provided by BASF). High surfactant concentrations (1000 times the CMC), are required to ensure sufficient surface concentrations during the rapid bubble generation.

6.2.3 Role of the polymerisation time

Our ingredients were fixed, though not their concentrations. Of importance is the role of the polymerisation time, the total time it takes for the sample to polymerise, regulated by the initiator and accelerator concentration. As we want to separate polymerisation from foam generation solidification should take as long as possible. With the recipe used, polymerisation starts immediately when ingredients are mixed but only in the last stage solidification occurs. So for this recipe we want foam generation and solidification to be sufficiently separated.

However for successful *foam* polymerisation we found that the polymerisation time is absolutely crucial. We performed preliminary "shake tests", in which a polydisperse foam is generated by shaking vigorously the closed test tube immediately after Liquid I and Liquid II have been mixed. For reasons which we do not yet fully understand, the foam structure was only successfully preserved in the polymer material when the polymerisation reaction was sufficiently fast. At longer polymerisation times the system phase-separated and expelled the

solvent and bubbles from the gel matrix, which left behind a solid polymer block crowned by an aqueous foam which did not polymerise. An illustrative example of this effect is provided in Figure 6.3, where a sample with a polymerisation time of 5 seconds is contrasted with one of 15 minutes. We investigated this effect more quantitatively by varying systematically the polymerisation time by tuning the accelerator and initiator concentrations at constant room temperature, see Table 6.2.

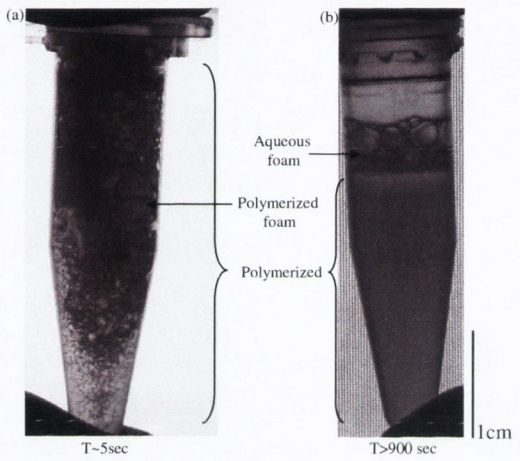


Figure 6.3: The difference between shake test samples with a polymerisation time of 5 seconds (a) and 15 minutes (b). In (a) the foam polymerises, whilst in (b) bubbles and water are expelled from the gel matrix, leaving behind a solid polymer block and an aqueous, non-polymerisable foam.

Figure 6.4 shows the change of polymerisation time with the initiator and accelerator concentrations as determined for a liquid volume of one milliliter at room temperature. It can be seen that the polymerisation time can be tuned very easily over several orders of magnitude.

To observe the influence of the polymerisation time on the success of foam polymerisation, we again generated polydisperse foams in a 1.5 *ml* reaction tube by vigorous shaking immediately after Liquid I and Liquid II (0.5 *ml* of each) were mixed, but now for a whole range of combinations of initiator and accelerator concentrations. Two samples were generated for each recipe. To check the foam stability, the first sample was imaged immediately after generation, remained in the sealed tube over night and was imaged again the next day, to see if foam was still present. The second sample was taken out of the tube immediately after generation and was cut in half along its length. The parts were imaged then and for a second time after they had dried for 2 days at room temperature.

Figures D.3, D.4 and D.5 in Appendix D.2 summarise the results for a range of poly-

Component	Quantity [g]	Liq
Acrylamide(p)	20	I
N.N'-Methylenbis(acrylamide)(p)	0.53	I
N,N,N',N'-Tetramethylethylendiamine(l)(Temed)	0.53/1.57/3.12 (1ml=0.78g)	I
Fairy(l)	0.66	I
Distilled water(l)	50	I
Sodiumperoxodisulfate(p) (Sops)	0.17/0.5/1/4/8	II
Fairy(l)	0.66	II
Distilled water(l)	50	II

Table 6.2: Ingredients used for radical polymerisation, divided over the two liquids I and II. The quantities are given for solution with a total volume of 100ml. The Temed and Sops concentrations are varied here to adjust the polymerisation time.

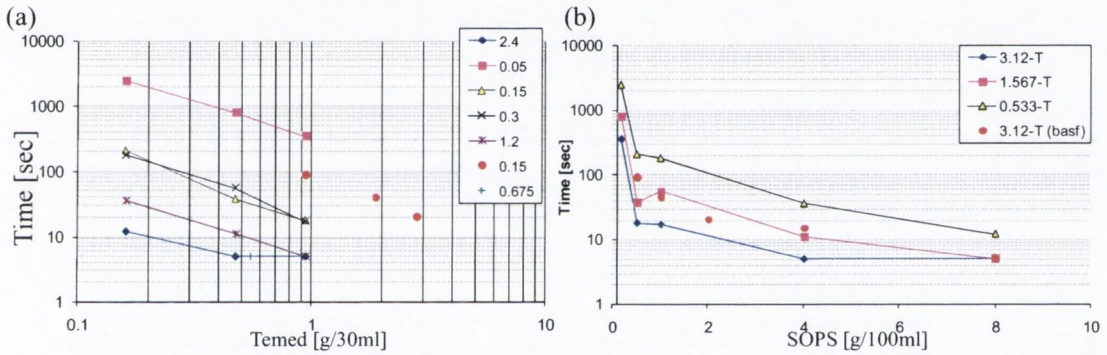


Figure 6.4: Polymerisation times at room temperature for various initiator (Sops) and accelerator (TEMED) concentrations.

merisation times respectively. We see that foam polymerised only when the polymerisation reaction was completed in less than 17 seconds. For longer polymerisation times an increasingly pronounced *phase separation* occurred, which led to the formation of a solid polymer block and an aqueous foam, which did not polymerise and hence collapsed [173, 174]. This type of phase separation is also named Polymerisation Induced Phase Separation (PIPS). The transition from polymerising foams to phase separation lies between 12-17 seconds as can be seen in Figure D.3. This indicates that polymerisation times need to be below 17 seconds for our recipe.

In an attempt to find the relevant parameters that control the phase separation we performed simple experiments in which we varied a range of conditions, including the temperature, concentration of water and cross-linker, or the use of a polymerisable surfactant [171, 175]. Some details of this investigation are listed in Appendix D.3. Reduction of temperature by cooling the sample and application of polymerisable surfactants appeared to have

some effect, but we have not reached any firm conclusions yet.

For all further work we therefore chose to use the standard recipe which polymerised in 11 seconds (Table 6.3). This is short enough to avoid phase separation but also long enough to avoid complete polymerisation before bubbles and foam samples are generated as we will see later.

Component	Quant.[g]	Liq I	Liq II
Acrylamide(p)	20	x	-
N.N'-Methylenbis(acrylamide)(p)(Mb)	0.53	x	-
N,N,N',N'-Tetramethylethylendiamine(l)(Temed)	1.57	x	-
Lutensol AT 18(p)	0.18	x	-
Distilled water(l)	48	x	-
Sodiumperoxodisulfate(p)(Sops)	4	-	x
Lutensol AT 18(p)	0.18	-	x
Distilled water(l)	50	-	x

Table 6.3: The final recipe selected by us with a polymerisation time of 11 seconds. Note that the two liquids are added 1:1 in volume.

6.3 Mixing of ingredients within the bubble generator

In Chapter 2 we described our method of microbubble generation using the flow focusing technique. This is also the technique we used with the polymerisable ingredients. With the short polymerisation time we need to avoid polymerisation within the bubble generator and have the start of polymerisation as close to the bubble generation as possible. Therefore ideally, mixing of the two liquids occurs within the generator. In the flow focusing technique bubbles are generated in the laminar flow regime[1] [7, 12, 49]. This means that mixing can only occur due to diffusion at the liquid interface and not turbulence within the liquids [176, 177].

We tested four new designs with different ways of dual liquid injection, shown in Figure 6.5, on their mixing abilities. Design (a) is a simple junction where one gas and two liquid flows combine and flow out through the orifice as seen in the 'Expected flow' cross section of the outlet channel in Figure 6.5. The two liquids do not mix and have equal flow rates so this is the expected flow pattern. Design (b) is a double junction, where the inlets of the two

[1] In the laminar regime the Reynolds number Re, the ratio between the inertial forces/viscous forces, is smaller than 2100.

liquids alternate for each the junctions. This is expected to result in a flow pattern, where the first junction forms a similar pattern as design (a) but which is joined at both sides by a second influx of liquids I and II which alternated sides. Design (c) attempts to surround the gas flow by one liquid which is surrounded by the second liquid, to create a maximum contact area between the two liquids. This is achieved by having the entrance of the outlet channel in between the two inlets of Liquid I and II. Design (d) has an identical purpose but here it is obtained by injecting Liquid I in front of Liquid II. While the flow profile is quite unpredictable it is expected the two liquids will flow over each other.

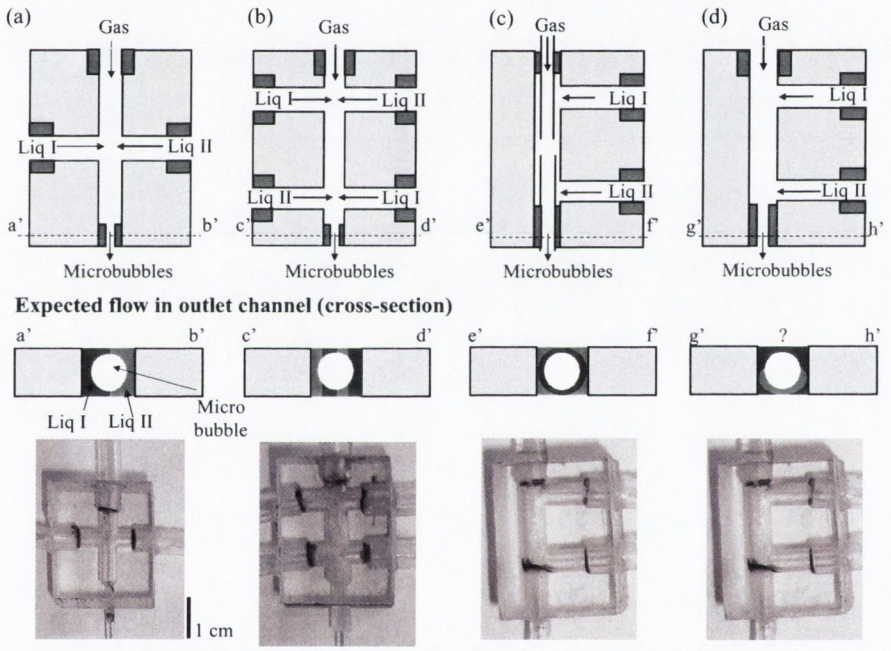


Figure 6.5: The four different designs tested for mixing. The expected flow shows cross section of the outlet channel. The results of their performance is shown in Table 6.4. Design (a) was shown to be the best, based on these factors.

The tests on the mixing abilities were carried out with two liquids, both containing water and the commercial detergent Fairy Liquid and one was coloured with ink. The bubble generation in design (a) is recorded using a high speed camera *(Photron ultima FASTCAN APS-RS)*. In Figure 6.6 an image sequence is shown recorded at 22500 fps. The time step between the images is 1.1 milliseconds or 25 frames. It is seen that the two liquids do not mix, the flow is laminar and mixing due to diffusion is not sufficient to induce instant mixing.

In addition to controlling the mixing, the bubble generator must also create monodisperse bubbles. Dead volume where either bubbles or liquid can accumulate must be avoided as this

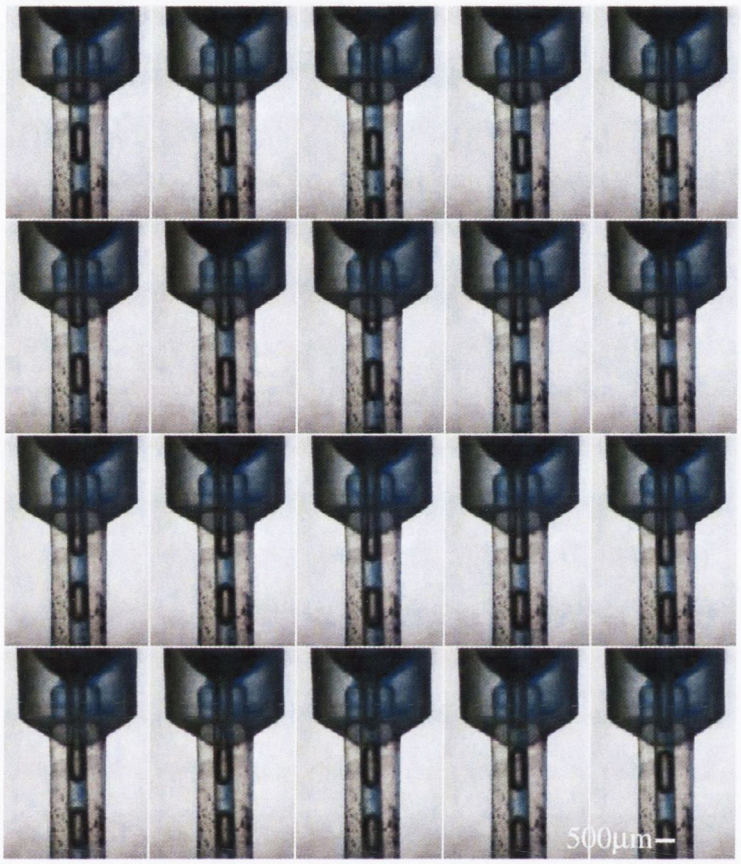


Figure 6.6: An image sequence of the bubble generation in Design (a), made with the high speed camera at 22500 fps. The time step between the images is 1.1 milliseconds or 25 frames. The two liquids used are Fairy solutions, one colored with blue ink. No mixing occurs. The bubble generation occurs as the (dark) gas thread narrows and breaks up in equally sized bubbles.

Design	(a)	(b)	(c)	(d)
Microbubble Generation	+	+/-	-	+
Mixing	-	+/-	+	+
No obstructing bubbles in channel	+	+/-	-	+/-
Easy manufacturing	++	+	-	+

Table 6.4: Properties of the different designs, shown in Figure 6.5.(++= very good, +=good, +/-=average, -=bad.)

may lead to obstruction to liquid flow or polymerisation inside the bubble generator. Finally as occasionally complete internal polymerisation makes the bubble generator useless, it should be a relatively simple device to manufacture. The results of tests on microbubble generation, mixing, obstructing bubbles in the channel and easy manufacturing are shown in Table 6.4.

From the tests described we concluded that design (a) appears to be the best considering the above described factors. Even though proper mixing of the ingredients could be a problem, it turned out that this was not the case. Design (d) could have been an option as well but as some obstruction of bubbles was observed in this design with surfactant solution, it is expected to lead to internal polymerisation and quick blocking of the channel when using the polymerisable ingredients. As tests using the polymerisable ingredients were successful with design (a), no further tests were performed with design (d).

6.4 Generation of ordered polymerised foam structures

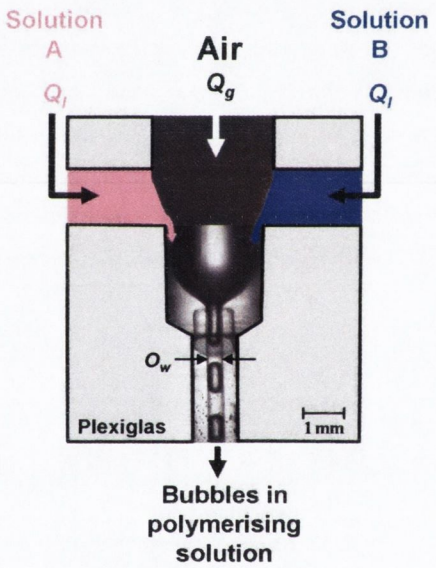


Figure 6.7: Foam generation: air and the two solutions Liquid I & Liquid II are simultaneously forced at constant flow rate through a narrow capillary (250, 500, 550 or 1000 μm), in which the gas thread breaks up into highly monodisperse bubbles. Polymerisation starts during bubble formation, i.e. when Liquid I and II come into contact.

For the generation of the ordered polymerised structures we used the recipe provided in Table 6.3 with a polymerisation time of 11 seconds and the simple bubble generator shown in Figure 6.7 with an orifice width of $O_w = 550\ \mu m$, liquid flow rates Q_l of 2-3.3 ml/min and a gas flow rate of $Q_g = 0.4\ ml/min$.

In Section 4.9 we showed that by confinement in wedges and between parallel plates bubble order in crystalline structures. This technique was used as well here to generate bulk, layered foam structures. To create thread structures we collected bubble in tubes where they formed ordered structures dependent on the bubble size and tube radius. The polymerisation

reaction was such that the viscosity increased dramatically only at the end, which allowed the bubbles to order in the foam structures, before complete polymerisation and solidification.

Polymerised foams in the form of layers

Sandwiched between two glass plates, the foam self-ordered into crystal-like, hexagonally close-packed structures (Chapter 4). We varied the plate spacing to select between different structures consisting of one, two, three or more layers of bubbles. Examples of such structures directly after polymerisation are shown in Figure 6.8.

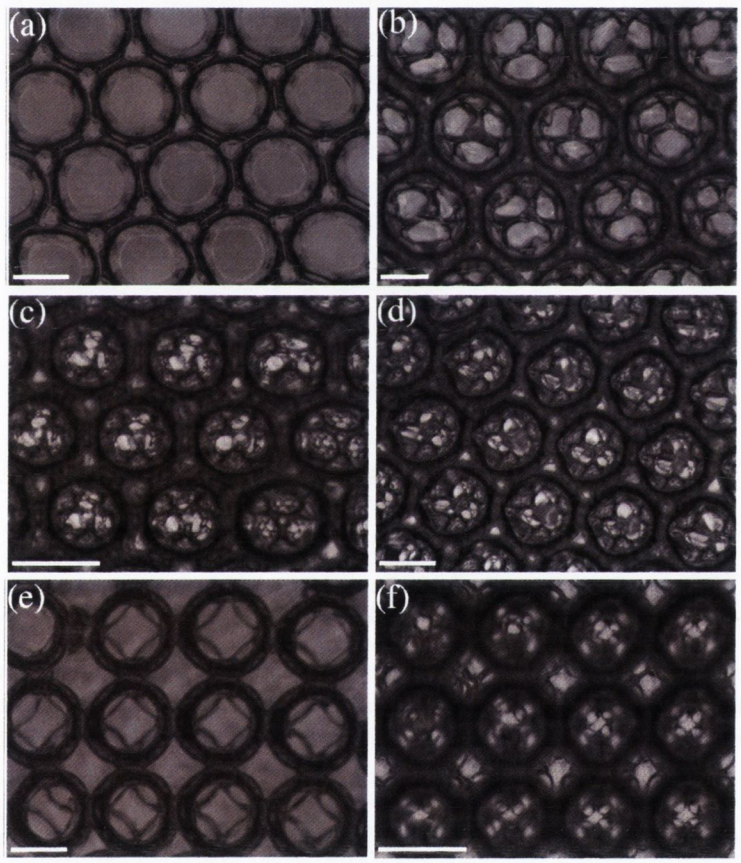


Figure 6.8: Different hexagonally closed packed stackings of monodisperse bubble layers in a confined wedge, photographed directly after polymerisation. (a) a monolayer, (b) two layers, (c) three layers stacked according to a hcp crystalline structure, (d) three layers stacked according to a fcc(111) crystalline structure (e) two square layers, (f) three layers ordered according to a fcc(100) crystalline structure. (The white bars correspond to 300 μm)

The samples show the same structures as seen in the liquid foams. The size of the samples was limited, due to the requirement of the rapid polymerisation time combined with

the production rate of the bubbles.

We generally obtained open-cell polymer foams, where the thin films between the bubbles were not present (anymore). They did not polymerise. The polymerisation of thin films present in the liquid foams was highly influenced by the presence of oxygen radicals. The oxygen radicals react with the formed polymer radicals and terminate the reaction [178]. However, it is expected closed-cell foams can be generated and controlled by reducing the presence of oxygen by using nitrogen instead of air, degassing of the solutions and increasing the rate of polymerisation. Further investigations are required to support such expectations.

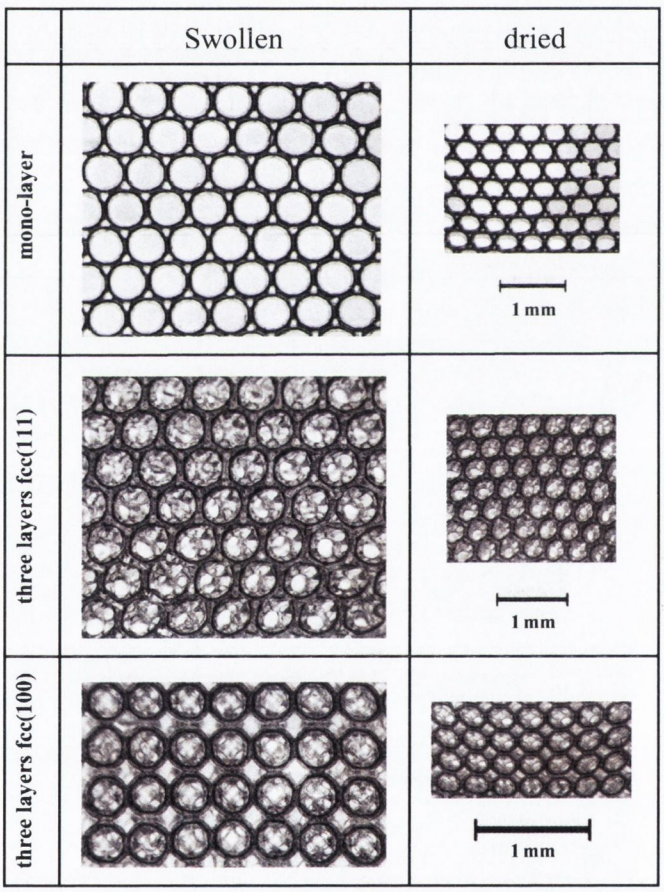


Figure 6.9: Examples of ordered polymerised foam layers in the swollen and dried state. Images in each row have the same scale.

As the foams were made of hydrogels, they could be dried and rewetted entirely reversibly (i.e. without destroying their structure) by absorbing multiple times their own weight in water. Examples of this are shown in the swollen and dried states in Figure 6.9. (Note that

during the drying or wetting stages, the samples should not stick to solid surfaces to ensure the significant change in volume does not deform or break the foam.)

Polymerised foams in the form of threads

By confining the foam in narrow tubes, bubbles self-organise into highly ordered threads whose structure depends on the ratio between the bubble size and the tube diameter. The bubbles were injected into different tubes until the moment when the bubbles could not flow anymore due to solidification. Examples of dried and wetted threads are shown in Figure 6.10 compared with the structures (2-1-1, 4-2-2, etc.) known from experiments with the liquid foams.

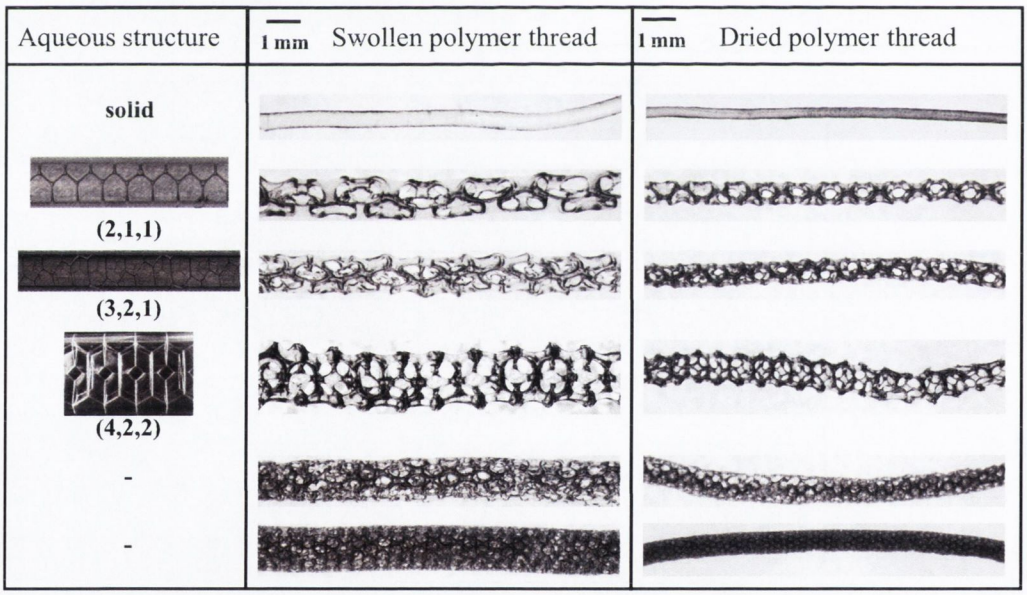


Figure 6.10: Thread-like foam structures formed by polymerising under confinement of a tube, in a swollen (middle column) and dried state (right column). Dependent on the bubble size and tube diameter different structures are generated, as can be found in aqueous foam structures as well (left column), which are labeled according the phyllotactic notation [5].

Such foam threads have the advantage that they can be woven, knitted, knotted, etc. into other meta-materials, hence providing a versatility of great promise to industrial applications. This is illustrated by the woven examples shown in Figure 6.11.

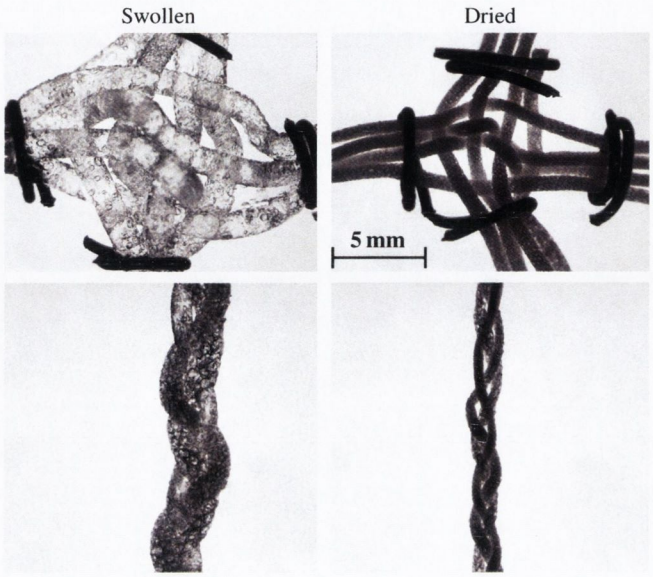


Figure 6.11: Weaving with the polymerised bubble threads. The future of solid foams? (All images have the same scale.)

6.5 Hydrogel foams as super-absorbers

We found that open-cell micro-foams made of hydrogels have super-absorbing properties, not only in terms of volume absorbed but also in terms of the time required to absorb. As demonstrated in Figure 6.12, if a drop of liquid is deposited onto the surface of such a foam, it is very rapidly (order of a second) sucked into the interconnected bubble network due to capillary forces (stage I, top row of Figure 6.12). This leads to an apparent disappearance of the bubbles due to equal refractive indices of the water and the hydrogel. The foam volume remains constant. Once in the foam, the liquid has a very large gel surface available through which it can penetrate into the gel matrix (over the course of a minute in our case) (stage II, bottom row of Figure 6.12). This stage II is characterised by an expansion of the foam and an apparent re-appearance of bubbles as they re-fill with air.

The combination of capillary suction and large surface area available for absorption results in a significantly higher absorption rate than that of a solid hydrogel. This would suggest, for example, the solid hydrogel grains currently used for super-absorbers could be replaced with hydrogel foams.

Ordered foam structures are not required for such purposes, but is expected to improve liquid invasion into the porous structure. Another promising possibility for foam generation would be to allow foam to drip from the outlet of the bubble generator such that the foam

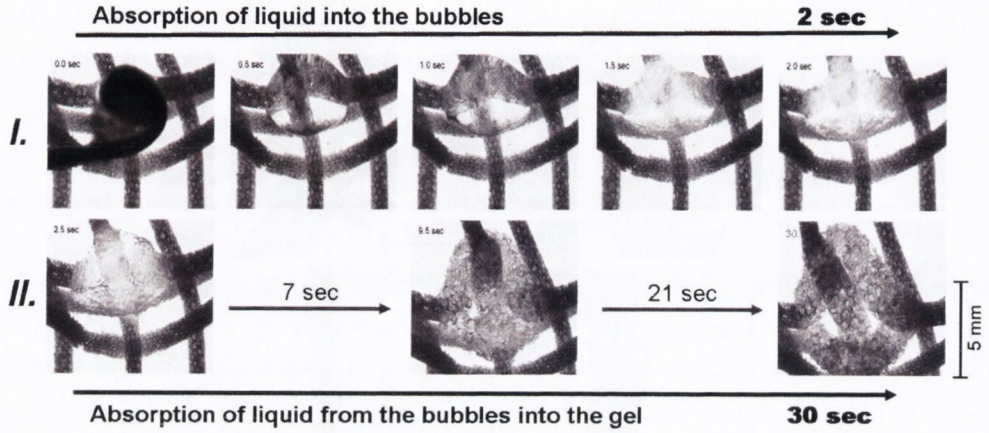


Figure 6.12: Absorption of water into a foamed hydrogels with micro-bubbles is significantly faster than into a pure hydrogel due to a two-stage process: I. Water is rapidly absorbed into the pores of the foam. II. Water is transferred from the pores into the gel via the large surface area available.

drops polymerise during the free fall and form a polymerised droplet with several bubbles inside.

6.6 Discussion

Despite the success of this feasibility study, many questions and problems must still be resolved before the method is suitable for industrial applications:

Polymer properties

The dried polymerised foam structures are very brittle as a result of the rapid polymerisation which leads to short polymer chains. Further work is required to find decisive factors to control the phase separation. If we can avoid it, the polymerisation times can be varied over longer time spans enabling a wider range of structural properties.

Scale up

The overall production rate of one single microfluidic device is very small in comparison to typical volumes required for industrial production (tonnes per day). This problem could be resolved by parallelising a large number of such devices or changing to a completely new bubble generation method, especially if the monodispersity is not a necessity.

Overall foam volumes are currently also limited by the short polymerisation times required to avoid phase separation. Within the parameter ranges presented here we can generally

only fill a volume with a maximum of ~1000 bubbles, before solidification of the first bubbles occurs.

This quick polymerisation leads to side effects such as buckling [5] (Figure 6.13) of the solidifying foam. This is due to mechanical shear caused by solidification of the foam whilst bubbles are still depositing in the confining container. If this shear is sufficiently small, the buckled structure relaxes once the confinement is removed. This is demonstrated in Figure 6.13.

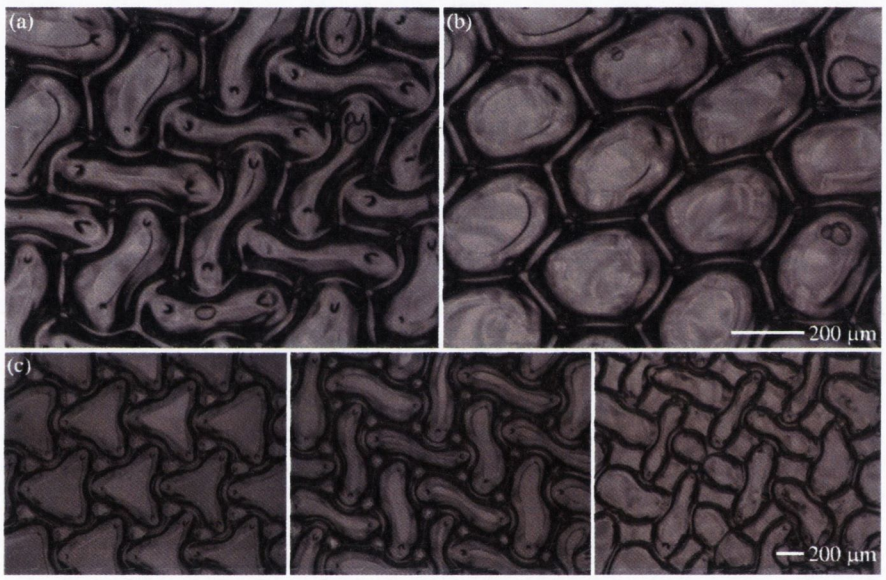


Figure 6.13: Buckling as a result of stresses exerted on the bubble structures. When the stress is released the bubbles transform from their (a) buckled shape to their (b) spherical shape. Different buckling patterns can be found based on the stress distribution in the samples (c).

The polymerisation of acrylamide as performed here releases a significant amount of heat, which could pose serious problems for the generation of large foam quantities.

Imperfections

It is impossible to make perfectly ordered bubble arrangements. In bulk volumes, perfectly ordered patches ($\approx 10 - 50$ bubbles across) are joined together by grain boundaries - as shown in Figure 4.5. The slight polydispersity of the bubbles and relaxation time before polymerisation contributes to the amount of imperfections. The larger deviation in bubble size makes that the order is less easily found and the bubbles require time to rearrange into ordered structures. Gentle shearing and sufficient relaxation time significantly reduce the number of grain boundaries, but these imperfections will remain a persistent ingredient if

producing sheets or bulk foam of industrial dimensions.

Perfection in structure can, however, be achieved easily under extreme confinement, as is the case for bubbles confined in tubes not much wider than a few bubble diameters (Figure 6.10). The generation of very long threads without defects is therefore possible if sufficient care is taken.

Liquid/solid fraction

So far we have only concentrated on making foams in the 'wet limit', which means that they contain enough liquid such that the bubbles remain spherical. Dryer foams with polyhedral cells could be achieved by either adjusting the flow rate ratio (Chapter 2) or by artificially draining a wet foam after it has been formed by applying an external pressure drop [21], as explained in Section 4.10. So far the rapid polymerisation time does not allow drainage and polymerisation of thin films has not been successful either. For both methods, foam stability is of greater importance as the time between generation and polymerisation (solidification) needs to be longer.

Solidification for exploration of three dimensional crystalline microfoams

In Chapter 4 we described three dimensional crystalline microfoams. We concluded from the top and bottom observations, observations during deposition and the repetitive occurrence of bidispersive top layers, that the foams are crystalline throughout the whole structure. Three dimensional visualisation was problematic due to foam stability. Solidification is an option to overcome this. However, solidification of the large three dimensional structures with this polymerisation method is not possible yet, since bubble generation is not quick enough in combination with the required high polymerisation speed.

The key solution to many of the issues mentioned above lies in an extension of the polymerisation time, which requires a far more thorough understanding of the parameters controlling the phase separation. In general, the radical polymerisation allows little control over the onset of polymerisation, which is set as soon as both liquids (in our case) come into contact. For this reason, the development of polymerisation routes initiated by heat or light seem highly desirable.

6.7 Conclusions

In summary, the radical polymerisation is proven to be a successful method to polymerise foams. We show that with this method the polymerisation and foam formation can be suf-

ficiently separated to produce polymerised, ordered foam. Phase separation limits us in the sample sizes, sample quality with respect to rearrangements and ordering and we are limited in the variation of material properties of the final polymerised foams. Also, thin films could not be polymerised yet.

Initial tests show that the dried hydrogel with bubbles exhibit a much quicker absorption rate than when no bubbles are present. Furthermore, the techniques explored should be made applicable to many different types of polymer, not just hydrogels. With this first successful investigation into the feasibility of the method, an entirely new toolbox has become available to produce finely controlled monodisperse polymer foams.

The applications of such materials range from absorbent polymer materials in the case of hydrogels, to providing the ability to apply much thicker coats of polymer suspensions than is feasible with current techniques. The development of absorbing, structured threads opens up new avenues of research into novel materials which can be woven into a myriad of materials, from ropes, to sheets giving a flexibility of application never before seen in such hydrogels.

This work has shown that the potential of monodisperse polymer foams is one which can be realised in a respectively easy way. Further work is needed to fully develop these techniques to an industrial scale. Further research into this highly adaptable method of material production can now focus on applications and technique rather than feasibility.

6.8 Outlook

Having laid the foundation for the subject, a much more systematic approach is required from this point forward which closely combines investigations into the chemical and physical aspects of the subject. We have explored many fundamental issues in particular the stability of foams made from monomer solutions and phase separation upon polymerisation. Here we provide some suggestions for next steps to be taken in the further development of the subject, both from an fundamental and engineering perspective.

Phase separation

As we have seen, the key problem has been the phase separation in this recipe that occurs between the polymer network and the bubbles. To optimise the manufacturing process it is absolutely essential to understand (and therefore control) the parameters which influence this separation. Better control will give the bubbles more time to order, enabling us to make larger

foam structures and giving more flexibility in the variation of material properties of the final polymerised foams. Temperature and use of a polymerisable surfactant should be studied. Simple experiments should be designed to study the behaviour of bubbles in a polymerising and cross-linking gel matrix, and to study the polymerisation of thin films. Investigations of thin film polymerisation would also provide insight into the criteria for obtaining open-cell versus closed-cell foams.

Foam stability

With the desire to enable a larger separation between foam generation and polymerisation (or solidification) also stability will become more important. Systematic studies need to be conducted to find appropriate means of stabilising foams made from monomer (or polymer) solutions. Such means can include standard surfactants (polymerisable or non-polymerisable) or surface active polymers. Of particular promise are foams stabilised by particles, which can be stable for months [179].

Mechanical properties of ordered polymer foams

In order to apply our method to a wide range of products, it will be essential to establish a range of polymer recipes and polymerisation methods. It will be important to study systematically the mechanical properties of various ordered polymer foams (sheets, bulk, threads) as a function of their structural parameters (bubble size, order, liquid fraction, etc.). This may greatly contribute to our understanding of the mechanical properties of solid foams in general, which have until now mostly been measured on polydisperse, disordered foams due to the the lack of more structured samples.

Scaling up- production rates, continuous production

Monodisperse bubble generators with a significantly higher foam output need to be designed. This may be possible by parallelising the flow-focusing principle introduced here.

Also, the continuous generation of foam threads, foam drops and sheets is required, so that bubbles are produced at one end of the process, whilst they polymerise at the other. In the case of threads, this could either be performed using a lubricant, as suggested in Figure 6.14 based on the work performed by Jeong *et al.* [180]. The authors discuss continuous generation of micro scale fibers and tubes by photopolymerisation. Another method could be having the thread freely suspended in air (as is known from the manufacture of glass fibers [168]). The radical polymerisation where the reaction occurs instantly after ingredients are mixed will be ideal for the continuous generation of adsorbent threads (Figure 6.14).

The dried hydrogel is now used as adsorption material in the form of solid grains. Another

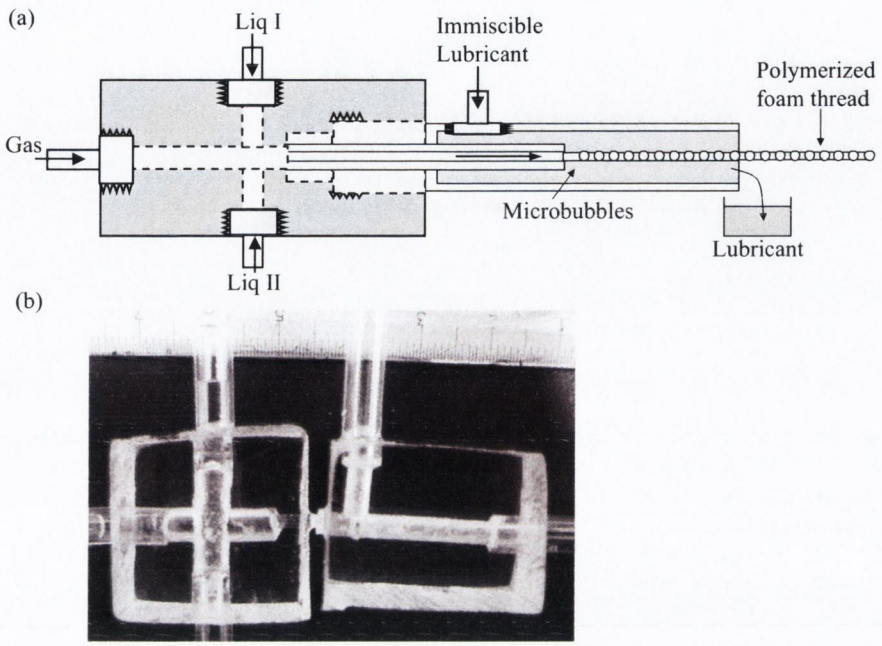


Figure 6.14: An example of a bubble generator design for the continuous generation of threads, including the addition of a lubricant; (a) the schematic overview,(b) the experimental device.

idea would be to form porous hydrogel drops such that the adsorption goes quicker. A way to obtain that would be to create drops filled with bubbles dripping from the outlet of the bubble generator. They can polymerise while they fall or they can polymerise when fall into a bath with an initiator.

Additives

The ordered foams can be 'doped' with a range of materials to provide additional features. Of particular promise would be the addition of carbon nanotubes, which could simultaneously provide conductivity and un-equaled mechanical strength [181]. Other additives could be particles to stabilize interfaces instead of surfactants [179].

In summary, the proposed method of using ordered liquid foam structures for the generation of ordered solidified foam structures shows great prospectives for future applications. However maintenance of foams is not always desired and in the next chapter we discuss the application of static charge as a method to rupture microfoams.

Chapter 7

Foam rupture by static electricity

7.1 Introduction

Hitherto we discussed the creation and characterisation of microfoams while considering the existence of foams useful. However, in many technical processes either foam formation is unwanted as it can limit technical processes or after its use it needs to break down quickly. There is thus as much research focused on creation and stabilisation of foams, as is dedicated to destabilisation or break-up of foams. A variety of methods exist to avoid foam formation or to destroy foams quickly.

Generally three kinds of methods are available to this end [182]; mechanical rupturing, thermal rupturing and rupturing by addition of chemical agents named *defoamers* or *antifoams* [1, 183]. Use of ultrasound, rotors or sprinkler systems are examples of mechanical rupturing methods [184–186]. In thermal rupturing either heat is used to vaporise the bubble or the foam is frozen and then broken [182]. Pahl and Franke [182] give a comprehensive overview of different methods, their applications and advantages or disadvantages.

In this chapter we describe a newly discovered method to mechanically break foam by charging the foam surface with static electricity. The resulting Rayleigh instability ruptures the individual bubbles. In Section 7.2 we discuss the principles of the instability which originally was found for *droplets*. We explore in Section 7.4 the effect of charge on a single *bubble* and show that it undergoes the same instability. Finally we extend this towards multiple bubbles in Section 7.5, where we show how charge can be used to break a large amount of foam, according to the same principle as a Rayleigh instability in a single bubble.

7.2 Principles of the Rayleigh instability

Lord Rayleigh was the first to theoretically describe the instability in charged *droplets* in 1882 [187], which is now referred to as the Rayleigh instability[1]. He showed that a droplet in an electric field with sufficient charge present on the surface, deforms into an ellipsoid. The ellipsoid becomes unstable such that the tip of the ellipsoid elongates and ejects charged droplets, significantly decreasing the charge on the initial bubble.

The instability can be described as a balance between surface tension forces and electric forces. The surface tension force on the droplet surface attempts to minimise the surface area, resulting in a spherical droplet. Dependent on the strength of the external electric field, charges tend to distribute on the surface of the droplet, which can be considered as a conductor, such that they have the lowest potential energy. The charge at the surface is expressed as charge density $\sigma = \epsilon_0 E$, with E representing force per charge (or electric field) and ϵ_0 the permittivity of free space ($\epsilon_0 = 8.854 \times 10^{-12}[\frac{C^2}{Nm^2}]$). The electrostatic forces caused by the charge present create a pressure on the surface which counteracts the surface tension pressure [188]. The pressure balance on the surface of the droplet can be expressed as:

$$\frac{\epsilon_0 E^2}{2} = \frac{2\gamma}{r_a}, \tag{7.1}$$

with r_a as the local radius of the droplet and surface tension γ [188, 189]. Note that in the case of a bubble i.e. with two interfaces the surface tension forces become $\frac{4\gamma}{r_a}$. When the electric field is large enough electric forces dominate and pull the droplet apart. According to the Poisson equation, charge density will depend on the curvature of the droplet [188]. The larger the curvature of the droplet, the more charge will accumulate there, which will result in a larger electric force. Once a local curvature disturbance at the surface causes the charge to accumulate, the electrostatic force will induce the droplet to increase its curvature locally even more, where more charge subsequently accumulates, creating an even larger curvature change and destructing force and so on. The electric forces will thus completely overtake the surface tension and stretch the droplet until charged droplets are ejected. By re-writing Equation 7.1, with $E = \frac{q}{4\pi\epsilon_0 r^2}$, the ratio between electrostatic and surface tension pressures of a spherical droplet of radius r becomes [187, 190]:

$$X = q^2/(64\pi^2\epsilon_0\gamma r^3), \tag{7.2}$$

[1]The Rayleigh instability should not be confused with the *Rayleigh-Taylor* instability, which concerns the instability occurring at a liquid-liquid interface, with different densities. Also it should not be confused with *Rayleigh-Plateau* instability, which is driven by surface minimisation and causes fluid columns to break up in droplets or gas threads surrounded by liquids into bubbles.

with charge q and X is named the fissility. The onset of the instability occurs when the fissility becomes greater than unity. This effect in droplets is typically a micro-scale process and has recently been captured in micrometer sized droplets by Duft *et al.* [190], see Figure 7.1.

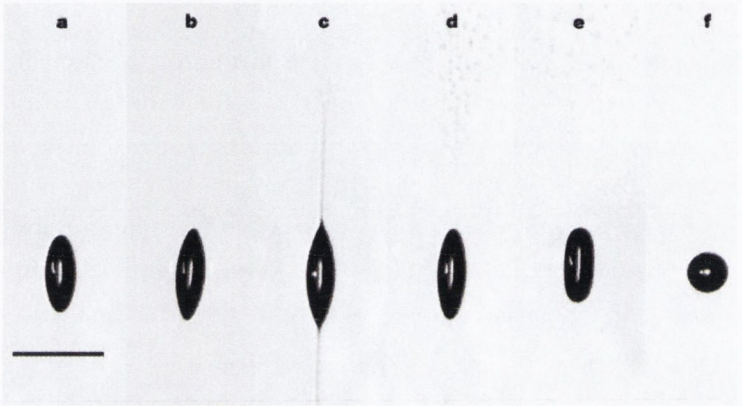


Figure 7.1: The observations made by Duft *et al.* [190] of a levitated droplet of ethyleneglycerol undergoing the Rayleigh instability. The scale bar represents $100\mu m$. The droplet becomes unstable and deforms into an ellipsoid and in picture (c) the ejection of charged droplets is visible. The droplets carry away the majority of the charge and the bubble becomes stable again (f).

The charge on the droplet accumulates at the outer surface and inspection of the fissility formula shows that the only parameter which depends on the properties of the liquid phase is the surface tension. This suggests that bubbles might undergo a similar instability, but on length scales of several orders of magnitude larger. Deformation due to gravity occurs at larger volumes for bubbles than for droplets, due to the lower mass of the bubble at equal volumes.

The dynamics of charged hemispherical *bubbles* in contact with a conductive plate was first studied by Wilson and Taylor in 1925 [191], using the bubble as a larger scale model to study the Rayleigh instability in droplets. Note that these bubbles are completely surrounded by air and just consist of a thin film which is in contact with a conducting plate, which is different from the microbubbles we have discussed so far in this thesis. It was found that in a uniform external electric field a hemispherical bubble deforms into an ellipsoid and, if the potential is of sufficient magnitude, a jet of liquid is expelled from the long axis of the ellipsoid. Taylor published almost forty years later [192] a final article where he studied the effect in greater detail, concluding that a charged liquid surface can only form a stable cone with an tip angle of 89.6°. Today the conal shape formed after deformation of the liquid

interface is known as a Taylor cone. However, Zeleny started already in 1914 [193, 194] the first experiments on unstable cones at the tip of a capillary under the influence of a potential difference. The principles of Zeleny's experiments and the Taylor cone are these days applied and investigated for fine droplet formation by electro-spraying (or electrohydrodynamic EHD spraying) as in inkjet printers and paint sprayers [188].

The main challenge in understanding the droplet formation mechanism and its analytical description is the simultaneous determination of (i) the shape of the charged interface based on the balance of the pressures and (ii) the relation between the electric field and potentials expressed in the Gauss law [195, 196]. Taylor [192] simplified the problem by assuming a fixed geometry of a cone to obtain an analytical solution for the shape of stable cone (with the tip angle of 89.6 degrees) in an electric field. To avoid limiting results to specific geometric conditions, numerical simulations are commonly used [195, 197] and also in our description of the instability in a single bubble in Section 7.4.3 we make use of computer simulations.

7.3 Experimental method

We carried out a straightforward experiment using a Van de Graaff generator to charge our bubbles and foams.

For the single bubble we used a number of conductive aluminium cups with diameters varying from 3 to 7 centimeter. These were filled with a solution of commercial surfactant Fairy Liquid at 1% volume fraction in water and 2.5% volume fraction glycerol to increase stability by limiting drainage due to an increased viscosity. A bubble was blown in the solution and inflated until the height of the bubble was equal to the cup radius, such that the contact angle with the solution was 90^o, as shown in Figure 7.2 (a). When the bubbles were larger they tend to fly off completely, like Naudin showed in an experiment for the demonstation of the effect of electrostatic pressure [198].

The macrofoams with bubbles with a diameter larger than one centimeter were generated by blowing with a needle in the solution present in a shallow cup. The microfoams were made with the microfluidic flow focusing device (Chapter 2) using a solution of 1% volume fraction of commercial surfactant Fairy Liquid in water. The dry foam samples were taken from a drained and slightly coarsened foam. The wet foam was made by direct deposition onto the conducting surface. We used either a circular or square flat metal plate, as shown in Figure 7.2 (b). No cups were used to contain microfoams, as the elevated edges of the cup prevent the foam from breaking below the edge height, as we explain later in Section 7.5.2.

The bubbles and foams are assumed to have perfectly conductive surfaces completely in

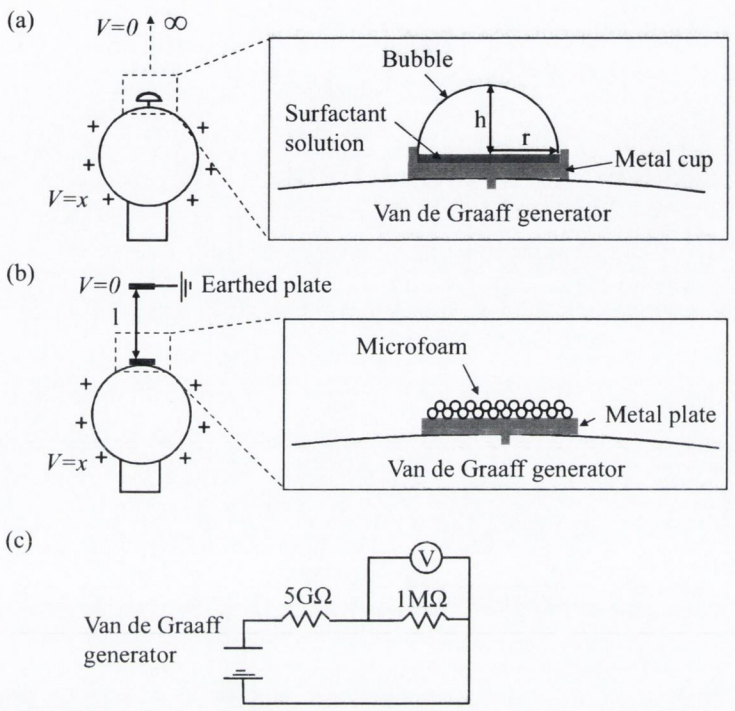


Figure 7.2: The experimental set-up. The bubble(a) or foams (b) are placed in a cup or metal plate on top of a Van de Graaff generator. The Van de Graaff generator is charged and the behaviour of the charged foam is recorded with either a digital camera or a high speed camera. With a potential divider circuit (c), we determine the voltage on the Van de Graaff generator.

contact with the liquid pool and therefore can be regarded as an equipotential with the surface of the Van de Graaff electrode.

A Van de Graaff generator was chosen rather than a high voltage DC source as potentials of up to 200 kV could easily, and safely, be generated. The voltage on the Van de Graaff generator was measured using a TDS-210 Tektronics oscilloscope, connected to the equipment using a voltage divider, as shown in Figure 7.2 (c). The voltage was measured over a smaller resistor matching the internal resistance of the oscilloscope (1MΩ). The voltage on the electrode could be varied by altering the speed of the motor driving the Van de Graaff belt. The current discharge through the 5GΩ resistor also stabilised the potential on the electrode.

We recorded the process with both a normal digital camera (15 fps) and a high speed camera (up to 1000 fps, PCO 1200hs). The data generated with the digital camera was used

to measure the height of the bubble over time and the high speed camera data was used to visualise the dynamics of the instability in the bubbles.

7.4 A charged hemispherical bubble

7.4.1 Experimental observations

Unlike Wilson and Taylor in 1925 [191] we have the availability of a high speed camera to observe the Rayleigh instability in a hemispherical bubble. We observed that below a certain potential the hemispherical bubble deformed into a stable oscillating hemi-ellipsoid. Above the critical voltage, however, the bubble became unstable and elongated until it broke. We observed two different ways of breaking up. (i) It was noticed that when the bubble was not in sufficient contact with the liquid, the bubble ruptured directly after it formed a triangular cone. (ii) When the bubble was in full contact with the liquid, the bubble could take different shapes. Figure 7.3 shows a typical sequence of images of the shapes then observed.

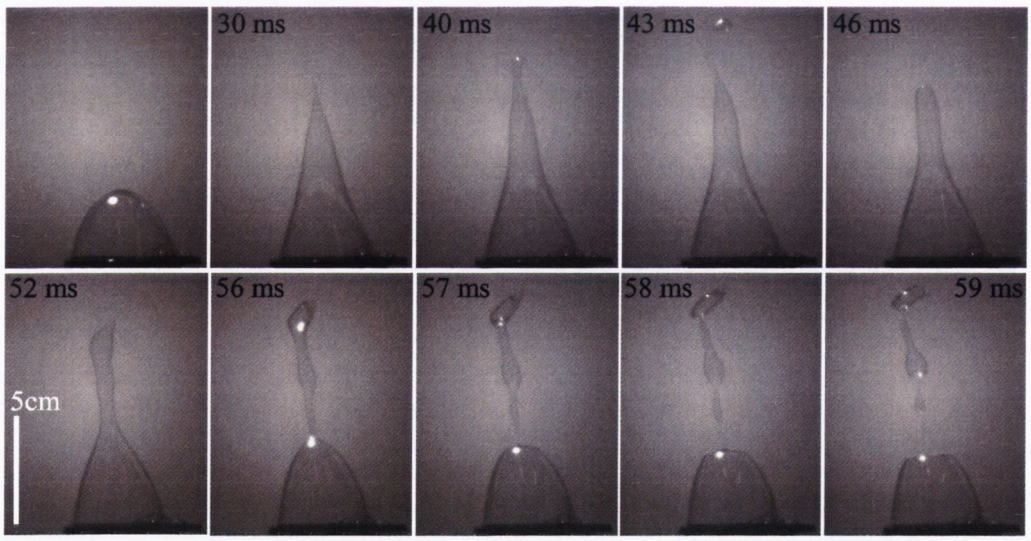


Figure 7.3: The Rayleigh instability in a charged hemispherical bubble on top of the Van de Graaff generator. Note that after 52 *ms* the formed column becomes unstable (Rayleigh-Plateau instability) and breaks off in new highly charged bubbles.

We found that the instability can be characterised by a distinct set of stages, shown in Figure 7.4. Firstly the hemispherical bubble (stage 1, Figure 7.4) deforms, developing a sharp tip along the long axis of the ellipsoid while ejecting small charged droplets (stage 2), as described by Wilson and Taylor [191]. Thereafter charged droplets of liquid are ejected from the

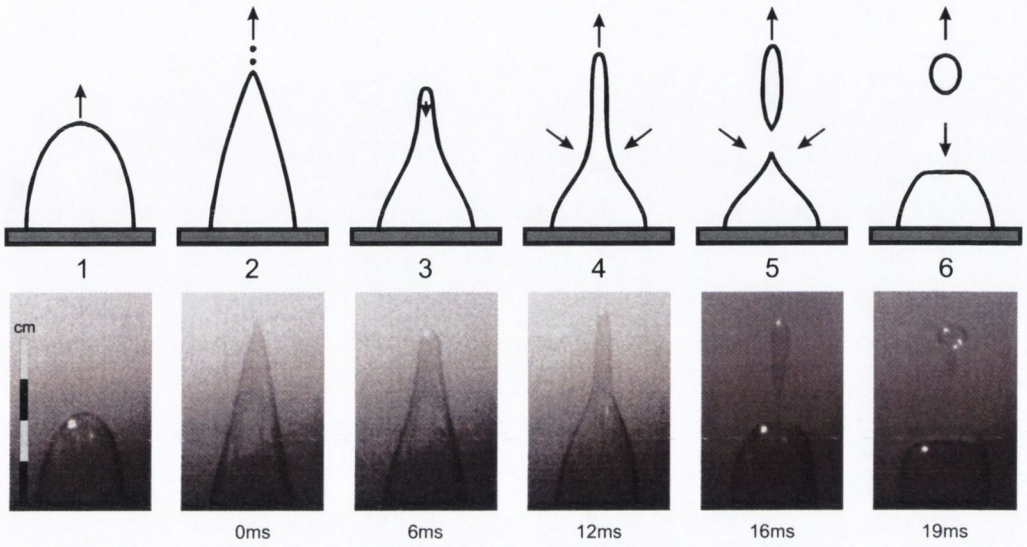


Figure 7.4: The development of the Rayleigh instability in a bubble schematically presented in different stages. (1) The elongation of the bubble results in a triangular shaped bubble (2) off which charged droplets are ejected. This is followed by a stage (3,4) where the bubble wall starts to collapse but at the same time the top of the bubble forms a long column. This column becomes unstable and collapses forming a new bubble (5), which removes itself from the initial bubble as both contain charge of equal sign. The initial bubble recovers its hemispherical shape (6).

tip of the cone, which appears to cause a collapse of the tip (stage 3). Stage 4 is characterized by an inward collapse of the sides of the cone along with growth of a cylindrical column along the long axis. We also found that this cylindrical column could form a tip and eject charged droplets. This column collapses in a Rayleigh-Plateau instability (stage 5), which results in the formation of one or more child bubble(s) (stage 6). Stages 3-6 have to our knowledge not been observed before. Note that dependent on the bubble size and voltage the behaviour of the bubbles under influence of charge changes, creating the difference between the sequence seen in Figure 7.3 and 7.4.

The bubble collapses into an ellipsoid after the ejection of child bubble(s) due to the charge on the bubble being carried away by the child bubble(s) and the radius of the parent bubble decreasing due to the volume loss. The child bubble is repelled away from the parent bubble because they have equal charge signs. The maximum height of the cylindrical column before collapse can reach several times the initial height of the bubble, as shown in Figure 7.3. From our observations, see Figure 7.3 between 52-57 ms, it appears that the cone formation repeats along the length of the column, one on top of the other without collapse of the whole column. Small Taylor cones can also occur at the tip of the column.

At higher voltages a stage occurs in which the bubble oscillates between stages 2 and 3 repeatedly, ejecting droplets from the tip of the cone.

7.4.2 Experimental estimation of the critical voltage

To find the voltage at which the bubbles become unstable, we initially steadily but slowly raised the voltage until the liquid film ruptured (within one minute). However, this gave widely varying results for the critical voltage. On longer timescales the effects of film drainage and evaporation could have played a role. So instead, we allowed the Van de Graaff generator to charge immediately above the critical voltage and found the point on the charge curve, generated by the attached oscilloscope, at which the bubble ruptured. We found that this method gave more consistent results. The rupture points can clearly be seen, in Figure 7.5, on curves of voltage against time as an abrupt drop in the measured voltage. This voltage drop is due to charge leaving with the ejected droplets due to bubble rupture.

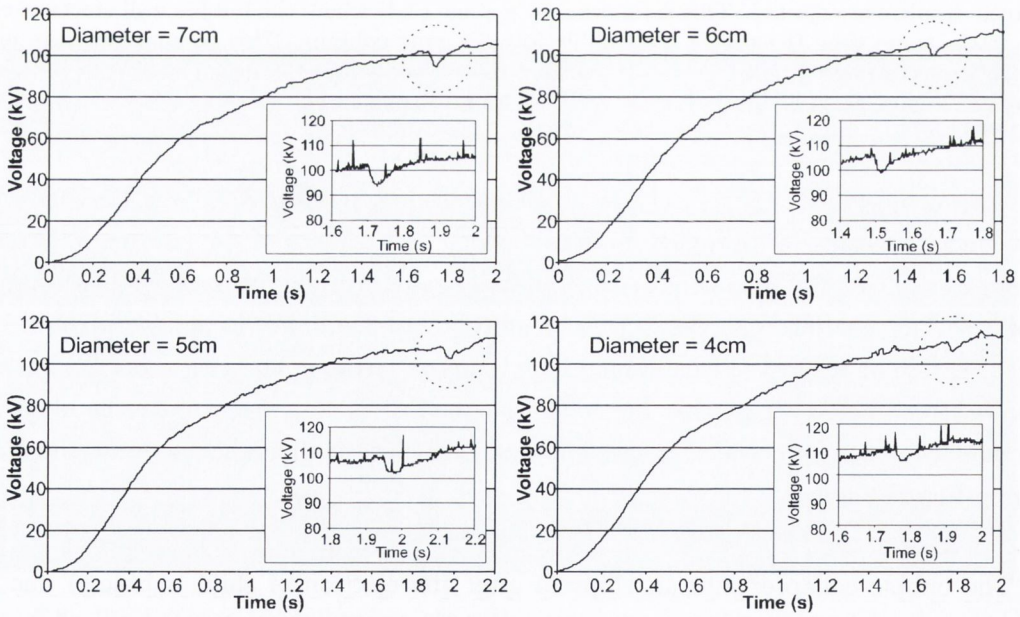


Figure 7.5: The voltage on the droplet versus time during the charging of bubbles with different diameters. The drop in the voltage corresponds to breaking of the bubble and part of the charge is taken away by droplets.

It can be seen that smaller bubbles require a higher potential before rupturing takes place, as shown in Figure 7.6. This tendency agrees with a dimensional argument proposed by Taylor showing that the critical voltage for a charged bubble is inversely proportional to

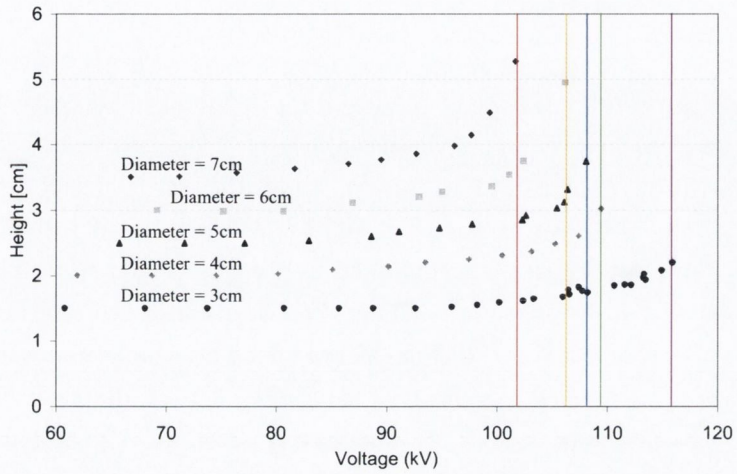


Figure 7.6: The height increase of the hemispherical bubble with increasing potential difference until rupture indicated by the vertical lines, for different sizes of bubbles. For a larger bubble less voltage is needed to break the bubble.

the initial radius. Our data shows an inverse proportionality as seen in Figure 7.7. As the data is obtained from images made at 30 frames per second the bubble edges are not sharp. This led to an large error estimation of $\pm 2\ mm$ in the estimated bubble radius.

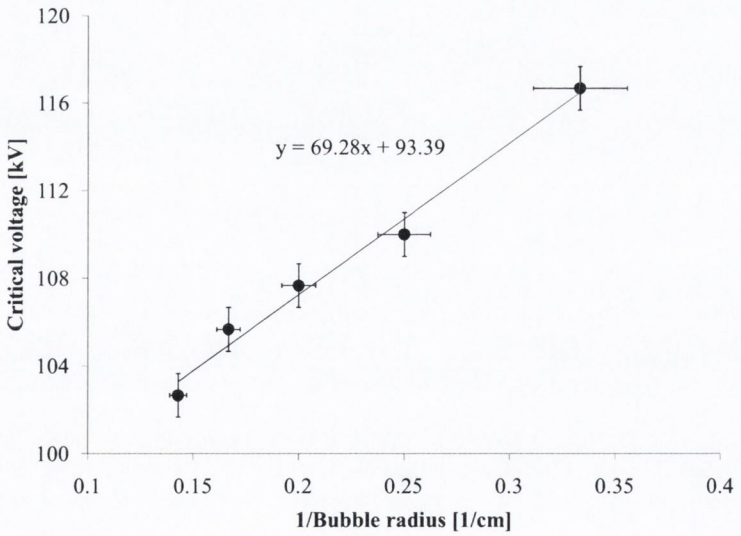


Figure 7.7: The inverse bubble radius versus the critical voltage, showing a linear proportionality as Taylor [192] argued.

7.4.3 Simulations

To gain more insights into the nature of the Rayleigh instability and particularly the process of the creation of secondary bubbles, the dynamics of a charged bubble at the instability point were simulated by a member of our group, James Hilton, using self-developed software. The software uses the 'level set method', a well known grid based technique for modeling multi-phase flows, first presented by Sethian and Osher [71]. The method provides extremely efficient and straightforward means of tracking the evolution of the interfaces within a fluid system, in our case the surface of the charged bubble. The simulations were carried out on a single hemispherical interface representing a bubble of 4 cm diameter. The surface was assigned a constant surface potential. By setting the potential, V, the local electric field E can be calculated by taking $E = dV/dn$, with n as the surface normal. With Gauss's law $\oint EdA = \frac{Q}{\epsilon_o}$, the surface charge Q, can be calculated over a small surface A. By obtaining the electric field and the local charge, the force on the surface F, can be determined using $F = Eq$. Then the new shape can be calculated based on the balance between the surface tension force and the electric force in the absence of gravity. The numerical model was validated by simulating the Rayleigh instability in a charged droplet.

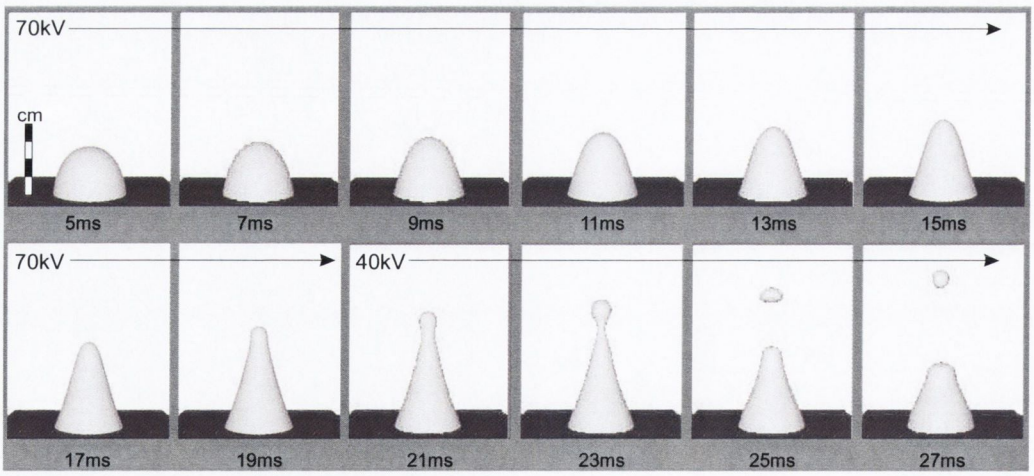


Figure 7.8: Simulation results of the Rayleigh instability in a charged hemispherical bubble using the Level-set method. The ejection of a new bubble in the simulation occurs only if there is a drop in the voltage, here dropping from 70 kV to 40 kV at time=21 ms. (Courtesy of James Hilton).

The simulations show that below a certain potential the bubble remains stable and deforms into an ellipsoid for the 50 kV - 65 kV data. However, for voltages above 70 kV the bubble is unstable and elongates along the ellipse axis into a conical shape. We did not

observe the formation of a liquid film column, such as Figure 7.4 (4), in the simulations at a constant potential. However, in the simulation we disregarded ejection of charged droplets (Figure 7.4 (2)) as only one interface is considered. It is likely that charged droplets ejected from the tip of the cone reduced the voltage instantaneously, similar to the voltage drops we measured in bubble break up (Figure 7.5). We therefore included manually in the simulations a voltage drop from 70 kV to 40 kV after the cone has formed. This resulted in the creation of a child bubble as can be seen in Figure 7.8 and as was observed in the experiment.

The numerical experiments therefore suggest that the collapse of the cone is due to ejected charged droplets reducing the voltage over the bubble, which causes the bubble to partly collapse and form a column. The column then breaks apart according to the Rayleigh-Plateau instability, based on surface energy minimisation, resulting in the formation of secondary or 'child' bubbles.

7.4.4 Discussion

Quantitatively the simulations do not match the experimental results. The voltage drop in simulations needed to induce column collapse is significantly larger than our measurements show when the whole column collapses (Figure 7.5). While the critical voltages are of the correct order of magnitude, they are lower than the estimated voltages shown in Figure 7.6. This difference could be either due to assumptions in the simulations or to the set-up of the experiment. The simulation shows the correct behaviour and is a good base for further refinement. For example the simulations could not capture yet the formation of very long columns at the tip of the bubble.

The experimental set-up should be improved in terms of its capability to store charge. Instead of using a Van de Graaff generator we could use a highly charged capacitor. The bubble could then be placed on either of the plates. We will be limited by the breakdown voltage of the medium between the plates, which depends on the gas, gas pressure, temperature and plate separation [199], as we do not want electric discharge between the plates before the bubble becomes unstable.

This work on the Rayleigh instability in single bubbles has distinct parallels with electro-spray ionisation. In electro-spray ionisation, droplets are formed by a flow of liquid through a highly charged capillary. The generation of droplets can be divided into different modes, dependent on the applied voltage, liquid flow rate, polarity and fluid characteristics [200]. The stages of typical electro-spray droplet formation for non-viscous liquids are defined by

the shape of the meniscus and jet behaviour. They include 'dripping mode', 'micro dripping mode', 'spindle mode', 'multispindle mode', 'oscillating jet mode', 'cone (short) jet mode', 'multijet mode' and 'ramified jet mode' [200–202].

Note that in the dripping mode hydrodynamics and gravity (dependent on the scale) still overrule the electrostatic forces as the applied voltage is not high enough yet to overcome the surface tension forces. The system is then comparable with the bubble generation described in Chapter 2. In this mode voltage is below the critical limit, which is not the case for our unstable single bubbles, so we can not compare the dripping mode to the modes occurring in the unstable bubbles. Of the other modes the spindle mode is most similar to our observations. The spindle mode in droplet spraying, shown in Figure 7.9 (a), shows an elongation of the liquid at the capillary, which breaks up into droplets, after which the meniscus re-shapes into a hemisphere and the process starts again. The spindle mode corresponds to a very long irregular film column collapsing into multiple bubbles of varying radii, shown in Figure 7.9 (b).

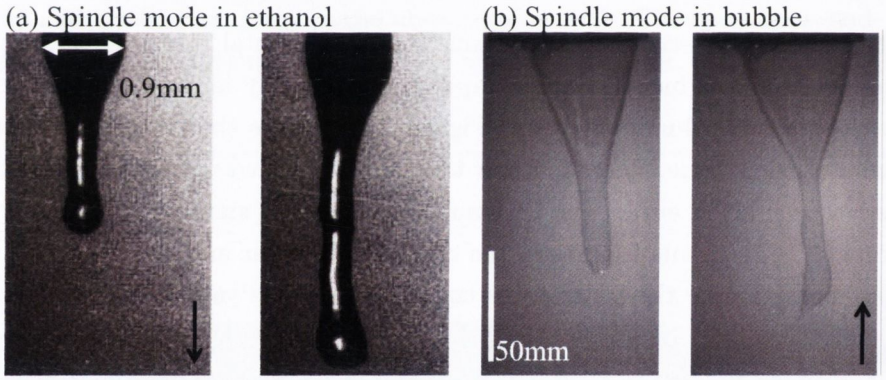


Figure 7.9: (a) The spindle mode pictured by Jaworek and Krupa [200] in comparison to similar behaviour seen in charged bubbles (b). Note that the bubble images are rotated by 180◦ for ease of comparison. The black arrows mark the direction of gravity.

In the microdripping mode a stable conal liquid meniscus is formed, from the tip of which single droplets are formed, which are smaller than the capillary diameter as can be seen in Figure 7.10 (a). This corresponds well with the formation of one single bubble from a conal shaped bubble, that appears to collapse during the process, after which the jet retracts and the process repeats, shown in Figure 7.10 (b).

A cone-jet mode presents a stable regime where a Taylor cone is formed from the tip of which regular droplets are ejected. This has not been seen in our case with the formation of bubbles. Although, as mentioned, we saw conal shaped bubbles from which droplets were ejected. No internal liquid is necessary to create droplets as long as the liquid supply through

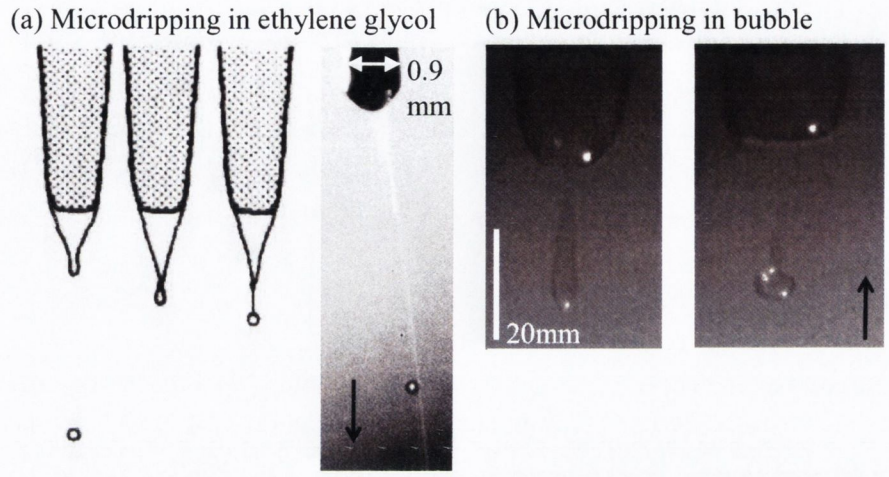


Figure 7.10: (a) The microdripping mode drawn by Cloupeau et al. [202] and pictured by Jaworek and Krupa [200] in ethylene glycol show a similar behaviour seen in charged bubbles (b). Note that the latter images are rotated by 180◦ for ease of comparison. The black arrows mark the direction of gravity.

the film is sufficient.

An idea to try in the future is to use a gas supply below the bubble and a continuous liquid supply to create microbubbles, similar to Loscertales [203] where micro-encapsulations were generated using dual fluids released from a charged capillary where the outer fluid could be polymerised.

Both the experiments and simulations described here, on the single bubble becoming unstable due to static electricity can be a macroscopic system to help the understanding of the modes discussed in electro-spraying. It is easier to observe and in the case of bubbles no internal liquid is present influencing the instability. By comparing the two systems a better understanding might be developed on the hydrodynamics involved in electro-spraying.

7.5 Break-up of foams

We have shown that a single bubble can be broken due to the Rayleigh instability with a static charge above a critical limit. Here we discuss the effect of static charge on different kinds of foam. We make the distinction between macrofoams, containing bubbles with diameters of several centimeters and microfoams, which are foams with bubble diameters below 1 *mm*. The ability to observe details at this scale are limited by the zoom capabilities of the camera.

7.5.1 Macrofoam

Figure 7.11 shows our observations when a foam structure with a height of 5 cm was placed on the Van de Graaff generator and charged. Initially the complete foam structure rose up, whereafter individually the surface bubbles underwent the Rayleigh instability, similarly as seen for a single bubble, described in Section 7.4. Charge is only present at the outer surface of the foam structure so only the surface bubbles become unstable. After a bubble breaks a new bubble is exposed to the surface and becomes unstable. This continues until all the bubbles are broken, if the charge is sufficient for each bubble to reach the critical limit to destabilise. Instabilities occurred at different locations simultaneously and are of equal charge signs. The cones formed will therefore repulse and point away from each other.

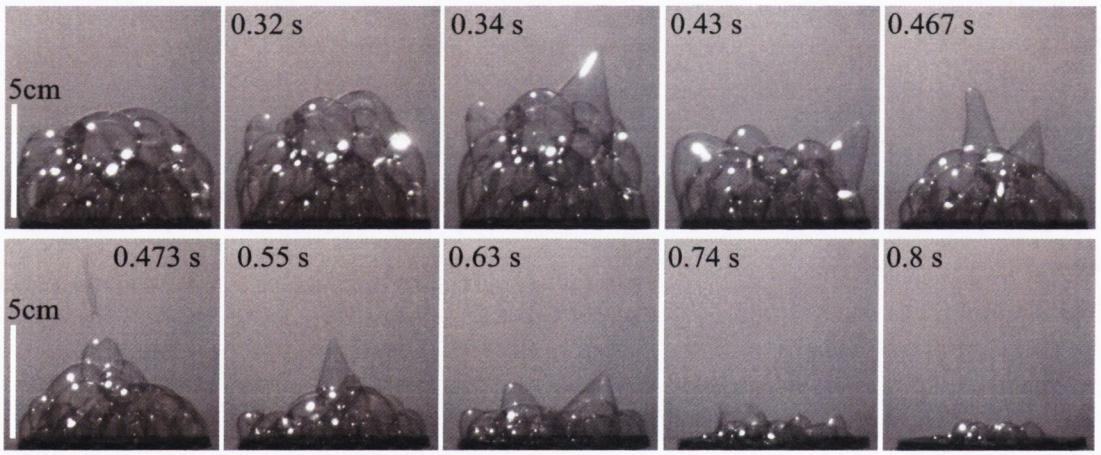


Figure 7.11: The effect of charge above the critical limit on a dry foam structure with bubble diameters of several centimeters. The surface bubbles individually undergo the Rayleigh instability and eventually break, exposing another bubbles at the surface which then undergo the same instability. This continues until the whole foam structure has disappeared.

The initial rising of the foam is comparable with the elongation of the single bubble, where the electric forces start to counteract surface tension. The foam is not completely stretched into a triangular shape. This is most likely due to the internal liquid films inside the foam structure increasing the area on which the surface tension acts but not where the electrostatic forces can act. No voltages were measured. The deformation of multiple bubbles due to electrostatic forces was mentioned by Ravaille [204], to our knowledge the breaking of foam by electrostatic forces has not been observed and studied before.

7.5.2 Microfoam

From the estimation of the critical voltage needed to break single bubbles, we found that smaller bubbles require higher critical voltages to destabilise. In the case of microbubbles the voltages therefore need to be much higher than for centimeter-sized bubbles. Due to the severe drainage of charge when using the potential divider, charge on the Van de Graaff generator was too low to break the microfoams. So here we will not have data on voltages present while carrying out the experiments. The bubble sizes are so small that detailed observations with the available high speed camera and lenses were not possible.

We performed four different experiments. We used wet and dry foams and a circular and square conductive plate to place them on the Van de Graaff generator. Note that we did not use cups to contain the foam. As we observed in the macrofoams instabilities occur only at the surface, where the charge accumulates. With micofoam in a cup, once the foam is broken and its height reaches the cup edge, charge will only accumulate at the edges of the cup and not at the foam surface anymore. The charge prefers high surface curvatures, which is at the edge of the cup. Instabilities can not occur as not sufficient charge is present at the foam surface and the remaining foam will not break.

Figure 7.12 illustrates the general observed behaviour of dry microfoam (average bubble size 800 μm) over time and under the influence of charge on a circular plate. Initially, instabilities occurred everywhere on the surface of the foam. The precise details of the sequence of breaking are not known yet. Note that in experiments with a monolayer of bubbles with a bubble diameter of $\sim$1 cm we observed that when one bubble broke, a cascade of breaking bubbles occurred around the bubble. It appears the surrounding bubbles locally obtained a higher potential, which then caused them to break. This seems contradictory as we previously saw a potential drop when a bubble breaks with the charge taken away by droplet formation. On the Van de Graaff generator the surface will be immediately recharged. It is possible charge accumulates at the surrounding bubbles due to the temporary deformation from the collapse of the bubble. Liger-Belair [89] described this temporary deformation (3 milliseconds) after collapse of a bubble in a monolayer creating a 'flower shape', driven by surface tension where the bubbles surrounding the bursting bubble deform towards the cavity then the point effect accelerates charge accumulation tending to rupture the bubble. It is possible an effect like this and a resulting cascade of breaking bubbles can occur as well at the surface of the foams, but this needs to be further explored in the future.

Initially, because instabilities occurred everywhere the foam volume shrank relatively quickly. At the stage between 13 and 20 seconds (see Figure 7.12) the foam formed a global

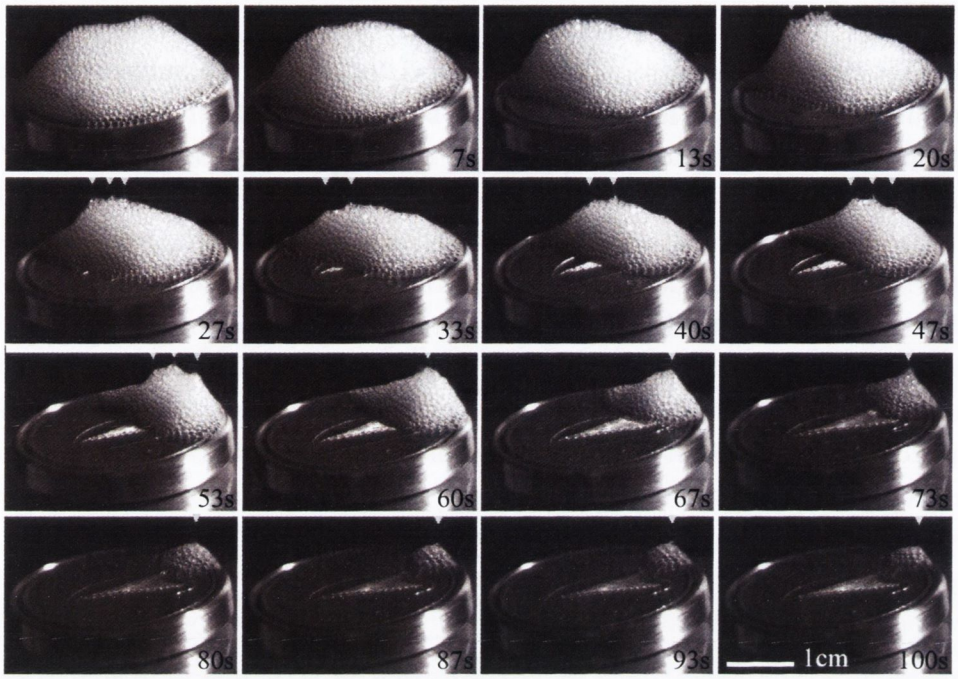


Figure 7.12: The effect of charge above the critical Rayleigh limit on a *dry* foam structure with bubble diameters of below 1 *mm* on a *circular* metal plate. Initially the instabilities occur everywhere on the surface of the foam and the foam structure shrinks uniformly and relatively quickly. After 13 seconds, seemingly randomly, global peaks are formed and only there the bubbles can undergo the instability. The triangles at the top of the images mark these peaks. In time only one peak remains.

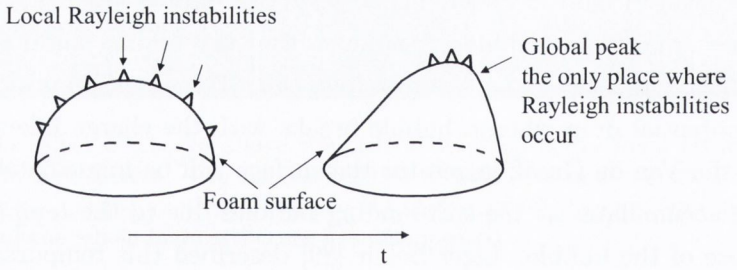


Figure 7.13: The difference in the locations of the instabilities for dry foam in time. Initially Rayleigh instabilities occur in bubbles all over the surface, in time the foam deforms creating a peak where the instabilities occur.

peak, as illustrated in Figure 7.13. This was where the bubbles migrated to and where instabilities occurred, as charge accumulates at these peaks. Depending on the size of the peak at different places bubbles could undergo the Rayleigh instability and liquid was seen to be deposited onto the Van de Graaff generator beside the charged plates. The places where

instabilities occurred are marked as triangles at the top of the images in Figure 7.12. In time the peaks decreased in size and number of peaks decreased until one remained. The estimated rate of rupturing is 0.4 l/hr with an area/volume ratio of 2.1 m^{-1}. It took 100 seconds with use of charge to break down the foam, while break down due to coarsening of the same volume of foam took 2 hours.

It was seen that after 80 seconds the water and bubbles were ejected from the foam, instead of just the bubbles becoming unstable. It is suspected that the potential is high enough for the water itself to undergo the Rayleigh instability forming a Taylor cone containing remaining bubbles.

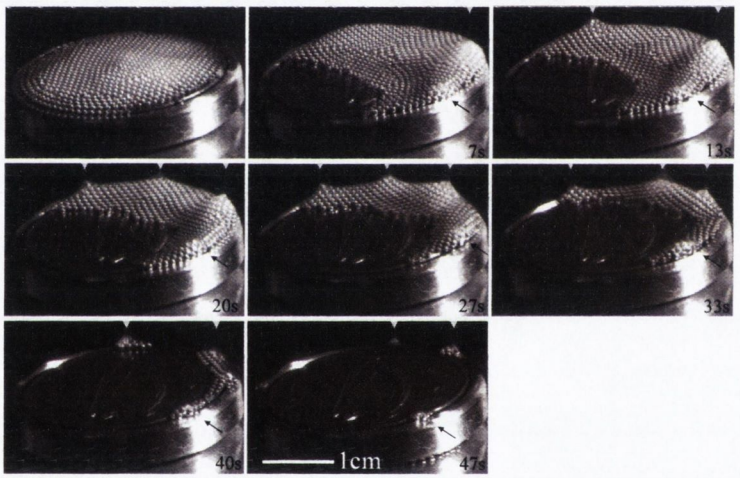


Figure 7.14: The effect of charge above the critical Rayleigh limit on a *wet* foam structure with bubble diameters of 800 μm a *circular* metal plate. From the start of charging the foam, local peaks are formed where the bubbles become unstable and break up.

To gain more details on the effect of liquid fraction we used the same set-up with very wet foam, of an estimated liquid fraction of 36%. We carried out experiments with several layers of wet foam. In Figure 7.14 the effect of sufficient charge on 3 layers of wet bubbles is shown with an average bubble diameter of 800 μm. Different than for dry foams, local peaks were now formed from the onset of charging where bubbles underwent the instability. They formed only at one side of the plate. This is possibly because once a peak is formed it attracts bubbles into the curved interface. Because there was not enough foam to cover the whole plate, foam moved to one side and this enabled more peaks to form. The amount of peaks decreased in time along with the decrease in foam volume.

Many bubbles were ejected with the liquid, which fell on the surface of the Van de Graaff

generator beside the charged plate containing the foam. We conclude that the liquid fraction influences the way the foam adapts its geometry to the charge present at the surface, which is the highest at the largest curvatures. With a higher liquid fraction the geometry deforms more easily into local peaks. The bubbles migrate towards the peaks as due to buoyancy forces they like to go to the highest point of the interface curvature and at the tip of the peak the bubbles undergo the instability.

The location of the local peaks can be influenced by the shape of the conductive plate used. With the use of a square plate the corners of the plate induce the peaks to be formed there. At the corners of the square plate the electric field is stronger. Figures 7.15 and 7.16 show the effects of the use of a square plate on wet and dry foam.

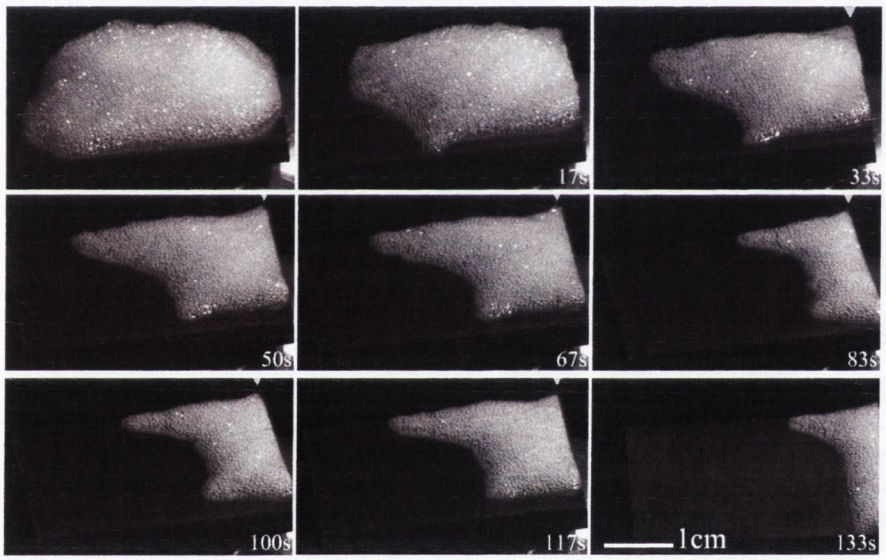


Figure 7.15: The effect of charge above the critical Rayleigh limit on a *dry* foam structure with bubble diameters of below one mm on a *square* metal plate. As with the dry foam on a circular plate, initially bubbles become unstable everywhere at the surface and in time local points are formed where bubbles become unstable and break. In the case of a square plate, charge likes to accumulate in corners and the peaks are formed at the corners of the square.

The dry foam (Figure 7.15) showed initially local Rayleigh instabilities, but after 33 seconds the foam formed a peak at one of the corners of the square where bubbles underwent the instability. Wet foams (Figure 7.16) showed formation of instabilities immediately at the tip of the corners. Occasionally bubbles broke at the surface, as is pointed out in Figure 7.16 zoomed in on the surface.

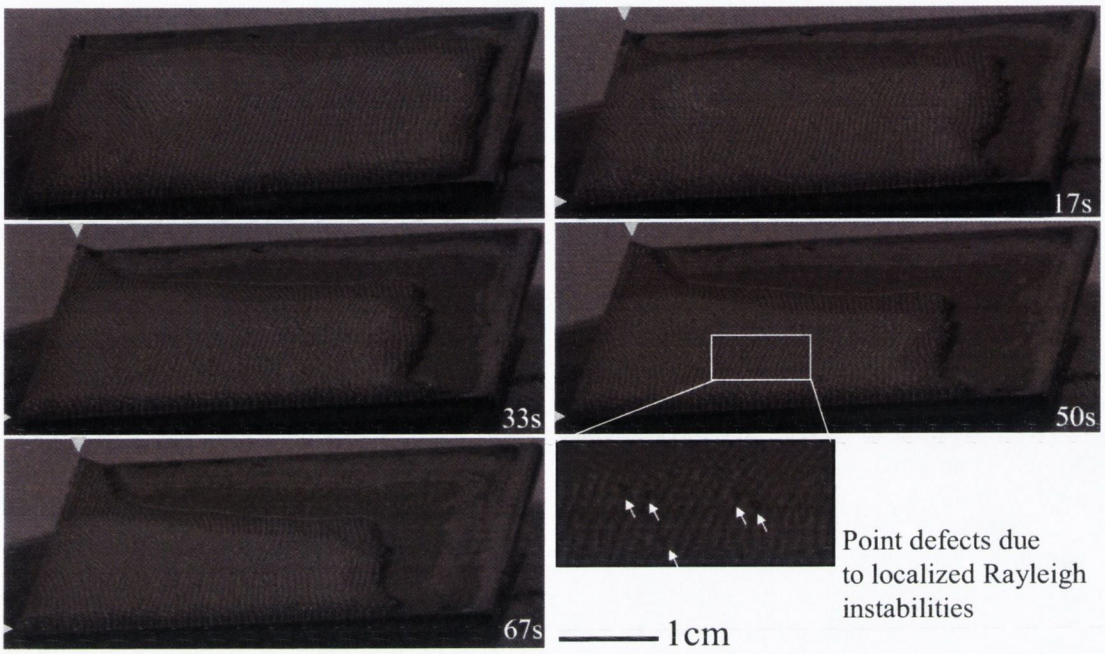


Figure 7.16: The effect of charge above the critical Rayleigh limit on a *wet* foam structure with bubble diameters of 400 μm on a *square* metal plate. From the onset of charging, the bubbles break at the corners of the square metal plates until they are all gone. Occasionally bubbles break at the surface as is pointed out in the picture zoomed in on the surface.

7.5.3 Discussion

These initial experiments show that it is possible to break foams with static electricity. No potential measurements could be performed with the current set-up. This could be solved using the set-up described in Section 7.4.4.

When the foams have a higher liquid fraction, the system can deform to form peaks where charge can accumulate. This can be seen in magnetic fluids as well [188] under the influence of surface tension and magnetic forces, where peaks can arise over the whole surface. In electrospraying the 'multijet mode' (or multiple jet mode) shows similarities with our observations, see Figure 7.17, with the occurrence of multiple jets at the perimeter of the capillary with a further flat liquid meniscus [200].

The number of jets depends on the applied voltage [200]. In foams, the maximum number of peaks we have observed so far is four always located along the plate edges. Due to the curved elevated surface bubbles will migrate towards the peaks. Breaking bubbles at the peaks seems to occur less effectively. Sometimes complete bubbles fly off and liquid droplets can be seen falling on the surface of the Van der Graaff generator. A situation can arise where the bubble acts as an internal cone and liquid at the surface becomes unstable and forms jets

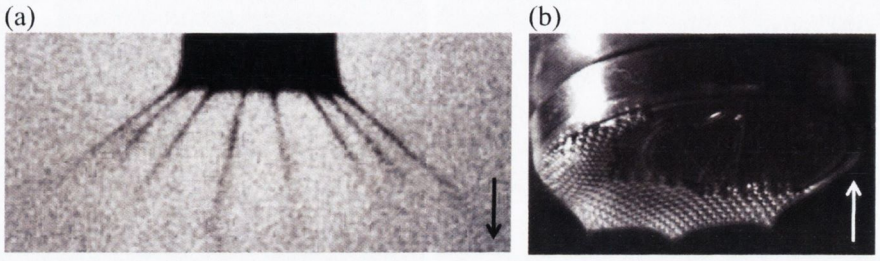


Figure 7.17: (a) The multijet mode in ethanol at the outlet of a capillary (outer diameter 0.9 mm) [200] is comparable with (b) the multiple jet formation in critically charged wet foam at the edges of a circular conductive plate (diameter 2 *cm*). The arrows mark the direction of gravity.

similar to the cone jet mode described by Chen *et al.* [205] when spraying with an internal static liquid and external liquid. The internal static liquid can be compared with the bubble forming a cone over which the external liquid, or in our case the surfactant solution, can flow and form unstable liquid jets which eject charged droplets. It is possible the applied voltage could be high enough for the liquid to become unstable. This can be seen if we compare the voltages for distilled water which start with the spindle mode around 10 kV [200], with the voltages we measured in the single bubble experiments at approximately 10 times higher. This will need to be explored in more detail in future research.

7.6 Conclusions and Outlook

We have studied the Rayleigh instability in bubbles and showed with sufficient charge present a similar mechanism comparable with the Rayleigh instability in droplets occurs, but at a much larger scale. For the first time the instabilities in bubbles were observed with a high speed camera. We observed new stages in the instability not observed before by Wilson and Taylor. The dynamics of charged bubbles appear to be almost identical to early electro-spraying modes. This break up is of crucial importance to the electro-spraying process and we suggest that charged bubbles can be used as a macroscopic model for understanding the break off of liquid droplets in the early stages of electro-spraying. The system also serves as an excellent demonstration model for the interplay of surface tension and electrostatic forces on a macroscopic level.

The set-up should be improved further to carry out more accurate measurements, especially as this method for foam breaking has the prospect to be further developed into a novel industrial scale method. It appears to be a reasonably quick and easy method, in the sense that the foam only needs to be placed in the right environment to completely rupture.

For the actual development into an industrial application more insights need to be gained into how to optimise the charge density over the foam such that the foam breaks quickly. The geometry of the conductive plates should be adapted such that the charge can be divided optimally over the surface to break the foam quickly. We showed the liquid fraction influences how the instabilities occur and therefore also needs further attention. Further work is also required to explore if instabilities occurring randomly all over the surface are indeed beneficial over local peaks for quick rupturing of the foam. The most efficient balance between drainage time and foam breaking times also needs to be found.

The properties of the foams can affect the performance of the method as well. For example, in electro-spraying the liquid conductivity and viscosity appear to have a large effect on the different modes achieved [201]. Many other questions arise regarding the industrial application of this method. For further rupture optimisation we need to find out which mode breaks the bubble the quickest. If liquid needs to be recovered applying the method, we need to consider how much this yields in our case. If the method could be used to separate minerals from a foam captured during flotation process we must think about how well the system would work with particle in the foam.

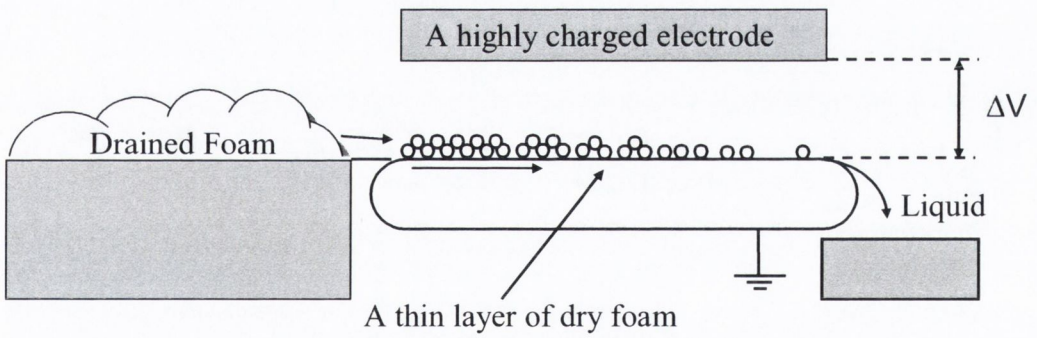


Figure 7.18: Sketch of a possible industrial set-up of the foam breaking device based on the application of the Rayleigh instability on foams.

In Figure 7.18 a sketch is given of a suggested industrial set-up. The foam can be transported on a conveyor belt into a localised electric field for the necessary amount of time to break all the bubbles. The localised field is generated by placing a highly charged plate above the conveyor belt, which itself needs to be conductive but remains earthed. This is different from the set-ups we used in the experiments described previously, where the foam was placed on the charged plate, with the earthed plate located above it. The principle will remain the

same, charge will collect at the surface of the foam, foam becomes unstable and breaks if the charge is sufficient. The liquid is at the end of the belt collected for reuse.

Overall there are good prospects for development of this subject into an applicable method to break foam.

Chapter 8

General conclusion and outlook

The work presented in this PhD thesis has revealed new insights into crystalline microfoams. Bragg and Nye in 1947 used the crystalline microfoams as a comparison to crystalline atomic structures. However the crystalline microfoams themselves show many interesting features, which have only recently become of interest for further study with the easy generation of equally sized microbubbles, using the microfluidic flow focusing technique and better imaging techniques.

With the found linear relation for our designed bubble generator between the bubble diameter, the orifice width O_w and ratio of the gas and liquid flow rate Q_g/Q_l to the power of $\sim$ one third we can generate each bubble size wanted. Orifice length, viscosity in a flow rate controlled device and surfactant choice are shown not to play a role in the determination of the bubble size. The effect of interface mobility can not be ruled out yet as the experiments with dodecanol were inconclusive due to the large surfactant concentration present. For future designs, the geometry of the bubble generator appears critical as we found for our design a hitherto unknown 'squeezing regime' at low liquid and gas rates regime, hindering the microbubble generation. The dimensions of the inlet channel have shown to play a role. This will need further investigation for example with the use of simulations as in this way, different parameters can be easily isolated and their influence can be identified. This could also be used to design the most optimal bubble generator according to the wishes of the user.

The created microbubbles spontaneously and quickly form crystalline microfoams. They demonstrate unique optical properties. Observed fractal patterns were used with the application of computational ray tracing techniques to show bubbles order in the crystalline structures fcc(111), fcc(100) and hcp. These ray tracing techniques, a 2D ray path visualisa-

tion and a 3D commercial animation program are shown to be of great help in the derivation of the exact geometric dimensions of foams. Optical foam patterns give illusive images of foams, which are therefore often wrongly interpreted. For each experimental set-up and foam geometry, new interpretations need to be performed, due to the large dependence on the light source dimensions and position as well as the camera position and settings. The method could be extended to analyse foam images by different illumination methods of the samples or complicated foam structures generated with other software dealing with generation of complex foam structures.

The microfoams can be forced into different crystalline structures based on the orientation of the top layers by confining them. This could be of interest for further studies where the influence of crystalline structure of foams is studied for example in acoustics, (polarised) light, rheological properties and drainage behaviour. Beside wedges and parallel plates also confinement with side boundaries should be tried, for example with hexagonal or square sides or by creating a wedge with its opening angle pointing down different structures can be made.

The creation of ordered dry foams was until now not straightforward. However we showed by drainage of the crystalline microfoams, easily dry ordered foams can be made, suitable for further exploration of properties of bulk ordered dry foams. The dynamic transition from the dry to wet structures will also be of fundamental interest for further exploration.

The evolution of crystalline microfoams exposed to the air showed a remarkable fast disappearance of the top layer, shown to be dependent on the number of layers, combined with a sequential occurrence of bi-disperse top layers. This effect in itself is interesting and need further investigation. Also because the effect can be followed for up to 6 layers. However for the study of the crystalline microfoams it is not desirable. For example, together with coarsening, it obstructs application of 3D imaging techniques such as MRI scanning, which is now not possible due to long imaging time related to the high spatial resolution needed. The optical patterns and terraces at the bottom of the sample suggest 3D order throughout the entire structure, as well as the repeated occurrence of bidisperse layers. Solidification of the spontaneously formed crystalline microfoams may enable visualisation with long imaging times.

With the knowledge gained on the formation of ordered *liquid* foams, we formed for the first time solidified crystalline microfoams by polymerisation, consisting of several layers or threads of wet foam created under confinement. This shows great prospects for the future

where crystalline liquid foams can be a template for development of ordered solid materials. Polymerisation of foams showed for these ingredients as well some limiting factors, mainly the phase separation which forced us to use fast polymerisation rates to be able to polymerise the foams. This limits the variability in polymer characteristics like mechanical strength when being dry or sample size with the current bubble generation speed of several hundred bubbles per second. The foaming of the super absorber shows great prospects in the further increase of absorption speed of the material. The polymerisation speeds needed so far do not allow for large samples to be made such that spontaneous ordered samples can be made. Phase separation needs therefore to be understood. However, the foamed polymer samples show better absorption rates compared to the bulk solid samples, a great potential for foamed polymers for future applications.

We used for the polymerisation a recipe of a superabsorber, but other recipes can be used and the technique is expected to also be applicable to metal foams. Therefore adaption will be needed for managing the high temperatures needed for melting the metal as well as the high surface tensions which could hamper bubble generation.

We developed a method to extend the lifetime of the microfoams by polymerisation, but the presence of foams are not always desired. We have shown here that static electricity can be used to significantly decrease the lifetime of the foam. First described for droplets by Lord Rayleigh [206] and later shown for semi-hemispherical bubbles by Taylor [192] bubbles undergo an instability and break if charged high enough. This instability in bubbles by itself shows many interesting features for the first time observed with the high speed camera. Different stages in the instability show similarities with the different modes present in electro spraying, where the dynamics are still not fully understood. The bubbles can be of help for further clarification of the dynamics.

The results of this study showed the potential of the application of static electricity for development into a foam rupturing method. The set-up needs to be adapted to reach higher potentials and investigations need to be performed on the most optimal geometry of the carrier plate such that the charge used is most efficient to break individual bubbles of the foam.

In this thesis we have focused on the properties of the crystalline microfoams but its occurrence itself still leaves many questions. From literature research it becomes very clear the microbubbles are unique in their spontaneous and fast ordering into familiar crystalline structures. Templating has shown in simulations and experiments to have some effect on the ordering but is not the dominating factor, neither is the deposition rate. Surfactant choice

and ingredients are found not to have a profound influence. The wetness, spherical shape and impact of new bubbles arriving into the structure are expected to play a large role in the ability of the bubbles to rearrange. Hydrodynamics of liquid flowing out of the structure and stresses could be other factors influencing the ordering of the microbubbles. These are the factors to be considered in future research on the reasons as to why or the mechanism by which the microbubbles find their order so easily. Further simulations and experiments need to be performed. They could involve the use of floating equally sized hard sphere particles in the size range of the used bubbles. Freezing of the final structure and cutting it afterwards would enable observation of the occurred (dis)order.

Summarising, the main experiments and simulations suggested for the future are:

- Exploration of the role of the geometry of the bubble generator on the bubble generation, combined with simulations.
- Design experiments combined with simulations testing the effect of hydrodynamics, stresses, impact of arriving bubbles in the structure on the occurrence of order in crystalline microfoams.
- Explore the occurrence of order in floating beads of sizes equal to the microbubbles used in this thesis.
- Three-dimensional visualisation of the crystalline microfoams, for example with X-ray tomography or two-photon microscopy.
- Solidification of crystalline microfoams of more than 5 layers.
- Use of different materials for the solidification to create a diversity in foamed materials with its own unique properties, for example metal foam.
- Explore more methods to force microbubbles to order in specific crystalline structures, for example by the use of side boundaries and extend the search for other crystalline structures with the help of variations of confinement.
- A static study of the structural transition of the wet ordered foams to dry ordered foams. This can be extended to the dynamic transition from wet to dry foams during drainage.
- Simulations on the spontaneous re-organisation of the top layer bubbles during its diffusion.

- Simulations and more controlled experiments should be performed on the Rayleigh instability in single bubbles, especially in comparison to the dynamics of the instability in droplets.
- Create an improved version of the set-up to break foams which can more easily be scaled up to industrial scales, for example using a capacitor. Thereby investigations need to be performed to find the most optimal shape of the carrier plate to distribute the charge evenly over the foam surface.

Overall in this thesis work we have shown some unique properties of crystalline microfoams. It leaves many questions to be answered and areas to be investigated in future research. However, the findings so far have already shown opportunities for future applications and may crystalline microfoams continue to bear more 'bubbles' in the future!

CHAPTER 8 GENERAL CONCLUSION AND OUTLOOK

Appendix A

Simulating and interpretating images of surface Plateau borders with computational ray-tracing techniques

In this appendix we discuss the analysis of optical images of a surface Plateau border or liquid bridge between two plates by applying the computational method proposed in Chapter 3. We relate the geometry of the cross-section of a liquid bridge to its imaging properties in a defined computational set-up which contains an infinite, diffusive light source where we consider only the parallel light. A range of stripe patterns is observed, which allows us to establish mathematical relations between the patterns and the geometry of the bridge by the use of the 2D ray-path visualisation program, described in Section 3.3.3.

A.1 Surface Plateau borders

In many experiments foams consist of a single layer of bubbles only ('quasi-two dimensional foam' or 'Hele-Shaw configuration'), consisting of thin films, which meet in so-called *Plateau borders* or are attached to the plates by *surface Plateau borders*. The surface Plateau borders then form *liquid bridges* which connect both glass-plates. The shape of these bridges (and therefore their optical properties), depends on the liquid content of the foam and the wetting properties of the plates. An illustrative example of such a foam with a non-transparent liquid phase is shown in Figure A.1.

The same geometries and optical challenges are encountered in the study of rivulet insta-

bilities [207], in which a narrow stream of soap solution descends under gravity between two narrowly spaced, vertical glass plates.

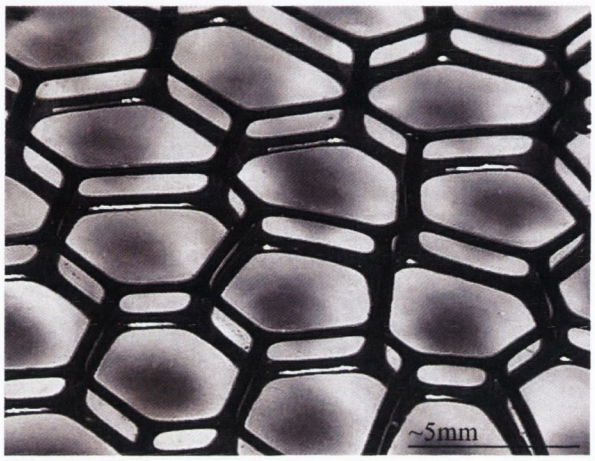


Figure A.1: An illustrative example of a monolayer of non-transparent foam between two glass-plates with 2 *mm* spacing. (Courtesy of E. Janiaud, [208])

We focus initially on the optical properties of the liquid geometry, neglecting the contribution of the glass plates, to simplify the analysis and presentation of the results. We show then that generally the influence of the glass plates is negligible in many cases.

A.2 Experimental set-up

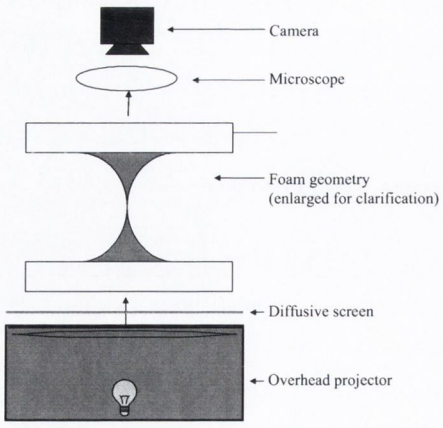


Figure A.2: A sketch of the experimental set-up to observe a liquid bridge using transmitted diffusive light and a microscope.

As sketched in Figure A.2, in our set-up an overhead projector with a diffusive screen

transmits diffusive white light through the liquid bridge, which is imaged through a microscope (magnification 1-3x, $\approx$ 20 *cm* away from the foam) using a digital camera (Coolpix Nikon 4500). Where feasible, we compared computational images qualitatively with experimental ones. The liquid bridges were made vertically between two glass plates, with an aqueous solution with Fairy Liquid (1% volume fraction).

A.3 General description of the geometry and patterns

Here we give a general description of the observed patterns of a liquid bridge dependent on the geometry for a set-up with an infinite light source and observation of parallel light source. In the Sections A.4 and A.5 we discuss in more detail the origin of the patterns and create if possible mathematical relations between the optical patterns and the geometrical dimensions of the liquid bridge.

The left column of Figure A.3 shows the various cross-sections of the liquid bridge for increasing liquid fraction ϕ.

At low liquid fraction (*Regime I*) surface Plateau borders are connected by a thin film. Assuming that the soap solution wets the plates perfectly, the Plateau border boundary is made up of two quarter-arcs of circles [5], whose radius of curvature R is determined by the pressure difference ΔP between the gas and liquid (also named capillary pressure) given by the Young-Laplace equation in 2D:

$$\Delta p = \frac{\gamma}{R}, \tag{A.1}$$

where γ is the interfacial tension. In this regime, the width of the liquid bridge is given by $W = 2R$ (neglecting the film thickness). Beyond a critical liquid fraction the Plateau borders merge, marking the beginning of *Regime II*. The gas/liquid boundaries now form semi-circles, whose radius R is set by the plate spacing S as $R = S/2$. In this regime the Plateau border width does not scale linearly with the Plateau border curvature. The second and third column of Figure A.3 show the corresponding computational images (3D Studio Max), with and without glass plates, back-lit with an infinitely large diffusive light source. One observes three symmetrical pairs of black stripes, which we number 1-3 according to the order of their appearance with increasing liquid fraction (See Table A.1). We label the *inner boundary* B_i of the stripe the side which is closest to the centre of the liquid bridge. The other side is called the *outer boundary* B_o. See Figure A.4 for the detailed labeling scheme.

In Regime I one pair of stripes (*Pair 1*) is present. The outer stripe boundary is clear and sharp, whilst the inner boundary faints towards the centre of the liquid bridge. As a result of

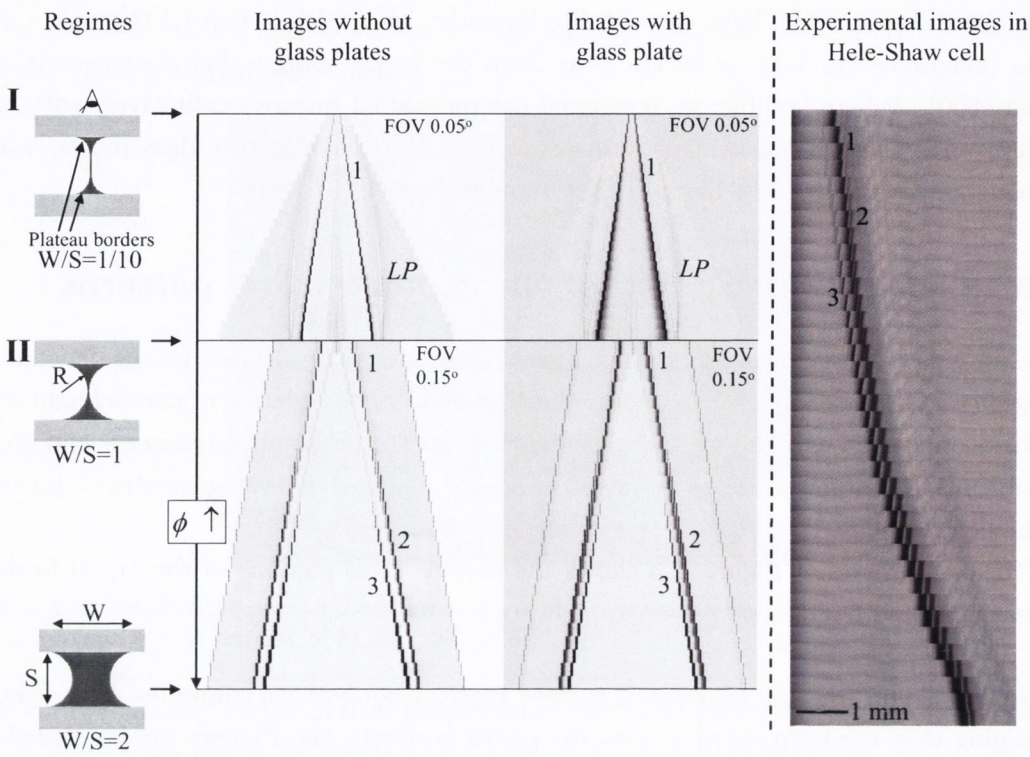


Figure A.3: The evolution of the optical pattern of a liquid bridge with increasing liquid fraction ϕ. The left column shows the geometry of specific cross-sections of the liquid bridge, whilst the two central columns display the corresponding computational images (3D Studio Max) with and without glass plates observed from top. The right column shows the same pattern evolution observed in experiments. The images are characterised by three pairs of black stripes (labeled 1, 2 and 3). Note that the glass plates only influence the intensities, but not the pattern itself (see also Section A.6). 'LP' marks the shading introduced by the lower Plateau border. FOV stands for field of view. See for an enlarged version, page 189).

the scaling properties of the geometry in this regime, the location of Pair 1 is scale invariant, its location is always at the same relative position to the width of the Plateau border, as we will further explain in Section A.4.

At the beginning of Regime II (Section A.5), Pair 1 is still present, but thins with increasing W with its inner boundary moving outwards. The location does not scale linearly with the width of the Plateau border anymore. Pair 1 disappears for $W/S \approx 1.72$. A second pair of stripes, *Pair 2* appears for $W/S \approx 1.33$, located further away from the centre of the liquid bridge. Pair 2 is not scale invariant. As W increases the outer boundary remains constant relative to the curved gas/water interface, whilst the inner boundary moves inwards.

At $W/S \approx 1.44$ a third pair of stripes appears (*Pair 3*). As in the case of Pair 2, the

outer boundary remains constant relative to the curved gas-water interface, whilst the inner boundary moves inwards as W increases. For $W/S > 2$, Pair 2 and 3 merge progressively.

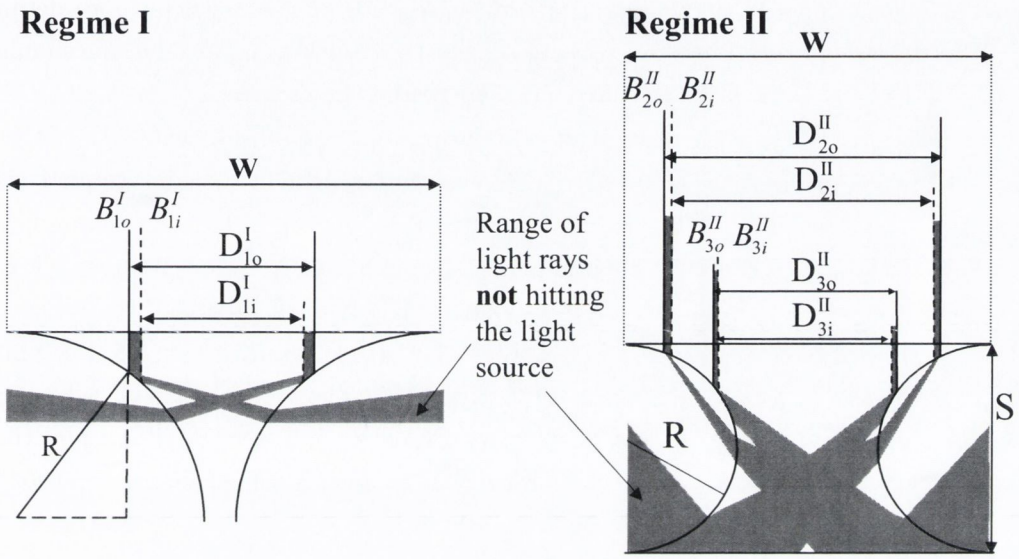


Figure A.4: Labeling scheme used for liquid bridges of width W in the Sections A.4 and A.5. Stripe boundaries are labeled B^z_{xy}, their separation D^z_{xy}. z denotes the regime (I or II), x denotes the stripe number, (1, 2 or 3), and y denotes whether it is the outer ($y = o$) or inner boundary ($y = i$) of the stripe.

Pair	Boundary	Steady appearance if:	Use boundary
1	B^I_{1o}, B^{II}_{1o}	$0 < W/S < 1.62$	x
1	B^I_{1i}, B^{II}_{1i}	$0 < W/S < 1.00$	-
2	B^{II}_{2o}	$1.33 < W/S < 2.46$	x
2	B^{II}_{2i}	$3.40 < W/S < 6.70$	x
3	B^{II}_{3i}	$1.44 < W/S < 2.57$	x
3	B^{II}_{3o}	$6.70 < W/S < 14.61$	-

Table A.1: Summary of the appearance and steadiness of the black stripes in Regime I and II, valid with and without glass plates (as describe in Section A.6), based on the 2D ray-tracing model and checked with 3D Studio Max simulations.

Note that *none* of the black stripes correspond to the actual boundary of the liquid bridge. They are images of the surroundings: as a result of the interplay of the curved gas/liquid interfaces of the object, the liquid bridge projects parts of the surrounding area into the camera, which does not emit any light. This becomes particularly clear within the concept

of backward-ray tracing, as explained later.

In the following sections the origin of the stripes will be discussed in more detail. For simplification and following the principle of backward ray tracing employed in the simulations, we describe all ray paths *backwards*, i.e. as coming from the camera.

Where possible, we provide mathematical relationships between the width W of the liquid bridge and the position of the stripes to guide experimentalists in their image analysis.

Figure A.4 shows the labeling scheme used in this section. The stripe boundaries are labeled B^z_{xy}, where z denotes the regime (I or II), x denotes the stripe number, $(1, 2$ or $3)$, and y denotes whether it is the outer $(y = o)$ or inner boundary $(y = i)$ of the stripe.

In our descriptions, *'top'* and *'bottom'*, (eg. the 'top Plateau border' or 'bottom glass-plate') refer to the object closest or furthest from the camera, respectively. All images are shown accordingly. The two sides of the surface Plateau borders in Regime I and the sides of the liquid bridge in Regime II will be named *first* or *second curved interface*, according to how the path of the ray proceeds through the structure.

We would like to remind the reader that there is no gravity involved in any of our calculations for example in affecting the shape of the top and bottom Plateau border.

A.4 Regime I

In Regime I only one pair of black stripes is present (Pair 1, Figure A.3), which scales with the width of the surface Plateau border. The bottom Plateau border is neglected in the calculations, as it has no influence, which will become obvious later. Making use of the symmetry of the system, Figure A.5 shows the relevant ray-paths through the left half of the top Plateau border, generated by our simplified 2D model (Section 3.3.3). It illustrates that the black stripe is an image of the surrounding area which does not emit light.

To illustrate the effect of a finite light source we will also consider for this regime the patterns created with a finite light source in Section A.4.2. We would like to remind in this analysis the camera is placed far away so we only observe parallel light.

A.4.1 Infinite light source

Pair 1, B^I_{1o}

As shown in Figure A.5, the outer boundary B^I_{1o} is determined by the ray which hits the curved gas/liquid interface at the critical angle Θ_c (Equation 3.3). It is then refracted upwards at the opposite curved liquid/gas interface and does not hit the light source.

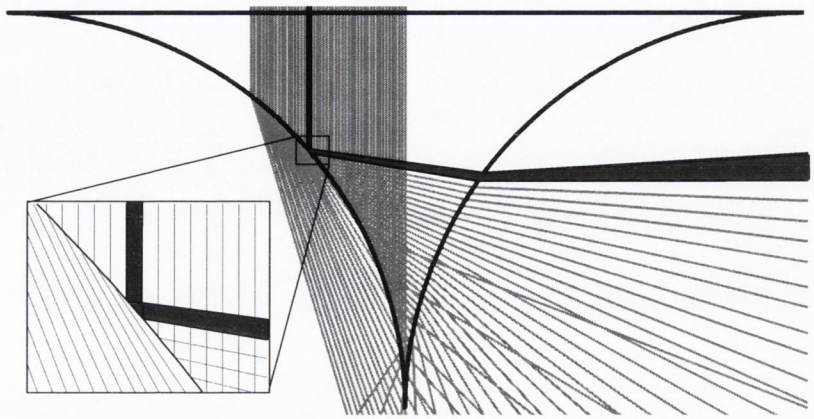


Figure A.5: Relevant ray paths through one side of a surface Plateau border in Regime I. The black stripe is an image of the surrounding area, which does not emit light.

Using the circular geometry of the gas/liquid interface, we can relate the Plateau border width W and the boundary separation D^I_{1o}, (Figure A.4) as

$$W = \frac{1}{[1 - \sin(\Theta_c)]} D^I_{1o}. \tag{A.2}$$

For a water/air system this becomes

$$W = 4.000 D^I_{1o}. \tag{A.3}$$

This equation can be used in experiments to check whether their system is in Regime I, by measuring whether $D^I_{1o} < 0.25S$, with the assumptions considered.

Pair 1, B^I_{1i}

The inner boundary, B^I_{1i} is determined by the ray which is totally reflected at the first liquid/gas interface and then refracted at the opposite water/gas interface such that it leaves the Plateau border *parallel* to the light source plane. Considering all the rays that are reflected at the first interface this boundary ray is the 'last' one which does not hit the light source (Figure A.5).

Using the geometry of the Plateau borders and Snell's law at each interface, we can numerically establish the relationship

$$W = 4.248 D^I_{1i} \tag{A.4}$$

for a water/air system.

Figure A.6 summarises the various parameters used in the derivation of Equation A.4. We need to describe a ray path, which consists of a total reflection (Equation 3.2) and refraction (Equation 3.1) at liquid/gas interfaces which are given by two touching quarter-arcs of circles. Boundary conditions are provided by the fact that the light enters the Plateau border perpendicular to the image plane and reaches the boundary of a light source (of size L and at distance H) at an angle δ. Assuming that $H >> R$ and $L >> R$ we can approximate

$$\delta = \text{atan}\frac{2H}{L}. \tag{A.5}$$

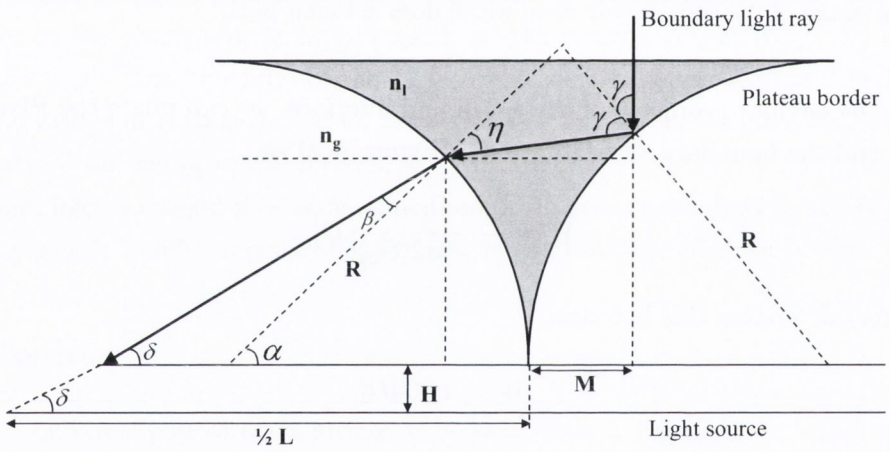


Figure A.6: Labeling scheme used to describe the boundary ray path B_{1I}^{I} through a liquid bridge in Regime I, for a finite light source, as described in Section A.4.2.

These conditions provide a set of four equations with $\delta \to 0$ corresponding to the case of an infinite light source ($H >> R$), which we solved numerically using MATLAB:

$$\begin{aligned} n_l \sin\eta &= n_g \sin\beta \\ 2\gamma + \eta - \beta - \delta &= \pi/2 \\ \tan(2\gamma) &= \frac{\sin\alpha - \cos\gamma}{2 - \cos\alpha - \sin\gamma} \\ \frac{D}{W} &= 1 - \sin\gamma \end{aligned} \tag{A.6}$$

Note that if δ is not equal to ~ 0, the light source is finite, which case we will discuss in Section A.4.2.

From the description of the boundaries of Pair 1 it can be concluded that the bottom

Plateau border does not play a role in the generation of the optical pattern, as the boundary rays never interfere with the bottom Plateau border. Part of the refracted rays can reach the lower Plateau border but this only introduces some shading, which is not scale-invariant and marked as LP in Figure A.3.

Neighbouring Plateau borders may have a significant influence on the pattern, unless they are sufficiently far away.

Influence of glass plates

The boundary B^I_{1o} is not influenced by glass plates. After having been refracted upwards, the rays get trapped between the two glass plates as a result of total reflection and therefore never hit the light source.

The boundary B^I_{1i} is influenced, because the light rays which are refracted downwards when leaving the liquid, can be totally reflected at the lower glass plate and therefore get trapped. Due to Fresnel effects this boundary becomes wider, but also less sharp. The boundary B^I_{1i} is therefore more difficult to define when including glass plates and therefore is not advised to be used for analysis purposes. See Section A.6 for more details.

A.4.2 Special case: Finite light source

Because of its relevance for many experiments we add here a special section, which investigates the effect of using a *finite* light source when imaging surface Plateau borders. The parameter of relevance here is the angle δ (Figure A.7), which is the minimum angle at which light from the light source can enter the Plateau border. δ can be approximated by

$$\delta \approx \text{atan}(\frac{2H}{L}), \tag{A.7}$$

where L is the width of the light source, when $H >> R$. This assumption is valid in most experiments.

Figure A.8 shows how the image changes with H/L, which corresponds to either changing the *size* or *position* of the light source. We see that with increasing H/L the black stripe thickens significantly and new stripes are introduced. We find that for $H/L < 0.01$ the light source can be considered effectively infinite.

With increasing H/L a second pair of stripes appears further away from the centre, which we label *f*. Its inner boundary B^I_{fi} changes little, while its outer boundary B^I_{fo} moves outwards significantly. For $H/L \to \infty$ this boundary approaches the actual boundary of the Plateau border. Hence if the incoming light is perpendicular to the image plane, the *full Plateau border width* W can be determined by measuring the width of the optical pattern.

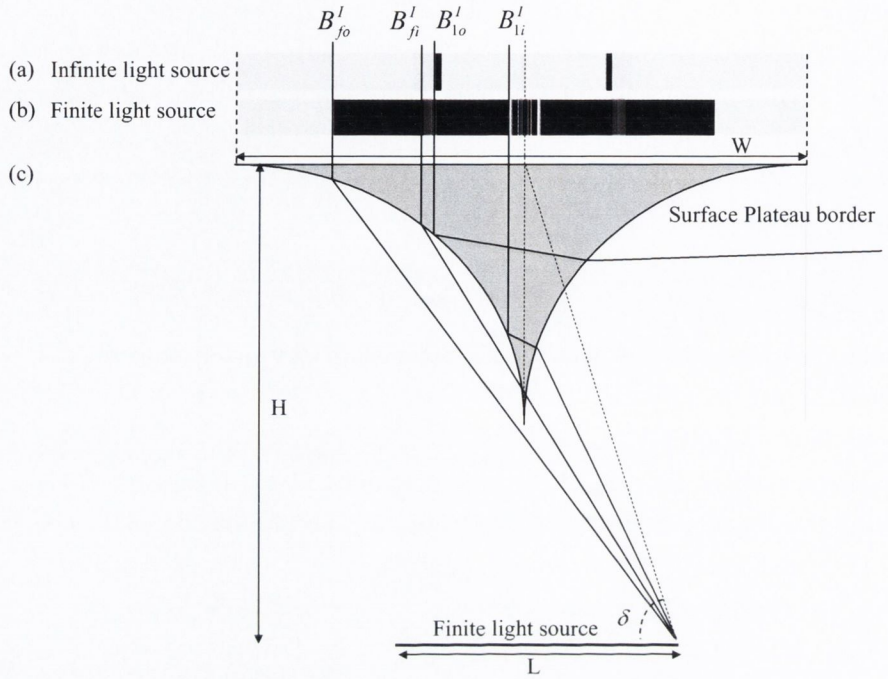


Figure A.7: Image of a surface Plateau border, either in front of an *infinite* light source (a) or a *finite* diffusive light source ($H/L = 4.4$), taken from the sequence of Figure A.8. (c) Sketch of the rays paths of the stripe boundaries through the surface Plateau border and corresponding and labeling scheme.

The limiting ray paths which determine the boundary of the stripes are sketched and labeled in Figure A.7. Some mathematical relationships relating their position to W and H/L are given in the following sections, using the set of Equations A.6.

Note that additional boundary conditions like non-transparent edges of a Hele-shaw cell can decrease the effective width of the light source and therefore change the pattern.

Boundary B^I_{1o} (Finite light source)

As in shown in Section A.4.1, this boundary is related to the angle of total reflection. It is therefore *independent* of H/L and given by Equation (A.3). Hence, measuring the separation between these boundaries provides an excellent measure of the true Plateau border width. Note that with increasing H/L this boundary becomes less well defined as a result of Fresnel effects, which darken the neighbouring light rays (Figure A.8). This is also the cause of boundary B^I_{fi}, which will therefore not be described here further.

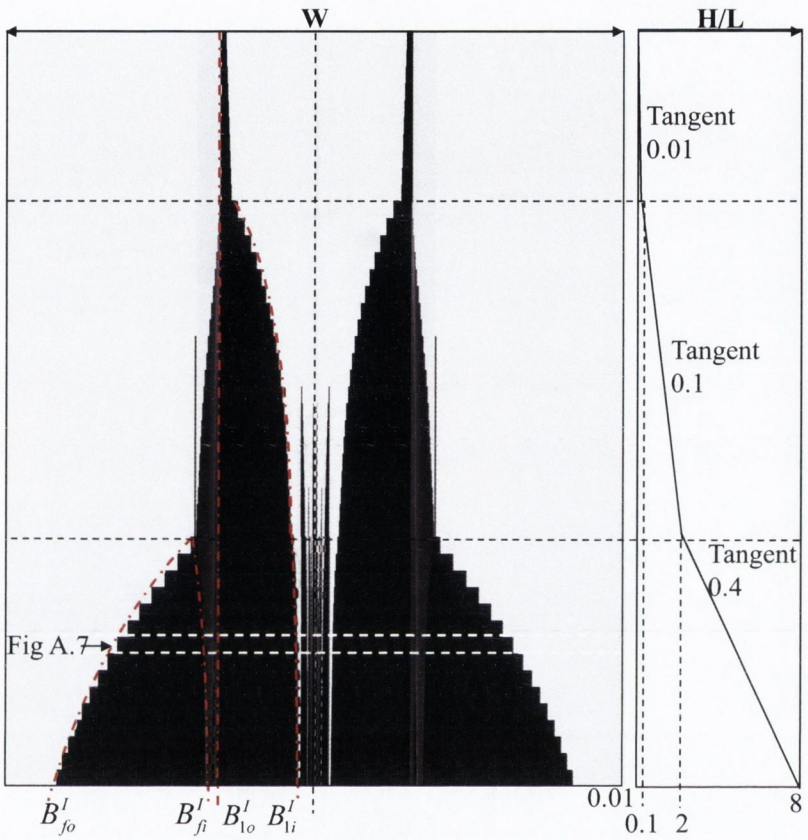


Figure A.8: (a) Computational prediction (3D Studio Max) of how the image of a surface Plateau border changes with H/L (vertical axis), where L is the size and H the position of the light source. (b) Three different step sizes between the images (tangent) are used to cover a large range of H/L ratios (and therefore $\delta's$). The marked section is used in Figure A.7.

Boundary B^I_{1i} (Finite light source)

With increasing H/L the boundary B^I_{1i} moves towards the centre of the Plateau border. As sketched in Figure A.7, this boundary is generated by the limiting ray which is reflected at the first curved liquid/gas interface and then refracted at the opposite curved gas/liquid interface. In order to find its position as a function of W, a set of Equations A.6 needs to be solved. The result is shown in Fig A.9 (a), where D_{1i}/W^I is plotted versus $\delta = \text{atan}(\frac{2H}{L})$. It shows that with increasing δ the boundary B^I_{1i} moves closer to the centre of the Plateau border with $D_{1i}/W^I = 0.04$ for $\delta = 90^o$ $(H/L \rightarrow \infty)$. In the limit $\delta = 0^o$ $(H/L \rightarrow 0)$ we recover $D_{1i}/W^I = 0.24$, which corresponds to the infinite light source and therefore to Equation A.4.

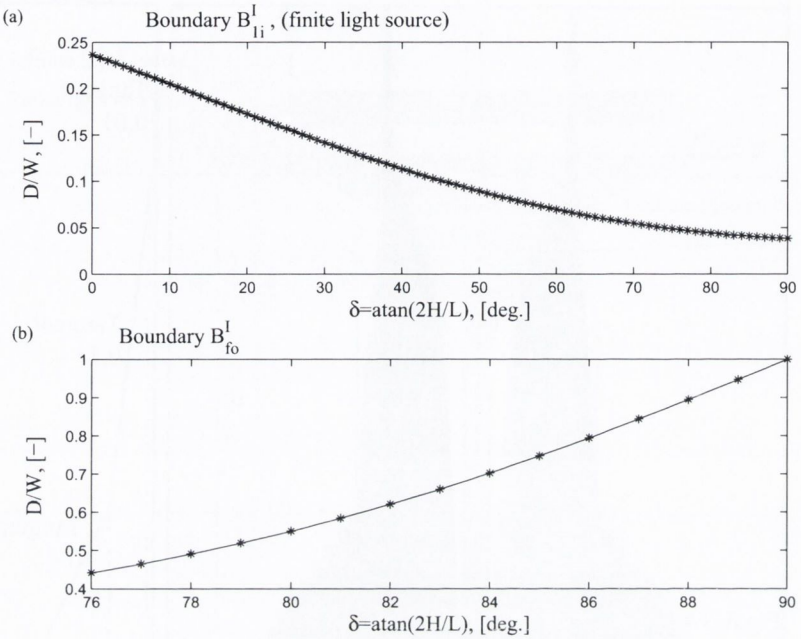


Figure A.9: (a) Development of boundary B^I_{1i} with H/L. (b) Variation of B^I_{fo} using Equation (A.8) with $\delta > 76^o$ (or $H/L > 2$).

Boundary B^I_{fo}

This is the outmost boundary of the stripe pattern, which is often incorrectly associated with the real width of the Plateau border. The boundary ray here is the image of the opposite boundary of the light source, which is refracted only once (see Figure A.7). From simple geometry and Snell's law (Equation 3.1) we find:

$$W = D^I_{fo}\left[1 - \sin\left\{\text{atan}\left(\frac{\cos(\delta)}{\frac{n_l}{n_g} - \sin(\delta)}\right)\right\}\right]^{-1} \tag{A.8}$$

with $\delta = \text{atan}\left(\frac{2H}{L}\right)$, which is plotted in Figure A.9 (b).

The B^I_{fo} appears at $\frac{H}{L} \approx 2$, see Figure A.8, which means $\delta > 76^o$. As seen in Figure A.8 and Figure A.9 (b), Equation A.8 makes clear that unless all the incoming light is truly perpendicular to the image plane, this measure significantly underestimates the true width W of the Plateau border.

For example, if the angle of the incoming light deviates by only 2^o from being perpendic-

ular, the Plateau border width is underestimated by approximately 10 %!

Influence of glass plates The same effects as discussed in Section A.4.1 hold here. The bottom plate has the additional effect of shifting the light rays coming from the light source such that its apparent size decreases (see Section A.6). Generally, this effect is negligibly small, but might have to be considered in some special experimental scenarios.

A.5 Regime II

In Regime II the two surface Plateau borders have merged and form two curved gas/liquid interfaces, which separate linearly as the liquid fraction increases. As this happens, not only the optical interaction between the curved interfaces changes, but also the bottom and top interface begin to play an important role. This causes Pair 1 to disappear (Section A.5.1) and introduces two new pairs of stripes: Pair 2 (Section A.5.2) and Pair 3 (Section A.5.3), which can be seen in Figures A.10 and A.11.

A.5.1 Pair 1

As seen in Figure A.10, with increasing width W all the rays which are totally reflected at the first curved liquid/gas interface hit the opposite curved interface at a lower point than they did in Regime I. The rays are therefore increasingly refracted towards the light source, which means that the inner boundary B_{1i}^{II} moves towards the outer boundary B_{1o}^{II}. At $W/S \approx 1.62$ the outer boundary is refracted towards the light source and Pair 1 disappears. For $1 < W/S < 1.62$ one finds that:

$$W = D_{1o}^{II} + 0.25S * \frac{1}{[1 - \sin(\Theta_c)] - 0.25S} or W = D_{1o}^{II} + S\sin(\Theta_c). \tag{A.9}$$

For a water/air system this becomes

$$W = D_{1o}^{II} + 0.75S. \tag{A.10}$$

A.5.2 Pair 2

Outer boundary, B_{2o}^{II}

Pair 2 appears at $W/S = 1.33$. Its outer boundary B_{2o}^{II} corresponds to the first ray which is totally reflected at the bottom interface after having been refracted twice at the curved

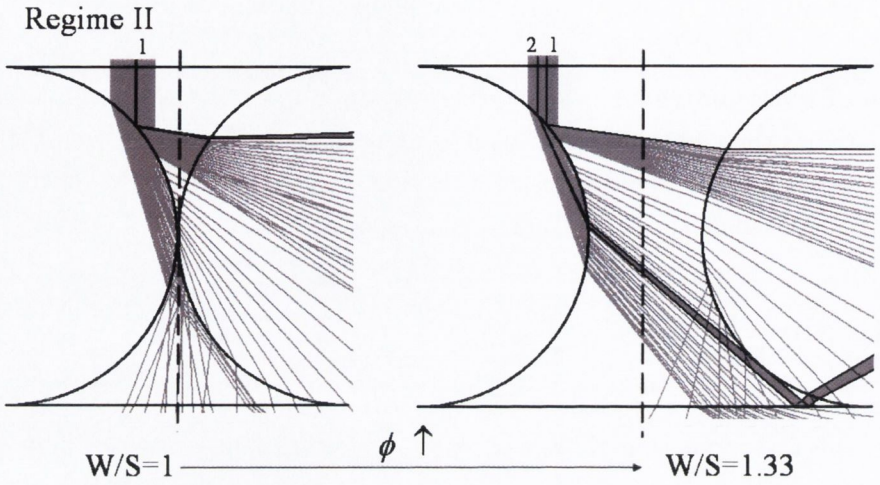


Figure A.10: Change in pattern generating mechanism at the beginning of Regime II from $W/S = 1$ to $W/S = 1.33$.

liquid/gas interface (Figure A.10). Solving the appropriate set of equations in the style of Equations A.6, we obtain

$$W = D_{2o}^{II} + 0.698S \tag{A.11}$$

for a water/air system.

This boundary remains constant for $1.33 < W/S < 2.46$. Beyond this, the boundary ray is reflected at the top interface, after which refraction at the second curved gas/liquid interface deflects the ray such that it reaches the light source. The evolution of these changes is shown in Figure A.12 for $2 < W/S < 4$.

Note that this boundary corresponds with the inner boundary B_i of the stripe of an individual bubble, described in Section 3.4. This boundary is only slightly lighter due to Fresnel effects.

Inner boundary, B_{2i}^{II}

Initially, the boundary B_{2i}^{II} changes with W as less rays of those, which have been refracted twice at the first curved interface, interfere with the second curved interface, before hitting the bottom interface. For $W/S > 3.25$ all of these rays are totally reflected at the bottom interface and the boundary is fixed with respect to the curved interface. The boundary ray is now the last one which is not totally reflected at the liquid/gas interface.

Using this information with the same set of equation employed for B_{2o}^{II}, we establish for

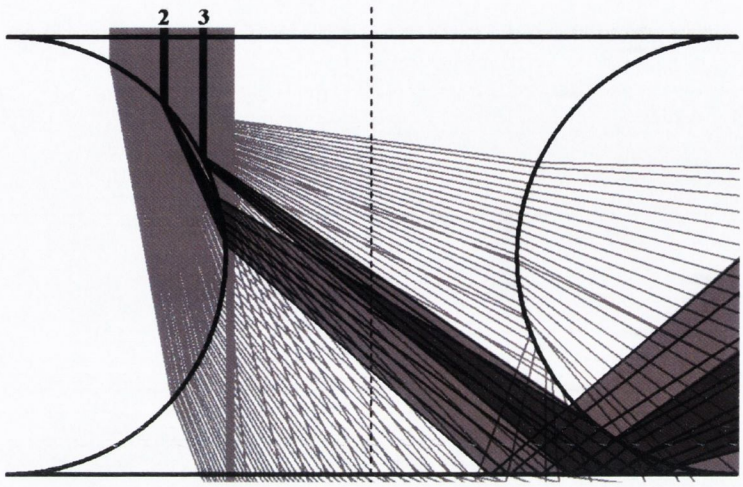


Figure A.11: Ray paths in a liquid bridge with $W/S = 1.66$, showing Pair 2 and 3. In Regime II reflection at the bottom interface plays a significant role.

B_{2i}^{II}:

$$W = D_{2i}^{II} + 0.75S. \tag{A.12}$$

This relationship holds until $W/S = 6.7$, beyond which the ray is reflected at the top interface. Overall (see Table A.1) we see that there is no stage at which the width of the stripe 2, given by $B_{2o}^{II} - B_{2i}^{II}$, remains constant as their regimes of steady appearance barely overlap.

A.5.3 Pair 3

Beyond $W/S = 1.44$ a third pair of stripes appears closest to the centre of the Plateau border, compared with Pair 1 and 2. As is clear from Figure A.11, the principles of its origin are very similar to those of Pair 2. The only difference now is that the rays which are totally reflected at the bottom interface, are those which have been totally reflected at the first curved liquid/gas interface.

Inner boundary, B_{3i}^{II}

The inner boundary is given by two equations of total reflection at the curved and bottom interface. We therefore obtain analytically

$$W = D_{3i}^{II} + \cos\left[\frac{\Theta_c}{2}\right] S. \tag{A.13}$$

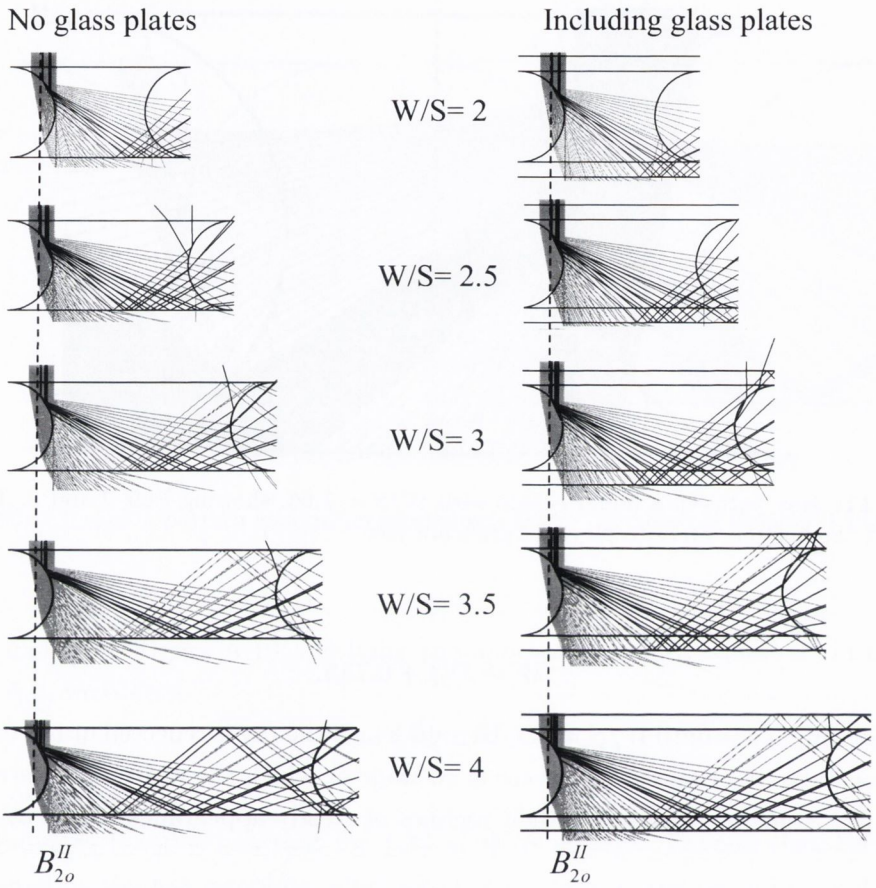


Figure A.12: The evolution of Pair 2 and 3 with increasing width of the liquid bridge ($2 < W/S < 4$), without and with glass plates. Only the ray paths of one side of the liquid bridge are shown.

Which gives

$$W = D_{3i}^{II} + 0.91S, \tag{A.14}$$

for a water/gas system with or without glass plates. This relationship holds for $W/S < 2.57$. Beyond this width the boundary ray interferes with the second curved interface, after being reflected at the top interface and can be refracted towards the light source, as shown in Figure A.12. Note that this boundary corresponds with the outer boundary B_o of the stripe of an individual bubble, described in Section 3.4.

Outer boundary, B_{3o}^{II}

Similarly to B_{2o}^{II}, this boundary is determined by the first ray which hits the bottom interface without first interfering with the second curved interface. B_{3o}^{II} therefore continuously changes

with W, the only limit being given by the first ray which is totally reflected at the first curved interface. Since this is the inner boundary ray of Pair 2 both stripes merge at $W/S \approx 6.7$.

Reflections at the top interface and interaction with the curved gas-water interface cause some rays between the boundaries B_{2o}^{II} and B_{3i}^{II} to escape towards the light source and become bright (starting at $W/S = 2.46$). Due to intensity loss these rays become increasingly vague as the liquid bridge widens and finally one stripe will be visible.

Note that the pattern of one side of an infinitely wide liquid bridge in Regime II is equivalent to the cross-section of each side of the bubble.

A.6 Influence of the glass-plates

Here we present some details on the effect of confining plates of thickness T and refractive index n_t, as mentioned in Sections A.4.1 and A.4.2.

A.6.1 Refraction

If light travels between two media of refractive indices n_1 and n_2, which are separated by a transparent plate (Figure A.13), the outgoing ray is translated by a distance s with respect to the incoming ray:

$$s = T(\tan\Theta_t - \tan\Theta_1), \tag{A.15}$$

with

$$\Theta_t = \operatorname{asin}\left(\frac{n_1}{n_t}\sin\Theta_1\right). \tag{A.16}$$

Note that s does not depend on the medium at the other side of the plate (n_2).

Introducing the plates only introduces a translation, which leads to an apparent size L^* of the light source, whether this L^* is larger or smaller than L depends on the distance H as indicated in Figure A.13.

The relationship between the angles of the incoming (Θ_1) and outgoing ray (Θ_2) is still given by Equation 3.1, independently of the properties of the plate.

A.6.2 Total reflection

The critical angle Θ_c for reflection at an interface with refractive indices of n_1 and n_2 such that $n_1 < n_2$ is given by

$$\sin\Theta_c = \frac{n_2}{n_1}. \tag{A.17}$$

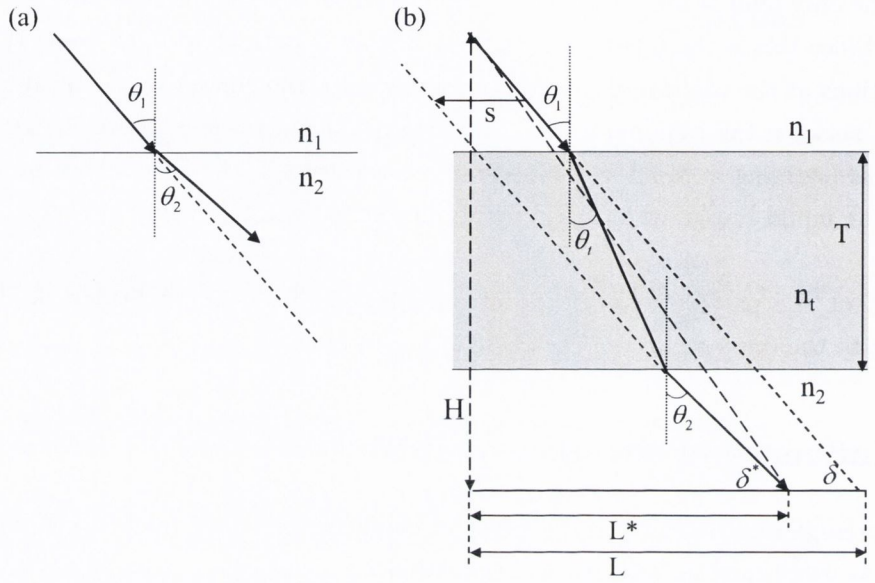


Figure A.13: The influence of the glass plate on a refracted ray. (a) shows the ray interaction on an interface between two materials with refractive indices n_1 and n_2. If $n_1 < n_2$ the incoming rays are refracted away from the normal (b) shows the influence of the path adding a transparent plate (refractive index n_t). The glass plate causes a shift given by Equation A.15. It can increase or decrease the apparent size of the light source, L^*, compared with L.

If a transparent plate is introduced (with $n_t > n_2$), the new critical angle is given by

$$\sin\Theta_c^* = \frac{n_2}{n_t}. \tag{A.18}$$

At the same time Snell's law must be satisfied at the $n_1 - n_t$ interface;

$$\frac{\sin\Theta_1}{\sin\Theta_c^*} = \frac{n_t}{n_1} \tag{A.19}$$

which (using Equation (A.18)) becomes

$$\sin\Theta_1 = \frac{n_2}{n_1} = \sin\Theta_c. \tag{A.20}$$

This proves that the critical ray, which is totally reflected in a liquid/gas system, is also totally reflected in a system with a confining transparent plate of *any* material (as long as $n_1 \leq n_2$).

However, as in the case of refraction, the transparent plate introduces a translation s' of the ray, as seen in Figure A.14, which can be quite significant. For an angle of incidence Θ_i

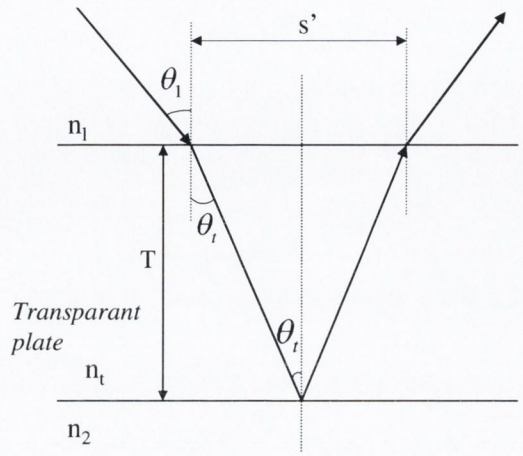


Figure A.14: The paths of rays that are reflected at the glass-gas interface. The ray in glass approaching the glass-gas interface at its critical angle, Θ_t, approached the glass under the critical angle of water/gas, Θ_1.

one finds that

$$s' = T\left[\tan\left\{(\text{asin}\left(\frac{n_2}{n_t}\sin\Theta_1\right)\right\}\right]^{-1}. \tag{A.21}$$

In Regime II the interaction with the bottom interface plays an important role in the stripe formation. Two aspects are important here. Firstly the comparison between total reflection at the water/air and water/glass/air interface and secondly the trapping of the rays between the glass plates.

As shown above, a ray which is totally reflected at a water/gas interface will also be be totally reflected at a water/glass/gas interface. Therefore, all arguments given above hold equally for systems with confining plates. This can in fact be generalised to any liquid/gas and liquid/transparent plate/gas interface. Therefore, for reasonably narrow liquid bridges (Regime I) and an effectively infinite light source, plates only have an influence on the intensity of the rays as a results of the Fresnel effects, but not on the pattern itself.

More care needs to be taken in the case of wide bridges (Regime II) in which light bounces between the glass plates multiple times. As discussed this can introduce a considerable side shift of the rays, which can lead to a serious delay in the change of patterns with respect to W.

Another effect of glass plates is that rays are trapped, if they happen to enter the glass through a liquid/glass interface and afterwards will only be reflected at the glass/gas parts

of the plates. Equally, they will stay trapped and become reflected if there is a thin layer of liquid on the glass, which is the case in Figure 3.6. However, this does not have an effect on the appearance of the optical pattern, as most of these rays were already not going to reach the light source.

In summary, we have shown more successful applications of the computational raytracing techniques, in this case for the analyse of optical images of liquid bridges.

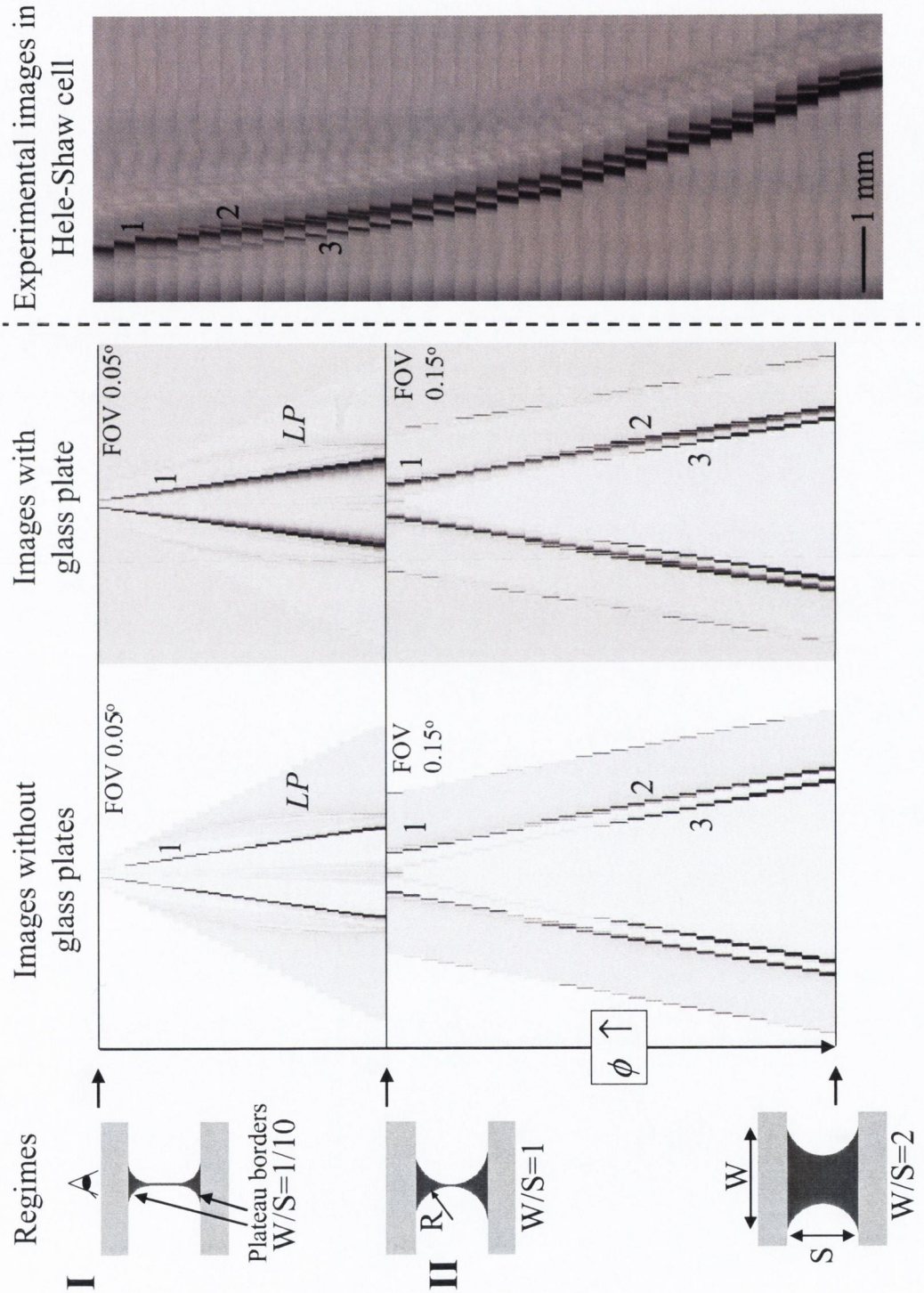


Figure A.15: Enlarged Figure A.3

APPENDIX A. IMAGES OF PLATEAU BORDERS

Appendix B

Coherent grain boundaries

We found different options of coherent grain boundaries as seen in Figure 4.5. It is interesting to know whether and how these boundaries evolve into the bulk of the foam.

Bragg and Nye describe in their paper [18] their view of twin boundaries between fcc(111) and fcc(100), between which they view a small angle visible in the oblique view. We will theoretically approach this problem and suggest an experimental approach to verify the predictions.

Theory of angle determination As the layer thickness of fcc(100) and fcc(111) differs, there are two options possible to form a fcc(111)-fcc(100) grain boundary. The layer below the first layer of fcc(100) can retreat (or move forwards) combined with fcc(111) moving forwards (or backwards). The optical patterns of the bubbles can be used to distinguish between the two cases (Chapter 3). The fcc(111) and fcc(100) structures do not proceed or retreat with the same step size. When one row of bubbles would be added, for fcc(100) the elongation is $2R$, for fcc(111) it is $\sqrt{3}R$. Also the heights of the packings layers are not equal, for fcc(100) the layer height is $\sqrt{2}R$, for fcc(111) it is $2\sqrt{2/3}R$. Therefore the two structures only match when they are placed at an angle as seen in Figure B.1. This angle α is theoretically equal to:

$$\alpha = \frac{\pi}{2} - atan\frac{\frac{1}{3}\sqrt{3}R}{2\sqrt{\frac{2}{3}}R} - atan\frac{\sqrt{2}R}{R}, \ \alpha \text{ becomes } 15.8^o \tag{B.1}$$

Note that here the angles are determined between the centres of the bubbles of two consecutive rows for the fcc(100) and fcc(111) structure, which are subtracted from 90° to obtain α, sketched in Figure B.1 (b).

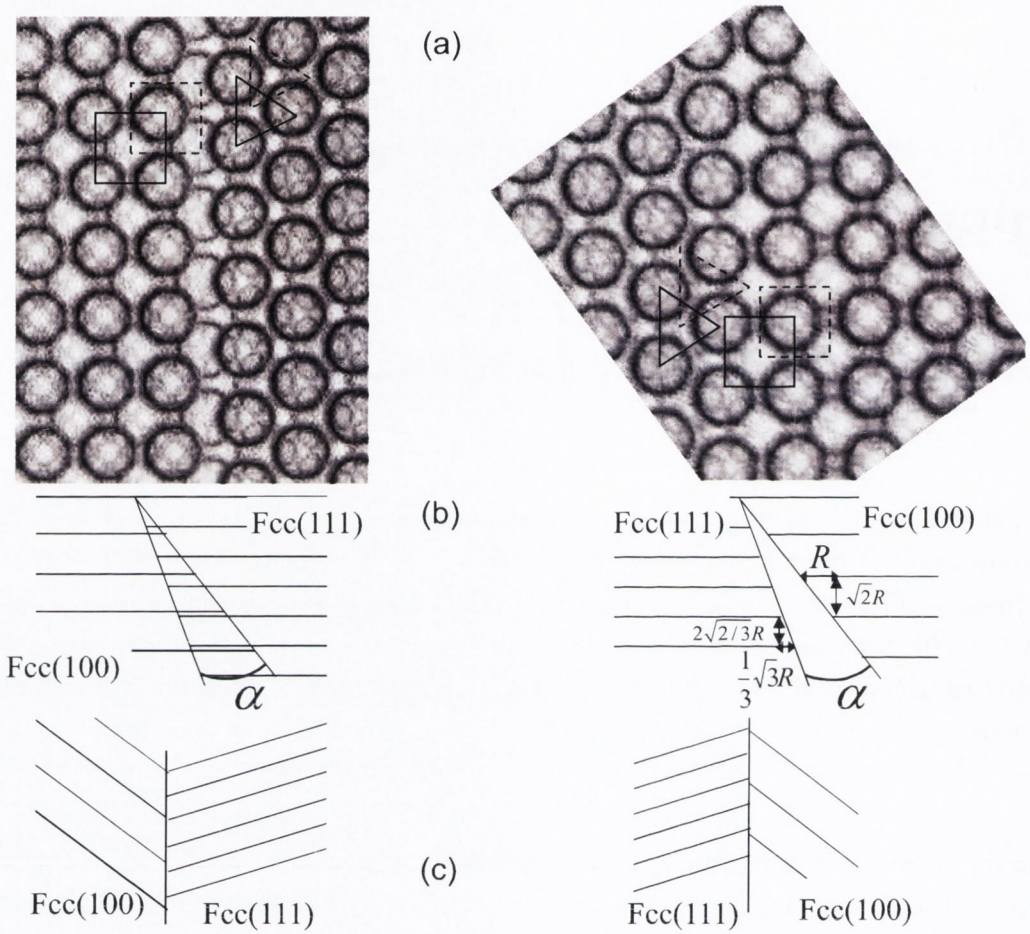


Figure B.1: Analysis of two options of the angle between twins. (a) Shows the two different options of the second layer. The fcc(100) layer can move forwards half a layer, combined with a fcc(111) moving backwards a quarter of a layer and opposite. The step size of movement is not equal and together with the fact that the layer height of fcc(111) and fcc(100) are equal, theoretically an overlap or gap is then created seen in (b). This results in an angle between the two grains as seen in (c).

Suggested experimental angle determination We would like to measure the angle α. By shining a concentrated laser beam on to the two surface of both fcc(111) and fcc(100), as shown in Figure B.2, and detect under which angle the reflected light is reflected back, it is expected the angle α between the two surface can be determined. By knowing the angle of reflection of the laser, β, and the measurable angle κ created by the laser line at the grain boundary, the angle α can be determined according to:

$$\alpha = \pi/2 - 2tan^{-1}\left[\frac{\tan(\kappa)}{\tan(\beta)}\right] \tag{B.2}$$

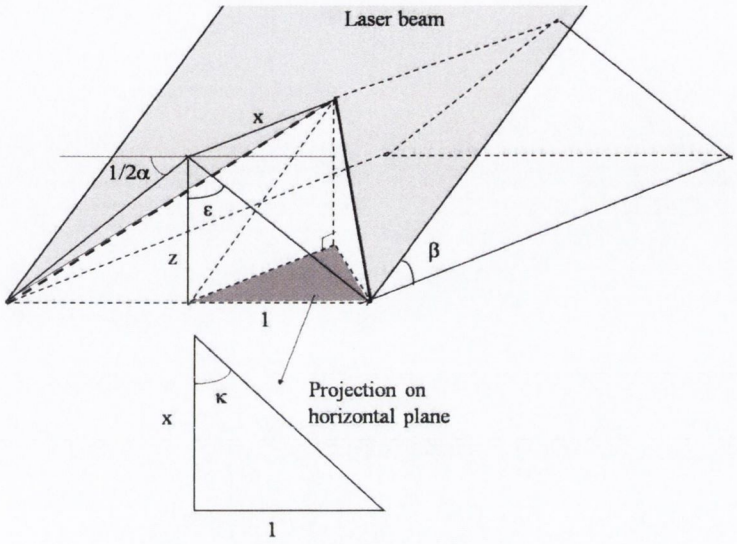


Figure B.2: The sketch of varies parameters involved in the analysis of the angle between an fcc(111) and fcc(100) grain.

It would be interesting to see whether the experimental results match with the predictions. The main reason why this is a difficult experiment is because we need to find an appropriate method to systematically make the ordered grain boundaries. Waiting until the boundaries appear in the generated bubble crystal and use them in the set-up is a too tedious task. Forcing crystalline foam growth of fcc(100) and fcc(111) by confinement with specific grain boundaries and let them growth until they meet could be an possibility which should be tried in the future.

Appendix C

Derivation of equations for the diffusion model

Here we derive Equations 5.1, 5.2, 5.4 and 5.5, which are used in Chapter 5 in the model describing gas diffusion through a bubble cap.

C.1 Derivation of Equation 5.1

The definition of the film permeability k according to Princen and Mason [209] is:

$$-\frac{dn}{dt} = kA\Delta C, \tag{C.1}$$

with n the numbers of moles of gas diffusing through the film, A the area of the film, ΔC the concentration difference of the diffusing gas over the film (mol per standard volume)

Using the ideal gas law, $P^{\circ}V = nRT$ with P° the absolute pressure, V the volume, R as the gas constant and T the temperature, $\frac{dn}{dt}$ can be written as:

$$\begin{aligned} n &= -\frac{P^{\circ}V}{RT} \\ -\frac{dn}{dt} &= \frac{1}{RT}\frac{d(P^{\circ}V)}{dt} \\ &= \frac{(P - P_L)}{RT}\frac{dV}{dt}, \end{aligned} \tag{C.2}$$

with P as air pressure and P_L vapor pressure.

ΔC can be expressed as:

$$\begin{aligned} \Delta C &= -\frac{n}{dV} \\ &= -\frac{\Delta P}{RT}, \end{aligned} \tag{C.3}$$

with ΔP the gas pressure difference between the atmosphere and inside the bubble.

Combining Equations C.1 and C.2 gives:

$$\frac{(P - P_L)}{RT}\frac{dV}{dt} = kA\Delta C \tag{C.4}$$

Replacing ΔC with Equation C.3, and assuming that the atmosphere is infinite and the liquid is nonvolatile, makes the P_L zero [157], which results in

$$-P\frac{dV}{dt} = kA\Delta P \tag{C.5}$$

C.2 Derivation of Equation 5.2

This equation relates the area of the top film with the two radii of the cap.

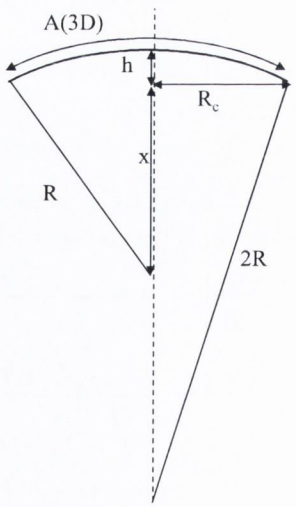


Figure C.1: The area of segment of a sphere A (in 3D) depends on its height h and radius R of the segment radius.

An area of a segment of a sphere, A can be expressed as:

$$A = \pi(R_c^2 + h^2). \tag{C.6}$$

In Figure C.1 the different variables are explained. h can be expressed using Pythagoras's theorem as:

$$\begin{aligned} x^2 &= 4R^2 - R_c^2 \\ h &= 2R - x \\ &= 2R - \sqrt{4R^2 - R_c^2} \end{aligned} \tag{C.7}$$

Merging Equations C.6 and C.7 leads to:

$$\begin{aligned} A_c &= \pi(R_c^2 + (2R - \sqrt{4R^2 - R_c^2})^2) \\ A_c &= \pi(R_c^2 + (4R^2 - 4R\sqrt{4R^2 - R_c^2} + 4R^2 - R_c^2)) \\ A_c &= \pi(8R^2 - 4R\sqrt{4R^2 - R_c^2}) \\ A_c &= \pi\left(8R^2 - 8R^2\sqrt{1 - \left[\frac{R_c}{2R}\right]^2}\right) \\ A_c &= \pi 8R^2\left(1 - \sqrt{1 - \left[\frac{R_c}{2R}\right]^2}\right) \end{aligned} \tag{C.8}$$

This is equal to Equation 5.2.

C.3 Derivation of Equation 5.4

Using both Equation C.5 and C.8 gives:

$$\begin{aligned} -P\frac{dV}{dt} &= \Delta P A_c k \\ -P\frac{dV}{dt} &= \Delta P \pi 8R^2\left(1 - \sqrt{1 - \left[\frac{R_c}{2R}\right]^2}\right)k \\ \frac{dV}{dt} &= \frac{8\pi\Delta P R^2 k}{-P}\left(1 - \sqrt{1 - \left[\frac{R_c}{2R}\right]^2}\right) \end{aligned}$$

Using for ΔP, $\frac{4\gamma}{R_c}$ which is $\frac{2\gamma}{R}$ and for $\frac{dV}{dt} = 4\pi R_c^2 \frac{dR}{dt}$, $\frac{dV}{dt}$ can be written as:

$$\begin{aligned} 4\pi R^2 \frac{dR}{dt} &= \frac{16\pi\gamma R^2 k}{R_c P}\left(\sqrt{1-\left[\frac{R_c}{2R}\right]^2}-1\right) \\ \frac{dR}{dt} &= \frac{4\gamma k}{R_c P}\left(\sqrt{1-\left[\frac{R_c}{2R}\right]^2}-1\right) \end{aligned} \tag{C.9}$$

From the force balance between buoyancy of the bubble, assuming that cap volume is negligible compared with the total bubble volume, and surface tension we obtain:

$$\begin{aligned} V\Delta\rho g &= \frac{\gamma}{R_b} A_c \\ \frac{4}{3}\pi R^3 \Delta\rho g &= \frac{\gamma}{R}\pi R_c^2 \\ R_c^2 &= \frac{4R^4\Delta\rho g}{3\gamma} \\ R_c &= 2R^2\sqrt{\frac{\Delta\rho g}{3\gamma}}, \end{aligned} \tag{C.10}$$

equal to Equation 5.3. Note that here the for the area of the cap R_c is used, not taken in account the curvature of the cap.

Integration of Equation C.9 using Equation 5.3 (or C.10) with the boundaries of R between R_0 and R and t between t_0 and t, using

$$\begin{aligned} U &= \frac{3P}{4\Delta\rho g}, \\ M &= \sqrt{\frac{\Delta\rho g}{3\gamma}}, \end{aligned}$$

gives:

$$\begin{aligned} \int_{t0}^{t} dt &= \int_{R_0^2}^{R^2} \frac{1}{\sqrt{1-M^2R^2}-1} U R dR, \\ \int_{t0}^{t} dt &= \frac{U}{2M^2}\int_{R_0^2}^{R^2} \frac{1}{\sqrt{1-M^2R^2}-1} dM^2R^2. \end{aligned}$$

C.3. DERIVATION OF EQUATION 5.4

Solving the integration using the computer program Maple we obtain:

$$\begin{aligned} t - t_0 &= \frac{U}{M^2}\left[-\frac{ln(R^2)}{2} - \sqrt{1-M^2R^2}\right. \\ &\quad \left. -\frac{ln(\sqrt{1-M^2R^2}-1)}{2} + \frac{ln(1+\sqrt{1-M^2R^2})}{2}\right]_{R_0^2}^{R^2} \\ t - t_0 &= \frac{U}{M^2}\left[-\frac{1}{2}ln\frac{(R^2)}{(R_0^2)} - \left[\sqrt{1-M^2R^2} - \sqrt{1-M^2R_0^2}\right]\right. \\ &\quad \left. -\frac{1}{2}ln\frac{(1-\sqrt{1-M^2R_0^2})}{(1-\sqrt{1-M^2R^2})} + \frac{1}{2}ln\frac{(1+\sqrt{1-M^2R^2})}{(1+\sqrt{1-M^2R_0^2})}\right]. \end{aligned}$$

The last factor can be written as:

$$ln\frac{(1+\sqrt{1-M^2R^2})}{(1+\sqrt{1-M^2R_0^2})} * ln\frac{(1-\sqrt{1-M^2R_0^2})}{(1-\sqrt{1-M^2R_0^2})} = ln\frac{(1+\sqrt{1-M^2R^2})(1-\sqrt{1-M^2R_0^2})}{M^2R_0^2},$$

such that

$$\begin{aligned} t - t_0 &= \frac{U}{M^2}\left[\left[\sqrt{1-M^2R_0^2} - \sqrt{1-M^2R^2}\right]\right. \\ &\quad \left. +\frac{1}{2}ln\frac{(R_0^2(1+\sqrt{1-M^2R^2})(1-\sqrt{1-M^2R_0^2})(1-\sqrt{1-M^2R_0^2}))}{RM^2R_0^2(1-\sqrt{1-M^2R^2})}\right]. \\ t - t_0 &= \frac{U}{M^2}\left[\left[\sqrt{1-M^2R_0^2} - \sqrt{1-M^2R^2}\right]\right. \\ &\quad \left. +\frac{1}{2}ln\frac{((1+\sqrt{1-M^2R^2})(1-\sqrt{1-M^2R_0^2})^2)}{RM^2(1-\sqrt{1-M^2R^2})}\right], \end{aligned}$$

$$ln\frac{(1+\sqrt{1-M^2R^2})}{R^2M^2(1-\sqrt{1-M^2R^2})} = ln\frac{1}{(1-\sqrt{1-M^2R^2})^2}.$$

This leads to:

$$\begin{aligned} t - t_0 &= \frac{U}{M^2}\left[\left[\sqrt{1-M^2R_{b0}^2} - \sqrt{1-M^2R^2}\right] + ln\frac{((1-\sqrt{1-M^2R_{b0}^2}))}{(1-\sqrt{1-M^2R^2})}\right] \\ t - t_0 &= \frac{3Pa}{4k\Delta\rho g}\left[\left[\sqrt{1-\frac{\Delta\rho g}{3\gamma}R_0^2} - \sqrt{1-\frac{\Delta\rho g}{3\gamma}R^2}\right] + ln\frac{((1-\sqrt{1-\frac{\Delta\rho g}{3\gamma}R_0^2}))}{(1-\sqrt{1-\frac{\Delta\rho g}{3\gamma}R^2})}\right]. \end{aligned}$$

This is the equation Ghosh used in his article [88]. Simplifying the equation it can be written as:

$$t = t_0 + \frac{U}{k} * \left[\sqrt{1-B} - \sqrt{1-CR^2} + ln\frac{1-\sqrt{1-B}}{1-\sqrt{1-CR^2}}\right] \tag{C.11}$$

with

$$U = \frac{3P}{4\Delta\rho g}$$

$$B = \frac{R_0^2\Delta\rho g}{3\gamma}$$

$$C = \frac{\Delta\rho g}{3\gamma},$$

equal to Equation 5.4 in the main text.

C.4 Taylor expansion of Equation 5.4

Here we derive Equation 5.5 from Equation 5.4:

$$t = t_0 + \frac{U}{k} * \left[\sqrt{1-B} - \sqrt{1-CR^2} + ln\frac{1-\sqrt{1-B}}{1-\sqrt{1-CR^2}}\right] \tag{C.12}$$

with

$$U = \frac{3P}{4\Delta\rho g}$$

$$B = \frac{R_0^2\Delta\rho g}{3\gamma} = C * R_0^2$$

$$C = \frac{\Delta\rho g}{3\gamma},$$

We apply the Taylor expansion, only the linearised term $f(x) = f(a) + f'(a)\frac{(x-a)}{1!}$. As our function is too complex to apply the Taylor expansion directly to the whole equation we applied the Taylor expansion to the separate factors in the equation. For $\sqrt{1+x}$ around x=0 this is $1 + \frac{1}{2}x$, for $ln(1-x)$ this is $-x - \frac{x^2}{2}$. We label the term X as X^{T*} when the Taylor expansion is applied as the next step in the derivation.

C.4. TAYLOR EXPANSION OF EQUATION 5.4

$$
\begin{aligned}
t &= t_0 + \frac{U}{k} * \left[\sqrt{1-B} + ln(1-\sqrt{1-B}) - \sqrt{1-CR^2}^{T*} - ln(1-\sqrt{1-CR^2})^{T*}\right] \\
t &= t_0 + \frac{U}{k}\left[\sqrt{1-B} + ln(1-\sqrt{1-B}) - 1 - CR^2/2 - ln(CR^2/2)\right] \\
t &= t_0 + \frac{U}{k}\left[\sqrt{1-B} - 1 + ln(1-\sqrt{1-B}) + CR^2/2 - ln(\frac{BR^2}{2R_0^2})\right]
\end{aligned}
\tag{C.13}
$$

The terms ln(1-$\sqrt{1-B}$) and -ln(B/2) cancel each other out.

$$
\begin{aligned}
t &= t_0 + \frac{U}{k}\left[\sqrt{1-B}^{T*} - 1 + CR^2/2 - ln(\frac{R^2}{R_0^2})^{T*}\right] \\
t &= t_0 + \frac{U}{k}\left[1 - B/2 - 1 + CR^2/2 - \frac{BR^2}{2R_0^2} - ln(\frac{R^2}{R_0^2})\right] \\
t &= t_0 + \frac{U}{k}\left[B/2 * (R^2/R_0^2 - 1) - 2ln(\frac{R}{R_0})\right] \\
t &= t_0 + \frac{U}{k}\left[B/2 * (R^2/R_0^2 - 1) - 2\left[\frac{R}{R_0} - 1 - \frac{1 - 2R/R_0 + R^2/R_0^2}{2}\right]\right] \\
t &= t_0 + \frac{U}{k}\left[B/2 * (R^2/R_0^2 - 1) - 4\frac{R}{R_0} + 3 + \frac{R^2}{R_0^2}\right]
\end{aligned}
\tag{C.14}
$$

When $R \approx R_0$ the term $B/2 * (R^2/R_0^2 - 1) \approx 0$. The equation then becomes:

$$
\begin{aligned}
\frac{t - t_0}{\frac{U}{k}} &\approx \left[\frac{R^2}{R_0^2} - 4\frac{R}{R_0} + 3\right] \\
\frac{R}{R_0} &= 2 \pm \sqrt{1 + \frac{t - t_0}{U/k}}^{T*} \\
\frac{R}{R_0} &= 2 - (1 + \frac{t - t_0}{2U/k}) \\
\frac{R}{R_0} &= 1 - 1/2\frac{t - t_0}{U/k} \\
t - t_0 &= -(\frac{R}{R_0} - 1) * 2\frac{U}{k}
\end{aligned}
\tag{C.10}
$$

Finally resulting in the Equation 5.5:

$$t = t_0 - \frac{3P}{2k\Delta\rho g} * \left[\frac{R}{R_0} - 1\right] \tag{C.10}$$

Appendix D

Foam solidification

D.1 Preliminary results on generation of gelatine foam and frozen foam

Beside solidification of the foam by polymerisation we made attempts to jellify the foam using gelatine, secondly we tried to freeze foams either slowly by putting it in a freezer or quick using liquid nitrogen.

D.1.1 Gelatine foams

We used a commercial gelatine to jellify our foams. Gelatine is a protein in powder form that when mixed with water forms a gel (jelly), which solidifies depending on the temperature. Generally this melt temperature is around 35^oC [210]. We used nitrogen and perfluorhexane to generate bubbles and Fairy Liquid as surfactant. Samples were made at high temperatures ($\sim 60^oC$) and temperatures close to the melt temperature. The important differences in the samples lies in the viscosity difference at the time of sample generation and the time necessary for the sample to cool down until solidification.

When the samples were made at high temperatures bubbles could be created and were able to rearrange to form ordered structures. The samples were afterwards left to cool down. The cooling down lasted so long that coarsening occurred before the jelly was solidified and actually expansion occurred of the surface bubbles due to the use of perfluorhexane. A closed cell gelatine foam was formed. In the samples non-uniform cooling let to stress in the structures causing deformation of the bubble shape.

In the case where the temperature approached the melt temperature before the samples were generated, the viscosity had increased drastically such that the bubbles did not order anymore.

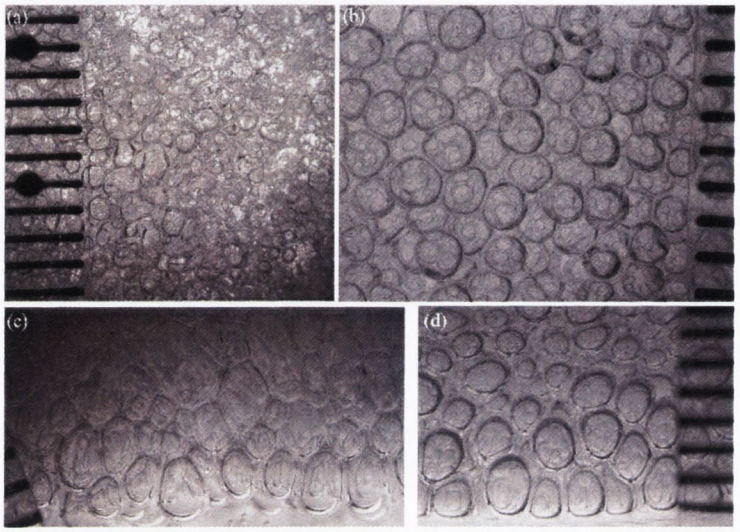


Figure D.1: Examples of jelly foam, made at high temperatures having a long cooling down period leading to coarsening and bubble deformation.(half mm scale)

D.1.2 Frozen foam

After the foam sample was made in the conventional way the sample was cooled. Either by just placing it in a freezer of a fridge (-18^oC) or with the use of liquid nitrogen (cryogenic freezing) where the sample is cooled down until -196^oC.

The slowly frozen samples made in the fridge were clearly affected by sublimation. The bubbles at the interface were broken. Condensate covered the sample quickly. The foam was frozen and showed as far as visible features of the original sample, of ordered arrangements of bubbles. Part of the sample was already melting interfering with observations. In Figure D.2 the result is shown of a sample out of a covered petridish 5 minutes after it was removed from the freezer. The bubbles in the middle of the sample are not affected by the melt and coarsening yet and the bubbles are seen to be still spherical and ordered.

Attempts to quickly freeze a sample by dipping a cup into a bath of liquid nitrogen froze the foam but sublimation was severe not leaving much left of the foam. Maybe the use of a closed cup to hold the sample could have prevented this, but this was not available at that moment.

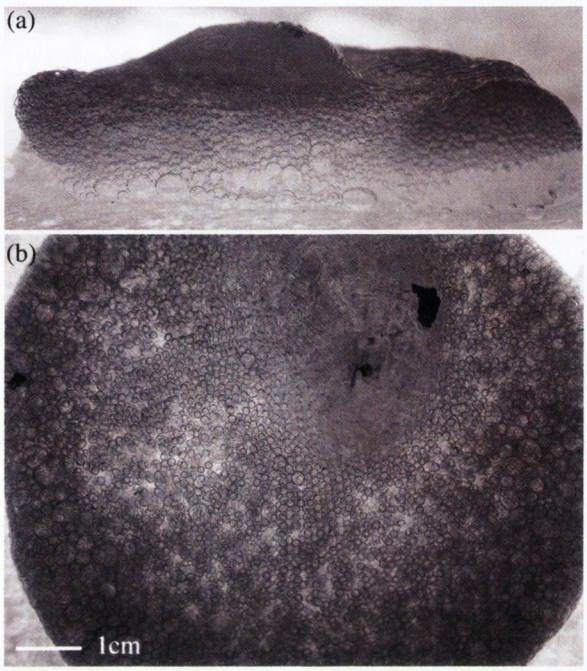


Figure D.2: Example of frozen foam. (a) the side view, (b) the top view. The sides of the sample are already melting and coarsening, where the middle of the sample is still frozen. It shows the bubbles remained spherical and ordered.

D.1.3 Discussion

Both our jellification and freezing methods need improvement. For the jellification we need to find the balance between a temperature low enough such the cooling down is short enough so that coarsening does not appear before solidification. However temperature also needs to be high enough such that the viscosity remains low enough for ordering of the bubbles to occur within the timespan of solidification. The cooling of the sample should be as uniform as possible as deformations can occur in the structure due to stresses.
The freezing resulted in frozen foam samples. Ideally the samples remain sealed during freezing to reduce sublimation. The handling afterwards needs to be improved by handling the sample in a cooled environment. Especially if we would like to cut the sample or make a 3D visualisation.

D.2 Role of polymerisation time

An overview of all the polymer samples taken, with different polymerisation times by changing the concentration of the accelerator (Temed) and initiator (Sops).

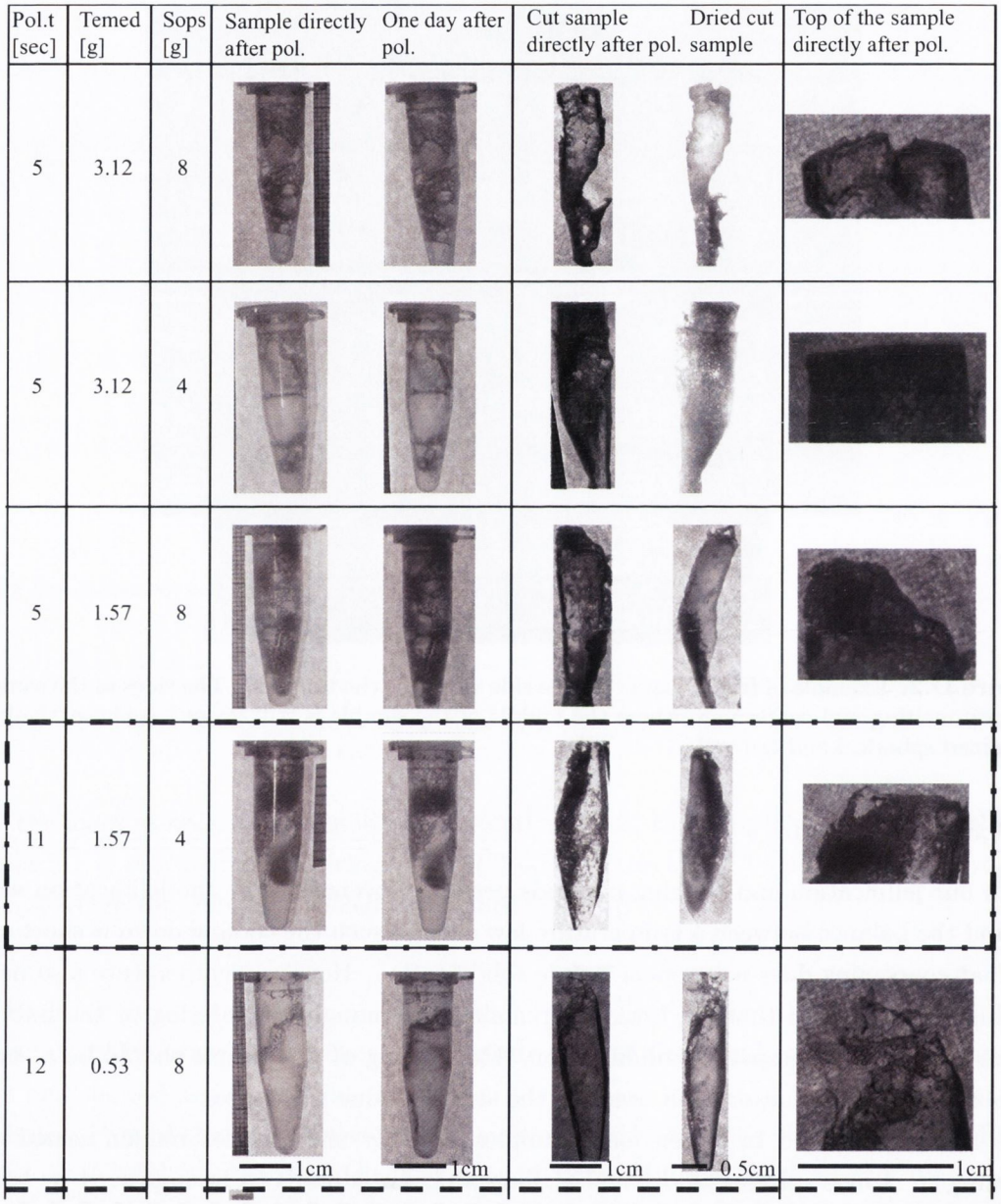


Figure D.3: Influence of the polymerisation time (first column) on foam polymerisation. The second and third column provide the accelerator (Temed) and initiator (Sops) concentration (recipe in Table 6.2). The fourth column shows the samples within the tube directly after polymerisation and after one day. The fifth column shows the cut samples, directly after polymerisation and after drying. The sixth column shows a close-up of the top of the cut samples directly after polymerisation. In these samples all of the foam is polymerised. The recipe of 11 seconds in the marked box is our base recipe for the generation of ordered foam. The dotted line marks the transition between foam polymerisation and phase separation of the foam.

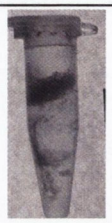
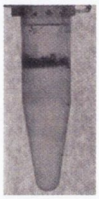
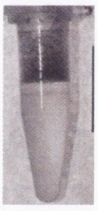
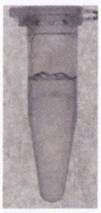
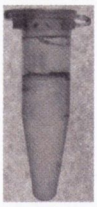
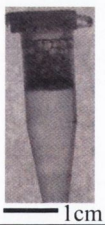
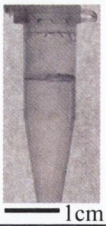
Pol.t [sec]	Temed [g]	Sops [g]	Sample directly after pol.	One day after pol.	Cut sample directly after pol.	Dried cut sample	Top of the sample directly after pol.
17	3.12	1					
18	3.12	0.5					
36	0.53	4					
38	1.57	0.5					
56	1.57	1	 1cm	 1cm	 1cm	 0.5cm	 1cm

Figure D.4: Influence of the polymerisation time (first column) on the success of foam polymerisation. The second and third column provide the accelerator (Temed) and initiator (Sops) concentration (recipe given in Table 6.2). The fourth column shows the images of the samples within the tube directly after polymerisation and after one day. The fifth column shows the cut samples, directly after polymerisation and after drying. The last column shows a close-up of the top of the cut samples directly after polymerisation. In all these samples phase separation occurred

Pol.t [sec]	Temed [g]	Sops [g]	Sample directly after pol.	One day after pol.	Cut sample directly after pol.	Dried cut sample	Top of the sample directly after pol.
180	0.53	1					
207	0.53	0.5					
350	3.12	0.17					
812	1.57	0.17					
2460	0.53	0.17	1cm	1cm	1cm	0.5cm	1cm

Figure D.5: Influence of the polymerisation time (first column) on the success of foam polymerisation. The second and third column provide the accelerator (Temed) and initiator (Sops) concentration (recipe given in Table 6.2). The fourth column shows the images of the samples within the tube directly after polymerisation and after one day. The fifth column shows the cut samples, directly after polymerisation and after drying. The last column shows a close-up of the top of the cut samples directly after polymerisation. In all these samples phase separation occurred.

D.3 Investigation of parameters controlling the phase separation in the radical polymerisation

Phase separation in polymerisation is the occurrence of a thermodynamic instability such that the polymer phase separates from the solvent, which contains also the bubbles. In our case the phase separation negatively influences the polymerisation of foams.

Here we discuss our preliminary study on parameters of phase separation (Section 6.2.3). We varied a range of parameters in some very basic and qualitative experiments, to gain insight into some of the key factors which control the phase separation. We used as a base recipe with a polymerisation time of 38 seconds (Figure D.4 and Table 6.2), which we found to be a desirable time span needed between foam generation and polymerisation.

Viscosity

An increased viscosity would be expected to slow down local dynamics and hence phase separation. We therefore replaced part of the water with glycerol, such that we reached a 40 % glycerol content, which increases the viscosity from 1 to 7 $mPas$. Larger viscosities were avoided to ensure reliable bubble generation. We did not observe a noticable effect on the phase separation.

Polymerisable surfactants

Using polymerisable surfactants [171] may reduce the expulsion of bubbles from the polymer network, as the surfactants become a part of the network themselves. We used Adeka reasoap ER10 and SR10 (provided by BASF), both 0.66 ml per 100 ml solution. Here phase separation still occurred, but the amount of bubbles which remained in the gel was clearly increased. However the bubbles which remained trapped were noticeably deformed.

Concentration of crosslinker

Phase separation is expected to be less dramatic with decreasing quality of crosslinker, as a 'looser' network can maintain a larger amount of water. We decreased the amount of N.N'-Methylenbis(acrylamide) by a factor of 3.3 (0.167 g per 100 ml solution instead of 0.53 g), but did not notice any significant effect on the phase separation.

Solvent concentration

If the expulsion of bubbles is based on the phase separation between the polymer network and the solvent, decreasing the amount of solvent should reduce the effect. We therefore decreased the water content to the minimum amount possible (the acrylamide solution already

contained 50 volume% water), such that in the final recipe Liquid I contained 6 g and Liquid II 6.65 g of water. This dramatic change in water content remained without noticeable effect on the phase separation. It was expected to decrease the phase separation, however, as a side effect the reduced water content leads to a significantly higher reaction temperature, which in turn may increase phase separation, hence provides a competing mechanism. These competing factors might therefore resulted in no noticeable effect.

Temperature
Reducing the temperature prolongs the polymerisation time at (what seems) a similar degree of phase separation. We have not been able to isolate its precise effect.

The question remains whether the gas bubbles are in the solvent because the solvent is lighter than the formed polymer or because of chemical reasons. The bubbles will prefer the location as close to the surface as possible due to buoyancy forces. If the latter was to be the case an experiment with a heavier solvent than the formed polymer might resolve this question.

We conclude from these qualitative tests that a reduction of temperature and the use of the polymerisable surfactants may have a positive effect on extending the onset before phase separation in our recipe. However, a much more systematic approach is required e.g. by the creation of a phase diagram based on the different factors, to understand and control properly this phenomenon, which is at the heart of successful foam polymerisation.

Bibliography

[1] P. R. Garrett, editor. *Defoaming*, volume 45 of *Surfactant Science Series*. Marcel Dekker, New York, 1993.

[2] N. Matubayashi, H. Matsuo, K. Yamamoto, S. Yamaguchi, and A. Matuzawa. Thermodynamic quantities of surface formation of aqueous electrolyte solutions - i. aqueous solutions of NaCl, $MgCl_2$, and $LaCl_3$. *Journal of Colloid and Interface Science*, 209(2):398–402, 1999.

[3] J. T. Davies and E. K. Rideal. *Interfacial Phenomina*. Academic Press, New York-London, 2 edition, 1963.

[4] J. A. F. Plateau. *Statique expérimentale et théorique des liquides soumis aux seules forces moléculaires*. Gauthier-Villars, Paris, 1873.

[5] D. Weaire and S. Hutzler. *The physics of foams*. Clarendon Press, Oxford, 1999.

[6] A. Saint-Jalmes and D. Langevin. Time evolution of aqueous foams: drainage and coarsening. *Journal of Physics-Condensed Matter*, 14(40):9397–9412, 2002.

[7] A. M. Ganan-Calvo and J. M. Gordillo. Perfectly monodisperse microbubbling by capillary flow focusing. *Physical Review Letters*, 87(27):274501, 2001.

[8] W. Drenckhan and D. Weaire. Discrete microfluidics. In Colloids Elsevier Science and Surfaces A, editors, *EUFoam 2006*, Potsdam, Germany, 2006.

[9] A. M. Ganan-Calvo. Generation of steady liquid microthreads and microns-sized monodisperse sprays in gas streams. *Physical Review Letters*, 80(2):285–288, 1998.

[10] A. M. Ganan-Calvo. Perfectly monodisperse microbubbling by capillary flow focusing: An alternate physical description and universal scaling. *Physical Review E*, 69(2):027301, 2004.

[11] P. B. Umbanhowar, V.Prasad, and D. A. Weitz. Monodisperse emulsion generation via drop break off in coflowing stream. *Langmuir*, 2000(16):347–351, 1999.

[12] J. M. Gordillo, Z.Cheng, A. M. Ganan-Calvo, M. Marquez, and D. A. Weitz. A new device for the generation of microbubbles. *Physics of Fluids*, 16(8):2828–2834, 2004.

[13] T. Thorsen, R. W. Roberts, F. H. Arnold, and S. R. Quake. Dynamic pattern formation in a vesicle-generating microfluidic device. *Physical Review Letters*, 86(18):4163–4166, 2001.

[14] A. S. Utada, E. Lorenceau, D. R. Link, P. D. Kaplan, H. A. Stone, and D. A. Weitz. Monodisperse double emulsions generated from a microcapillary device. *Science*, 308(5721):537–541, 2005.

[15] E. Rosa and M. A. Fortes. Private communication, 2006.

[16] Kenneth A. Brakke. The surface evolver. *Experimental Mathematics*, 1(2), 1992.

[17] M. U. Vera and D. J. Durian. Enhanced drainage and coarsening in aqueous foams. *Physical Review Letters*, 88(8):088304, 2002.

[18] L. Bragg and J. F. Nye. A dynamical model of a crystal structure. *Proceedings of the Royal Society of London Series A-Mathematical and Physical Sciences*, 190(1023):474–481, 1947.

[19] J. F. Nye. Private communication, 2005.

[20] A. van der Net, W. Drenckhan, D. Weaire, and S. Hutzler. The crystal structure of bubbles in the wet foam limit. *Soft Matter*, 2(2):129–134, 2006.

[21] Reinhard Hohler, Yann Yip Cheung Sang, Elise Lorenceau, and Sylvie Cohen-Addad. Osmotic pressure and structures of monodisperse ordered foam. *Langmuir*, 24(2):418–425, 2007.

[22] D. J. Tritton and C. Egdell. Chaotic bubbling. *Physics of Fluids a-Fluid Dynamics*, 5(2):503–505, 1993.

[23] C. S. Smith. On blowing bubbles for Braggs dynamic crystal model. *Journal of Applied Physics*, 20(6):631–631, 1949.

[24] P. Perrin. A one-step method to create and immobilize the ordered structures of fluid dispersions. *Langmuir*, 16(11):4774–4778, 2000.

[25] A. M. Ganan-Calvo and A. Barrero. A novel pneumatic technique to generate steady capillary microjets. *Journal of Aerosol Science*, 30(1):117–125, 1999.

[26] I. Cohen, H. Li, J. Hougland, M. Mrksich, and S. R. Nagel. Using selective withdrawal to coat microparticles. *Science*, 292:265–267, 2001.

[27] P. Garstecki, M. J. Fuerstman, and G. M. Whitesides. Nonlinear dynamics of a flow-focusing bubble generator: An inverted dripping faucet. *Physical Review Letters*, 94(23), 2005. 234502.

[28] L. Martin-Banderas, M. Flores-Mosquera, P. Riesco-Chueca, A. Rodriguez-Gil, A. Cebolla, S. Chavez, and A. M. Ganan-Calvo. Flow focusing: A versatile technology to produce size-controlled and specific-morphology microparticles. *Small*, 1(7):688–692, 2005.

[29] E. Lorenceau, Y. Y. C. Sang, R. Hohler, and S. Cohen-Addad. A high rate flow-focusing foam generator. *Physics of Fluids*, 18(9), 2006. 097103.

[30] W. Drenckhan, S. J. Cox, G. Delaney, H. Holste, D. Weaire, and N. Kern. Rheology of ordered foams - on the way to discrete microfluidics. *Colloids and Surfaces a-Physicochemical and Engineering Aspects*, 263(1-3):52–64, 2005.

[31] S. Ramakrishnan, R. Kumar, and N. R. Kuloor. Studies in bubble formation; 1. bubble formation under constant flow conditions. *Chemical Engineering Science*, 24(4):731–747, 1969.

[32] S. C. Chuang and V. W. Goldschmidt. Bubble formation due to a submerged capillary tube in quiescent and coflowing streams. *Mechanical Engineering*, 92(10):705–711, 1970.

[33] Hasan N. Oguz and Andrea Prosperetti. Dynamics of bubble growth and detachment for a needle. *Journal of Fluid Mechanics*, 257:111–145, 1993.

[34] P. Snabre and F. Magnifotcham. I. formation and rise of a bubble stream in a viscous liquid. *European Physical Journal B*, 4(3):369–377, 1998.

[35] Bernhard J. Meister and George F. Scheele. Drop formation from cylindrical jets in immiscible liquid systems. *Aiche Journal*, 15(5):700–706, 1969.

[36] K. Chen and H. J. Richter. Instability analysis of the transition from bubbling to jetting in a gas injected into a liquid. *International Journal of Multiphase Flow*, 23(4):699–712, 1997.

[37] DeeracFluidics. *Microdispenser*. www.deerac.com.

[38] A. Bhunia, S. C. Pais, Y. Kamotani, and I. H. Kim. Bubble formation in a coflow configuration in normal and reduced gravity. *Aiche Journal*, 44(7):1499–1509, 1998.

[39] A. Sevilla, J. M. Gordillo, and C. Martinez-Bazan. Bubble formation in a coflowing air-water stream. *Journal of Fluid Mechanics*, 530:181–195, 2005.

[40] H. Tsuge, S. Hibino, and U. Noijma. Volume of a bubble formes at a single submerged orifice in a flowing liquid. *International Chemical Engineering*, 21(4):630–636, 1981.

[41] T. Kawakatsu, Y. Kikuchi, and M. Nakajima. Regular-sized cell creation in microchannel emulsification by visual microprocessing method. *Journal of the American Oil Chemists' Society*, 74(3):317–321, 1997.

[42] J. H. Xu, S. Li, G. G. Chen, and G. S. Luo. Formation of monodisperse microbubbles in a microfluidic device. *Aiche Journal*, 52(6):2254–2259, 2006.

[43] P. Garstecki, M. J. Fuerstman, H. A. Stone, and G. M. Whitesides. Formation of droplets and bubbles in a microfluidic T-junction - scaling and mechanism of break-up (vol 6, pg 437, 2006). *Lab on a Chip*, 6(5):693–693, 2006.

[44] P. Garstecki, M. J. Fuerstman, and G. M. Whitesides. Oscillations with uniquely long periods in a microfluidic bubble generator. *Nature Physics*, 1(3):168–171, 2005.

[45] T. G. Mason and J. Bibette. Shear rupturing of droplets in complex fluids. *Langmuir*, 13(17):4600–4613, 1997.

[46] P. Perrin. Amphiphilic copolymers: A new route to prepare ordered monodisperse emulsions. *Langmuir*, 14(21):5977–5979, 1998.

[47] P. Perrin, N. Devaux, P. Sergot, and F. Lequeux. Shear-induced formation of ordered monodisperse emulsions stabilized by an associating amphiphilic polyelectrolyte. *Langmuir*, 17(9):2656–2663, 2001.

[48] G. I. Taylor. The formation of emulsions in definable fields of flow. *Proceedings of the Royal Society of London. Series A*, 146(858):501–523, 1934.

[49] P. Garstecki, L. Gitlin, W. DiLuzio, and G. M. Whitesides. Formation of monodisperse bubbles in a microfluidic flow-focusing device. *Applied Physics Letters*, 85(13):2649–2651, 2004.

[50] P. Garstecki, A. M. Ganan-Calvo, and G. M. Whitesides. Formation of bubbles and droplets in microfluidic systems. *Bulletin of the Polish Academy of Sciences*, 53(4):361–372, 2005.

[51] S. L. Anna, N. Bontoux, and H. A. Stone. Formation of dispersions using "flow focusing" in microchannels. *Applied Physics Letters*, 82(3):364–366, 2003.

[52] Qingyi Xu and Mitsutoshi Nakajima. The generation of highly monodisperse droplets through the breakup of hydrodynamically focused microthread in a microfluidic device. *Applied Physics Letters*, 85(17):3726–3728, 2004.

[53] C. Priest, S. Herminghaus, and R. Seemann. Generation of monodisperse gel emulsions in a microfluidic device. *Applied Physics Letters*, 88(2):024106, 2006.

[54] M. W. Weber and R. Shandas. Computational fluid dynamics analysis of microbubble formation in microfluidic flow-focusing devices. *Microfluid Nanofluid*, 3:195–206, 2007.

[55] Image J. *http://rsb.info.nih.gov/ij/*.

[56] Jan-Paul Raven. *Generation, flow and manipulation of a microfoam.* PhD thesis, Universite Joseph Fourier, 2007.

[57] Jan-Paul Raven. Private communication, 2008.

[58] W. E. Forsythe (1954) and Knovel (2003). Smithsonian Physical Tables (9th revised edition), table 314. page pp. 322. Smithsonian Institution Press.

[59] M. Durand, G. Martinoty, and D. Langevin. Liquid flow through aqueous foams: From the Plateau border-dominated regime to the node-dominated regime. *Physical Review E*, 60(6):R6307, 1999.

[60] O. Pitois, C. Fritz, and M. Vignes-Adler. Liquid drainage through aqueous foam: study of the flow on the bubble scale. *Journal of Colloid and Interface Science*, 282:458–465, 2005.

[61] W. Drenckhan, H. Ritacco, A. Saint-Jalmes, A. Saugey, P. McGuinness, A. van der Net, D. Weaire, and D. Langevin. Fluid dynamics of rivulets between plates. *Physics of Fluids*, 19(102101), 2007.

[62] J. P. Raven and P. Marmottant. Periodic microfluidic bubbling oscillator: Insight into the stability of two-phase microflows. *Physical Review Letters*, 97(15), 2006. 154501.

[63] J.G. Roof. Snap-off of oil droplets in water-wet pores. *Society of Petroleum Engineers Journal*, 2504:85–90, 1970.

[64] A. R. Kovscek and C. J. Radke. Fundamentals of foam transport in porous media. In *Foams: Fundamentals and applications in the petroleum industry.* American Chemical Society, 1994.

[65] W. R. Rossen. Foams in enhanced oil recovery. In R.K. Prud'homme and S.A Khan, editors, *Foams, Theory, Measurement and Application*, volume 57 of *Surfactant Science Serie*, pages 413–464. 1995.

[66] K. T. Chambers and C. J. Radke. Capillary phenomena in foam flow through porous media. In N.R. Morrow, editor, *Interfacial phenomena in petroleum recovery*, volume 36. Dekker, New York, 1990.

[67] W. R. Rossen. A critical review of roof snap-off as a mechanism of steady state foam generation in homogeneous porous media. *Colloids and Surfaces A: Physiochemical and Engineering Aspects*, 225:1–24, 2003.

[68] W. R. Rossen. Snap-off in contricted tubes and porous media. *Colloids and Surfaces A: Physiochemical and Engineering Aspects*, 166:101–107, 2000.

[69] M. Chen, Y. C. Yortsos, and W. R. Rossen. Insights on foam generation in porous media form pore-network studies. *Colloids and Surfaces A: Physiochemical and Engineering Aspects*, 256:181–189, 2005.

[70] Quoc P. Nguyen. *Dynamics of foam in porous media.* PhD thesis, Delft University of Technology, 2004.

[71] S. Osher and J. Sethian. Fronts propagation with curvature -dependent speed: Algoritms based on Hamiltonon-Jacobi formulation. *Journal of Computational Physics*, 79(1):12–49, 1988.

[72] D. J. Durian, D. A. Weitz, and D. J. Pine. Dynamics and coarsening in 3-dimensional foams. *Journal of Physics-Condensed Matter*, 2:SA433–SA436, 1990. Suppl. A.

[73] D. J. Durian, D. A. Weitz, and D. J. Pine. Scaling behavior in shaving cream. *Physical Review A*, 44(12):R7902–R7905, 1991.

[74] F. Sebba. *Foams and biliquid foams-aphrons.* Chichester, Wiley, 1987.

[75] D. J. Pine, D. A. Weitz, P. M. Chaikin, and E. Herbolzheimer. Diffusing-wave spectroscopy. *Physical Review Letters*, 60(12):1134–1137, 1988.

[76] J. C. Earnshaw and A. H. Jaafar. Diffusing-wave spectroscopy of a flowing foam. *Physical Review E*, 49(6):5408–5411, 1994.

[77] M. U. Vera, A. Saint-Jalmes, and D. J. Durian. Scattering optics of foam. *Applied Optics*, 40(24):4210–4214, 2001.

[78] D. S. Langley and P. L. Marston. Critical-angle scattering of laser-light from bubbles in water - measurements, models, and application to sizing of bubbles. *Applied Optics*, 23(7):1044–1054, 1984.

[79] C. Bongiovanni, A. Dominguez, and J. P. Chevaillier. Understanding images of bubbles. *European Journal of Physics*, 21:561–570, 2000.

[80] G. M. Hansen. Mie scattering as a technique for the sizing of air bubbles. *Applied Optics*, 24(19):3214–3220, 1985.

[81] Autodesk. 3D Studio Max, www.autodesk.com/3dsmax, 2006.

[82] Cebas. Final render, www.finalrender.com.

[83] Maxwellrender. www.maxwellrender.com, 2006.

[84] Mathworld. Matlab, www.mathworks.com/products/matlab/.

[85] Eugene Hecht. *Theory and problems of optics.* Schaum's outline series. New York, London, McGraw-Hill Book company, 1975.

[86] Andrew S. Glassner, editor. *An introduction to ray tracing.* London Academics, 1989.

[87] Nicolas Bremond, Abdou R. Thiam, and Jerome Bibette. Decompressing emulsion droplets favors coalescence. *Physical Review Letters*, 100(024501), 2008.

[88] P. Ghosh and V. A. Juvekar. Effect of temperature on permeation of air through thin liquid films. *Journal of Chemical Engineering of Japan*, 36(6):711–715, 2003.

[89] G. Liger-Belair and P. Jeandet. Capillary-driven flower-shaped structures around bubbles collapsing in a bubble raft at the surface of a liquid of low viscosity. *Langmuir*, 19(14):5771–5779, 2003.

[90] A. A. elKader and J. C. Earnshaw. Stability of two-dimensional foam. *Philosophical Magazine a-Physics of Condensed Matter Structure Defects and Mechanical Properties*, 76(6):1251–1260, 1997.

[91] Y. Ishida. In Geoffrey Allan Chadwick and David Anthony Smith, editors, *Grain boundary structure and properties*, page Chapter 3. Academic press, London, 1976.

[92] E. Fukushima and A. Ookawa. Some characters of the soap bubble raft in vibrating state. *Journal of the Physical Society of Japan*, 10(11):970–981, 1955.

[93] E. Fukushima and A. Ookawa. The transition structure of the grain boundary observed in soap bubble raft. *Journal of the Physical Society of Japan*, 8(1):129–130, 1953.

[94] E. Fukushima and A. Ookawa. Observation of the grain boundary in soap bubble raft .1. static feature of the grain boundary. *Journal of the Physical Society of Japan*, 8(5):609–614, 1953.

[95] R. Philips. *Crystals, Defects, Microstructures; Modeling across scales.* Cambridge University Press, Cambridge, 2001.

[96] H. J. Schope. Formation of dried colloidal monolayers and multilayers under the influence of electric fields. *Journal of Physics-Condensed Matter*, 15(33):L533–L540, 2003.

[97] M. M. Nicolson. The interaction between floating particles. *Proceedings of the Cambridge Philosophical Society*, 45(2):288–295, 1949.

[98] O. Pouliquen, M. Nicolas, and P. D. Weidman. Crystallization of non-brownian spheres under horizontal shaking. *Physical Review Letters*, 79(19):3640–3643, 1997.

[99] Gary W. Delaney. *Computational studies of the structure and dynamics of packings of grains and bubbles.* PhD thesis, Trinity College Dublin, Ireland, 2006.

[100] D. Wolf. Chapter modelling and computer simulation of granular media. In *Computational Physics*, pages 64–95. Springer-Verlag Berlin, 1996.

[101] O. Carvente and J. C. Ruiz-Suarez. Crystallization of confined non-Brownian spheres by vibrational annealing. *Physical Review Letters*, 95(1), 2005. 018001.

[102] L. V. Woodcock. Computation of the free energy for alternative crystal structures of hard spheres. *Faraday Discussions*, 106(106):325–338, 1997.

[103] D. Weaire and R. Phelan. A counterexample to Kelvin conjecture on minimal-surfaces. *Philosophical Magazine Letters*, 69(2):107–110, 1994.

[104] S. Herminghaus. http://www-dcf.ds.mpg.de/build.php/rseemann/digitalmicrofluidicsenglish.html, 2008.

[105] Robert Brown. A brief account of microscopical observations made in the months of June, July and August, 1827, on the particles contained in the pollen of plants; and on the general existence of active molecules on organic and inorganic bodies. *Edinburgh New Philosophical Journal*, pages 358–371, 1828.

[106] T. Aste and D. Weaire. *The pursuit of perfect packing.* Institute of Physics Publishing, 2000.

[107] D. A. Weitz. Packing in the spheres. *Science*, 303(5660):968–969, 2004.

[108] J. Kepler. Strena seu de nive sexangula (on the six-cornered snowflake). 1611.

[109] Thomas C. Hales. Historical overview of the Kepler conjecture. *Discrete and computational geometry*, 36(1):5–20, 2006.

[110] G. Y. Onoda and E. G. Liniger. Random loose packings of uniform spheres and the dilatancy onset. *Physical Review Letters*, 64(22):2727–2730, 1990.

[111] D. E. Wolf. Modelling and computer simulations of granular media. In K.H. Hoffmann and M. Schreiber, editors, *Computational Physics.* Springer-Verlag, Berlin, 2001.

[112] Y. Nahmad-Molinari and J. C. Ruiz-Suarez. Epitaxial growth of granular single crystals. *Physical Review Letters*, 89(26), 2002. 264302.

[113] P. Bartlett and W. van Megen. Physics of hard-sphere colloidal suspensions. In Anita Mehta, editor, *Granular Matter, an interdisciplinary approach*, pages 195–257. Springer-Verlag, 1994.

[114] A. van Blaaderen. Colloidal molecules and beyond. *Science*, 301(5632):470–471, 2003.

[115] D. H. Everett. *Basic Principles of Colloid Science.* Royal Society of Chemistry Paperbacks. Royal Society of Chemistry, 1988.

[116] R. K. Prud'homme and S. A. Khan, editors. *Foams, Theory, Measurements, and Applications*, volume 57 of *Surfactant Science Series.* Marcel Dekker, Inc., New York, 1996.

[117] B. V. R. Tata. Colloidal dispersions and phase transitions in charged colloids. *Current Science*, 80(8):948–958, 2001.

[118] Ian W. Hamley. *Introduction to Soft matter, Polymers, Colloids, Amphiphiles and Liquid crystals.* John Wiley and Sons, LTD, Chichester, 2000.

[119] H. Lowen. Colloidal soft matter under external control. *Journal of Physics: Condensed Matter*, 13:R415–R432, 2001.

[120] J. X. Zhu, M. Li, R. Rogers, W. Meyer, R. H. Ottewill, W. B. Russell, and P. M. Chaikin. Crystallization of hard-sphere colloids in microgravity. *Nature*, 387(6636):883–885, 1997.

[121] X. Xian, A. V. Petukhov, M. M. E. Snel, I. P. Dolbnya, Dgal Aarts, G. J. Vroege, and H. N. W. Lekkerkerker. Depletion-induced colloidal crystals at a wall characterised by small-angle X-ray diffraction. *Journal of Applied Crystallography*, 36:597–601, 2003.

[122] H. Miguez, F. Meseguer, C. Lopez, A. Mifsud, J. S. Moya, and L. Vazquez. Evidence of fcc crystallization of SiO_2 nanospheres. *Langmuir*, 13(23):6009–6011, 1997.

[123] Mayoral R., Requena J., Moya J. S., Lopez C., Cintas A., Miquez H., Meseguer F., Vazquez L., Holgado M., and Blanco A. 3D long range ordering in an SoO_2 submicrometer-sphere sintered superstructure. *Advanced Materials*, 9(3):257–260, 1997.

[124] O. D. Velev. Self-assembly of unusual nanoparticle crystals. *Materials Science*, 312:376–377, 2006.

[125] P. N. Pusey, W. Vanmegen, P. Bartlett, B. J. Ackerson, J. G. Rarity, and S. M. Underwood. Structure of crystals of hard colloidal spheres. *Physical Review Letters*, 63(25):2753–2756, 1989.

[126] P. N. Pusey and W. Vanmegen. Phase-behavior of concentrated suspensions of nearly hard colloidal spheres. *Nature*, 320(6060):340–342, 1986.

[127] D. J. W. Aastuen, N. A. Clark, L. K. Cotter, and B. J. Ackerson. Nucleation and growth of colloidal crystals. *Physical Review Letters*, 57(14):1733–1736, 1986.

[128] J. L. Harland, S. I. Henderson, S. M. Underwood, and W. van Megen. Observation of accelerated nucleation in dense colloidal fluids of hard-sphere particles. *Physical Review Letters*, 75(19):3572–3575, 1995.

[129] U. Gasser, E. R. Weeks, A. Schofield, P. N. Pusey, and D. A. Weitz. Real-space imaging of nucleation and growth in colloidal crystallization. *Science*, 292(5515):258–262, 2001.

[130] O. D. Velev and A. M. Lenhoff. Colloidal crystals as templates for porous materials. *Current Opinion in Colloid and Interface Science*, 5(1-2):56–63, 2000.

[131] A. van Blaaderen, R. Ruel, and P. Wiltzius. Template-directed colloidal crystallization. *Nature*, 385(6614):321–324, 1997.

[132] J. P. Hoogenboom, A. Yethiraj, A. K. van Langen-Suurling, J. Romijn, and A. van Blaaderen. Epitaxial crystal growth of charged colloids. *Physical Review Letters*, 89(25):256104 1–4, 2002.

[133] Yadong Yin and Younan Xia. Growth of large colloidal crystals with their (100) planes oriented parallel to the surface of supporting substrates. *Advanced Materials*, 14(8):605–608, 2002.

[134] J. P. Hoogenboom, A. K. van Langen-Suurling, J. Romijn, and A. van Blaaderen. Epitaxial growth of a colloidal hard-sphere hcp crystal and the effects of epitaxial mismatch on crystal structure. *Physical Review E*, 69(5):051602, 2004.

[135] W van Megen and S. M. Underwood. Change in crystallization mechanism at the glass transition of colloidal spheres. *Nature*, 362:616–618, 1993.

[136] N. A. Clark, A. J. Hurd, and B. J. Ackerson. Single colloidal crystals. *Nature*, 281:57–60, 1979.

[137] I. Cohen, T. G. Mason, and D. A. Weitz. Shear-induced configurations of confined colloidal suspensions. *Physical Review Letters*, 93(4), 2004.

[138] E. Kumacheva, P. Garstecki, W. Hongkai, and G. M. Whitesides. Two-dimensional colloidal crystals obtained by coupling of flow and confinement. *Physical Review Letters*, 91(12), 2003.

[139] S. Hutzler, D. Weaire, and R. Crawford. Moving boundaries in ordered cylindrical foam structures. *Philosophical Magazine B*, 75(6):845–857, 1997.

[140] A. Fortini and M. Dijkstra. Phase behaviour of hard spheres confined between parallel hard plates: manipulation of colloidal crystal structures by confinement. *Journal of Physics-Condensed Matter*, 18(28):L371–L378, 2006.

[141] B. V. R. Tata, D. Boda, D. Henderson, A. Nikolov, and D. T. Wasan. Structure of charged colloids under a wedge confinement. *Physical Review E*, 62(3):3875–3881, 2000. Part B.

[142] W. Drenckhan, D. Weaire, and S. J. Cox. The demonstration of conformal maps with two-dimensional foams. *European Journal of Physics*, 25:429–438, 2004.

[143] D. Weaire and R. Phelan. Optimal design of honeycombs. *Nature*, 367:123, 1994.

[144] P. Pieranski, L. Strzelecki, and B. Pansu. Thin colloidal crystals. *Physical Review Letters*, 50(12):900–903, 1983.

[145] S. Neser, C. Bechinger, P. Leiderer, and T. Palberg. Finite-size effects on the closest packing of hard spheres. *Physical Review Letters*, 79(12):2348–2351, 1997.

[146] M. Schmidt and H. Lowen. Freezing between two and three dimensions. *Physical Review Letters*, 76(24):4552–4555, 1996.

[147] M. D. Lacasse, G. S. Grest, and D. Levine. Deformation of small compressed droplets. *Physical Review E*, 54(5):5436–5446, 1996.

[148] Shiyi Chen, Gary D. Doolen, and Kenneth G. Eggert. Lattice-Boltzmann fluid dynamics, a versatile tool for multiphase and other complicated flows. *Los Alamos Science*, 22:98–110, 1994.

[149] H. D. Young and R. A. Freedman. *University Physics*. Addison-Wesley series in Physics. Addison-Wesley, 9th edition, 1996.

[150] J. Lambert, I. Cantat, R. Delannay, A. Renault, F. Graner, J. A. Glazier, I. Veretennikov, and P. Cloetens. Extraction of relevant physical parameters from 3D images of foams obtained by X-ray tomography. *Colloids and Surfaces a-Physicochemical and Engineering Aspects*, 263(1-3):295–302, 2005.

[151] C. P. Gonatas, J. S. Leigh, A. G. Yodh, J. A. Glazier, and B. Prause. Magnetic-resonance images of coarsening inside a foam. *Physical Review Letters*, 75(3):573–576, 1995.

[152] J. Lambert, I. Cantat, R. Delannay, R. Mokso, P. Cloetens, J. A. Glazier, and F. Graner. Experimental growth law for bubbles in a moderately "wet" 3D liquid foam. *Physical Review Letters*, 99(5), 2007. 058304.

[153] C. Monnereau and M. Vignes-Adler. Dynamics of 3D real foam coarsening. *Physical Review Letters*, 80(23):5228–5231, 1998.

[154] R. Krustev, D. Platikanov, and M. Nedyalkov. Permeability of common black foam films to gas, II. *Colloids and Surfaces a-Physicochemical and Engineering Aspects*, 123:383–390, 1997.

[155] A. M. Ganan-Calvo, J. M. Fernandez, A. M. Oliver, and M. Marquez. Coarsening of monodisperse wet microfoams. *Applied Physics Letters*, 84(24):4989–4991, 2004.

[156] A. G. Brown, W. C. Truman, and J. W. McBain. Transfer of air through adsorbed surface films as a factor in foam stability. *Journal of Colloid Science*, 8:508, 1953.

[157] H. M. Princen and S. G. Mason. Permeability of soap films to gases. *Journal of Colloid Science*, 20(4):353–375, 1965.

[158] H. M. Princen, J. T. Overbeek, and S. G. Mason. Permeability of soap films to gases : 2. a simple mechanism of monolayer permeability. *Journal of Colloid and Interface Science*, 24(1):125–130, 1967.

[159] R. Krustev, D. Platikanov, and M. Nedyalkov. Permeability of common black foam films to gas, I. *Colloids and Surfaces a-Physicochemical and Engineering Aspects*, 79(1):129–136, 1993.

[160] H. M. Princen. Shape of a fluid drop at a liquid-liquid interface. *Journal of Colloid Science*, 18(2):178–195, 1963.

[161] R. M. Muruganathan, R. Krustev, H. J. Muller, H. Mohwald, B. Kolaric, and R. von Klitzing. Foam films stabilized by dodecyl maltoside. 1. film thickness and free energy of film formation. *Langmuir*, 20(15):6352–6358, 2004.

[162] W. E. Forsythe (1954) and Knovel (2003). Smithsonian Physical Tables (9th revised edition), table 626. page pp. 592. Smithsonian Institution Press.

[163] M. G. Rasul. Buoyancy force in liquid fluidized beds of mixed particles. *Particle and Particle Systems Characterization*, 16(6):284–289, 1999.

[164] M. C. Ruzicka. On buoyancy in dispersion. *Chemical Engineering Science*, 61(8):2437–2446, 2006.

[165] R. Krustev and H. J. Muller. An apparatus for the measurement of the gas permeability of foam films. *Review of Scientific Instruments*, 73(2):398–403, 2002.

[166] F. G. Gandolfo and H. L. Rosano. Interbubble gas diffusion and the stability of foams. *Journal of Colloid and Interface Science*, 194(1):31–36, 1997.

[167] Kenneth C. Lowe, Michael R. Davey, and J. Brian Power. Perfluorochemicals: their application and benfits to cell culture. *Trends in Biotechnology*, 16(6):272–277, 1998.

[168] Hans-Georg Elias. *An introduction to polymer science.* VCH Verlagsgesellschaft mbH, Weinheim, 1997.

[169] Robert G. Gilbert. *Emulsion polymerisation, a mechanistic approach.* Academic Press, London, 1995.

[170] San Hyun Park and Younan Xia. Fabrication of three-dimensional macroporous membranes with assemblies of microspheres as templates. *Chemical Materials*, 10:1745–1747, 1998.

[171] S. E. Friberg and J-H. Fang. Foams from aqueous systems of polymerizable surfactants. *Journal of Colloid and Interface Science*, 118(2):543–551, 1987.

[172] W. R. Palani Raj, Mohan Sasthav, and H. Micheal Chueng. Formation of polymeric foams from aqueous foams stabilized using a polymerizable surfactant. *Journal of Applied Polymer Science*, 49(8):1453–1470, 1993.

[173] S. Durmaz and O. Okay. Phase separation during formation of poly(acrylamide) hydrogels. *Polymer*, 41:5729–5735, 2000.

[174] J. B. Nephew, T. C. Nihei, and S. A. Carter. Reaction-induced pahse separation dynamics: A polymer in a liquid crystal solvent. *Physical Review Letters*, 80(15):3276–3279, 1998.

[175] Terry L. Guckes, Mark A. McHugh, Charles Cozewith, and L. Hazelton. Phase separation processes. *United States Patent*, 4 946 940(232 713), 1988.

[176] J. M. Ottino and S. Wiggins. Introduction: mixing in microfluidics. *Philosophical Transactions of the Royal Society of London Series A-Mathematical Physical and Engineering Sciences*, 362(1818):923–935, 2004.

[177] H. A. Stone, A. D. Stroock, and A. Ajdari. Engineering flows in small devices: Microfluidics toward a lab-on-a-chip. *Annual Review of Fluid Mechanics*, 36:381–411, 2004.

[178] P. J. Flory. *Principle of Polymer Chemistry.* Cornell University Press, Ithaca, New York, 1953.

[179] Urs T. Gonzenbach, Andre R. Studart, Elena Tervoort, and Ludwig J. Gauckler. Ultrastable particle-stabilized foams. *Angewandte Chemie International Edition*, 45(21):3526–3530, 2006.

[180] Wonje Jeong, Jeongyun Kim, Sunjeong Kim, Sanghoon Lee, Glennys Mensing, and David J. Beebe. Hydrodynamic microfabrication via 'on the fly' photopolymerization of microscale fibers and tubes. *Lab Chip*, 4:576–580, 2004.

[181] Yonglai Yang, Mool C. Gupta, Kenneth L. Dudley, and Roland W. Lawrence. Novel carbon nanotube- polystyrene foam composites for eectromagnetic interference shielding. *Nanoletters*, 5(11):2131–2134, 2005.

[182] M. H. Pahl and D. Franke. Schaum und schaumzerstorung- ein uberblick. *Chem. Ing. Tech.*, 67:300–312, 1995.

[183] V. Bergeron, P. Cooper, C. Fischer, J. Giermanska-Kahn, D. Langevin, and A. Pouchelon. Polydimethylsiloxane (PDSM)-based antifoams. *Colloids and Surfaces A: Physiochemical and Engineering Aspects*, 122:103–120, 1997.

[184] M. Postema, P. Marmottant, C. T. Lancee, S. Hilgenfeldt, and N. de Jong. Ultrasound-induced microbubble coalescence. *Ultrasound in Medicine and Biology*, 30(10):1337–1344, 2004.

[185] Yoshihiro Chikamori, Yoshihiko Shibata, and Yoichi Shimizu. Foam-breaking device. *http://www.freepatentsonline.com/EP0376634B1.html*, (EP19890313467), 1989.

[186] B. Furchner and A. Mersmann. Foam breaking by high speed rotors. *Chemical Engineering Technology*, 13:86–96, 1990.

[187] Lord Rayleigh. On the equilibrium of liquid conducting masses charged with electricity. *Philosophical Magazine*, 14:184–186, 1882.

[188] Adrian G. Bailey. *Electrostatic spraying of liquids*, volume 10 of *Electrostatics and electrostatic applications series*. Research studies press LTD, Somerset, 1988.

[189] David J. Griffiths. *Introduction to Electrodynamics*. Prentice Hall, Upper Saddler River, New Jersey, third edition, 1999.

[190] D. Duft, T. Achtzehn, R. Muller, B. A. Huber, and T. Leisner. Coulomb fission - Rayleigh jets from levitated microdroplets. *Nature*, 421(6919):128–128, 2003.

[191] C. T. R. Wilson and G. I. Taylor. The bursting of soap-bubbles in a uniform electric field. *Proceedings of the Cambridge Philosophical Society*, 22:728–730, 1925.

[192] G. I. Taylor. Disintergration of water drops in an electric field. *Proceedings of the Royal Society of London. Series A*, 280:383–397, 1964.

[193] J. Zeleny. The electrical discharge from liquids points, and a hydrostatic method of measuring the electric intensity at their surfaces. *The Physical Review*, 3(2):69–91, 1914.

[194] J. Zeleny. Instability of electrified surfaces. *The Physical Review*, 5(1):1–7, 1917.

[195] G. Joffre, B. Prunet-Foch, S. Berthomme, and M. Cloupeau. Deformation of liquid menisci under the action of an electric field. *Journal of Electrostatics*, 13:151–165, 1982.

[196] J. A. Cross. *Electrostatics: principles, problems and applications.* IOP Publishing Limited, Bristol, 1987.

[197] Tatsushi Matsuyama, Takuya Abe, and Hideo Yamomoto. Lattice Boltzmann method study of Rayleigh instability of a charged droplet. *Advanced Powder Technology*, 18(1):93–104, 2007.

[198] Jean-Louis Naudin. The Lafforgue's electrostatic pressure experiment, http://jnaudin.free.fr/lfpt/html/lelpv1.htm, 2002.

[199] Kenneth L. Kaiser. *Electrostatic discharge.* Taylor and Francis Group, 2006.

[200] A. Jaworek and A. Krupa. Classification of the modes of EHD spraying. *Journal of Aerosol Science*, 30(7):873–893, 1999.

[201] S. O. Shiryaeva and A. I. Grigor'ev. The semiphenomenological classification of the modes of electrostatic dispersion of liquids. *Journal of Electrostatics*, 34:51–59, 1995.

[202] M. Cloupeau and B. Prunetfoch. Electrohydrodynamic spraying functioning modes - a critical-review. *Journal of Aerosol Science*, 25(6):1021–1036, 1994.

[203] I. G. Loscertales, A. Barrero, I. Guerrero, R. Cortijo, M. Marquez, and A. M. Ganan-Calvo. Micro/nano encapsutation via electrified coaxial liquid jets. *Science*, 295(5560):1695–1698, 2002.

[204] Maurice Ravaille. *Electrostatique, Electrocinétique.* Collection de Sciences Physiques. Bailliere J.B. et fils, 1964.

[205] X. P. Chen, L. B. Jia, X. Z. Yin, J. S. Cheng, and J. Lu. Spraying modes in coaxial jet electrospray with outer driving liquid. *Physics of Fluids*, 17(3), 2005. 032101.

[206] Lord Rayleigh. On stability of jets. *Proceedings of London Mathematics Society*, 4(10):4–13, 1878.

[207] W. Drenckhan, S. Gatz, and D. Weaire. Wave patterns of a rivulet of surfactant solutions in a Hele-Shaw cell. *Physics of Fluids*, 2004.

[208] E. Janiaud. *'Élasticité, Morphologie et Drainage Magnétique dans les Mousses Liquides.* PhD thesis, Université Paris 7, 2004.

[209] H. M. Princen and S. G. Mason. Shape of a fluid drop at a fluid-liquid interface .1. extension and test of 2-phase theory. *Journal of Colloid Science*, 20(2):156–172, 1965.

[210] C. G. B. Cole. Gelatin. In Frederick J Francis, editor, *Encyclopedia of Food Science and Technology*, pages 1183–1188. New York: John Wiley and Sons, 2nd edition, 2000.